

# **Stoping Sequence Optimization based on Slope Stability Assessment Using Finite Element Modelling Method**

By

Huawei Xu

A thesis submitted in partial fulfillment of the requirements for the degree of

Doctor of Philosophy

in

Mining Engineering

Department of Civil and Environmental Engineering

University of Alberta

© Huawei Xu, 2021

## **ABSTRACT**

Sublevel stoping mining method is widely used in Canada to excavate the steeply dipping orebodies. With such mining method, stope is the basic excavation element, and sill pillars are reserved to prevent the transfer of mining-induced stress among different mining levels, and the mined-out stope voids are backfilled. However, recovering sill pillars can trigger catastrophic problems. To safely recover the sill pillars, a feasible recovery scheme is a great challenge with most mining operations in underground mining.

To reach the objectives of this research thesis, a Canadian diamond mine was analyzed as the case study and a full size three-dimensional finite element model of the mine was developed by using the finite element method (FEM) with the application of ABAQUS codes. Laboratory tests were conducted to achieve the rock mechanics parameters of kimberlite, backfilled cemented rockfill (CRF). The developed numerical model was calibrated and verified by comparing the data from the FE model and the recorded in-situ data to conduct to proposed analysis.

According to the analysis results, firstly, the influences of different excavation and backfilling length effects on the stope sidewalls are almost the same, which makes the numerical modelling analysis productive by combining the excavation and backfilling schedules in large size numerical model. Then, for the optimum location of last mined stope, with the influence of backfilling, last mined stopes during production should be at the center of the level, and in sill pillar recovery, last mined stopes should be at least four-stope-width away from the two mining level edges. For the stability of the boundary of the kimberlite mining pipe, it has higher possibility of instability during the mining activities, especially for the accesses to the stopes in deeper mining levels. Finally, the three proposed schemes of sill pillar recovery were assessed. All three recovery schemes were

proved to be feasible to recover the sill pillars, and the scheme of starting from both sills (SBS) was the optimum scenario.

## **PREFACE**

This thesis is an original work by Huawei Xu. This study was supported by the Natural Sciences and Engineering Research Council of Canada (NSERC) under Collaborative Research and Development (CRD) Grant and the Chinese Scholarship Council (CSC). Chapter 3 was based on paper “Xu, H., Apel, D. B. (2020). Optimum location of last-mined stope with the influence of backfilling. *Journal of Sustainable Mining*”, “Xu, H., Apel, D. B. (2021). Study of the influence of backfilling on stability and location of remaining stopes in sill pillar recovery. *International Journal of GEOMATE*”. Chapter 4 was based on paper “Xu, H., Apel, D. B., Wang, J., Wei, Ch., Pourrahimian, Y (2021). Investigation of backfilling step effects on stope stability. *Mining*”. This study was supported by the Natural Sciences and Engineering Research Council of Canada (NSERC) under Collaborative Research and Development (CRD) Grant and the Chinese Scholarship Council (CSC).

This collaborative research was led by Professor Derek Apel at the University of Alberta with guidance from the industrial collaborator represented by Mr. Jan Romanowski, the superintendent of underground mine technical services at Diavik Diamond Mine, Canada.

## DEDICATION

This thesis is dedicated to:

*My great parents Gengyin Xu and Wang Li*

*My lovey three sisters: Weihua Xu, Jiehua Xu and Xianghua Xu*

## ACKNOWLEDGEMENTS

I would like to present my greatest gratitude to my supervisor Dr. Derek B. Apel for his supporting supervision, and encouragements during my study and research period. I want to thank him for his patience and passing to me his knowledge based on his inimitable academic achievement and industrial experience.

I would like to thank my parents. Both my parents had no high education background, but they encouraged me all the time to pursue the higher education. All the achievements owe to them.

I would like to express my gratitude and appreciation to the thesis examining committee members: Dr. Wei Liu and Dr. Yashar Pourrahimian for their precious time and constructive criticisms and comments. They brought out the best in me.

With a special mention to Dr. Mohammadali Sepehri, Dr. Yunayuan Pu, Bob Andrea Lingga, Chong Wei, Jun Wang, my dear colleagues in general. It was an amazing time to work with you.

I would like to thank Dr. Doug Booth for giving me advice about three-dimensional models in AutoCAD and Dr. Samer Adeeb for answering my questions regarding to Abaqus.

This research has been enabled by using the supercomputer resources provided by WestGrid and Compute/Calcul Canada. I would like to thank Mr. Chris Want, and Mr. Kamil Marcinkowski, the WestGrid's support team members, for their outstanding work helping me to use the supercomputers during this research.

I am also grateful to the Chinese Scholarship Council (CSC) that provides me all the living cost during my PhD career. Thank you.

Thanks for all your encouragement!

# TABLE OF CONTENT

ABSTRACT.....	ii
PREFACE.....	iv
DEDICATION.....	v
ACKNOWLEDGEMENTS.....	vi
TABLE OF CONTENT.....	vii
LIST OF TABLES.....	xi
LIST OF FIGURES.....	xii
LIST OF ABBREVIATIONS.....	xvii
LIST OF SYMBOLS.....	xix
CHAPTER 1: INTRODUCTION.....	1
1.1 Introduction.....	2
1.2 Problem statement.....	4
1.3 Literature review.....	5
1.4 Research methodology.....	10
1.5 Organization of thesis.....	11
CHAPTER 2: ROCK MECHANICS LABORATORY EXPERIMENTS AND FINITE ELEMENT ANALYSIS MODEL ESTABLISHMENT AND MODIFICATION.....	13
2.1 Introduction.....	14
2.2 Case study background of Diavik Diamond Mine.....	14
2.2.1 Sublevel stoping and blasthole stoping mining method.....	17
2.3 Methodology.....	18
2.3.1 Finite element method.....	19
2.3.2 Laboratory test for rock mechanics parameters.....	20
2.3.2.1 Brazilian tensile test.....	22
2.3.2.2 Uniaxial compressive strength test.....	24
2.3.2.3 Triaxial compressive strength test.....	28
2.3.3 Input parameters in the finite element (FE) model.....	30
2.4 Model simplification and modification.....	33
2.4.1 Model geometry simplification and modification.....	33
2.4.2 Finite element mesh density convergence study.....	37
2.4.3 Excavation scheme modification and simplification.....	40

2.4.3.1 Comparison of three principal stresses between scenario M and NM .....	40
CHAPTER 3: EXCAVATION LENGTH EFFECTS AND BACKFILLING LENGTH EFFECTS ON	
STOPE STABILITY .....	
3.1 Literature review of excavation length effect on stope stability .....	51
3.1.1 Five various excavation scenarios.....	54
3.1.2 Excavation length effect on displacement.....	55
3.1.3 Excavation length effect on major principal stress .....	60
3.1.4 Excavation length effect on potential damage initiation (DI).....	66
3.1.5 Influence of mining depth on excavation length effect.....	71
3.1.6 Comparison of consumed CPU time among different excavation scenarios .....	74
3.1.7 Conclusions.....	76
3.2 Backfilling step effect on stope stability.....	78
3.2.1 Literature review .....	78
3.2.2 Backfilling step scenarios .....	81
3.2.3 Results and discussion .....	83
3.2.3.1 Backfilling step effect on sidewall displacement.....	84
3.2.3.2 Backfilling step effect on major principal stress.....	89
3.2.3.3 Backfilling step effect on sidewall stress concentration factor (SCF) .....	94
3.2.3.4 Discussions .....	100
3.2.3.5 Conclusions.....	101
3.3 Chapter summary .....	103
CHAPTER 4: OPTIMUM LOCATION OF THE LAST-MINED STOPE IN MINING LEVEL	
DURING MINING AND PILLAR RECOVERING WITH THE INFLUENCE OF BACKFILLING	
4.1 Optimum location of the last-mined stope with the influence of backfilling.....	106
4.1.1 Stope configuration at mining levels .....	106
4.1.2 Literature review .....	107
4.1.3 Last-mined stope location scenarios .....	109
4.1.4 Displacement of chosen location in the overcut .....	112
4.1.5 Displacement of chosen location in undercut .....	115
4.1.6 Discussions and Conclusions .....	118
4.2. Optimum location for the last-mined stope in sill pillar recovery .....	119
4.2.1 Last mined stope location scenarios.....	120
4.2.2 Results and discussion .....	123
4.2.3 Conclusions.....	126
4.3 Chapter summary .....	127

CHAPTER 5: ASSESSMENT OF THE STABILITY OF STOPE ACCESSES AND HAULAGE CONNECTIONS .....	129
5.1 Introduction.....	130
5.2 Rockburst potential criteria.....	134
5.2.1 Criterion of tangential stress (CTS) .....	134
5.2.2 Energy-based burst potential index.....	134
5.2.3 Criterion of elastic strain energy .....	135
5.3 Stability assessment of stope access intersection.....	137
5.3.1 Assessment of the rockburst potential of stope access intersection .....	138
5.3.1.1 Energy based burst potential index (BPI) of the stope accesses .....	140
5.3.1.2 Tangential stress criterion (Ts) of the stope accesses .....	144
5.4 Stability assessment of haulage accesses .....	150
5.4.1 Energy based burst potential index (BPI) of the haulage drift accesses .....	151
5.4.2 Tangential stress criterion (Ts) of the haulage drift accesses .....	154
5.5 Comparison of the stability of stope accesses to the stopes at three locations.....	157
5.6 Chapter summary and conclusions .....	161
CHAPTER 6: ASSESSMENT OF FEASIBILITY OF RECOVERING SILL PILLAR AND COMPARATIVE STUDY OF THREE SCHEMES OF SILL PILLAR RECOVERY .....	163
6.1 General background of sill pillars at Diavik diamond mine .....	164
6.2 Literature review .....	165
6.3 Calibration and verification of the finite element (FE) model.....	167
6.3.1 Initial stress state of geostatic step.....	167
6.3.1 Mining induced ground displacement at monitoring zones .....	168
6.4 Schemes of sill pillar recovery.....	172
6.4.1 Stress condition around the mining pipe A154N pre-sill-pillar-recovery.....	172
6.4.2 Proposed three sill pillar recovery schemes.....	174
6.5 Comparison of displacement at four prisms among the three sill pillar recovery schemes .....	176
6.6 Displacement of the upper levels caused by sill pillars .....	179
6.7 Assessment of the stope and haulage accesses stability among three pillar recovery schemes .....	182
6.7.1 Assessment of the stope access stability among three pillar recovery schemes .....	182
6.7.1.1 Tangential stress criterion (Ts) .....	182
6.7.1.2 Energy based burst potential index criterion (BPI).....	190
6.7.2 Assessment of the haulage drift stability among three pillar recovery schemes.....	197
6.7.2.1 Tangential stress criterion (Ts) .....	197
6.7.2.2 Energy based burst potential index criterion (BPI).....	201

6.8 Chapter summary and conclusions ..... 204

CHAPTER 7: SUMMARY, CONCLUSION AND RECOMMENDATIONS ..... 207

7.1 Summary of the research ..... 208

7.2 Conclusions of this research ..... 211

7.3 Recommendations for future work ..... 216

BIBLIOGRAPHY ..... 217

Appendix I: Laboratory Test Results Plots ..... 235

Appendix II: Numerical Simulation Steps ..... 242

## LIST OF TABLES

Table 2.1 Kimberlite and CRF sample rock type.....	21
Table 2.2 Total number of tested samples with effective results .....	22
Table 2.3 Tensile strength of kimberlite samples .....	23
Table 2.4 UCS test results.....	27
Table 2.5 Triaxial test results of kimberlite and CRF samples .....	29
Table 2.6 Rock mass properties introduced in numerical model .....	30
Table 2.7 CPU time for the first ten simulation steps.....	39
Table 2.8 CPU time comparison between scenario NM and M.....	43
Table 3.1 Five excavation scenarios .....	54
Table 3.2 Five backfilling scenarios .....	83
Table 5.1 Rockburst tendency prediction based on CTS .....	134
Table 5.2 Rockburst rating system based on SED .....	136
Table 6.1 Comparison of the displacement between in-situ data and the FE model computation .....	172
Table 6.2 Sill pillar recovery induced displacement at monitoring zones .....	178
Table 6.3 Sill pillar recovery induced displacement at upper levels.....	181
Table 6.4 Rockburst tendency prediction based on CTS .....	182

## LIST OF FIGURES

Figure 2.1 Aerial view of Diavik Diamond Mine .....	14
Figure 2.2 Location of three pipes .....	15
Figure 2.3 Views inside a BHS stope and an open void by SLR.....	15
Figure 2.4 Stope configuration and mining sequence.....	16
Figure 2.5 Apparatus for Brazilian, UCS and Triaxial Test .....	20
Figure 2.6 Example of Brazilian test load figure (A154N-U435-09).....	23
Figure 2.7 Kimberlite samples before Brazilian test.....	24
Figure 2.8 Kimberlite samples after Brazilian test.....	24
Figure 2.9 Example of UCS test of sample (A154-U438-06).....	26
Figure 2.10 Kimberlite samples for UCS test .....	26
Figure 2.11 CRF sample and small kimberlite sample for UCS test .....	27
Figure 2.12 Kimberlite samples for triaxial test.....	28
Figure 2.13 Backfilled CRF sample and Hoek cell of triaxial test .....	28
Figure 2.14 Laboratory test workflow .....	32
Figure 2.15 Three-dimensional concept profile of Diavik underground mining pipe .....	33
Figure 2.16 Full size model outline of Diavik Diamond Mine .....	34
Figure 2.17 Monitor prisms on open pit bench .....	35
Figure 2.18 Comparison of displacement among three scenarios.....	36
Figure 2.19 Vertical stress at bottom of N9175 .....	36
Figure 2.20 Modified model size outline of Diavik Diamond Mine.....	37
Figure 2.21 Finite element (FE) mesh of model .....	38
Figure 2.22 Comparison example of mesh density.....	38
Figure 2.23 Major principal stress comparison between scenario M and NM .....	41
Figure 2.24 Intermediate principal stress comparison between scenario M and NM .....	41
Figure 2.25 Minor principal stress comparison between scenario M and NM .....	42
Figure 2.26 Consumed CPU time decrease comparison between scenario M and NM.....	43
Figure 2.27 Profile of 3D FE model with A154N mined.....	44
Figure 2.28 Fracture boundary between granite and kimberlite pipe .....	45
Figure 2.29 Initial computed geostatic step stress condition in FE model.....	46
Figure 2.30 Simulation steps at one level in FE model.....	47
Figure 3.1 Profile of mining pipe A154N and stope S2-133 .....	53
Figure 3.2 Five excavation scenarios of stope S2-133.....	54
Figure 3.3 Displacement of stope S2-133 two sidewalls in ML#9200 .....	56
Figure 3.4 Displacement of stope S2-133 two sidewalls in ML#Sill2.....	56
Figure 3.5 Displacement of stope S2-133 two sidewalls in ML#9100 .....	57
Figure 3.6 Displacement of stope S2-133 two sidewalls in ML#9050.....	58
Figure 3.7 Displacement of stope S2-133 two sidewalls in ML#9025 .....	59
Figure 3.8 Displacement of stope S2-133 two sidewalls in ML#8975 .....	59
Figure 3.9 Major principal stress of stope S2-133 two sidewalls in ML#9200 .....	61
Figure 3.10 Major principal stress of stope S2-133 two sidewalls in ML#Sill2.....	62
Figure 3.11 Major principal stress of stope S2-133 two sidewalls in ML#9100 .....	62

Figure 3.12 Major principal stress of stope S2-133 two sidewalls in ML#9050 .....	63
Figure 3.13 Major principal stress of stope S2-133 two sidewalls in ML#9025 .....	64
Figure 3.14 Major principal stress of stope S2-133 two sidewalls in ML#8975 .....	65
Figure 3.15 DI of two sidewalls of stope S2-133 in ML#9200 .....	67
Figure 3.16 DI of two sidewalls of stope S2-133 in ML#Sill2.....	67
Figure 3.17 DI of two sidewalls of stope S2-133 in ML#9100 .....	68
Figure 3.18 DI of two sidewalls of stope S2-133 in ML#9050 .....	69
Figure 3.19 DI of two sidewalls of stope S2-133 in ML#9025 .....	70
Figure 3.20 DI of two sidewalls of stope S2-133 in ML#8975 .....	70
Figure 3.21 Comparison of displacement among six mining levels .....	72
Figure 3.22 Comparison of major principal stress among six mining levels.....	72
Figure 3.23 Comparison of damage initiation (DI) among six mining levels.....	73
Figure 3.24 CPU time for different excavation scenarios at each mining level.....	74
Figure 3.25 Comparison of CPU time between SCN#5 and SCN#1 at each level .....	75
Figure 3.26 Profile of analyzed levels and stope S2-133 .....	81
Figure 3.27 Five backfilling step scenarios .....	82
Figure 3.28 Displacement of two sidewall middle at level ML#8975 .....	84
Figure 3.29 Displacement of two sidewall middle at level ML#9025 .....	85
Figure 3.30 Displacement of two sidewall middle at level ML#9050 .....	86
Figure 3.31 Displacement of two sidewall middle at level ML#9100 .....	86
Figure 3.32 Displacement of two sidewall middle at level ML#Sill2 .....	87
Figure 3.33 Displacement of two sidewall middle at level ML#9200 .....	88
Figure 3.34 Comparison of displacement among six levels of scenario SCN#5 .....	88
Figure 3.35 Major principal stress of two sidewall middle of level ML#8975.....	89
Figure 3.36 Major principal stress of two sidewall middle of level ML#9025.....	90
Figure 3.37 Major principal stress of two sidewall middle of level ML#9050.....	91
Figure 3.38 Major principal stress of two sidewall middle of level ML#9100.....	91
Figure 3.39 Major principal stress of two sidewall middle of level ML#Sill2 .....	92
Figure 3.40 Major principal stress of two sidewall middle of level ML#9200.....	93
Figure 3.41 Comparison of major principal stress among six levels of scenario SCN#5.....	94
Figure 3.42 <i>SCF</i> of two sidewall middle at level ML#8975 .....	95
Figure 3.43 <i>SCF</i> of two sidewall middle of level ML#9025 .....	96
Figure 3.44 <i>SCF</i> of two sidewall middle of level ML#9050 .....	96
Figure 3.45 <i>SCF</i> of two sidewall middle of level ML#9100 .....	97
Figure 3.46 <i>SCF</i> of two sidewall middle of level ML#Sill2.....	98
Figure 3.47 <i>SCF</i> of two sidewall middle of level ML#9200 .....	99
Figure 3.48 Comparison of <i>SCF</i> of SCN#5 among six mining levels .....	100
Figure 4.1 Stope mining and backfilling in level N9050 and N9075 .....	106
Figure 4.2 Example scenarios with overcut of Case-1.....	110
Figure 4.3 Example scenarios with undercut of Case-2.....	110
Figure 4.4 Example scenarios with overcut of Case-3.....	111
Figure 4.5 Chosen comparison location in overcut.....	112

Figure 4.6 Overcut displacement at node1, node3 of cases C1 and C3 .....	112
Figure 4.7 Overcut displacement at node2, node6 of cases C1 and C3 .....	113
Figure 4.8 Overcut displacement at node4, node8 of cases C1 and C3 .....	114
Figure 4.9 Overcut displacement at node5, node7 of cases C1 and C3 .....	115
Figure 4.10 Undercut displacement at node1, node3 of cases C2 and C3 .....	115
Figure 4.11 Undercut displacement at node2, node6 of cases C2 and C3 .....	116
Figure 4.12 Undercut displacement at node4, node8 of cases C2 and C3 .....	117
Figure 4.13 Undercut displacement at node5, node7 of cases C2 and C3 .....	117
Figure 4.14 Profile of sill pillar location.....	121
Figure 4.15 Example stope location layout of sill pillar .....	122
Figure 4.16 Displacement at Node-1, Node-3 in both overcut and undercut.....	123
Figure 4.17 Displacement at Node-2, Node-6 in both overcut and undercut.....	124
Figure 4.18 Displacement at Node-4, Node-8 in both overcut and undercut.....	125
Figure 4.19 Displacement at Node-5, Node-7 in both overcut and undercut.....	125
Figure 5.1 Schematic three rockburst potentials .....	132
Figure 5.2 Rockburst cases at Diavik Diamond Mine .....	133
Figure 5.3 Profile of stope access and intersection.....	137
Figure 5.4 Rock failures in the stope access at Diavik diamond mine.....	138
Figure 5.5 Stope access and haulage drifts between level N9050 and N9075.....	139
Figure 5.6 Analyzed four corners in undercut and overcut.....	140
Figure 5.7 BPI of the stope access at right-edge stope in five mining levels.....	141
Figure 5.8 BPI of the stope access at middle stope.....	142
Figure 5.9 BPI of the stope access at left-edge stope.....	144
Figure 5.10 Ts of the stope access at right-edge stope in five mining levels.....	145
Figure 5.11 Ts of the stope access at middle stope in five mining levels .....	146
Figure 5.12 Ts of the stope access at left-edge stope in five mining levels .....	148
Figure 5.13 Profile of stope and haulage access .....	150
Figure 5.14 BPI of the stope access at right-edge haulage drift.....	151
Figure 5.15 BPI of the stope access at middle haulage drift.....	152
Figure 5.16 BPI of the stope access at left-edge haulage drift.....	153
Figure 5.17 Ts of the stope access at right-edge haulage drift access.....	154
Figure 5.18 Ts of the stope access at middle haulage drift access .....	155
Figure 5.19 Ts of the stope access at left-edge haulage drift access.....	156
Figure 5.20 Comparison of BPI of three stope accesses in L#9000 .....	157
Figure 5.21 Comparison of BPI of three stope accesses in L#9050 .....	158
Figure 5.22 Comparison of BPI of three haulage accesses in L#9000 .....	159
Figure 5.23 Comparison of BPI of three haulage accesses in L#9050 .....	160
Figure 6.1 Profile of two sill pillars in pipe A154N .....	164
Figure 6.2 Aerial view of Diavik diamond mine .....	165
Figure 6.3 Initial computed maximum stress in FE model at geostatic step.....	168
Figure 6.4 Monitor prisms on open pit bench .....	168
Figure 6.5 Computed displacement in FE model before sill pillar recovery .....	169

Figure 6.6 Displacement comparison between in-situ data and FE model at CRF-S .....	170
Figure 6.7 Displacement comparison between in-situ data and FE model at CRF-N.....	171
Figure 6.8 Yield zones before the recovery of the two sill pillars .....	173
Figure 6.9 Maximum tangential stress before the recovery of the two sill pillars.....	173
Figure 6.10 Profile of sill pillar recovery scheme of SBS .....	174
Figure 6.11 Profile of sill pillar recovery scheme of SS1 .....	175
Figure 6.12 Profile of sill pillar recovery scheme of SS2 .....	175
Figure 6.13 Comparison of displacement at monitored prism 280-12 and 280-10.....	176
Figure 6.14 Comparison of displacement at monitored site S01-02 and N01-02.....	177
Figure 6.15 Displacement after the recovery of two sill pillars (by scheme SS1).....	179
Figure 6.16 Chosen monitored location on upper bench levels .....	179
Figure 6.17 Displacement comparison at monitored location .....	180
Figure 6.18 Stope access and Haulage drifts to Sill-1 .....	183
Figure 6.19 Profile of chosen corners in overcut and undercut .....	183
Figure 6.20 Ts of right-edge stope access to undercuts in Sill-1 .....	184
Figure 6.21 Ts of middle stope access to undercuts in Sill-1.....	185
Figure 6.22 Ts of left-edge stope access to undercuts in Sill-1 .....	186
Figure 6.23 Ts of right-edge stope access to overcuts in Sill-1 .....	187
Figure 6.24 Ts of right-edge stope access to undercuts in Sill-2 .....	188
Figure 6.25 Ts of right-edge stope access to overcuts in Sill-2 .....	189
Figure 6.26 BPI of right-edge stope access to undercut in Sill-1.....	192
Figure 6.27 BPI of middle stope access to undercut in Sill-1 .....	193
Figure 6.28 BPI of left-edge stope access to undercut in Sill-1 .....	194
Figure 6.30 BPI of right-edge stope access to undercut in Sill-2.....	196
Figure 6.31 BPI of right-edge stope access to overcut in Sill-2.....	197
Figure 6.32 Chosen haulage drift access locations in Sill-1 .....	198
Figure 6.33 Ts of right-edge haulage drift access to undercuts in Sill-1 .....	199
Figure 6.34 Ts of middle haulage drift access to undercuts in Sill-1.....	200
Figure 6.35 Ts of left-edge haulage drift access to undercuts in Sill-1.....	201
Figure 6.36 BPI of right-edge haulage access in Sill-1.....	202
Figure 6.37 BPI of middle haulage access in Sill-1 .....	203
Figure 6.38 BPI of left-edge haulage access in Sill-1 .....	203
Figure 7.1 Visual summary of the research methods.....	210
Figure AI-1 Mohr-Coulomb curve of Kimberlite sample of A154N pipe.....	235
Figure AI-2 Mohr-Coulomb curve of Kimberlite sample of A154S pipe.....	235
Figure AI-3 Mohr-Coulomb curve of Kimberlite sample of A418 pipe.....	236
Figure AI-4 Mohr-Coulomb curve of backfilled CRF of A154N pipe .....	236
Figure AI-5 UCS test of backfilled CRF of A154N pipe.....	237
Figure AI-6 UCS test of Kimberlite of A154N pipe.....	237
Figure AI-7 Tensile strength estimation of Kimberlite of A154N pipe.....	238
Figure AI-8 Tensile strength estimation of Kimberlite of A154S pipe .....	238
Figure AI-9 Tensile strength estimation of Kimberlite of A418 pipe.....	239

Figure AI-10 Uniaxial strength estimation of Kimberlite of A154N pipe.....	239
Figure AI-11 Uniaxial strength estimation of Kimberlite of A154S pipe.....	240
Figure AI-12 Uniaxial strength estimation of Kimberlite of A418 pipe.....	240
Figure AI-13 Triaxial failure strength estimation of Kimberlite of A418 pipe with 1.5MPa confinement .....	241

## LIST OF ABBREVIATIONS

2D	Two-Dimensional
3D	Three-Dimensional
ASTM	American Society for Testing and Materials
BHS	Blasthole Stopping
BMVK	Black Macrocrystic Volcaniclastic Kimberlite
BPI	Burst Potential Index
BT	Brazilian Test
C1	Case-1
C2	Case-2
C3	Case-3
CPU	Central Process Unit
CRF	Cemented Rockfill
CTS	Criterion of Tangential Stress
DDM	Diavik Diamond Mine
DN1	Down Left Corner
DN2	Down Right Corner
DI	Damage Initiation
ESR	Energy Storage Rate
FE	Finite Element
FEM	Finite Element Method
GSI	Geological Strength Index
ISRM	International Society for Rock Mechanics
LSCT	Liner Strain Conversion Transducers
LVDT	Linear Variable Differential Transducer
ML	Mining Level
MK	Magnetic Lapilli Rich Macrocrystic Volcaniclastic Kimberlite
MRK	Mud-Rich Volcaniclastic Kimberlite
PEM	Point-Estimate Method
PK	Pyroclastic Kimberlite
PKX	Olive & Macrocrystic-rich Pyroclastic Kimberlite
RMR	Rock Mass Rating
SLR	Sublevel Longhole Retreat
SBS	Start from Both Sills

SCN	Scenario
SCF	Stress Concentration Factor
SMC	Study of Mesh Convergence
SS1	Start from Sill 1
SS2	Start from Sill 2
Ts	Tangential stress criterion
UCS	Uniaxial Compression Strength
UL	Upper Level
UP1	Up Left Corner
UP2	Up Right Corner
VCR	Vertical Crater Retreat

## LIST OF SYMBOLS

$\sigma_1$	Major Principal Stress
$\sigma_2$	Intermediate Principal Stress
$\sigma_3$	Minor Principal Stress
$\sigma_c$	Uniaxial Compressive Strength
$\sigma_t$	Tensile Strength of Rock Sample
$\sigma_h$	In-situ Horizontal Stress
$\sigma_v$	In-situ Vertical Stress
$K$	Lateral Coefficient of Stress
$m_i$	Hoek-Brown criterion intact material constant
$\Phi$	Friction Angle
$\gamma$	Unit Weight of Rock Mass
$\nu$	Poisson Ratio of Rock
$E$	Young's Modulus
$\epsilon$	Strain
$D$	Diameter
$H$	Height
$\Omega$	Resistance

## CHAPTER 1: INTRODUCTION

*This chapter presents an overview of the research. It discusses the general background of the study; the statement of the problem; the objectives of the study, and the proposed methodology. At the end, the organization of the thesis is outlined.*

## 1.1 Introduction

Sublevel open stoping is a mining method in which ore is blasted from different levels of elevation, and the ore is removed from one level at the bottom of the mine. The orebody is mined in open stopes normally backfilled after being excavated, and the stopes are usually large and in a vertical direction. According to the directions of drilling patterns and blasting, sublevel mining methods can be classified into three categories: (i) blast-hole stoping (BHS), (ii) vertical crater retreat (VCR), and (iii) longhole stoping.

Many diamond mines in Canada have adopted the sublevel stoping method or one of its variations, e.g., blast-hole stoping (BHS) and sublevel long-hole retreat (SLR). BHS is a method that generally contains two sublevels and a certain amount of preparation of the stope before the mining activities are processed. In BHS, one sublevel is for production, also called the undercut, and another sublevel is for drilling, also called the overcut. In SLR, the blocks are excavated by a series of up-hole stopes starting from the far end of the level, then the ore is removed through the production drifts. Using such methods, the orebody is mined out using separate blocks that are divided into stopes. In the sublevel stoping mining method, usually the sill pillars are left between mining blocks to prevent the transferring of mining-induced stress among different mining zones. While trying to extract precious mineral resources, diamond mine operators have a great interest in recovering sill pillars to improve their economic margins. However, the recovery of sill pillars can cause safety problems, especially for mines located close to or underneath large bodies of water. Previous mining processes may have changed the stress conditions in the mine field and caused the redistribution of the stress field. Meanwhile, mining engineers are interested in finding out whether or not the used CRF can bear the mining-induced stresses. Rational recovery of the

sill pillar, safety of the haulage drifts, and optimum location of the last mined stope in the sill pillars play a significant role in the feasibility of sill pillar recovery.

Mining stopes are the excavated blocks of ore and play a significant role in overall mining activity. The stability of stopes before, during, and after excavation often attracts the attention of the mining engineers. Stope failure may result in prolonged production interruption, ore dilution, equipment loss, and even fatality.

Haulage drifts or the main drifts in the mine site, as the main arteries of the mine, play a significant role in transporting the valuable ore with its minerals out of the mining zone. Therefore, assessing the stability of the haulage drifts is an important step in the mine planning process. During mining development, some haulage drifts will be excavated before the excavation of the stopes which connect to the haulage drifts. Then, the excavation of the nearby stopes will induce the change of the stresses and strains of the drifts. This can be attributed primarily to the stress redistribution caused by the removal of ore from the stopes. Mining-induced stress changes and related rock mass relaxation can drastically influence the stability of underground openings. It must also be realized that for many situations associated with deep excavations, it may not be possible or practical to install crack-meters to measure the in-situ stress state. Knowing the stress and strain change trend of each individual drift and haulage is very important, and the numerical simulation method can provide an effective method to analyze the stress and strain change trend of the drifts and haulages. Also, the numerical simulation model can be used to rehearse the mining sequence and give a full history of stress and strain changes during the entire mining process.

To recover the sill pillars safely, this research tries to determine the optimum location of the last mined stope by comparing the areas of the relaxation zone and yielding zone. Moreover, the lengths of drifts that connect the last crossing cuts and the main haulage drifts at each level will be

determined by assessing the stability of the drifts by changing the distance. Finally, a rational ground displacement to excavation step will be developed as a key factor to assess the feasibility of reclamation of the crown pillars.

## **1.2 Problem statement**

When it comes to the stability assessment of stopes, much work has been done on displacement prediction, mining-induced stress assessment, and rock support design. However, the work on the selection of the location of the last-mined stope has rarely discussed, especially in relation to the influence of the CRF backfilling mining method. The location of the last-mined stope with crosscuts plays a key role in mining safety and the resource recovery rate in each level. The rational location of the last-mined stope can not only guarantee the recovery of all resources but also, with lower instability of the crossing cuts below and above the last-mined stope. Besides, most research focuses on the isolated stopes, which is a common practice with the room-pillar mining method but not using the BHS method. With the BHS method, after the excavation of one stope, this stope is backfilled with CRF before the next stope is removed. The stability of the adjacent stope, which is mined at the next step, is very important as it will impact the crossing cuts and nearby drifts.

Usually, most of the research focuses on one isolated tunnels or drifts, which cannot provide a comprehensive analysis of the change trend of the mining-induced stresses. Most stability assessments are conducted without the assumption of the influence of backfilling. Those assessment are made based on the initial stresses and mining-induced stresses. However, backfilled stopes can work to mitigate mining-induced stress despite the strength of the backfill being generally lower than that of the initial rock mass.

Predictions about failure mechanisms, stresses changes, and potential failure zones can be better understood when using numerical modelling. The use of two-dimensional (2D) models provides

time-saving methods and thus are currently widely used. However, analyzing the redistribution of mining-induced stresses in mining stopes and drifts in two-dimensional (2D) is not adequate. Compared to three-dimensional (3D) models, the limitations of two-dimensional (2D) models are obvious, in that they can only give the two directions of the mining site, the stresses are three-dimensional. The direction of the stress also changes during the mining process, and the stress that may induce the failure may not be presented well by the two-dimensional (2D) models, which may produce misleading results. Three-dimensional models can avoid this defect and provide the three-dimensional (3D) changes of stresses and strains.

For the recovery of sill pillars, most current research focuses on room-pillar mining method. However, in these cases, the overburden is still the intact rock mass, and the stress movement and concentration are caused by the layers above the mining level. Most of the cases do not take the backfill into account. Then, the relations between the strength of the CRF, the stress redistribution and ground displacement are not properly assessed.

### **1.3 Literature review**

Pillar recovery is the practice of forming a series of pillars and then partially or totally extracting some or all of the pillars, usually with mining operations retreating out of a panel. Pillar recovery has a history of being the most hazardous form of underground mining, and it has a reputation for being an art as much as a science.

Historically, pillar recovery has always been an integral part of underground mining. Crown and sill pillars are initially left in place to support the great weight of the overburden. Pillar extraction likely accounts for about one-third of the production at some mines (Mark et al., 2003, 2007). Many pillars can account for about 75% of the room-pillar production in North American mines (Mark and Gauna, 2017). Unless these pillars are subsequently recovered, the orebodies in these

---

pillars can never be recovered. Pillar recovery in underground mining is a significant consideration for maximizing resource recovery and mining operations. Meanwhile, during the process of pillar recovery, many risks can be induced, such as overlaying rock subsidence, and pillar failure. The stability assessment of the ground subsidence and mining-induced stress redistribution plays a key role in safe pillar recovery.

Initially, microseismic detection was widely used to monitor the seismic activities caused by the pillar recovery processes. Henning et al. (1992) conducted a series of investigations by employing microseismic analysis and filed instrumentation to examine the geomechanics factors that affect recovery of sill pillars. Hudyma and Potvin (1994, 2000) carried out a detailed study of microseismics, conventional ground control instruments, numerical modelling, and visual observations to understand the mechanisms of pillar failures. Mark et al. (1995, 1997a, 1997b, 2001, 2003, 2005) and Iannacchione et al. (2009) analyzed the strengths and weaknesses of MHRA techniques and assessed the major hazard risks to evaluate sill pillar recovery in two room-pillar mines. Zur et al. (2004) used the enhanced cemented rock-fill for pillar recovery, and the pillars took advantage of the passive confinement effect of CRF to increase the post-peak load bearing ability. Zhukova et al. (2018) used the monitored underground seismic registrations and mathematical models of stress-strain conditions to improve the safety operations under the geodynamic conditions caused by pillar recovery.

With the development of numerical simulation technologies, powerful simulation can give researchers a better understanding of the phenomena and mechanisms of failure. Numerical methods are widely accepted in mine design and feasibility studies. Langston et al. (2006) created a two-dimensional (2D) mining stopes model with Phases<sup>2</sup> to design stope layout, extraction procedures, and ground support, which were successively applied to recover the pillar in a

---

palladium and platinum mine. Labrie et al. (2007) carried out a two-phase in-situ experiment by monitoring sill pillar behaviour, and the experiment was able to detect and monitor changes in rock structures close to failure, and it defined a clear inflection point which could be used as a stop point of the sill pillar. Ghasemi et al. (2010) proposed a new method to assess the risk of pillar recovery operations and classified risk into four states (low, medium, high, and very high) by using the PR-risk indicator. Ghasemi et al. (2012) assessed roof fall risk during retreat mining in room-pillar coal mines. Beruar et al. (2011) developed proper stope sequencing to avoid highly stressed areas during the pillar recovery process by using the MAP3D boundary element program. Sainsbury et al. (2002, 2014) examined the stability and failure mechanisms of undermined stabilized rockfill and simulated pillar recovery by replacing the orebodies with laboratory tested stabilized rockfill, which solved the technical risks associated with the proposed extraction method. Valley et al. (2012) optimized the mining sequence by applying both active and passive methods, and they suggested new directions for the different methods and indicated their potential shortcomings. Townend et al. (2014) proposed five mitigation strategies (upper retreat mining, conversion overhand cut-and-fill to underhand cut-and-fill, conversion cut-and-fill to BHS, de-stress drilling schemes, and a combination of all four methods) to mitigate high stress concentrations while mining sill pillars. Apel et al. (2017) developed a full three-dimensional (3D) finite element model to predict the ground response to each sequence of the mining process and suggested a proper ground support system in the area around a sill pillar. Li et al. (2017) compared storage energy, the sum of fractured energy consumption and friction energy consumption to conduct the assessment of pillar recovery. Sun et al. (2018) used the laboratory tested cemented paste backfill material for pillar recovery in the room-pillar mining method. Zhou et al. (2018) investigated the instability of large mined-out areas triggered by dynamic disturbance resulting

from residual pillar recovery. Kyei et al. (2018) analyzed the fragmentation sizes of blasted rocks and selected the suitable rock particle size which was used for backfilling the mined-out stopes for the sake of sill pillar recovery.

A stope, as the basic excavation element of the sublevel open stoping mining method in underground mining, plays a key role in the whole production process. A number of researchers and scholars have carried out many studies on the design of the size and shape of stopes to guarantee the stability of the stopes during mining activities. Mathews et al. (1980) initially proposed a stability graph to predict open-stope stability, and this method was based on a limited number of cases. Chen et al. (1983) showed that stope height was found to be a critical design parameter, and that delayed backfilling of a large-sized open stope at a great depth did not appreciably change the magnitude and distribution of boundary stresses. Bai et al. (1998) presented a new algorithm to optimize stope design for the sublevel stoping mining method with two parameters: (i) the maximum distance of a block from the raise and (ii) the horizontal width required to bring the farthest block to the raise. Cai et al. (1998) assumed tensile cracking as the dominant fracture mechanism for brittle rocks under compressive pressure. Diederichs et al. (1999) explored the influence of residual tensile strength and boundary parallel relaxation on the failure process by using crack and rock-bridge analogues and updated the empirical stability assessment techniques for underground tunnels and mining stopes. Martin et al. (2003) provided examples to illustrate how the philosophy of the observational design method can be used to infer the in-situ stress state. Zhang and Mitri (2007) presented that previous beneath mining activities significantly affected the stability of stope walls by the method based on yield zone distribution. Cepuritis et al. (2010) back-analyzed hanging wall over-break data from longhole open stopes and established global relationships between velocity and plastic strain and marked increases in over-break. Idris

---

(2011a, 2011b, 2012) studied the stability of open stopes considering the variability in rock mass properties and divided rock mass into six strength classes. Cai (2011) presented a systematic assessment of uncertainty in rock mass characterization in rock engineering. Kurlenya et al. (2012) presented the estimation of stability of stopes in the bottom-up slice mining by modelling the stress-strain state and in situ observations. Urli and Esmaili (2016) presented the ore-skin design approach and showed that the minimum ore-skin thickness that is required depends on the quality of governed rock mass and could be a function of stope lifetime. Heidarzadeh et al. (2018) evaluated the individual and interactive effects of open stope geometrical parameters related to brittle damage of the surrounding rock mass.

Haulage networks are vital to underground mining operations as they constitute the arteries through which mined-out ore is transported to the surface. In the sublevel stoping method and its variations, haulage drifts are excavated as the primary accesses to the mining blocks that will be mined out. Most of the haulage drifts in deep underground mining experience high stresses which can induce haulage drifts instability. Drift instability could lead to serious consequences such as production delays, higher operational cost, injury to workers, or even fatalities. Significant effort is put into understanding the stability of these drifts and reinforcing them with suitable supports during the mine's life. Arjang and Herget (1997) suggested that most mining excavations were subjected to high stress conditions. Sjöberg et al. (2012) identified the failure mechanisms and quantified the controlling factors governing failure of haulage drifts. Zhang and Mitri (2007, 2008) and Abdellah (2015a, 2015b) defined the stability indicators, including displacement, stress, and the extent to which yield zones examine the stability of the haulage drift, through a two-dimensional nonlinear numerical model parametric study. Musunri et al. (2010) used random variables to determine the stability of underground haulage drift. Abdellah et al. (2011, 2013)

---

proved that same-level mining has a stronger influence on the stability of the haulage drift intersection than lower-level mining. Then, he examined the haulage drift safety with extent of yielding, and brittle shear failure as indicators, defined a minimum strength-to-stress ratio as failure criterion, and modified the “point-estimate method” (PEM) to study drift instability at the intersections. Yao et al. (2014) combined site observations, conceptual analysis to investigate the reasons for the poor rock-mass conditions in essential crossing cuts. Raju et al. (2015) found that same-level mining of nearby stopes had a more severe effect on the drift support system than lower-level mining. Li and Guo (2018) showed that the gangue-backfilling mining method reduced the overlaying ground subsidence. Shnorhokian et al. (2014, 2015, 2018) compared the extent of unstable rock mass using shear, compressive, and tensile instability criteria; and determined that shear criterion and tensile instability were the two main decided criteria. Basarir et al. (2019) used the extracted stresses from a three-dimensional (3D) global model into a two-dimensional (2D) local model of the gateway to analyze the stability of the gateway in the mine.

#### **1.4 Research methodology**

To research the above thesis objectives, a mine-size three-dimensional (3D) elastoplastic finite element (FE) model based on the real geometry of the case study mine was developed. The FE model was used to assess the stability of the underground mining structures during the process of excavation and backfilling.

The code of ABAQUS (Dassault Systèmes 2015) was applied to develop the 3D FE model. The three laboratory rock mechanics tests, Brazilian test, uniaxial compressive strength (UCS) test and the triaxial test, of the kimberlite and backfilled cemented rockfill (CRF) samples were conducted to achieve the parameters of the rock samples that were input to the 3D FE ABAQUS model. Due

to the default criterion in ABAQUS is Mohr-Coulomb criterion, then the RocLab Software (Rocscience Inc. 2002) was applied to convert the parameters of the rock sample properties.

Finally, the displacement monitor prisms were installed on the benches at the case study mine to validate the developed 3D FE model.

### **1.5 Organization of thesis**

*Chapter 1* of this thesis presents the overview of this research. It provides the general background of this study, a literature review based on the stated problems and objectives, the statement of problems, the objectives of this study and the proposed methodology of this study.

*Chapter 2* of this thesis presents the basic background of the case study Diavik Daimond Mine, an introduction of the mining method used in the case study, an basic introduction of the numerical finite element method applied in this study, the laboratory rock mechanics tests conducted to achieve the parameters of the rock samples, the simplification and modification of the geometry and mining activities of the finite element model, a study of mesh density convergence and consumed CPU time for the simulation, the simulation steps based on the real mining activities in the finite element model.

*Chapter 3* presents the study of excavation step length and backfilling step length effect on the stope stability by investigating the excavation-induced displacement, redistributed major principal stress, excavation-induced damage initiation (DI), stress concentration factor (SCF). This study paves the foundation of the study in the following chapters, *Chapter 4*, *Chapter 5* and *Chapter 6*.

*Chapter 4* presents the study of the optimum location of the last-mined stopes in each mining level during the normal mining production with the influence of backfilled CRF, and the optimum location of the last-mined stope in the process of the sill pillar recovery with the influence of backfilled CRF by applying the extracted redistributed stress from three-dimensional (3D) finite

element (FE) analysis model to the simplified two-dimensional (2D) finite element (FE) analysis model through a global-to-local method.

*Chapter 5* presents the study of the assessment of the stability of the stope accesses and haulage drifts during the process of excavation and backfilling by the investigation of the rockburst potential tendency applying the tangential stress criterion (Ts), energy-based burst potential index (BPI), and energy storage ratio (ESR). The goal is to locate the possible rockburst area in the A154N mining pipe during the process of excavation and backfilling.

*Chapter 6* firstly presents verification and validation of the developed finite element (FE) model by comparing the FE model computed results to the actual field data and site observations. Then this chapter presents the comparative study of the three different proposed recovery schemes of the two reserved sill pillars by comparing the sill-pillar-recovery-induced displacement of the surrounding dike and monitored prisms on the open pit benches. The possible rockburst in the process of sill pillar recovery is also assessed. The goal is to determine the optimum sill pillar recovery scheme.

*Chapter 7* presents the thesis summary and the research conclusions. The main contributions and the significance of this research are presented and discussed. In addition, the recommendations for the future study of the stability of the underground mining structures during the excavation and backfilling are provided.

---

## **CHAPTER 2: ROCK MECHANICS LABORATORY EXPERIMENTS AND FINITE ELEMENT ANALYSIS MODEL ESTABLISHMENT AND MODIFICATION**

*This chapter presents a case study of Diavik Diamond Mine which was used to implement the research methodology and research objectives. A full three-dimensional finite element model of the mine was constructed based on the real geometry of Diavik Diamond Mine. Rock mechanics laboratory tests were conducted on kimberlite samples and backfilled cemented rockfill (CRF) samples from Diavik Diamond Mine to measure the intact properties of kimberlite and CRF. The results of these laboratory tests were used to estimate the rock mass properties and calibrate the modelling input parameters of the finite element analysis. Finally, the numerical FE model was simplified and modified to achieve a better accuracy-and-time balance.*

## 2.1 Introduction

In this part, the Diavik Diamond Mine (DDM) was chosen as the case study to implement the proposed research methodology and reach the objectives. The full realistic three-dimensional (3D) elastoplastic finite element (FE) model was developed based on the real geometry of DDM. This finite element model was mainly used to analyze the mining-induced redistributed stress regime and the possible failure caused by the redistributed stress regime in mining pipe A154N. The kimberlite samples and backfilled cemented rockfill (CRF) samples shipped from DDM were conducted laboratory tests at the rock mechanics lab at the University of Alberta. The laboratory tests results were used to estimate the rock mass properties and calibrate the parameters input in the FE model.

## 2.2 Case study background of Diavik Diamond Mine

To research the objectives stated in Chapter 1, a case study of the Diavik Diamond Mine was used to illustrate and simulate the proposed procedure, and to implement the proposed methodology.

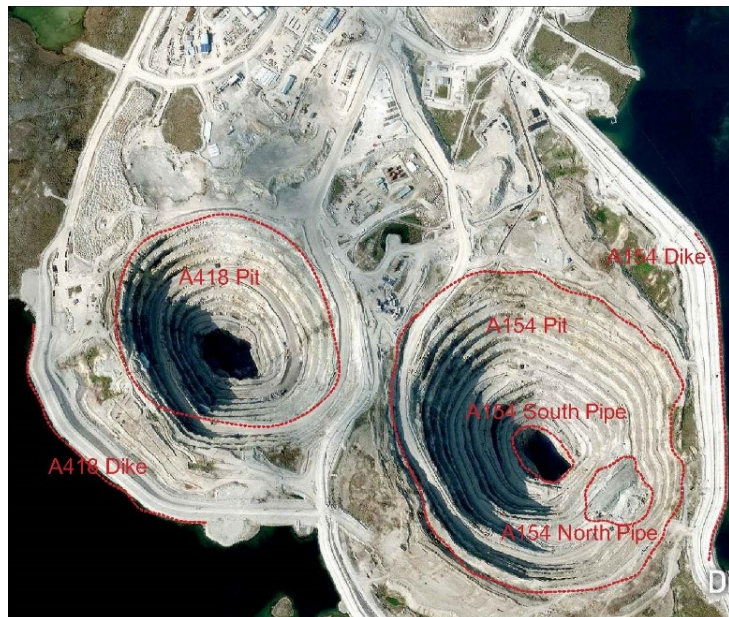


Figure 2.1 Aerial view of Diavik Diamond Mine (courtesy of Diavik Diamond Mine)

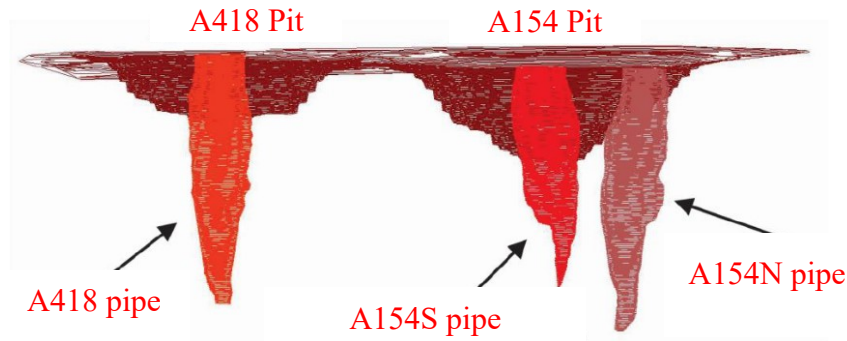


Figure 2.2 Location of three pipes (courtesy of Diavik Diamond Mine)

Diavik Diamond Mine (Diavik, 2011, 2012, 2015) is located on a 20 km<sup>2</sup> island in Lac de Gras, approximately 300 km northeast of Yellowknife, Northwest Territories, Canada. Diavik reserves are contained in three main diamond-bearing kimberlite pipes namely A154 north, A154 south, and A418 pipes, as shown in figure 2.1 and figure 2.2. The host rock mass is granite. All three pipes are located under the waters of Lac de Gras. To enable open pit mining, first the dikes were constructed, and then the water was drained and removed. After the completion of open pit mining, A418 and A154 kimberlite mining pipes were transferred to underground mining. And pit A154 has two kimberlite mining pipes, namely A154S (south) and A154N (north). Figure 2.1 and figure 2.2 illustrates the locations of the three main kimberlite pipes: A154 North, A154 South, and A418.



Figure 2.3 Views inside a BHS stope and an open void by SLR

The planned underground mining methods for the A154 North, A154 South, and A418 kimberlite pipes were SLR and BHS. SLR is being used in the A154S pipe and will be used in A418 pipe. BHS is being used in the A154N pipe for underground mining. Figure 2.3 shows one BHS stope in pipe A154N and one SLR open void in pipe A154S.

According to the updates from DDM, a newly founded third mining block is being mined in A154N pipe, and the sill pillars will be recovered. Then the researched topics in this thesis mainly focus on A154N pipe.

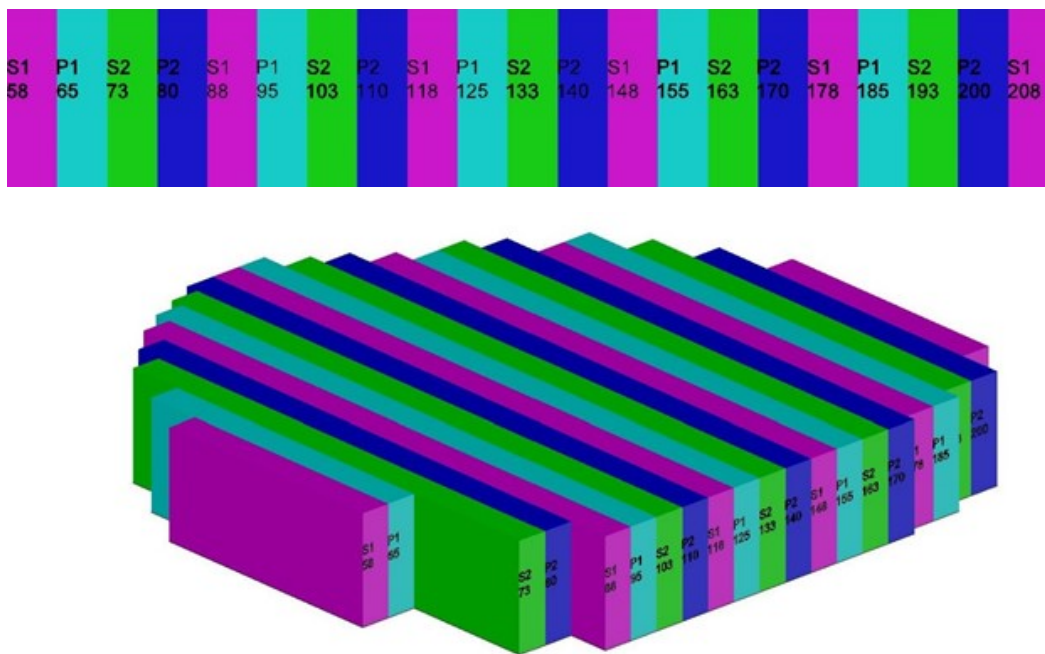


Figure 2.4 Stope configuration and mining sequence

Figure 2.4 shows an example configuration of mining stopes of one mining level in 154N pipe at the DDM. The stopes are represented with different colors to indicate the mining sequence. The color of pink, cyan, green, and blue present the mining sequence, respectively. Here, P stands for the primary sequence, P1 means that those stopes will be mined first in the primary sequence, P2 means the second round of mined stopes in the primary sequence. Then, S stands for the secondary sequence, S1 means the first round of mined stopes in the secondary sequence, and S2 means the

second round of mined stopes in the secondary sequence. When the mining activities of stopes starts, firstly, stope block P1-65 will be mined out, followed by P1-95. After the first round in the primary sequence finishes, the second round of primary sequence starts, and then the first round in secondary sequence starts, followed by the second round in secondary sequence, the stope of S2-193 will be the last mined-out stope in this level. In mining pipe A154N, the first mining blocks, Block A and Block B are mined simultaneously, at each mining block, the mining sequences are the same. There is a reserved sill pillar between the Block A and Block B. The excavation schedules are shown in detail in the appendix.

### **2.2.1 Sublevel stoping and blasthole stoping mining method**

Many underground mines in Canada have adopted sublevel stoping method or one of its variations, such as blasthole stoping (BHS) and sublevel longhole retreat (SLR), for the extraction of steeply dipping orebodies. According to the blast direction and drill patterns, the sublevel mining method can be classified into three main categories: i) vertical crater retreat (VCR); ii) blasthole stoping (BHS); iii) longhole stoping. Generally, BHS mining method has two sublevels, one sublevel is used for drilling blastholes, called overcut; another one sublevel is used for production and transporting the minerals, called undercut. Before the actual mining can be proceeded, a certain amount of preparation work should be done in overcuts and undercuts. Hustrulid et al. (2001) classified the features of the mines which apply BHS mining method, and the features are: i) host rock and orebody are competent, ii) orebody dip is steep, iii) boundaries of orebody are regular.

For most of the hard rock mines in Canada, the orebody blocks are usually steeply inclined. The main research area in this thesis is the mining pipe A154N at DDM which presents a vertical inclination. BHS mining method implements in a primary-secondary sequence manner. The stopes in the primary sequence will be excavated firstly. After the stopes in the primary sequence are

mined and backfilled, the excavation and backfilling process will be started in the secondary sequence. After the production of one mining level completes, the production process moves forward to the next mining levels till the whole mining blocks are backfilled. The mining pipe A154N is vertical inclination, then the stopes in the mining levels at pipe A154N are also vertical inclination. Generally, stopes have a large length compared with the stope height and stope width. In the pipe A154N at DDM, all the stopes have a width of 7.5 m, and the lengths are about 100 m or longer, and the approximate height is 30 m from sill to sill, including the 20 m high stope and 5 m high overcuts and undercuts.

### **2.3 Methodology**

Over the last four decades, with the rapid development of computer hardware and software, numerical modeling to simulate physical phenomena in rock mechanics and rock engineering has gained huge progress. Numerical modeling has the capacity to analyze and design of very complicated geotechnical problems at various engineering scales. Meanwhile, numerical modeling method has the advantages of safety, flexibility, timesaving compared to the other methods such as in-situ field measures and tests and laboratory physical simulation (Hudson and Feng 2007, 2010).

To date, numerical modeling method has gained popularity and been widely used for mining design problems. Using numerical modeling method to model elastoplastic, non-linear, and post-yield behavior of rock masses and the effects of in-situ stresses and excavation features on the mining works can help researchers to understand the “real world” in underground mining (Sepehri 2016, Wang et al. 2020). Thus, the application of the numerical simulation will be a good choice to investigate the influence of mining activities on the underground mining blocks and structures stability. By the application of the numerical simulation method, it can provide the prediction of

the possible and potential failures in the underground mining process by conducting the “rehearsal” of the whole mining process and help the researchers make the rational decision on the schedule and the future mining plans.

### **2.3.1 Finite element method**

Referring to the works of Jing et al. (2002, 2003), Hart (2003), Wiles (2006), and Cai (2008), numerical analysis can assist in the simulation of forced conditions on the rock mass and its response behaviors; this brings the advantage of predicting possible failures by identifying the observed mechanisms that governs failure in similar conditions. Numerical modelling plays a great role in the design and assessment of rock mass behavior; it gives us an opportunity for detailed evaluation and analysis of various mining and engineering problems and provides a broader and more detailed insight into the pre- and post-peak behavior of rock mass (Jing and Hudson 2002, Bobet et al. 2009).

The finite element method (FEM) is perhaps the most widely applied numerical method (Singiresu 2004, Cook et al. 2001, Adeb 2010) in engineering today because of its flexibility in handling material heterogeneity, non-linearity, and complicated boundary conditions and dynamic problems, with many well-developed and verified commercial codes with large capacities in terms of computing power, material complexity, and user-friendliness, according to Sun (2012), Sepehri (2013, 2016, 2017) and Wang (2021).

In this study, the behavior of kimberlite rock mass was analyzed using continuum models. Although in situ rock mass normally contains fractures and discontinuities, while modelling complex geometries of mine-size models including stopes, accompanying drifts and crossings, a continuum model with equivalent parameters can be used to model mining pipe stope behaviors as the pre-existing geo-fractures are distributed quite randomly in various directions and their sizes

are considerably smaller than the whole mine site. Then, a continuous, isotropic, homogeneous and elastic plastic rock mass can be assumed. A full realistic three-dimensional (3D) elastoplastic finite element model of the mine was developed. This finite element (FE) analysis model was used to determine the in situ and mining-induced stress regime at the mine. The goal is to seek a comprehensive understanding of stress redistribution regimes and yielding zones. To reach the objectives of this research, a full realistic three-dimensional numerical FE model based on the real geometry of DDM has been developed. Some simplification and modification were made to better simulate the mining process in the model.

### 2.3.2 Laboratory test for rock mechanics parameters

To acquire the strength properties of kimberlite rock mass and the backfilled cemented rockfill (CRF) that will be introduced into the numerical simulation model, three main laboratory tests were conducted: (i) indirect tensile strength test (Brazilian tensile test), (ii) the uniaxial compressive strength (UCS) test, and (iii) triaxial compressive test.

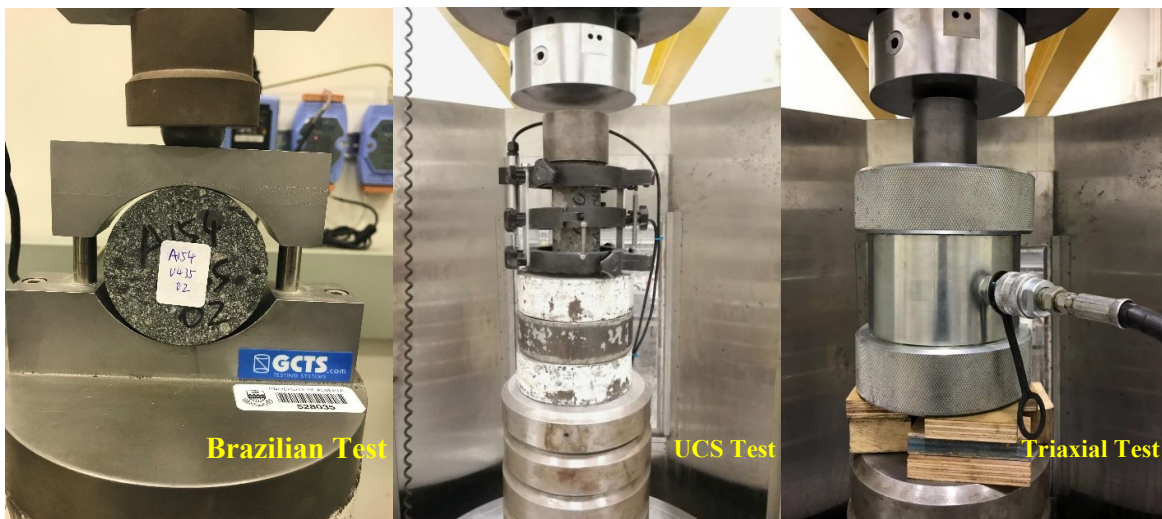


Figure 2.5 Apparatus for Brazilian, UCS and Triaxial Test

All the laboratory tests of these three experiments were conducted in the rock preparation and rock mechanics lab at the University of Alberta. The results from these three main laboratory tests were

used to calibrate and estimate the properties of the kimberlite rock mass in the numerical FE model. The apparatus used for the tests are shown in figure 2.5.

There are five different types of kimberlite at Diavik diamond mine, and all three pipes have these five types of kimberlite. To eliminate laboratory test errors and obtain accurate parameters, cylinder kimberlite samples were collected from all three pipes, A154S, A154N, and A418, and shipped to the lab at the University of Alberta. Cemented rockfill (CRF) from A154N were also collected and tested. Table 2.1 shows the location, rock types, and geological descriptions of the five kimberlite samples and CRF samples.

Table 2.1 Kimberlite and CRF sample rock type

<b>Rock Type</b>	<b>Geological Description</b>	<b>Pipe Location</b>
MK	Magnetic lapilli rich macrocrystic volcanoclastic Kimberlite	A154N, A418
MRK	Mud-rich volcanoclastic Kimberlite	A154N
VBMK	Volcanoclastic black macrocrystic Kimberlite	A154N
PK	Pyroclastic Kimberlite	A154S, A418
PKX	Pyroclastic olive& macrocrystic-rich Kimberlite	A154S
CRF	Mixed with small granite and kimberlite particles and cement	A154N

After receiving the shipped kimberlite samples from the Diavik diamond mine, all the samples were trimmed and prepared according to the ASTM D4543-08 (ASTM 2008, 2010, Bieniawski et al. 1979) procedure in the rock preparation lab at the University of Alberta. Some of the trimmed samples were dumped due to the fractures and cracks caused by the trimming procedure to keep the samples intact. Initially in total, there are 97 groups of Brazilian test, 73 groups of uniaxial

compression strength (UCS) tests and 65 groups of triaxial tests. However, due to some internal fractures caused by trimming process, some results were discarded. Table 2.2 shows the numbers of tested samples with effective results.

Table 2.2 Total number of tested samples with effective results

Test	Brazilian	UCS	Triaxial
A418	15	12	9
A154S	31	13	12
A154N	38	20	15
CRF	NA*	8	6

There are two different diameter sizes of kimberlite samples: one is 2.5 inches (63 mm), and the other is 1.8 inches (47.5 mm). First, all the 1.8 inches (47.5 mm) samples were prepared for the UCS test, and the sample size was 47.5 mm × 95 mm (diameter × height). The 63 mm samples were trimmed into two sizes. One size of sample was trimmed and prepared for the Brazilian test, and the size was 63 mm × 32 mm (diameter × height), with a diameter-to-height ratio of two. The other size of sample was for UCS and triaxial tests, and the size was 63 mm × 126 mm (diameter × height), with a diameter-to-height ratio of two. The backfilled CRF samples were cored from the backfilled stopes in pipe 154N at the mine site, and their diameter was 6 inches (152 mm). Also, the diameter-to-height ratio of the backfilled CRF sample was 2, with a size of 152 mm × 304 mm (diameter × height). All the sizes of the kimberlite and backfilling CRF samples were determined according to ASTM standards, and the shapes of the samples are cylindrical.

### 2.3.2.1 Brazilian tensile test

As an alternative simpler method to conducting a direct tensile test, the Brazilian test is widely used to determine tensile strength (Bieniawski et al. 1979). The purpose of the Brazilian test is to indirectly measure the uniaxial tensile strength of specimens. Also, the Brazilian test represents

the in-situ field condition, in which the tensile strength is acquired with the presence of compressive stress. The tensile strength of the samples can be calculated by the following equation (2.1).

$$\sigma_t = 2P/\pi DL \quad (2.1)$$

where,  $\sigma_t$  is the tensile strength (MPa),  $P$  is the failure load of the sample (N),  $D$  is the diameter of the sample (mm) and  $L$  is the thickness of the sample (mm).

Table 2.3 Tensile strength of kimberlite samples

Sample No.	Diameter (mm)	Height (mm)	$\sigma_t$ (MPa)
A418	62.98	31.46	7.01
A154S	63.26	32.76	12.74
A154N	63.05	32.08	11.66

Table 2.3 shows the results of the kimberlite samples from all three pipes, and all results are the average tensile strength values. Due to the particle sizes in the CRF samples are too large for the Brazilian test according to the ASTM standards (2008), then there were no Brazilian tests for CRF, shown as “NA\*” in the above table 2.2. Following figure 2.6 presents the load curve of the kimberlite sample A154N-U435-09 during the Brazilian test. At the peak load  $P$ , the sample fails.

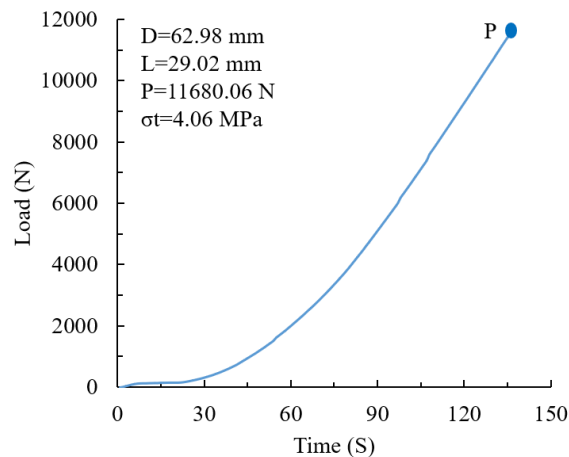


Figure 2.6 Example of Brazilian test load figure (A154N-U435-09)

Figure 2.7 and figure 2.8 show the samples before and after the Brazilian test. Generally, the fractures will initiate from the top and bottom contacted loading surfaces between the loading jaw and sample and get through the whole sample along with the diameter in vertical direction.



Figure 2.7 Kimberlite samples before Brazilian test

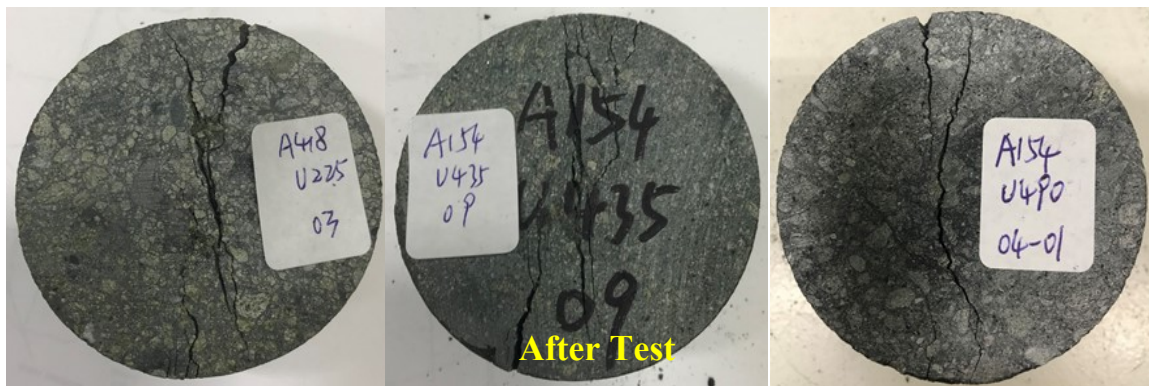


Figure 2.8 Kimberlite samples after Brazilian test

### 2.3.2.2 Uniaxial compressive strength test

The UCS test (ASTM 2010) is a simple and effective method to determine important rock strength properties such as uniaxial compressive strength ( $\sigma_c$ ), Young's modulus (E), and Poisson's ratio ( $\nu$ ). The uniaxial compressive strength (UCS) of the sample can be calculated by the following equations (2.2) and (2.3).

$$\sigma_c = P/A \quad (2.2)$$

$$A = \pi D^2 / 4 \quad (2.3)$$

where  $P$  is the maximum failure load (N) of the sample and  $A$  is the cross-section area ( $\text{m}^2$ ) of the sample,  $D$  is the diameter of the sample.

Young's modulus can be calculated by the axial strain ( $\varepsilon_a$ ) and lateral strain ( $\varepsilon_l$ ). and the axial and lateral strain can be calculated by the following equations (2.4) and (2.5).

$$\varepsilon_a = \Delta L/L \quad (2.4)$$

$$\varepsilon_l = \Delta D/D \quad (2.5)$$

where  $\Delta L$  is the length change of the axial gauge on the sample,  $L$  is the original length of the gauge;  $\Delta D$  is the change of the sample in diameter,  $D$  is the original diameter of the sample.

According to the method proposed by Brady and Brown (2004), there are two main Young's modulus can be calculated by the stress-strain curves.

i): Average Young's modulus  $E_{av}$ , and it is the average slope of the straight part of the stress-strain curve.

ii): Tangent Young's modulus  $E_t$ , and it is the slope of the 50% of the peak strength of the stress-strain curve.

Poisson's ratio is a key factor to reflect the deformable capacity of the sample in both vertical and horizontal directions. It can be calculated by the following equation (2.6).

$$\nu = -\frac{\text{slope of axial curve}}{\text{slope of lateral curve}} = -\frac{E}{\text{slope of lateral curve}} \quad (2.6)$$

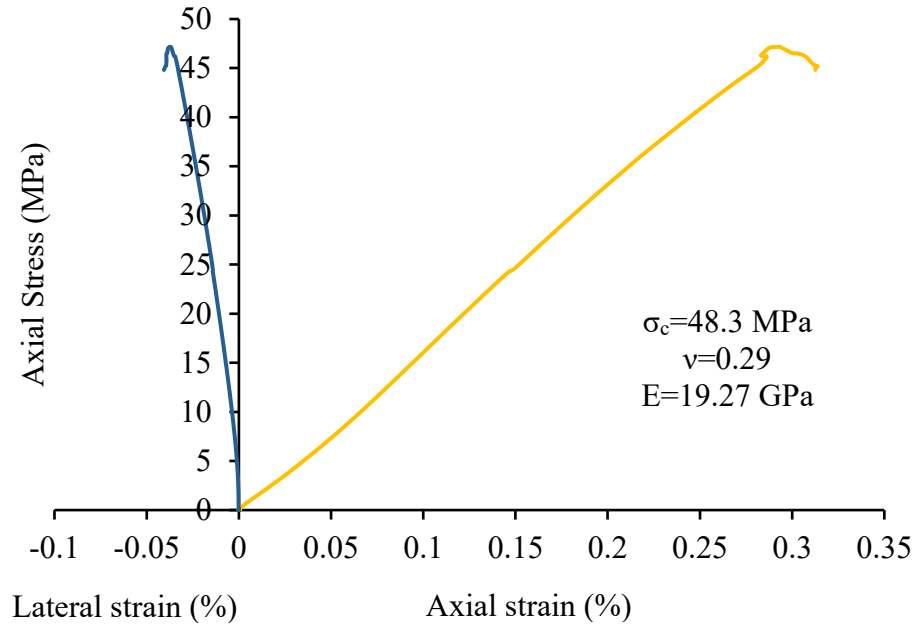


Figure 2.9 Example of UCS test of sample (A154-U438-06)

Figure 2.9 presents one example of the UCS test of sample 154N-U438-06. Following figure 2.10 shows examples of the kimberlite samples for the UCS test. The three samples on the left of the figure are the original samples cored from the A154N pipe and trimmed in the rock mechanics lab according to the ASTM (2010) standards. The three samples have the same size, 47.5 mm  $\times$  95 mm (diameter  $\times$  height). The three samples on the right side of the figure are the samples after the UCS tests, and they present the similar failure mode.



Figure 2.10 Kimberlite samples for UCS test

Because the backfilled CRF samples are of a large size, also the surfaces of the CRF samples do not meet the requirements suggested by ASTM, then the two separate linear strain conversion transducers (LSCT) were used instead of the strain gauges and the circle linear variable differential transducer (LVDT), as shown in figure 2.11. Moreover, for the smaller kimberlite samples with a size of 47.5mm × 95mm, the 350 Ω strain gauges were used.



Figure 2.11 CRF sample and small kimberlite sample for UCS test

After the completion of the UCS tests, the data was collected and analyzed. The total numbers of UCS are shown in table 2.2. Due to some samples have rich initial fractures, the results of this kind of sample vary significantly, and some results were discarded due to high dispersion. The results are shown in table 2.4.

Table 2.4 UCS test results

Sample No.	Diameter (mm)	Height (mm)	$\sigma_c$ (MPa)	E (GPa)	$\nu$
A418	62.99	127.6	51.39	17.26	0.4
A145S	62.80	128.6	51.48	20.07	0.3
A154N	63.16	129.2	72.63	44.42	0.2
CRF	152.33	305.3	8.46	4.22	0.4

### 2.3.2.3 Triaxial compressive strength test

Since the ABAQUS code employs the Mohr-Coulomb failure criterion (Coulomb 1773, Mohr 1900, Labuz et al. 2012), then the friction angle ( $\phi$ ) and cohesive strength ( $C$ ) of the kimberlite samples and CRF samples should be determined. The triaxial tests were conducted to achieve these parameters. The 2.5-inch Hoek cell was used to conduct the kimberlite triaxial test, as shown in above figure 2.5. The kimberlite samples of the triaxial test are illustrated in figure 2.12.



Figure 2.12 Kimberlite samples for triaxial test

Also, the 6-inch Hoek cell, shown in figure 2.13, was used to conduct the triaxial tests for the backfilled CRF samples instead of the 2.5-inch Hoek cell which was shown in figure 2.5.



Figure 2.13 Backfilled CRF sample and Hoek cell of triaxial test

In triaxial tests, the samples are subjected to a homogenous state of stress in which the intermediate principal stress ( $\sigma_2$ ) and the minor principal stress ( $\sigma_3$ ) are equal ( $\sigma_2=\sigma_3$ ), and both of them are less than the major principal stress ( $\sigma_1$ ) ( $\sigma_1 > \sigma_2=\sigma_3$ ). Conducting the triaxial tests is a best way to monitor, measure, analyze and understand the stress condition and behavior of the rock mass in the real in-situ field. The confinement pressure  $\sigma_3$  was determined according to the mining depth of the stopes location where the samples were cored and collected, and the mining depth was marked on the samples. For the determination and calculation of cohesive strength ( $C$ ) and the internal friction angle ( $\phi$ ), RocData (2019) was employed to plot the Hoek-Brown (2002) and Mohr-Coulomb curves, and to derive the cohesive strength ( $C$ ) and the internal friction angle ( $\phi$ ). The triaxial test results of kimberlite and the backfilled CRF samples are presented in table 2.5.

Table 2.5 Triaxial test results of kimberlite and CRF samples

Sample No.	Size (mm)		Failure stress	Confinement	C	$\phi$ (°)
	Diameter	Height	$\sigma_1$ (MPa)	$\sigma_3$ (MPa)	(MPa)	
A418	63.21	125.94	42.71	1.5	5.92	48.36
	63.30	129.19	48.78	3.0		
	62.96	131.17	60.61	4.0		
A154S	63.03	131.97	37.76	2.0	4.05	49.58
	62.97	124.50	42.18	3.0		
	63.19	130.91	52.52	4.0		
A154N	63.19	129.10	37.60	1.5	3.75	53.18
	63.07	129.50	42.78	2.5		
	63.18	130.07	63.91	4.5		
CRF	152.64	306.73	16.26	1.5	1.64	44.15
	150.94	304.27	25.43	2.5		
	150.83	304.57	30.21	4.0		

Due to the damages to some samples caused by the trimming process, such as the internal fractures which were invisible from the external surface, some of the results were not available for the usage

to plot the stress-strain curves and Mohr-Coulomb curves, then some of the results of the kimberlite and backfilled CRF are discarded. To make the parameter data more accurate and reliable, some laboratory test results from Sephri (2016) were referred to estimate the properties of the rock mass used in the numerical model in the following part.

### 2.3.3 Input parameters in the finite element (FE) model

The behavior of the rock was assumed to be governed by an elastoplastic constitutive relation based on the elasticity theory and the Mohr-Coulomb plasticity criterion. The intact rock strength parameters, such as UCS, elastic Young's modulus (E), Poisson's ratio ( $\nu$ ), tensile strength ( $\sigma_t$ ), cohesive strength (C), friction angle ( $\phi$ ), and the Hoek-Brown failure criterion intact material constant ( $m_i$ ), are measured through a series of rock mechanics tests (Brazilian, UCS and triaxial tests). In the following table 2.6, the parameters of kimberlite in A418 pipe are not included due to the removal of the A418 pipe in the numerical model, which will be stated in the following part. However, it is necessary to relate the intact properties of the rock, measured in the laboratory, to geological observations in the field and, subsequently, to estimate the rock mass strength properties. To do this, the generalized Hoek-Brown et al. (2002) failure criterion, Bieniawski's (1988) rock mass rating (RMR), and the geological strength index (GSI) (Hoek et al. 1992, Hoek 1994, Hoek et al. 1995, Hoek and Brown 1997) were used to estimate the rock mass properties.

Table 2.6 Rock mass properties introduced in numerical model

Rock Mass	Density ( $\text{kg/m}^3$ )	C (MPa)	$\phi$ ( $^\circ$ )	E (GPa)	$\nu$	$\sigma_c$ (MPa)
A154 South	2400	4.2	26.4	18.7	0.26	66
A154 North	2400	4.7	28.1	19.6	0.24	79
CRF	2200	1.2	41	4.45	0.24	7.43
Granite <sup>1</sup>	2600	9.3	45	24	0.3	130

<sup>1</sup> From Diavik technical report (2011) and Yip and Thomson (2015)

According to the Diavik technical report (2011) and Yip and Thomson (2015), the average RMR89 (Bieniawski 1988) value for the kimberlite is about 55, and the intact material constant value  $m_i$  (constant from general Hoek-Brown criterion) for kimberlite in A154S pipe is about 12.76.  $D$  is the disturbance factor and assumed to be 0. According to the GSI graph (Hoek 1994, Hoek et al. 1995), the GSI value for the kimberlite in A154S pipe is about 50. By using the following equations, the material constants in general Hoek-Brown criterion  $a$ ,  $m_b$  and  $s$  can be calculated.

$$a = 1/2 + (1/6)(e^{-GSI/15} - e^{-20/3}) = 0.5 \quad (2.7)$$

$$m_b = m_i e^{(GSI-100)/(28-14D)} = 12.76 e^{-1.79} = 2.13 \quad (2.8)$$

$$s = e^{(GSI-100)/(9-3D)} = e^{-5.55} = 3.8 \times 10^{-3} \quad (2.9)$$

After achieving the three material constants  $a$ ,  $m_b$  and  $s$  of general Hoek-Brown criterion, the corresponding equivalent friction angle  $\phi_e$  ( $^\circ$ ) and cohesive strength  $C_e$  (MPa) in Mohr-Coulomb criterion can be calculated by the following equations (Hoek et al. 2002, Hoek and Brown 1997):

$$\sigma'_{3n} = \sigma'_{3max} / \sigma_c \quad (2.10)$$

$$\sigma'_{3max} / \sigma'_{cm} = 0.47(\sigma'_{cm} / \gamma H)^{-0.94} \quad (2.11)$$

$$\phi_e = \arcsin\left(\frac{6am_b(m_b\sigma'_{3n})^{a-1}}{2(a+1)(a+2)+6am_b(m_b\sigma'_{3n}+S)^{a-1}}\right) = 29.37^\circ \quad (2.12)$$

$$C_e = \frac{\sigma_c(s(1+2a)+m_b\sigma'_{3n}(1-a))(m_b\sigma'_{3n}+S)^{a-1}}{(a+1)(a+2)\sqrt{1+(6am_b(m_b\sigma'_{3n}+S)^{a-1}/(a+1)(a+2))}} = 4.65MPa \quad (2.13)$$

$$\sigma'_{cm} = 2C_e \cos \phi_e / (1 - \sin \phi_e) = 15.89MPa \quad (2.14)$$

where  $a$ ,  $m_b$  and  $s$  are material constants in general Hoek-Brown criterion,  $\sigma'_{3max}$  is the upper limit of confinement over which the relationship between the Mohr-Coulomb and Hoek-Brown criteria is considered.

Above equations 2.7 to 2.14 present a calculation example to estimate the property parameters of rock mass based on laboratory tested parameters. Following this method achieves Table 2.6.

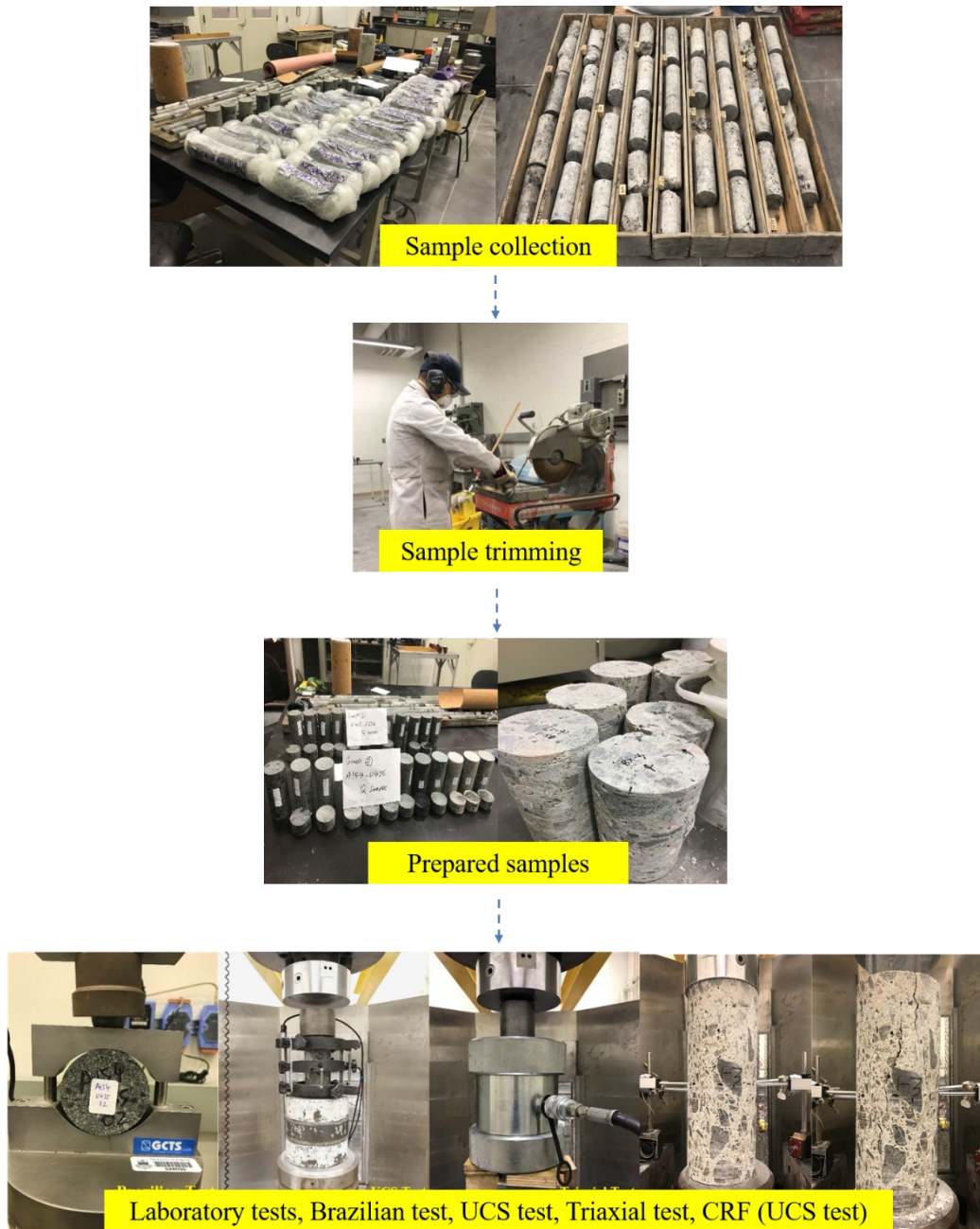


Figure 2.14 Laboratory test workflow

## 2.4 Model simplification and modification

### 2.4.1 Model geometry simplification and modification

When conducting the numerical study applying the finite element, size effect and boundary effect are two important factors that cannot be ignored. Although, larger numerical model can effectively minimize the influence of size effect and boundary effect, larger model has a larger amount of elements which will consume more CPU time to run the model. A balance between relative precise and correct results and consumed CPU time can be achieved to conduct the research more effective. A rational size and simple geometry numerical model can solve the problem with acceptable cost. Then creating a simple and accountable model determine the results and cost of the research. The FE model in this thesis is created based on the three-dimensional (3D) scanning AutoCAD kimberlite mining pipe and open pit slopes and benches profiles. In the view of finite element method, it is impractical to introduce all the details of the real geometry of the studied project. It is rational and scientific to modify and simplify the geometry of the studied project.

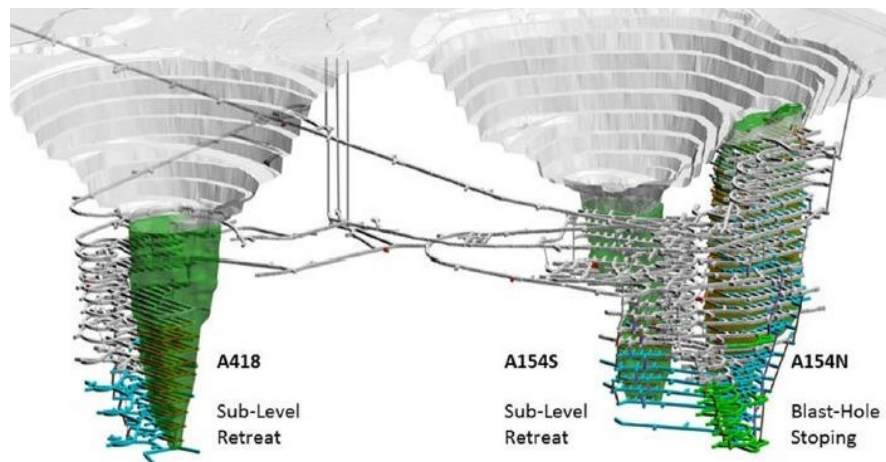


Figure 2.15 Three-dimensional concept profile of Diavik underground mining pipe

To ensure that the FE model can run successfully, some simplification and modification should be made. Figure 2.15 shows the scanned three-dimensional (3D) concept underground kimberlite

mining pipe profiles. Referring to the previous work done by Sepehri (2016), in that numerical model there was no second sill pillar and mining block C. However, according to the updated mine plans (Diavik 2012), there is a second sill pillar, which is shown as the stop line for the block B in mining pipe in the A154N pipe. Here, in the updated numerical model, the second pillar is added, as shown in figure 2.16. All three kimberlite mining pipes, A418, A154N, and A154S, were transferred to underground mining after the completion of open pit mining.

The finite element (FE) model in figure 2.16 was created based on the three-dimensional (3D) concept pipe profile in figure 2.15, and all three pipes are presented in this model. The domain dimensions, 2200m × 2200m × 800m (length × width × depth), are sufficient to eliminate the boundary effect of the model, and the sizes are shown in figure 2.16.

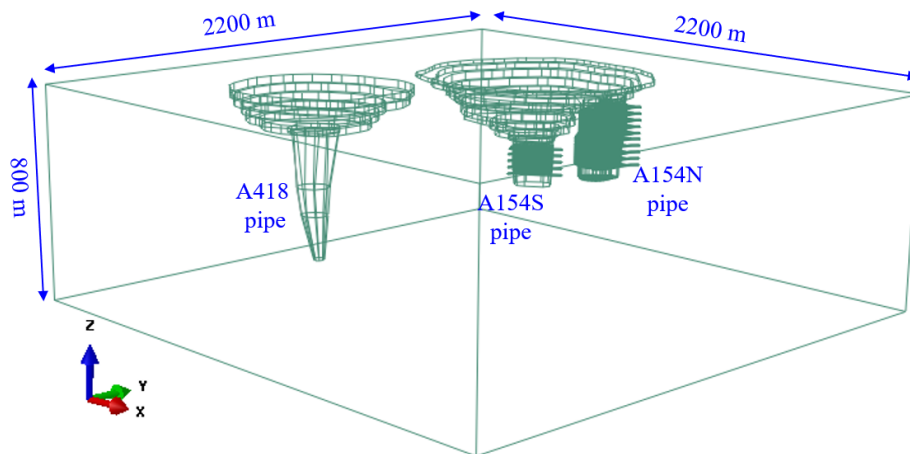


Figure 2.16 Full size model outline of Diavik Diamond Mine

The distances between the Z-axial of pipe A418 and the Z-axials of pipe A154S and A154N are around 880 m and 1177 m, respectively. To speed up the calculation time, pipe A418 is removed from the model to conduct the simplification. The modified finite element (FE) model is shown in figure 2.20.

To verify the feasibility and rationality of the removal of mining pipe A418, a study was conducted by comparing the displacement of the monitored prisms on the benches in the open pit.

On the mine site, there are four monitor prism spots, 280-10 prism, 280-12 prism, CRF-S prism and CRF-N prism installed on the benches of the A154 pit, as shown in figure 2.17. CRF-N prism was chosen to conduct the comparison.

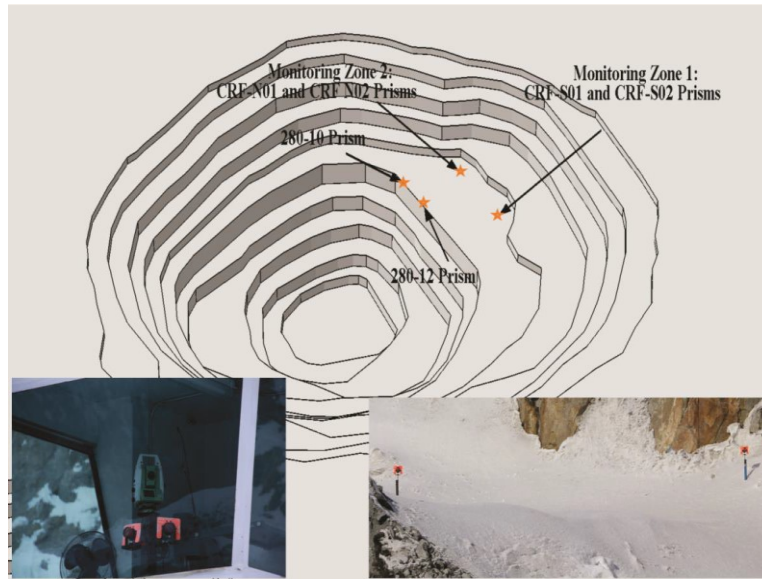


Figure 2.17 Monitor prisms on open pit bench (after Sepehri, 2016)

The first ten mining steps were run in the numerical FE model to conduct the comparative study, and the displacement results of the first ten simulation mining steps is shown in the following figure 2.18. The red curve with dots presents the displacement trend of the large model at CRF-N prism, and the black curve with squares presents the displacement trend of the small model at CRF-N prism. From the two curves, the differences of the displacement induced by the first ten mining steps between the large model and the small model are too small to count.

To make the simplification of the mining pipe geometry of the model more rational and reliable, the comparison of vertical stress was conducted among the three developed numerical analysis models. Two nodes at the same location of the same stope in mining level N9175 of both large and small models were chosen to compare the stress difference. As shown in figure 2.19, the difference in stress between the two models is negligible.

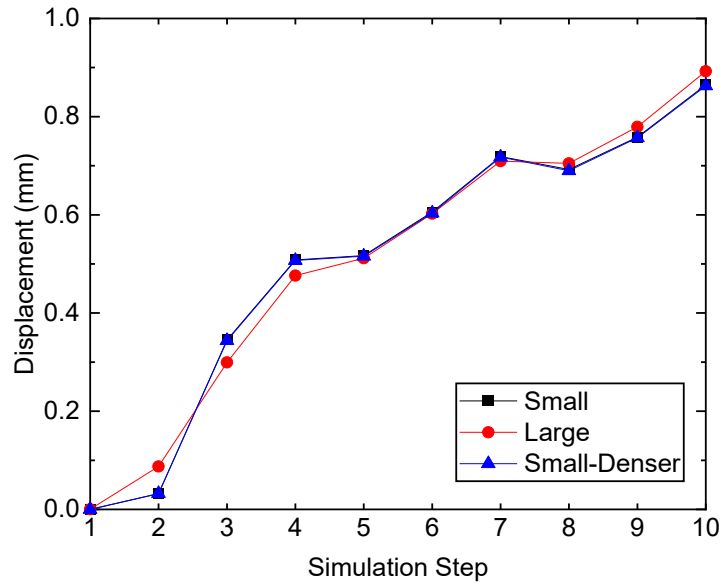


Figure 2.18 Comparison of displacement among three scenarios

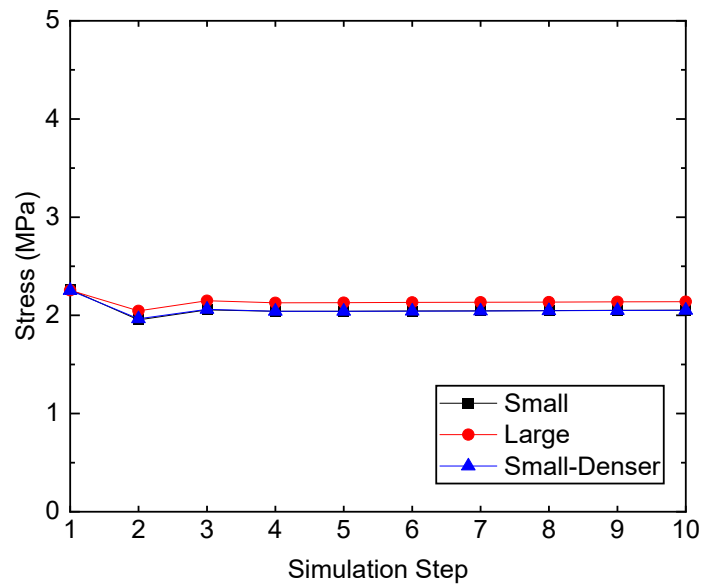


Figure 2.19 Vertical stress at bottom of N9175

Both the comparison of displacement and stress between the two models, the large model and small model, show tiny differences, while the CPU time used to run the first ten simulation steps

was reduced by 34.31%, as shown in table 2.7. As a result, the conclusion can be achieved that the modification and simplification of the geometry is reliable and feasible.

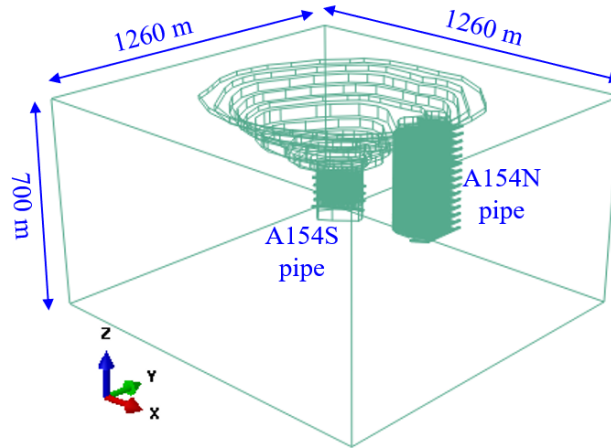


Figure 2.20 Modified model size outline of Diavik Diamond Mine

Then, it is rational to remove pipe A418 from the model geometry to reduce calculation time and speed up the numerical simulation analysis. The new model is shown in figure 2.20, and the domain has a size of  $1260\text{m} \times 1260\text{m} \times 700\text{m}$  (length  $\times$  width  $\times$  depth) in three dimensions.

#### 2.4.2 Finite element mesh density convergence study

The element mesh type (MT) of the ten-node quadratic tetrahedron (MT:C3D10) (Dassault Systemes, 2015) was used to discretize the analysis domain. This type of element can better represent the real unregular geometry shape of some structures in the mining pipe. C3D10 is a quadratic element, and it is better than linear element to achieve the results of excavation and backfilling of the stopes in the mining pipe. With C3D10 mesh type, each element has four corner nodes and six side nodes. Figure 2.21 illustrates the FE mesh of the model.

Generally, with the increase of the density of the mesh, the accuracy of the results improves as well. As the mesh is refined, the computer resources and calculation time required to run the simulation model increase significantly. A study of mesh convergence (SMC) was conducted to

achieve an optimum mesh scenario with consideration of simulation accuracy in the process of slope excavation.

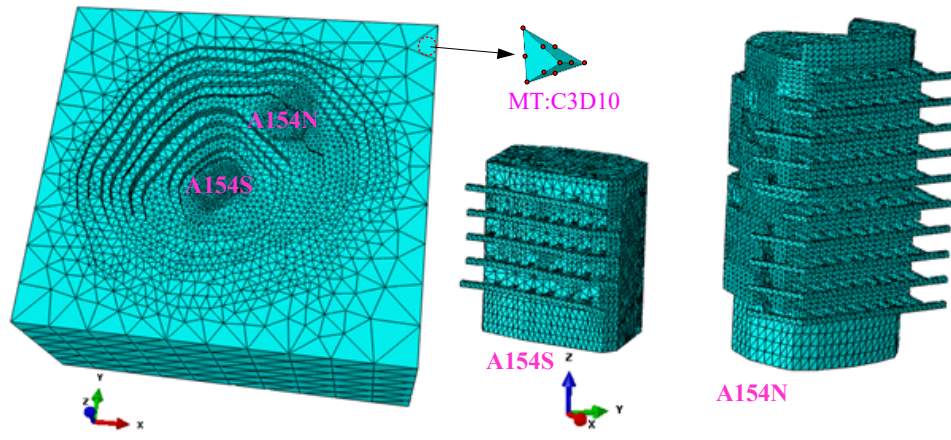


Figure 2.21 Finite element (FE) mesh of model

Two scenarios were proposed and conducted to achieve the optimum mesh density. The models of the two scenarios have the same geometry, and the density of the mesh number is the only changeable factor. One model is named Small, and the other is named Denser. The total number of elements and nodes in the two models is shown in table 2.7. Following figure 2.22 gives an example of different mesh density in the same area. The single element edge size of (a) is twice the element edge size of (b), the total number of elements increases more than three times.

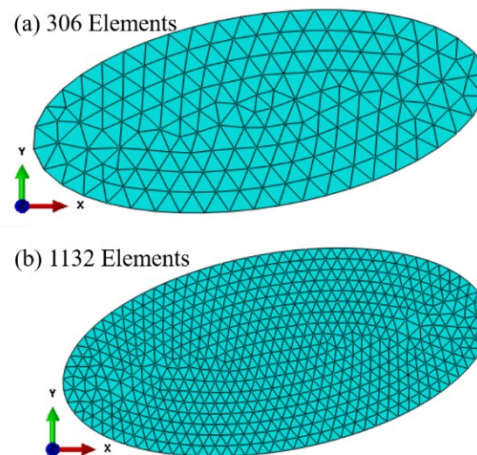


Figure 2.22 Comparison example of mesh density

As before, mining induced accumulated displacement and mining induced stress are chosen as the factors to check simulation accuracy, and the comparisons are shown in figure 2.18 and figure 2.19. For the displacement comparison, the displacement curves overlap each other, which means that they are almost identical. For the stress comparison at chosen nodes, one node shows an identical value, and another shows a tiny difference that is negligible considering the whole magnitude of the stress change trend.

Moreover, CPU time used for the simulation is another key indicator that should be taken into consideration. Table 2.7 presents the CPU time used to run the first ten simulation steps of both models. From table 2.7, the CPU time used for simulation the first mining steps reduces by 19.7% from the Small model to the Denser model.

Table 2.7 CPU time for the first ten simulation steps

Model scenario	Number of elements	Number of nodes	CPU time (hours)
Large	602233	818277	187.1
Small	399852	538880	122.9
Denser	442621	595530	147.1

Here, CPU time is the time to run the first ten steps in the numerical model.

From the comparison study of mining induced displacement and stress at the chosen locations among the three numerical models, Large model, Small model, Small denser model, the accuracy of the analysis done by the Small model is acceptable and reliable. Also, the Small model gives an advantage of saving CPU time by a decrease of 34.3% and 16.5% compared with the Large model and the Small denser model, respectively.

In summary, the Small model, with the simplified geometry of the three mining pipes, can be used to conduct the simulation of the excavation and backfilling steps of the whole process with consideration of the simulation accuracy and consumed CPU time.

### **2.4.3 Excavation scheme modification and simplification**

Both the mining pipe A154S and A154N were transferred to underground mining after the completion of open pit mining. However, the mining methods in pipes A154S and A154N are different, the BHS method is applied in mining pipe A154N, while the SLR method is employed for mining pipe A154S. Mining pipe A154N is underneath the open pit. The open pit ramps, slopes and benches are still functioning for the transportation of the ore and other supplement materials in-and-out the underground mining pipe A154N. The failure of the stopes in underground pipe A154N can contribute to the possible failure of the slopes and benches, then endanger the stability of the whole mine site. Then, the stability of the stopes and crossing cuts in mining pipe A154N plays a significant role during the entire mining process sequence. The research topic will mainly focus on the assessment and optimization of stopes and crossing cuts in mining pipe A154N. To simplify the model geometry, and ensure the influential factors are taken into consideration as many as possible, and reduce the unrelated influence factors, the influence of mining activities in mining pipe A154S will be checked.

#### **2.4.3.1 Comparison of three principal stresses between scenario M and NM**

Two scenarios were proposed and conducted to examine the influence of mining activities in mining pipe A154S on the mining pipe A154N. Scenario NM means the mining pipe A154S will not be mined, it will be kept intact. Scenario M means the mining pipe A154S will be mined following the mining scheme as initiated by the mine. Here, the three principal stresses, major principal stress, intermediate principal stress and minor principal stress, are chosen as the factors to conduct the study of comparison between these two mining scenarios. In the mining pipe A154N, the nodes on drift P1-65 of each stope from every mining level from level N9050 to level N9275 are chosen, and these nodes are closer to the mining pipe A154S compared to other nodes from

mining pipe A154N. Five haulage levels are listed to represent the all the chosen levels. The following three figures present the results of the comparison of the three principal stresses at the selected locations from several mining levels between the two different excavation scenarios of mining pipes.

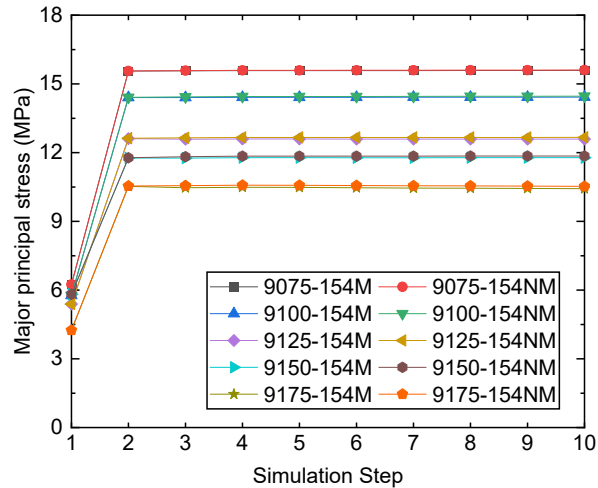


Figure 2.23 Major principal stress comparison between scenario M and NM

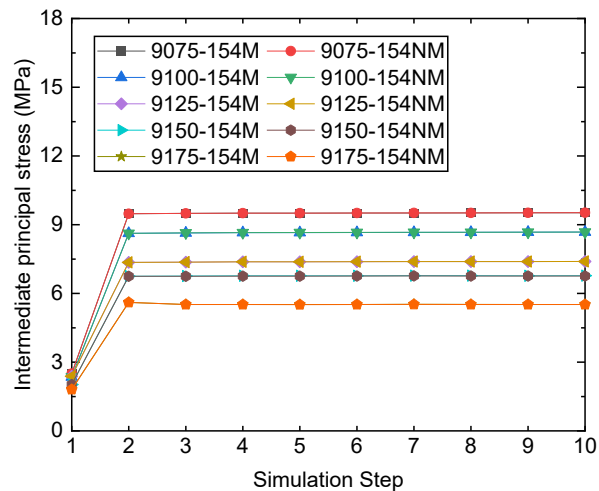


Figure 2.24 Intermediate principal stress comparison between scenario M and NM

The chosen nodes are the nodes that are nearest to the pipe A154S. Theoretically, they will be affected the most when the stopes are mining out in pipe A154S. From the above figure 2.23 and figure 2.24 and figure 2.25 the curves of the principal stresses overlap each other for the same mining level.

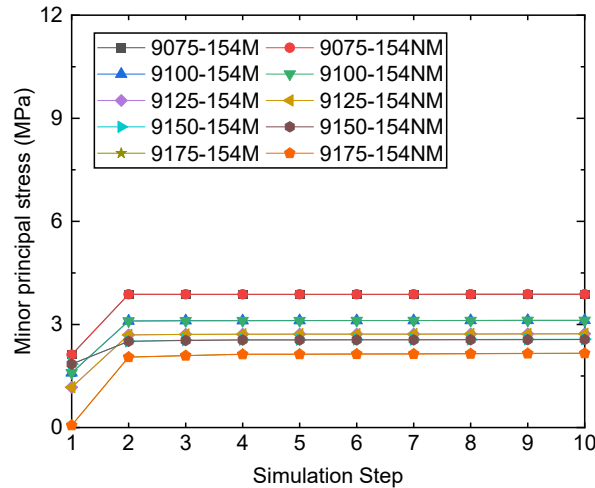


Figure 2.25 Minor principal stress comparison between scenario M and NM

For the first ten simulation steps, there is almost no difference in the three principal stresses, namely, major principal stress, intermediate principal stress and minor principal stress. This comparison between the three principal stresses proves that the excavation of pipe A154S has almost no influence on pipe A154N. Technically, the influence of the mining activities in mining pipe A154S on the principal stresses in mining pipe A154N is negligible. It is rational and reasonable to keep mining pipe A154S unmined when conduct the mining scheme simulation in mining pipe A154N.

#### 2.4.3.2 Comparison of consumed CPU time between scenario M and NM

When conducting the numerical studies, consumed CPU time to run the simulation analysis is a factor that should be take into consideration. Generally, more mining activities simulation, more

consumed CPU time. It is worth to compare the consumed CPU time between the scenario M and scenario NM.

Table 2.8 CPU time comparison between scenario NM and M

Scenarios	CPU time (seconds)			
	Step1-2	Step3-6	Step7-10	Total
NM	72995	138276	156650	367921
M	84526	167209	190715	442450

Table 2.8 shows the comparison of the consumed CPU time of the first ten excavation steps between two scenarios. For the first two steps, the consumed CPU time sees a 13.64% decrease, Step3-Step6 sees a 17.3% decrease, and Step7-Step10 has a 17.86% decrease. From scenario M to NM, the total consumed CPU time of the first ten simulation steps sees a 16.84% decrease. Figure 2.26 presents the comparison of consumed CPU time decrease percentage between scenario M and NM, with the simulation steps going forward, the consumed CPU time will increase constantly.

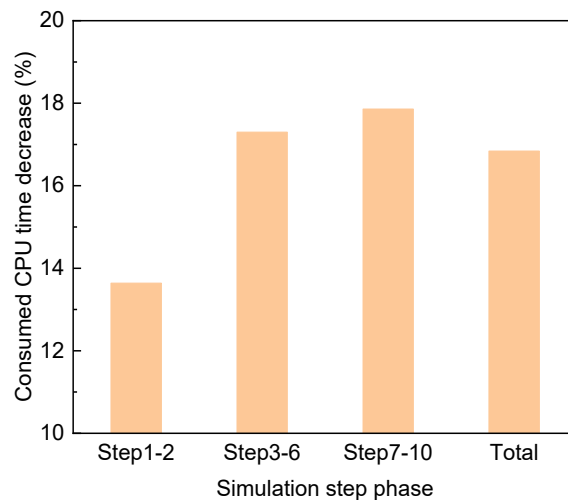


Figure 2.26 Consumed CPU time decrease comparison between scenario M and NM

From the above comparison of three principal stresses and consumed CPU time between scenario M and NM, keeping the mining pipe A154S unmined is technically feasible, and it will speed up the simulation. Figure 2.27 shows the profile of the 3D model with the mined A154N mining pipe, and the A154S mining pipe keeps intact.

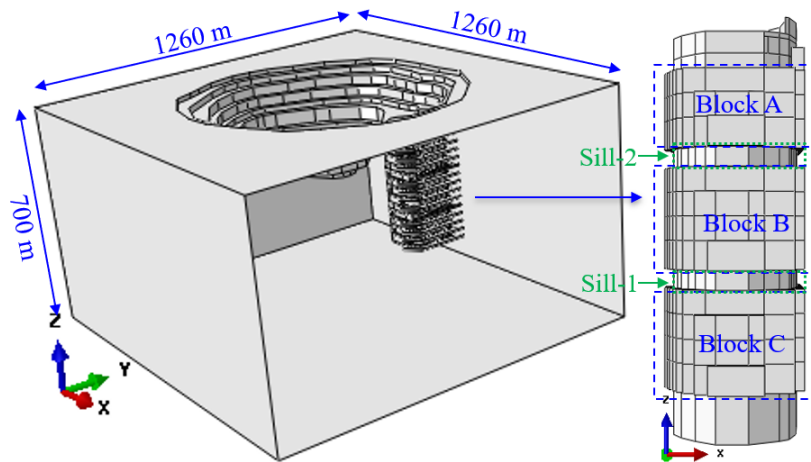


Figure 2.27 Profile of 3D FE model with A154N mined

## 2.5 Initial stress condition of the Small model

In underground engineering, before the start of excavation, all the underground structures are at the initial geo-stress condition. With the underground excavation proceeding, the initial in-situ stress condition will be disturbed, and the in-situ stress will be redistributed. With the increase of the mining depth, the in-situ stress presents a linear growth. When using the numerical model to analyze the underground excavation-induced redistributed stress fields, it is the very first and important step to define the pre-excavation/mining state of stress.

In underground engineering, the vertical component of in-situ stress is considered as the minor principal, especially with the increase of mining depth, horizontal stress component as the major.

The vertical component of in-situ stress can be calculated by the following equation (2.15).

$$\sigma_v = \gamma \cdot H \quad (2.15)$$

where  $\sigma_v$  is the vertical stress component,  $\gamma$  is the unit weight of rock mass, ( $\text{MN}/\text{m}^3$ ),  $H$  is the mining depth, (m) (Aydan and Kawamoto 1997, Aydan 2014, Hoek and Brown 1980).

In underground engineering, it is assumed that the three principal stresses are perpendicular to each other, and the major principal stress is perpendicular to the strike of the stopes and the intermediate principal stress is aligned to the strike of the stopes (Goodman 1989, Singh 2006, Taherynia et al. 2016). Following equations (2.16) and (2.17) are used for the calculation of the horizontal stress components:

$$\sigma_{hmin} = \sigma_v \cdot K_{min} \quad (2.16)$$

$$\sigma_{hmax} = \sigma_v \cdot K_{max} \quad (2.17)$$

where  $\sigma_v$  is the vertical stress component,  $K$  is the ratio between the horizontal and vertical stress component, and according to the in-situ measurement,  $K_{min}=1.2$ ,  $K_{max}=1.5$ .

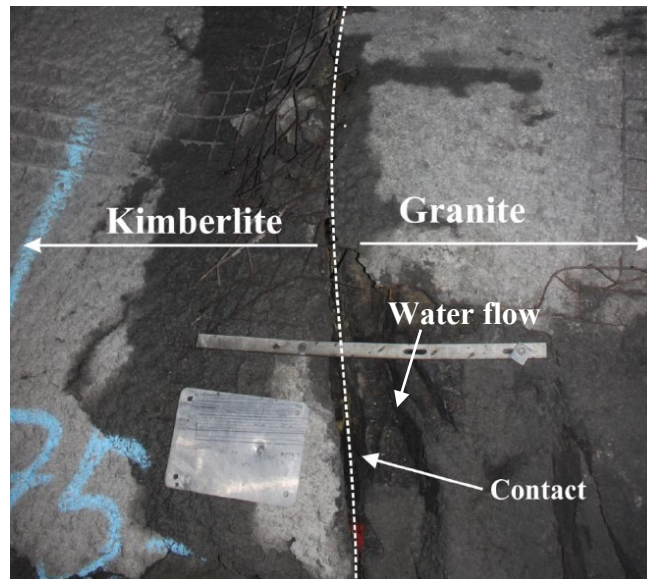


Figure 2.28 Fracture boundary between granite and kimberlite pipe (after Sepehri 2016)

Combined the geological history of the A154N pipe formation with the field observations (i.e. presence of water in the contact between host rock granite and A154N kimberlite pipe), it was concluded that the stress cannot transfer from the host rock to the A154N kimberlite pipe.

Moreover, the observed separated fractures between host rock granite and the A154N kimberlite pipe, as shown in figure 2.28, supports this hypothesis. Then, the stress regime inside the A154N kimberlite pipe is different from the one inside the granite and the A154S pipe. The equation (2.18) proposed by Terzaghi and Richart (1952) was used to estimate the  $K$  value inside the A154N kimberlite pipe:

$$K = \nu / (1 - \nu) \quad (2.18)$$

where  $\nu$  is the Poisson's ratio of the rock. For the design purpose, the value of  $\nu$  for A154N pipe is assumed to be 0.3; therefore, the  $K$  value for the inside of the kimberlite pipe in A154N is 0.43. As shown in figure 2.29, the magnitude of the maximum (major) in-situ principal stress in the model is estimated to be 27.2 MPa by the finite element (FE) model. This value can be verified using equations (2.15) and (2.17) as follows (according to the density of the burying rock mass layers, assuming  $0.026 \text{ MN/m}^3$  as the average unit weight of the overburden rocks):

$$\sigma_{Hmax} = K_{max} \sigma_V = 1.5 \times 700 \times 0.026 = 27.2 \text{ MPa} \quad (2.19)$$

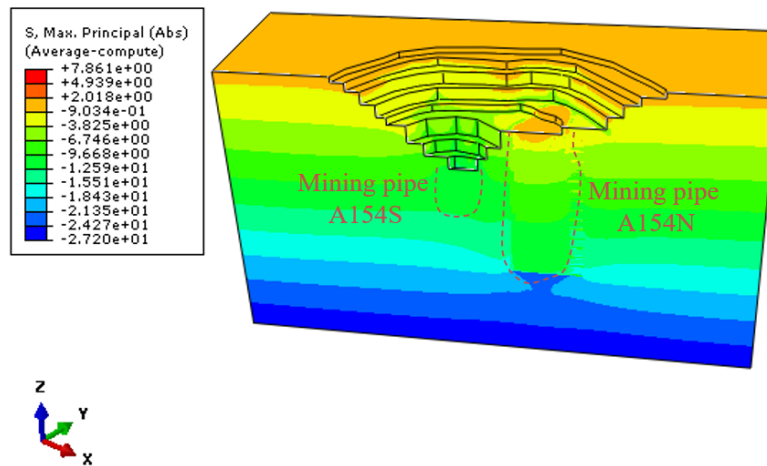


Figure 2.29 Initial computed geostatic step stress condition in FE model

It should be noted that in ABAQUS the compressive stress is assigned to be negative, which is different with the mining engineering laboratory terminology, in which the compressive stress is

assigned to be positive. In underground mining engineering, in most scenarios, the stresses are compressive stresses. In figure 2.29, the maximum negative stress is the compressive stress.

## 2.6 Simulation steps

To complete the excavation and backfilling of the three mining blocks, block-A, block-B and block-C, the developed numerical has 83 simulation steps based on the real mining schedule (Diavik 2011) and schemes of the case mine. For the recovery of the two sill pillars, the three proposed recovery schemes have different simulation steps. Scheme-1 (SBS) has 11 simulation steps starting the excavation and backfilling process at both sill pillars simultaneously. Scheme-2 (SS1) has 15 simulation steps starting from sill pillar 1 moving forward to sill pillar 2. Scheme-3 (SS2) has 15 simulation steps, while starting from sill pillar 2 moving forward to sill pillar1. These three sill pillar recovery schemes simulation steps will be discussed in detail in Chapter 6. It should be noted that all the 83 simulation steps are in the mining pipe 154N, since the A418 pipe is removed and the A154S pipe is kept unmined/intact. The developed FE model simulates the complete stress-strain path through the entire excavation and backfilling simulation steps.

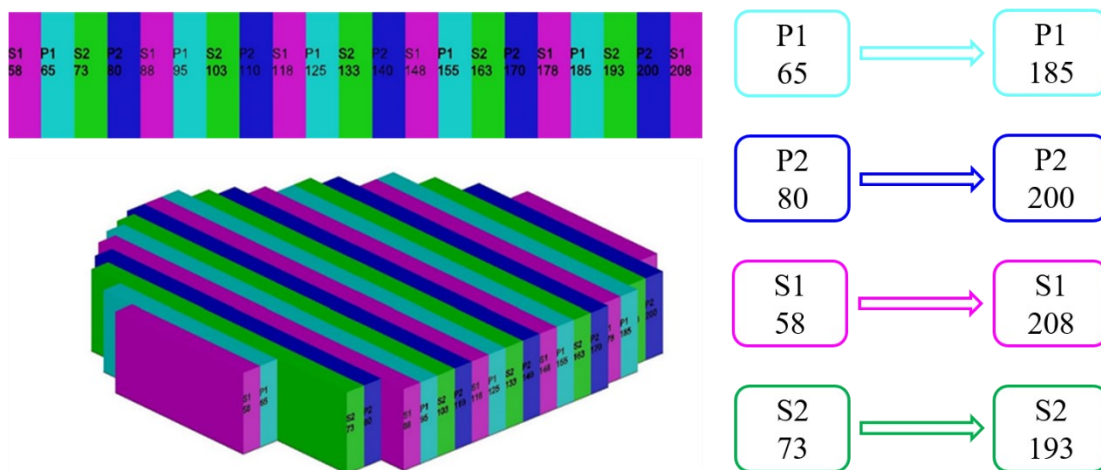


Figure 2.30 Simulation steps at one level in FE model

The first simulation step in the FE model is geostatic step, which calculates the initial stress state before the excavation of the underground openings. The second step is to excavate the main haulage drifts, then the excavation of stopes in mining level starts. Figure 2.30 presents an example simulation step scheme of mining level N9075. In this mining level, the mining production starts from the stope P1-65 (first round of the primary sequence) to stope P1-185, after the completion of first round, stope P2-80 (second round of the primary sequence) will be mined till stope P2-200. The stope S1-58 (first round of the secondary sequence) will be mined after the completion of primary sequence, the stope S3-193 (second round of the secondary sequence) is the last-mind stope in this mining level. In the simulation steps, after one stope is excavated in one step, it will be backfilled with cemented rockfill (CRF) in the next step. The simulation stops when the last mined stope is backfilled. The detailed simulation steps are attached to appendix A.

## **2.7 Summary and conclusion**

This chapter introduces the background of Diavik diamond mine, which is the used as the case study for the research topics of this thesis. The mining method of sublevel stoping and blasthole stoping (BHS) in the mining pipe A154N were introduced. The methodologies of finite element analysis and laboratory tests used for the research topics are introduced. A full size realistic three-dimensional (3D) finite element (FE) model based on the actual geometry of the mining pipes and open pits of the case study mine Diavik diamond mine was developed. To achieve the input parameters of the properties of the rock mass and backfilled CRF for the FE model, three types of laboratory rock mechanics tests, Brazilian test, uniaxial compressive strength (UCS) test, triaxial test, were conducted. The rock samples were cored and collected from underground stopes in Diavik diamond mine and trimmed, the three types of tests of kimberlite samples and backfilled CRF samples were conducted in the rock mechanics lab at the University of Alberta. The properties

of parameters such as Young's modulus, cohesion stress, tensile strength, internal friction angle were achieved.

Then, a study of simplification of the FE model geometry and modification of the mining sequence schemes in the mining pipe A154N and A154S was conducted. The mining pipe A418 was removed from the large model to reduce the size of the numerical model by comparing the displacement and stresses at the chosen locations between the two models. Furthermore, the mining sequence of mining pipe A154S was modified by keeping the mining pipe A154S intact during the analysis of the stress field of the mining pipe A154N in the process of excavation and backfilling the pipe by the comparison of the displacement and principal stresses at the chosen locations between the two proposed mining scenarios. The simplified and modified small FE model with a size of 1260m × 1260m × 700m (length × width × depth) was chosen to conduct research of this thesis topics. A study of mesh density convergence between the small model and small denser model was conducted to achieve a better accuracy-and-time balance by comparing the accuracy and consumed CPU time.

The pre-defined initial stress field in the FE model was set to simulate the initial stress state before the underground mining excavation, and the computed maximum stress in the FE model was verified by comparing with the calculation of the theoretical method. Finally, the mining sequences in Diavik diamond mine and the numerical simulation steps, including the proposed three recovery schemes of the two sill pillars, in the FE model, based on the actual production schedules and schemes of the case study Diavik diamond mine, in the FE model were introduced.

## **CHAPTER 3: EXCAVATION LENGTH EFFECTS AND BACKFILLING LENGTH EFFECTS ON STOPE STABILITY**

*Generally, the underground mining stopes are divided into two or three parts for excavation. In this thesis study, the main topics are about the whole mine site stability during the life-long of the mine site. Then speed up the simulation by combating the two or three stope parts is proposed. In this way, the single stope will be excavated by whole size, one excavation step mines one stope. This chapter presents the study of excavation length effect and backfilling length effect on the stope stability to check the reliability and feasibility of the proposed excavation scheme.*

### 3.1 Literature review of excavation length effect on stope stability

As many Canadian underground mining works progress into deeper and more complex geological environments, they are experiencing more and greater mining-induced-redistributed-stress induced rock damage initiation problems, which on occasion have seriously complicated influence on effective and efficient mining (Kaiser et al. 2000). Most of the tunnels experience the time dependent squeezing behavior, to better understand this behavior and deal with the possible rock mass damages during the excavation process of tunnels, many researchers are actively addressing these using many methods, such as analytical, empirical and numerical methods. Barla et al. (2001, 2010, 2012) proposed various approaches for tunnel design by assessing the interaction between rock mass and structures in the short-term and long-term in rock mass with time dependent squeezing behaviour. Rock mass squeezing phenomenon around the tunnels are widely studied by considering the various rates of advancing (Ghaboussi and Gioda 1977), analyzing the extension of microcrack length and development of EDZ (Golshani et al. 2007, Tang et al. 2018), time-dependent deformation and elastoplastic behavior (Malan 1999, 2002), in the means of semi-empirical back-analyze approach (Manh et al. 2015), analytical solution (Sulme et al. 1987), and numerical model(Ghaboussi and Gioda 1977, Golshani et al. 2007,Manh et al. 2015,Wang et al. 2011, Weng et al. 2010). The interaction mechanism between the tunnel excavation and tunnel stability are studied by analyzing the supports and reinforcements, model tests, underground research laboratory measurement and numerical simulation (Martino and Chandler 2004, Kishida et al. 2012, Funatsu et al. 2008, Zhang et al. 2019). Kielbassa and Duddeck (1991) proposed a simplified two-steps plane model approach to determine the stresses and deformations of both circular and non-circular tunnel during the excavation process. Gioda and Cividini (1996)

discussed the linear and non-linear viscous constitutive laws and developed the numerical methods to analyze the time dependent effect on performance in squeezing rocks.

In underground mining, generally, one stope will be divided into two, three or four equal parts for excavation. The divided part will be excavated step by step, and the stope will be mined one by one. Usually, researchers focus on only several stopes and develop simple models to study the excavation-induced stress redistribution and excavation-induced displacement. Two-dimensional (2D) models are widely used to make a fast assessment of the analysis. However, all the stopes in underground mining will be affected by the excavation of the adjacent stopes from upper and lower mining levels in three directions, then the 2D models cannot represent the real redistributed stress situation. Understanding the three-dimensional redistribution of excavation-induced stresses becomes essential given the adverse consequences such stresses will have on the host rock mass and the subsequent excavation activities. Using three-dimensional finite element numerical model can do a better job in exploring the near-field stress paths (Eberhardt 2001) and potential rockburst during the excavation (Sepehri et al. 2017, 2020), predicting mining-induced ground subsidence (Sepehri et al. 2017), analyzing time-dependent mechanical behaviour of the excavation damage zone (EDZ) (Pellet et al, 2009), studying the stope roof settlements, pore pressure distributions (Kasper and Meschke 2004), stresses and deformations in the lining during the shield-driven tunnel excavation (Kasper and Meschke 2004, Funatsu et al. 2008). To improve the tunnel stability, Kaiser et al. (2000) provided an overall framework for assessing the stability of underground openings in hard rocks, regardless whether the excavations are required for mining, nuclear waste or civil engineering applications. Langford et al. (2012) suggested the guidelines to determine the excavation damage zones (EDZs) by discussing the rock properties and analyzing the statistical distribution of the dimensions in the process of underground excavation.

By the usage of numerical method, researchers have done a lot to analyze the time dependent squeezing effect of the tunnels, the mechanism between the tunnel excavation and tunnel stability, reinforcement stability, et al. Though numerical modelling is powerful, sometimes it is time consuming, especially running a large size three-dimensional (3D) numerical model to analyze the effect of the whole excavation process scheme on the ground displacement and stress redistribution. Increasing the length of the excavation at each step can be an option to save the time to run the numerical model. While, whether the extended excavation length scheme scenario causing the same displacement and stress redistribution is rarely discussed. In this part, study of five different excavation scenarios with various excavation lengths at six different mining levels in mining pipe A154N will be conducted, as shown in figure 3.1. The six different mining levels are: ML#8975, ML#9025, ML#9050, ML#9100, ML#Sill2, ML#9200, from the bottom to the top of the mining pipe A154N. The elevation difference among these six chosen mining levels is 30m, and the mining depths of these six mining levels are: -450m, -420m, -390m, -360m, -330m, -300m, from ML#8975 to ML#9200, respectively.

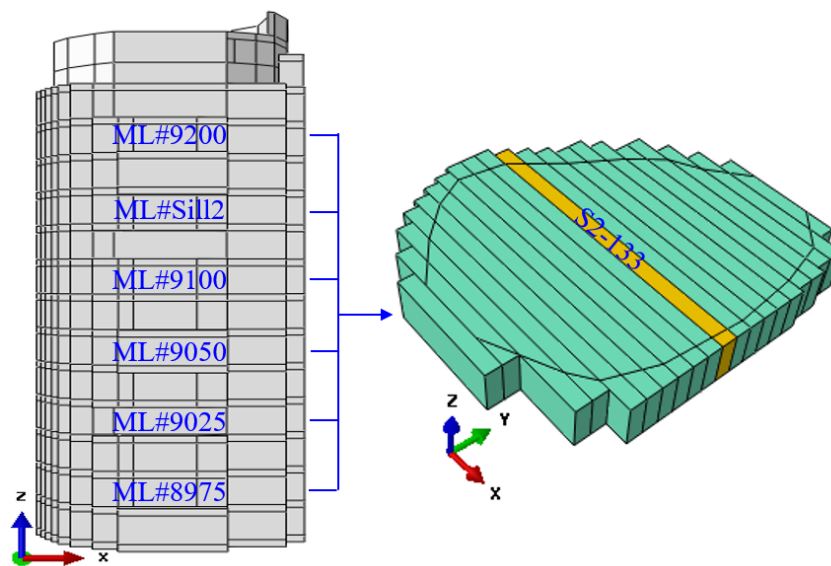


Figure 3.1 Profile of mining pipe A154N and stope S2-133

### 3.1.1 Five various excavation scenarios

The stope S2-133 in the middle of the mining level was chosen as the case study, as shown in figure 3.1. The stope S2-133 has a size of 7.5m × 20m × 150m (width × height × length). To better investigate the excavation length effect on the stope stability in mining pipe A154N, five different lengths of each excavation step are determined from 30m to 150m. Table 3.1 presents the proposed five excavation scenarios (SCNs) to conduct this study.

Table 3.1 Five excavation scenarios

Scenario	Part 1	Part 2	Part 3	Part 4	Part 5	Step	Each part length(m)
SCN#1	O	X	X	X	X	2	150
SCN#2	O	O	X	X	X	3	75
SCN#3	O	O	O	X	X	4	50
SCN#4	O	O	O	O	X	5	37.5
SCN#5	O	O	O	O	O	6	30

Note: Here, O stands for yes, X stands for no. Step stands for the steps needed to complete excavation.

Here, for scenario SCN#1, it has only one excavation part, and this part is the whole stope S2-133, and the excavation length is 150 m. It will take three steps to conduct SCN#2, which has two equal excavation parts, and each excavation part is 75 m long. Scenario SCN#3 has three equal parts, and each excavation step length is 50 m. Scenario SCN#4 has four equal parts and scenario SCN#5 has five equal parts, and each excavation part is 37.5 m and 30 m long, respectively. Figure 3.2 presents the five excavation parts scenario configurations. During the excavation process, the parts will be excavated one by one. (e.g. in SCN#5, P1→P2→P3→P4→P5)

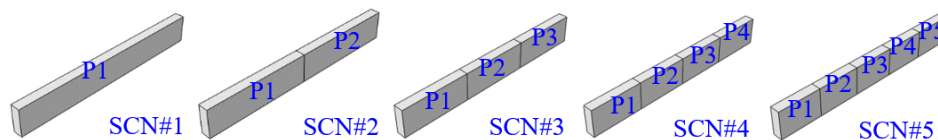


Figure 3.2 Five excavation scenarios of stope S2-133

In all five scenarios, the first simulation step Step1 (S1) is the geostatic step to calculate the initial state of stress before excavation. For scenario SCN#1, the second simulation step Step2 (S2) is to excavate the whole stope. In scenario SCN#2, it takes steps S2 and S3 to excavate P1 and P2, respectively. SCN#3 takes steps S2, S3 and S4 to excavate P1, P2 and P3. For scenario SCN#4, it takes four steps to complete the excavation, from step S2 to step S4. For scenario SCN#5, it takes five steps, S2, S3, S4, S5, S6, to finish the excavation.

### 3.1.2 Excavation length effect on displacement

Displacement is a representative explicit and significant factor to indicate the damages of the rock mass in the stopes caused by the excavation process. The displacements of the two sidewalls of neighbored to the excavated stope S2-133 are presented to achieve the comparison of the effect of the five different excavation scenarios at the six different mining levels, from level ML#8975 to ML#9200. It should be noted that, these five different excavation scenarios take various steps to complete the simulation work, from two steps to six steps as mentioned in table 3.1, to better present and compare the results of the different excavation scenarios, the result figures presented in the following part have the same x-axial, from step S1 to step S6. The dots on the presented curves represent the specific steps. Here, (a) presents the displacement on the left sidewall and (b) presents the displacement on the right sidewall, and the following figures have the same labels.

Figure 3.3 shows the displacement of the chosen points on both sidewalls of the stope S2-133 in mining level ML#9200. Following the excavation process, from step S1 to S6, the displacement increases constantly. The final displacements are almost the same and it is about 5 mm for all the five different excavation scenarios. On the left sidewall, for scenarios SCN#1 and SCN#2, as soon as the excavation finishes, the displacement reaches the maximum values. For the other three scenarios, SCN#3, SCN#4 and SCN#5, when the excavation is getting close to the monitored point,

the displacement increases slightly, when the excavation occurs at the point, the displacement increases dramatically, then with the excavation process moving forward and leaving the monitored point, the displacement with tiny increase till the final step ends. The final displacement on the right sidewall is about 4.5mm.

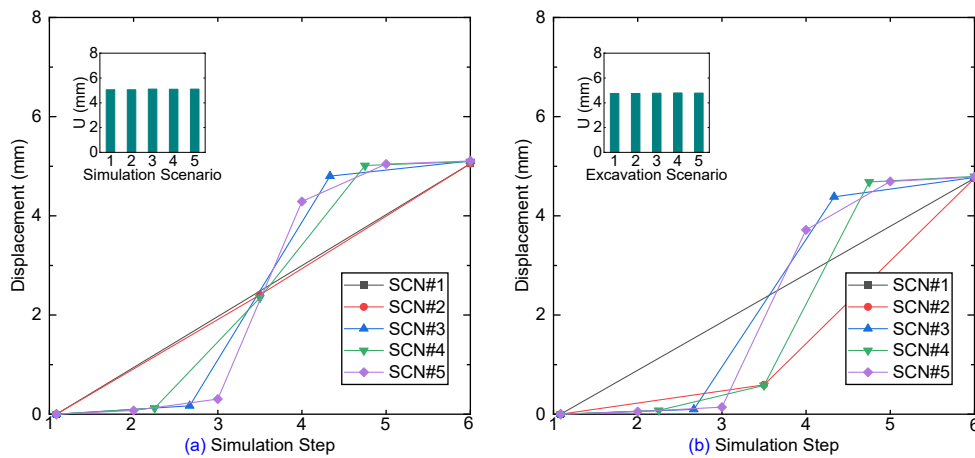


Figure 3.3 Displacement of stope S2-133 two sidewalls in ML#9200

The sidewall displacement/swelling in mining level ML#Sill2 is shown in following figure 3.4. The final displacement/swelling on both sidewalls is about 6.5mm for all five different excavation scenarios.

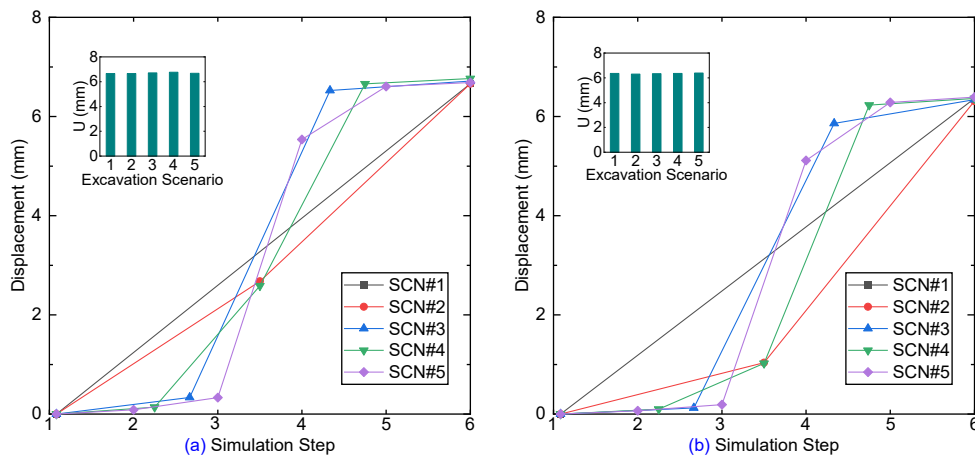


Figure 3.4 Displacement of stope S2-133 two sidewalls in ML#Sill2

According to excavation scenarios SCN#2 and SCN#4, when the excavation step occurs at the monitored points, it causes the same displacement/swelling on both sidewalls of stope S2-133. Due to the monitored points are at the middle center of the stope free surface, also at the middle center of the excavation part P2 and P3 for scenarios SCN#3 and SCN#5, respectively, then after the excavation of part P2 and P3 in these two scenarios, the displacement/swelling sees a dramatic increase, which is almost the whole displacement caused by the excavation. And for the scenario SCN#1, the excavation causes the displacement/swelling to the maximum value.

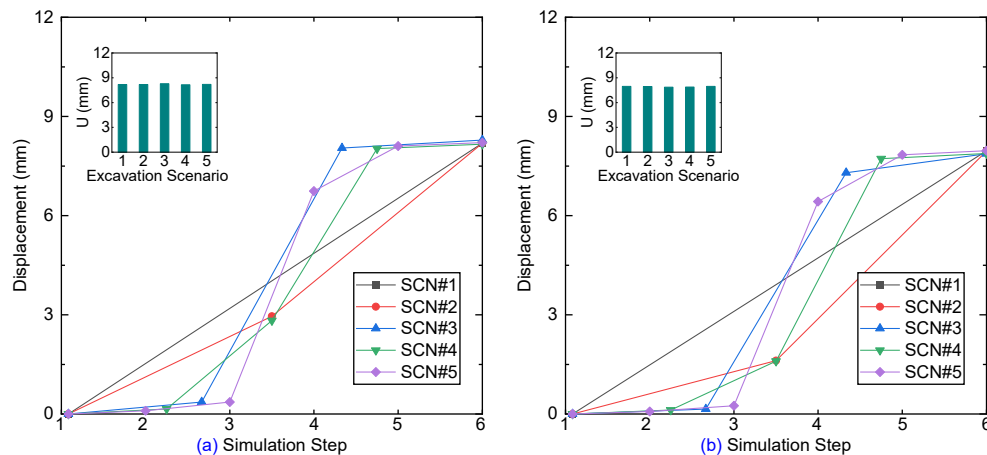


Figure 3.5 Displacement of stope S2-133 two sidewalls in ML#9100

Both the displacements on both stope sidewalls in ML#9100 are about 8mm, as shown in figure 3.5. For scenario SCN#1, the excavation step causes the immediate increase of displacement on the free surface of the sidewall in the stope S2-133, and it reaches the maximum value of displacement of 7.8 mm. Comparing with the figure 3.3, figure 3.4 and figure 3.5, for the scenario SCN#2 and SCN#4, the excavation part P1 in scenario SCN#2 and excavation part P2 in scenario SCN#4 cause an increasing initial displacement, from less than 0.5mm to over 1.5mm, from mining level ML#9200 to level ML#9100, at the left side of the sidewall in the stope S2-133. Same with mining level ML#9200 and level ML#Sill2, the last excavation step of scenarios SCN#3,

SCN#4 and SCN#5 cause no more increase of displacement for the monitored point, indicating the excavation at these locations has almost no influence on the monitored points.

Both sidewalls of stope S2-133 see an over 9.5 mm displacement in mining level ML#9050 for all five excavation scenarios, as shown in following figure 3.6. Excavation scenarios SCN#1 and SCN#2 present the similar trend with that of the other three mining levels, for the other three scenarios, SCN#3, SCN#4 and SCN#5, when the excavation is getting close to the monitored point, the displacement increases slightly, when the excavation occurs at the point, the displacement increases dramatically, then with the step of excavation process moving forward and leaving the monitored point, the displacement achieves very tiny increase till the final step ends. The initial displacement caused by excavation part P1 and P2 in SCN#2 and SCN#4 increase slightly.

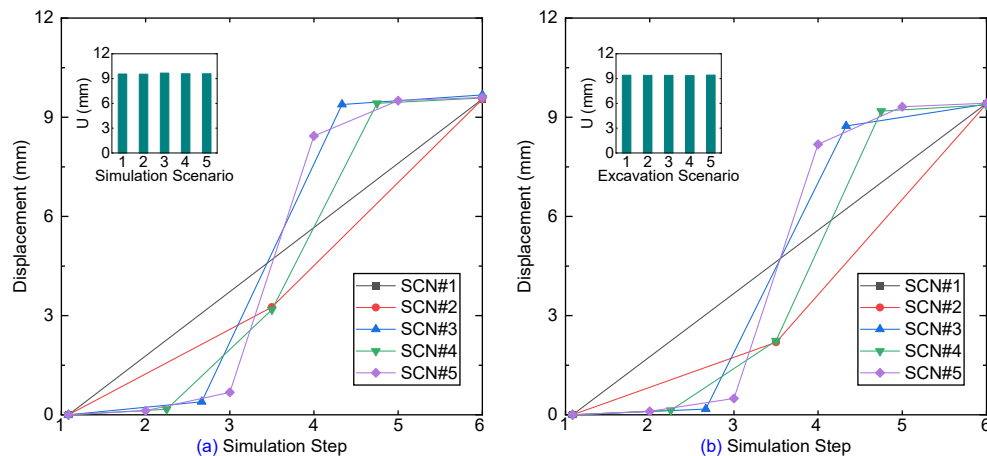


Figure 3.6 Displacement of stope S2-133 two sidewalls in ML#9050

With the increase of the mining depth, the final displacement on the sidewalls of the monitored points in stope S2-133 grows up gradually. Both sidewalls of mining level ML#9025 get an 11mm displacement caused by the excavation process, as shown in figure 3.7. On the left sidewall, for scenario SCN#4, the excavation of part P2 at step S3 triggers the displacement, and the following steps of excavation of part P3 at step S4 causes little displacement compared with excavation of

part P2. While on the right sidewall, the monitored point is close to the center of part P3, then most of the displacement is caused by the excavation of part P3 at step S4. For excavation scenarios SCN#3 and SCN#5, similar with the other mining levels, the excavation of the last part P4 and part P5 causes no more displacement increase to the monitored point, respectively.

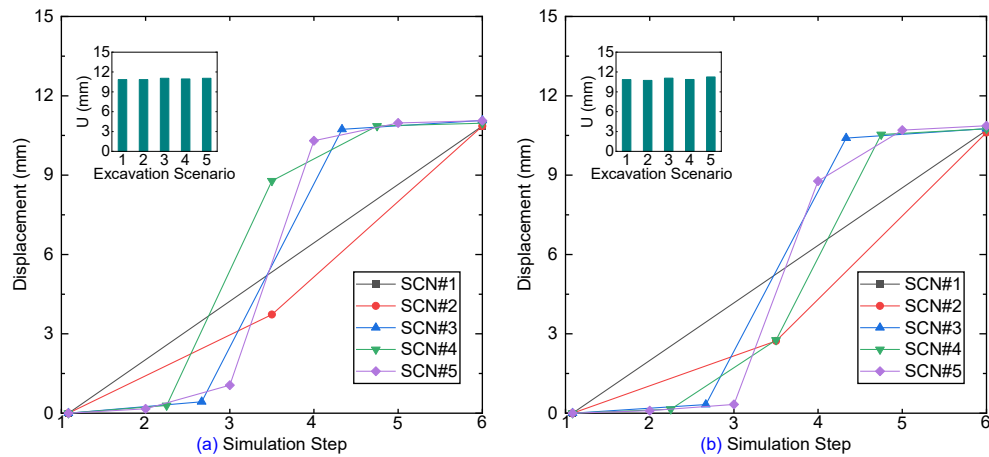


Figure 3.7 Displacement of stope S2-133 two sidewalls in ML#9025

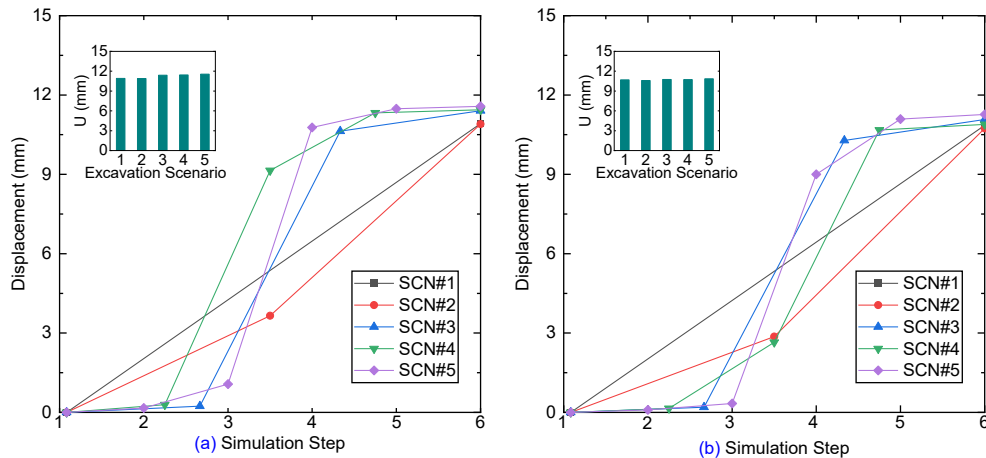


Figure 3.8 Displacement of stope S2-133 two sidewalls in ML#8975

For the deepest mining level ML#8975 in mining pipe A154, the final displacement of the monitored points on the sidewalls caused by the excavation is around 12mm in stope S2-133, which is larger than that of the other five mining levels, as shown in following figure 3.8. In both

mining level ML#9025 and ML#8975, on the left sidewall, for both scenarios SCN#2 and SCN#4, the excavation occurred at the monitored point causes different displacement, though the final displacement is very close.

According to the above six figures, the displacements of both sidewalls of the stopes at each mining level caused by the proposed five different excavation scenarios have a very close final value of displacement. With the increase of the mining depth, from mining level ML#9200 to level ML#8975, the displacement increases constantly from around 6 mm to over 12 mm, presenting a twice increase. From mining level ML #9200 to level ML#8975, the final excavation steps cause tiny additional increase of displacement for scenarios: SCN#3, SCN#4 and SCN#5. For scenario SCN#5, in which the last excavation step S6 is about 45m away from the monitored point, then the influential distance of the excavation step in horizontal is less than 45m.

### **3.1.3 Excavation length effect on major principal stress**

Stope excavation in underground engineering disturbs the initial stress state and causes the stress redistribution. The redistributed stress may cause the damage of the around rock mass in the stopes, even causes rockburst (Wang and Park 2003, Kaiser and Cai 2012, Sepehri 2016, Wang 2020). The major principal stress contributes as the main factor resulting the rock mass damage and stope failure. Then the redistributed major principal stress can be listed as a key factor used to assess the potential damage of the rock mass.

As presented in figure 3.9, the redistributed major principal stress starts to change from the same initial stress condition at geostatic step S1 in stope S2-133. After the finish of the last step of excavation, the major principal stress trends to reach almost the same final stress condition, with some increase and decrease during the excavation process. For mining level ML#9200, the final major principal stresses are less than 4 MPa for all five excavation scenarios. For both scenarios

SCN#2 and SCN#4, the monitored point is at the center of the stope sidewall and also the end of one excavation part, then the excavation occurs at the point, is cause stress concentration effect, shown in figure 3.9, the major principal stress has a peak value due to the stress concentration effect in these two excavation scenarios. After another excavation part removing, the major principal stress decreases dramatically for both scenarios SCN#2 and SCN#4. For the excavation scenario SCN#3 and SCN#5, the step excavation causes the most major principal stress decreases, at part P2 and P3.

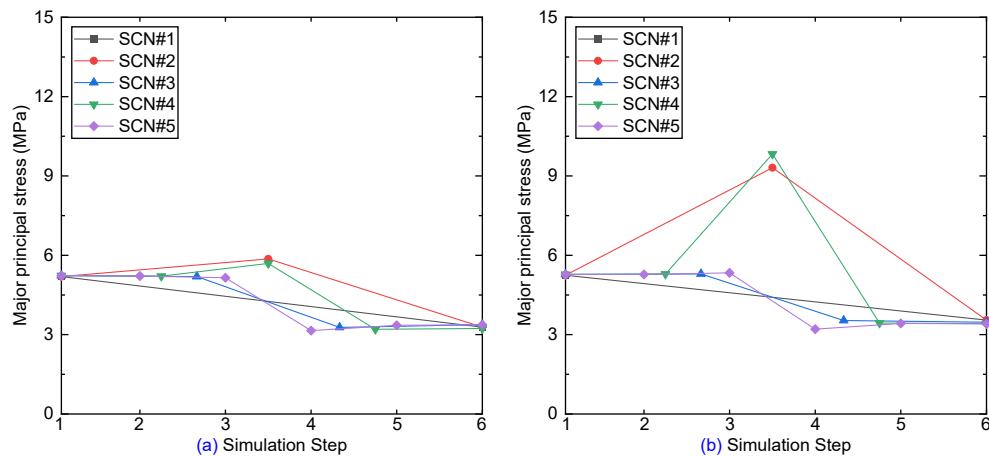


Figure 3.9 Major principal stress of stope S2-133 two sidewalls in ML#9200

The change trend of major principal stress of sidewalls in mining level ML#Sill2 is illustrated in figure 3.10. Due to the deeper mining depth, the initial major principal stress at geostatic step S1 is larger than that of mining level ML#9200, and it is 6.8MPa, and the final major principal stress is about 4.8MPa after the completion of the excavation of stope S2-133. The stress concentration effect on both sidewalls in stope S2-133, after the excavation of part P1 in scenario SCN#2 and part P2 in scenario SCN#4, is stronger than that of the mining level ML#9200, for example, the major principal stress reaches 12 MPa as soon as the excavation part P1 is removed in scenario SCN#2 in mining level ML#Sill2, while in mining level ML#9200, it is about 10MPa. Similar

with the mining level ML#9200, the scenarios SCN#3 and SCN#5 cause the major principal stress at the excavation step of P2 and P3, respectively. Scenario SCN#1 reaches the maximum principal stress with the other excavation scenarios at the monitored points, but in one excavation step.

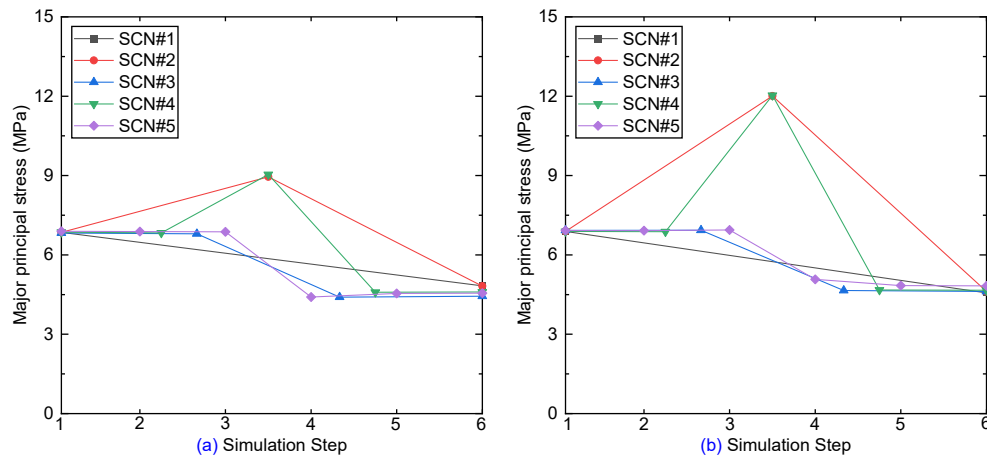


Figure 3.10 Major principal stress of stope S2-133 two sidewalls in ML#Sill2

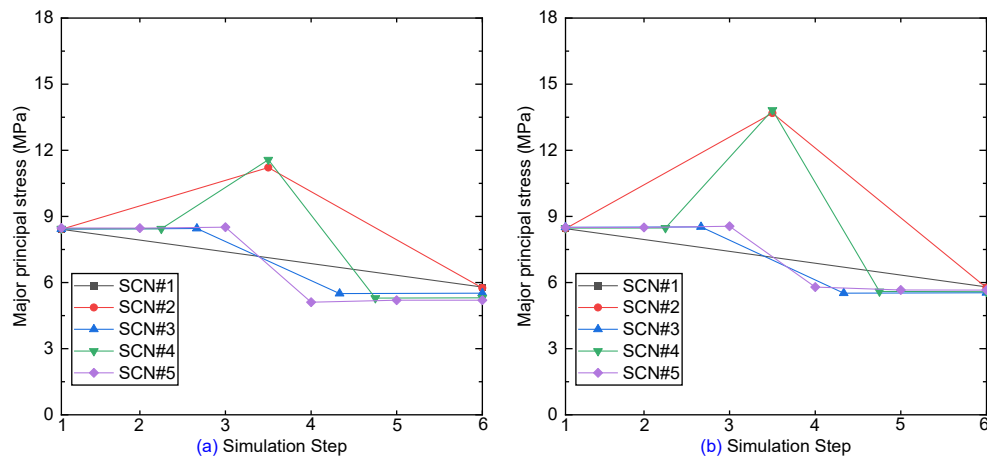


Figure 3.11 Major principal stress of stope S2-133 two sidewalls in ML#9100

Starting a value of 8.3MPa on both sidewalls in stope S2-133 in the mining level ML#9100, the major principal stress decreases constantly with the excavation process moving forward in scenarios SCN#1, SCN3 and SCN#5, compared with the excavation scenarios SCN#2 and SCN#4, which have an increase due to the stress concentration effect at the monitored pointed caused by

the excavation, as illustrated in figure 3.11. The major principal stress in all five excavation scenarios start at the same initial state and ends at the very close values, though some changes during the excavation process from the first removing of excavation part P1 to excavation part P5 in five scenarios, respectively.

With the mining levels going deeper, the initial major principal stress state at geostatic step S1 increases. In mining level ML#9050, the major principal stress starts from 9.83 MPa at step S1 to 6.35MPa at last excavation step in each scenario, with a decrease of 35.4%. All five excavation scenarios in mining level ML#9050 follow a similar trend with the previous three mining levels, ML#9200, ML#Sill2 and ML#9100, as presented in figure 3.12. Due to the stress concentration effect, after the excavation of part P1 in scenario SCN#2 and part P2 in scenario SCN#4, the redistributed major principal stresses witness an 37.33% increase on the left sidewall, from 9.83 MPa to 13.50 MPa, and an 51.37% increase on the right sidewall, from 9.83 MPa to 14.88 MPa, respectively. On the left sidewall, at the monitored points, the final major principal stress from scenarios SCN#1 and SCN#2 is little bit larger than that of the other scenarios, while on the right sidewall, in contrast with the left sidewall, the other three scenarios have bigger final results.

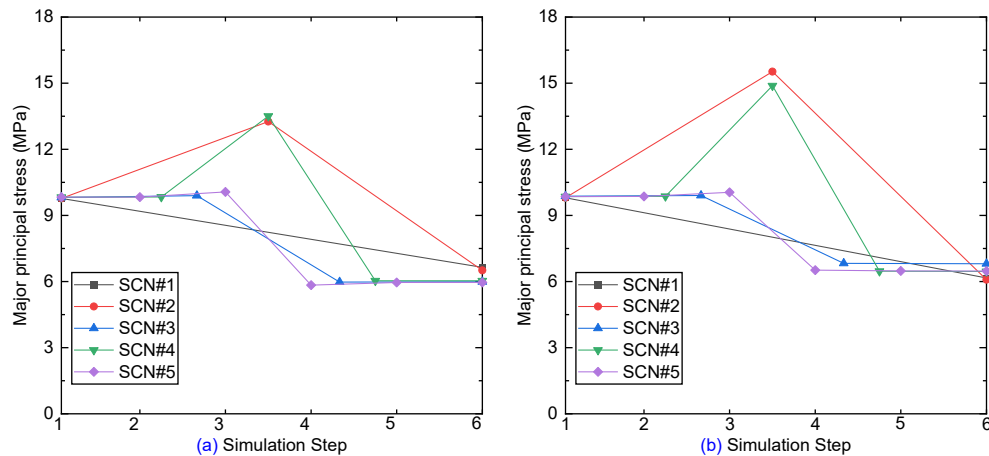


Figure 3.12 Major principal stress of stope S2-133 two sidewalls in ML#9050

Figure 3.13 presents the major principal stress changes trend during the excavation process of the five different excavation scenarios in the mining level ML#9025. For scenario SCN#1, after the excavation of the whole stope S2-133, on the left sidewall, the major principal stress sees a 30% decrease from 10.7MPa to 7.5Mpa, this is the stress release on the free surface of the sidewall caused by the excavation. On the right sidewall, the decrease is almost the same. For scenarios SCN#3 and SCN#5, due to the location of the monitored point on both sidewalls, the major principal stress has a gradual decrease, through the major decrease is during the excavation of part P2 in scenario SCN#3 and part P3 in scenario SCN#5. For the stress concentration effect, on the right sidewall, the scenarios SCN#2 and SCN#4 still gain a peak major principal stress due to the concentration, from 10.7MPa to 17MPa, which is a big concern during the actual excavation process. The major principal stress on the right sidewall is more easily concentrated than the major principal stress on the left sidewall.

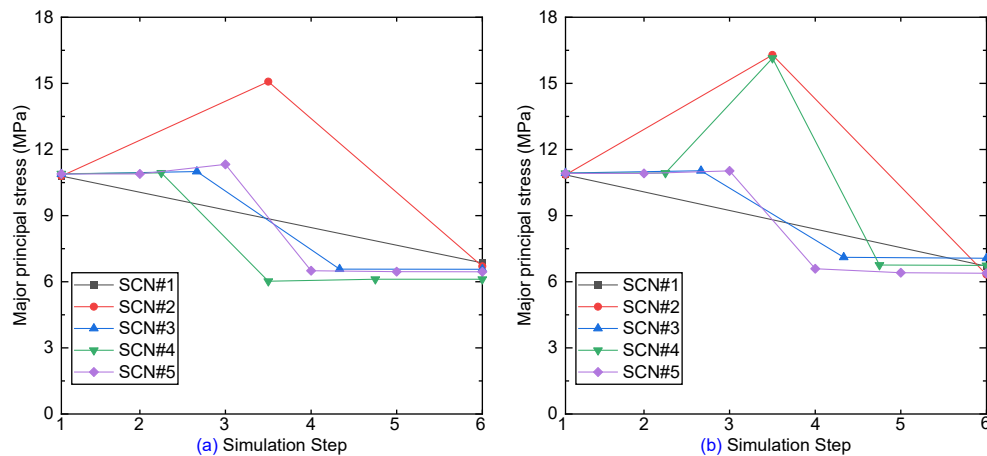


Figure 3.13 Major principal stress of stope S2-133 two sidewalls in ML#9025

As the deepest mining level among these six mining levels in pipe A154N, level ML#8975 starts the initial major principal stress from around 11.5MPa at step S1, and ends about 7MPa at last excavation step in each excavation scenario, with a 39% decrease at the monitored points at both

sidewalls among the five different excavation scenarios, as presented in figure 3.14. For scenario SCN#2, both sidewalls have a more than 50% increase due to the stress concentration effect after the excavation of part P1, which is similar with that of ML#9050, which is about 51%. All five excavation scenarios start at the same initial stress state of major principal stress and end at the almost identical major principal stress state.

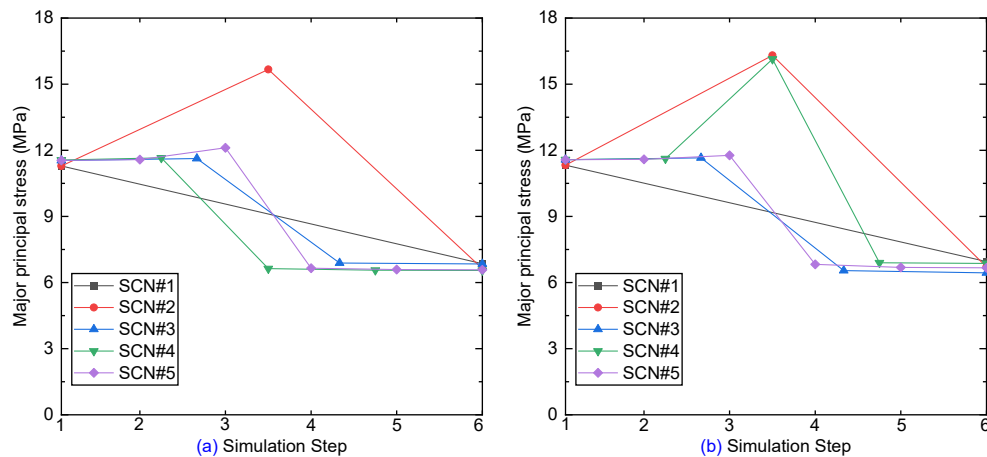


Figure 3.14 Major principal stress of stope S2-133 two sidewalls in ML#8975

As can be seen from the above figures of the major principal stress at the monitored points in the sidewalls in stope S2-133 in the six mining levels in pipe A154N, the initial major principal stress condition at geostatic step S1 constantly increases with the increase of the depths of mining levels, from mining level ML#9200 to ML#8975. With the increase of the depths of mining levels, scenarios SCN#2 and SCN#4 have a gradually significant increase of the stress after the process of step S2, which excavates the part P1 and part P2, respectively. While for scenarios SCN#1, SCN#3, and SCN#5, the stresses witness a slight decrease during the excavation process, and no stress concentration effect at the monitored points among these three scenarios. Also, the final major principal stresses are smaller than that of the intact stresses, which is a good proof of the stress release on the free surfaces of the sidewalls caused by the excavation process.

### 3.1.4 Excavation length effect on potential damage initiation (DI)

As Canadian hard rock mines go deeper, they are experiencing greater stress induced rock damage initiation problems, which on occasion have seriously complicated results in affecting the effective and efficient mining in the stopes. In underground engineering, excavation of stopes will cause the stress redistribution and damage initiation around the stope openings. To better assess the damages caused by the redistributed stresses in the stope rock mass, Castro et al. (1997, 2012) proposed the index of rock mass potential damage initiation (DI) to assess the potential damage zones around the excavation stope openings.

$$\sigma_{DI} = (\sigma_1 - \sigma_3) / \sigma_{ci} \quad (3.1)$$

where,  $\sigma_{DI}$  is the threshold stress for damage stress,  $\sigma_1$  and  $\sigma_3$  are the in-situ major principal stress and minor principal stress, respectively.  $\sigma_{ci}$  is the uniaxial compressive strength (UCS) of the intact rock samples tested in the lab.

In this part, the damage initiation on the free surfaces caused by the excavation on both sidewalls at the monitored points is presented for the comparison among the five different excavation scenarios at the six mining levels in the mining pipe A154N. Following figure 3.15 shows the rock mass damage initiation of the monitored points in the stope S2-133 in mining level ML#9200 in mining pipe A154N. Due to the shallower mining depth of level ML#9200, the excavation of the stopes only causes very minor damages at the monitored point with the process of excavation moving forward. Similar with the stress concentration effect, the damage initiation of scenarios SCN#2 and SCN#4 also see an increase after the excavation of part P1 in scenario SCN#2 and part P2 in scenario SCN#4, respectively. From simulation step S1 to step S6, on both sidewalls, there is almost no changes of DI, which means the excavation causes minimum damages at mining level ML#9200, though with the five different excavation scenarios.

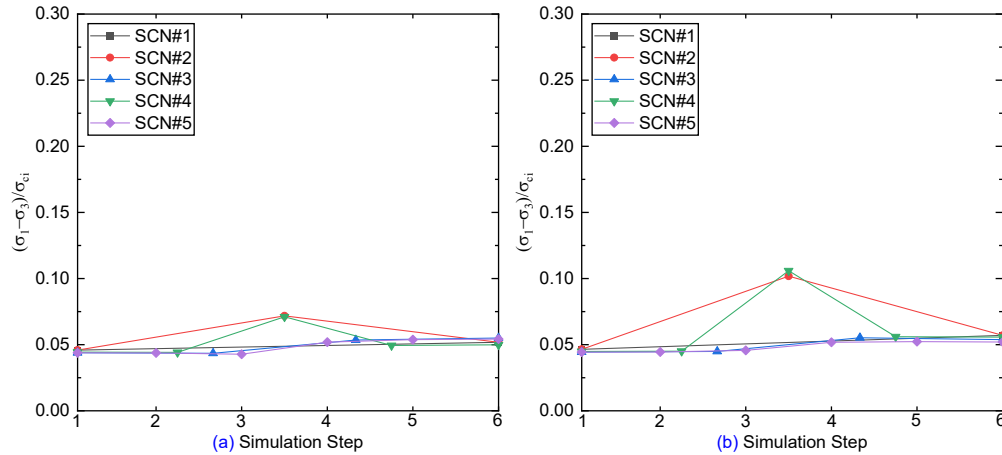


Figure 3.15 DI of two sidewalls of slope S2-133 in ML#9200

As for the mining level ML#Sill2, as shown in figure 3.16, in scenarios SCN#2 and SCN#4, the damage initiation sees an increase after the excavation of part P1 in scenario SCN#2 and part P2 in scenario SCN#4, respectively. While after the excavation of the other parts, P2 in scenario SCN#2 and P3 in scenario SCN#4, the damage initiation decreases to a value which is same with the values caused by the other three excavation scenarios. From the initial geostatic state to the state after the excavation of the whole slope S2-133, the damage initiation has a tiny increase compared with that in the mining level ML#9200.

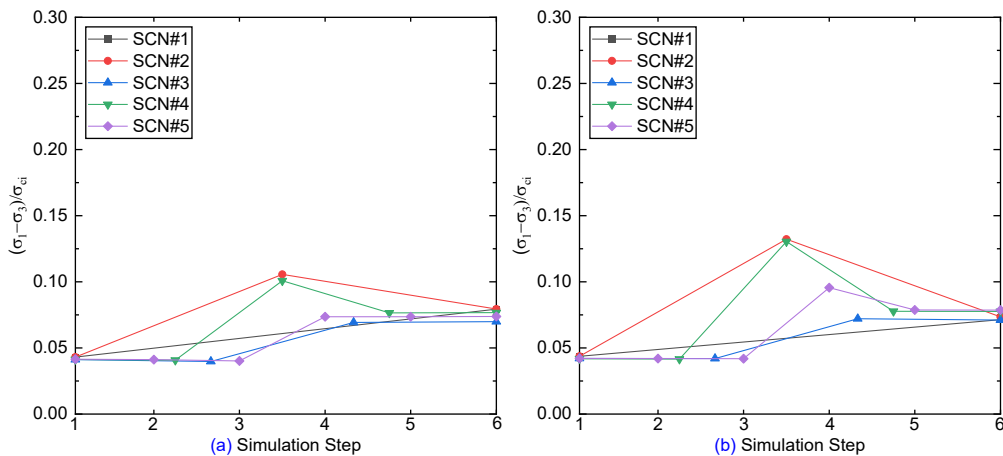


Figure 3.16 DI of two sidewalls of slope S2-133 in ML#Sill2

Starting at the initial state of 0.04 at step S1 and ending at the state of 0.1 at the final excavation step in each scenario, the damage initiation in stope S2-133 in mining level ML#9100 sees great increase along with the changes of major principal stress, as shown in figure 3.11 and figure 3.17. For scenarios SCN#2 and SCN#4, on the right sidewall, the damage initiation reaches to 0.15 due to the concentration of the redistributed principal stresses, and on the left sidewall, it reaches to 0.13, both these two values are larger than the final damage initiation states. The concentration of principal stress causes the damages on the free surface of the sidewalls due to the excavation. For the scenarios SCN#3 and SCN#5, where the monitored points are at the center of the free surface of the excavated parts, then there is no obvious increase of damage initiation during the whole process of the excavation simulation steps. With the differences in the excavation process, the final damage initiation state caused by the excavation is close. As for scenario SCN#1, at both sidewalls, after the excavation of the stope S2-133, the damage initiation reaches the maximum state.

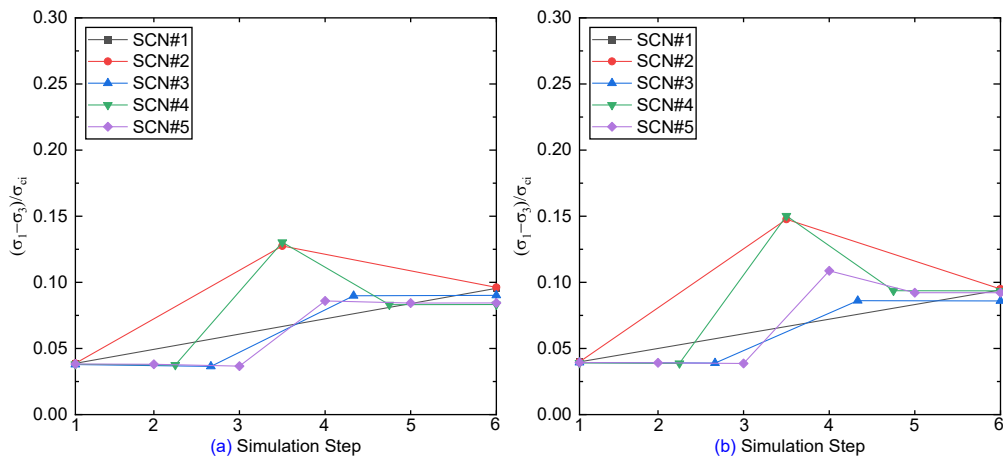


Figure 3.17 DI of two sidewalls of stope S2-133 in ML#9100

With the increase of the mining depths, the difference between the major principal stress and the minor principal stress presents a relation along with the theory of geo-stress, as presented by the

initial state of damage initiation. The final state of the damage initiation reaches a value over 0.1 at both sidewalls in the stope S2-133 in mining level ML#9050. Excavation scenarios SCN#3 and SCN#5 see a gradual increase of the damage initiation from the excavation of the first part P1, and the last excavation step in both scenarios causes no more damage to the monitored points.

For scenarios SCN#2 and SCN#4, the peak value of damage initiation reaches to 0.15 on the left sidewall, and on the right sidewall the peak damage initiation reaches 0.17, both scenarios have a more than three times increase from the initial state to the final step of the excavation. For scenarios SCN#1 and SCN#2, on the left sidewall, the final damage initiations are the same, and it is larger than that of the other three scenarios, in which the damage initiations are very close. For the right sidewall, the final damage initiations of scenarios SCN#1 and SCN#2 are the same, and they are little bit smaller than that of the other three scenarios, SCN#3, SCN#4 and SCN#5.

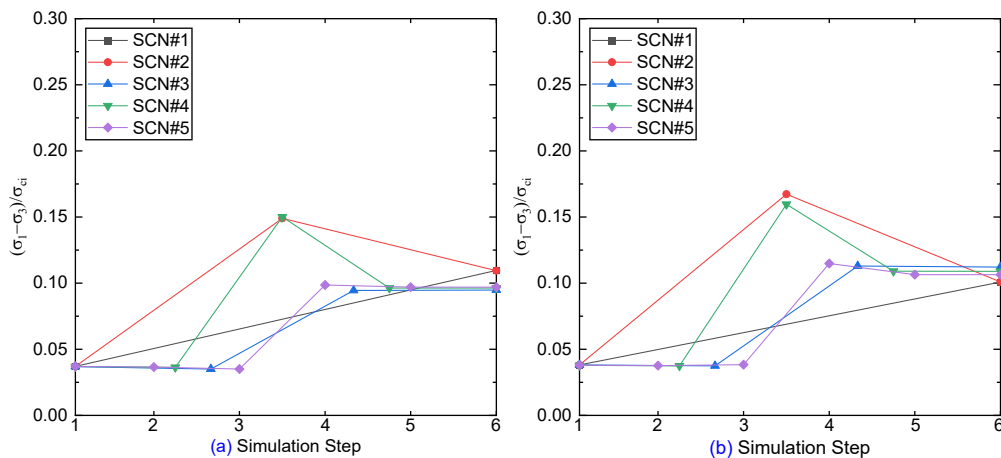


Figure 3.18 DI of two sidewalls of stope S2-133 in ML#9050

The two sidewalls in the stope S2-133 in mining level ML#9025 see a similar damage initiation changes trend on the free surfaces of the sidewalls. On the left sidewall, the peak damage initiation reaches 0.17 in the excavation scenario SCN#2, on the right sidewall, both the scenarios SCN#2 and SCN#4 see a peak one, and it is 0.17, as shown in figure 3.19. For the excavation scenario

SCN#5, the change on the right sidewall is larger than that on the left sidewall when the excavation step arrives at monitored points. For excavation scenarios SCN#3 and SCN#5, on both sidewalls, when the excavation step gets close, it causes stress release presenting decreases of DI, then the excavation step occurs at the monitored points, and the DI increases, and then stops at the stable state.

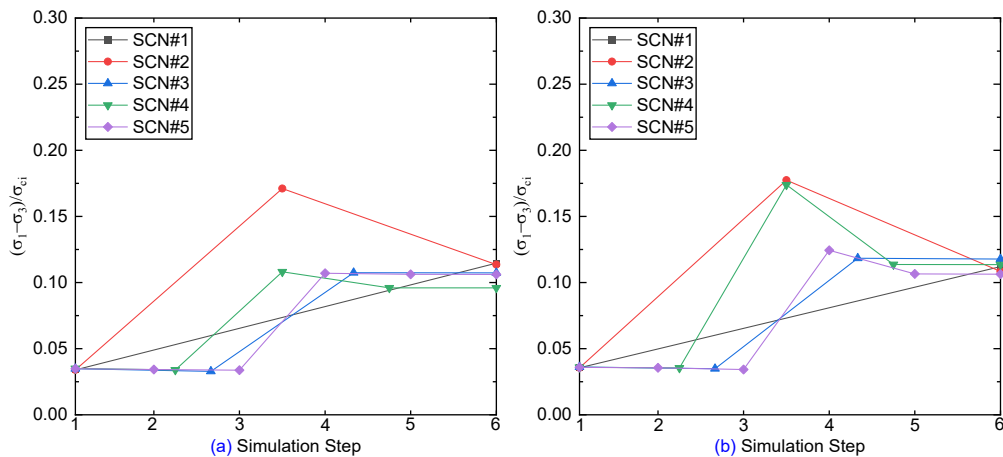


Figure 3.19 DI of two sidewalls of stope S2-133 in ML#9025

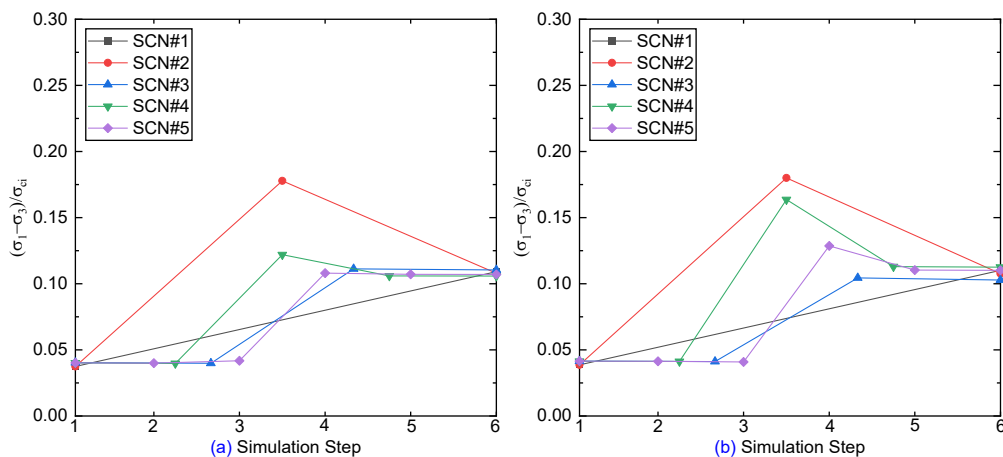


Figure 3.20 DI of two sidewalls of stope S2-133 in ML#8975

For mining level ML#8975, though it is the deepest mining level among the six levels, the starting initial damage initiation is almost same with the mining levels, ML#9050, ML#9025, as well as

the final damage initiation state, as shown in figure 3.18, figure 3.19 and figure 3.20. The excavation scenario SCN#2 has the maximum damage initiation during the excavation process on both sidewalls, and on the right sidewall, excavation scenario SCN#4 gets a larger one compared with scenarios SCN#1, SCN#3 and SCN#5, though the final states are the same among the five excavation scenarios.

From the above discussion of the damage initiation of the free surface of the sidewalls in the stope S2-133 in the six mining levels, the five different excavation scenarios cause the same results at the final state of the damage, through differences during the excavation process from scenario to scenario. The redistributed principal stresses caused by the excavation process contribute almost the same damage initiations in the rock mass of two sidewalls around the stopes at each mining level. Although the DI increases twice during the excavation process at both sidewalls, the damages can be assessed into minor scale according to the classifications proposed by Castro et al. (1997, 2012).

### **3.1.5 Influence of mining depth on excavation length effect**

According to the above results and discussion of the displacement, redistributed major principal stress and the rock mass damage initiation (DI) around the excavated stope openings, the results show that at different mining levels, from level ML#8975 to level ML#9200, the excavation length effect presents the similar trend. Following figure 3.21 presents the comparison of displacement of excavation scenario SCN#5 among the six mining levels. With the increase of the mining depth, the mining-induced displacement on the sidewalls increases constantly, from mining level ML#9200 to ML#8975, when the excavation activity reaches the monitored point location. From mining level ML#9200 to ML#9050, the increasement of displacement sees an increasing trend, and the final stage of displacement presents an identical difference. For mining level ML#9025

and ML#8975, the increasement of displacement still presents an increasing trend, similar with other four mining levels, while the difference between the final stage of displacement is smaller compared to the difference among the other four mining levels.

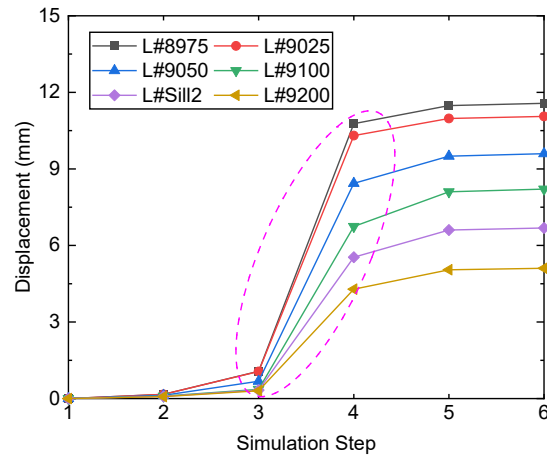


Figure 3.21 Comparison of displacement among six mining levels

Underground mining excavation causes the stress release on the free surface of the stope sidewalls, following figure 3.22 presents the changes trend of the redistributed major principal stresses on the sidewalls of stope S2-133 of the six mining levels of excavation scenario SCN#5.

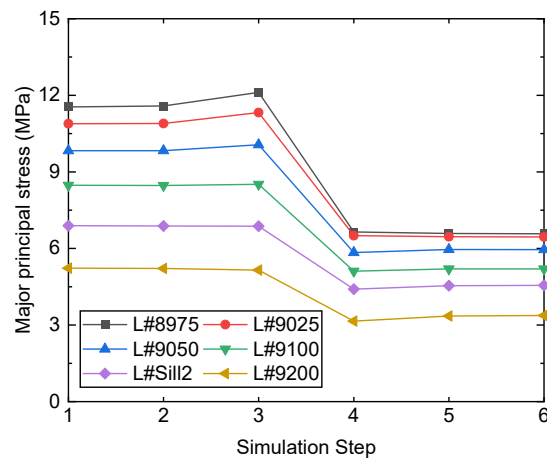


Figure 3.22 Comparison of major principal stress among six mining levels

The decrease of major principal stress shows a similar trend with that of the displacement, but in a contrary direction, and the stress release caused by the excavation contributes to this phenomenon. Also, the differences among the final stage of the major principal stresses from mining level ML#9200 to ML#9050 are identical, and the difference between mining level ML#9025 and ML#8975 is smaller compared to that among the other four mining levels, same as the case of displacement. The deeper the mining level is, the higher degree of the stress release caused by the excavation on the free surfaces of the sidewalls.

Figure 3.23 presents the comparison of excavation induced damage initiation (DI) in both sidewalls in stope S2-133 among six mining levels of excavation scenario SCN#5. Different with the change trend of displacement and major principal stress, the increase of excavation induced damage initiation (DI) sees a slight grows. The shallower the mining depth, the smaller degree of damage initiation (DI) on the stope sidewalls.

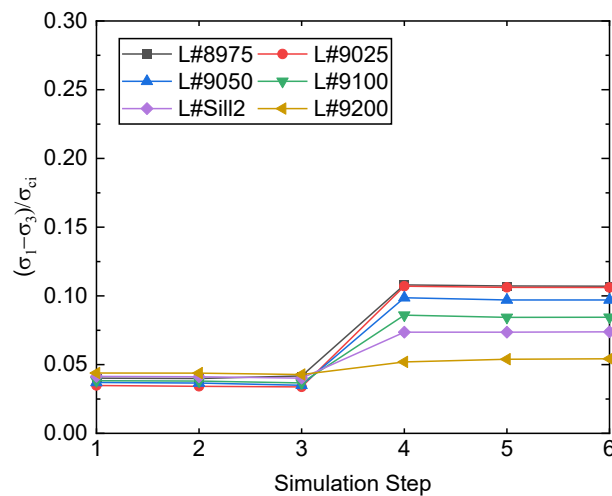


Figure 3.23 Comparison of damage initiation (DI) among six mining levels

From mining level ML#9200 to ML#9050, the damage initiation induced by the excavation sees gradual increase from the excavation step S3, when it reaches a stable state of damage initiation.

For mining level ML#9025 and ML#8975, they experience the same trend, even the same final damage initiation state, and figure 3.23 shows no difference between these two mining levels in the view of damage initiation.

The starting points are the same and the final values of each indication factors are almost the same at the same mining levels, which means the excavation length effect is rarely influenced by the mining depth, five different excavation scenarios cause almost the same results in sidewall displacement, redistributed major principal stress and the damage initiation (DI).

### 3.1.6 Comparison of consumed CPU time among different excavation scenarios

For numerical simulation method, the consumed CPU time for running the developed analysis model should be taken into consideration to make the analysis more productive. The consumed CPU time for the simulation can vary significantly among different simulation scenarios.

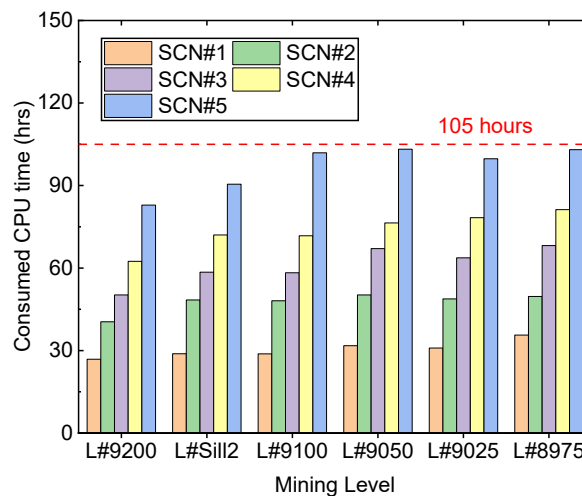


Figure 3.24 CPU time for different excavation scenarios at each mining level

The above figure 3.24 shows the consumed CPU time to run the numerical simulation excavation steps of the five proposed excavation scenarios. These six different mining levels present the similar trend of consumed CPU time among the five excavation scenarios, from scenario SCN#1

to scenario SCN#5. At each mining level, when the excavation steps increase, the consumed CPU time to run simulation increases. The consumed CPU time increases constantly from excavation scenarios SCN#1 to SCN#5 at each mining level.

At the same mining level, the consumed CPU time used in scenario SCN#5 is much more than the consumed CPU time used in excavation scenario SCN#1, as shown in figure 3.24. At the excavation scenario SCN#1, all the consumed CPU times at six different mining levels are less than 40 hours, while at excavation scenario SCN#5, the consumed CPU time of mining level ML#9200 and mining level ML#Sill2 are more than 80 hours. For excavation scenario SCN#5, the consumed CPU time for mining level ML#9100, ML#9050, ML#9025 and ML#8975 are more than 100 hours.

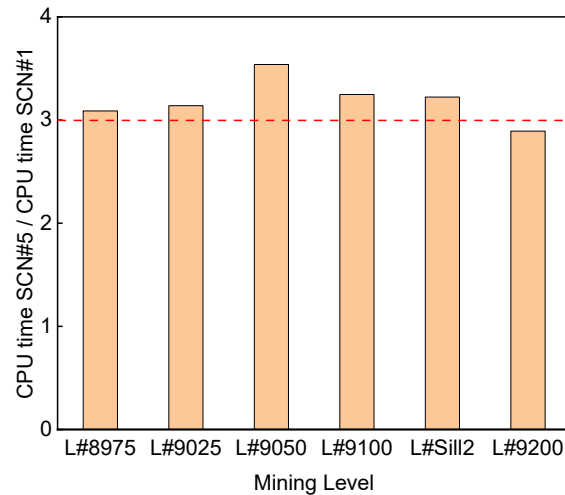


Figure 3.25 Comparison of CPU time between SCN#5 and SCN#1 at each level

Figure 3.25 illustrates the times of consumed CPU time between excavation scenario SCN#1 and excavation scenario SCN#5 at six different mining levels. As shown in figure 3.25, at each of the six different mining levels, the consumed CPU time used to run excavation scenario SCN#5 is about three times of the consumed CPU time used to run excavation scenario SCN#1. All these

values at all the six different levels are approximate the same. In this case, excavation scenario SCN#1 is more efficient and effective than excavation scenario SCN#5, and it will save about 66% of the consumed CPU time to complete the numerical simulation.

### 3.1.7 Conclusions

Based on the above results and discussion about the displacement, mining induced redistributed major principal stress, rock mass damage initiation and the consumed CPU time for the numerical simulation among the five different excavation scenarios with various excavation part length at six mining levels, the following conclusions can be achieved.

As for displacement of both sidewalls of the excavated stopes, compared with the other four excavation scenarios, excavation scenario SCN#1 results in almost the same final displacement with the other four excavation scenarios at six mining levels. With the increase of the mining depth, the same excavation scenario will cause larger final displacement at both the sidewalls of the excavated stopes, from mining level ML#9200 to ML#8975.

Excavation disturbs the initial stress state and causes the stress to redistribute, the redistributed major principal stress may cause the rock mass damages around the excavated stope openings. Here, the excavation plays a key role in the release of major principal stress at free surfaces on both sidewalls. Also, the initial redistributed major principal stress grows up with the mining levels going deeper, corresponding to the increase of the displacement of the sidewalls. Excavation scenario SCN#1 results in almost the same final major principal stress with other four excavation scenarios, from excavation step S1 to step S6, at each mining level.

As a key indicator to assess the potential rock mass damages, the damage initiation (DI) is used to assess the potential damages caused by the excavation steps of the five different scenarios. Diavik diamond mine is a hard rock mine, and the size of the single stope is so small compared with the

large size model, the excavation of the one single stope causes minimum damages in rock mass. The excavation scenario SCN#1 results almost the same results as other four excavation scenarios at each mining level.

Compared with the other four excavation scenarios, excavation scenario SCN#1 is more time efficient as well as reliable, according to the fact that it can save about 66% of the CPU time and get almost the same results in terms of displacement, major principal stress and potential rock mass damage initiation.

The excavation scenario SCN#1, which excavates the whole stope at one time, is an effective and efficient simulation excavation scenario, especially for the research focusing on the excavation-induced ground displacement and rock mass damages with a full size three-dimensional (3D) numerical model.

## 3.2 Backfilling step effect on stope stability

### 3.2.1 Literature review

With the mining production going deeper, applying backfilling to fill the mined-out stope voids has been widely used in underground mines over the past several decades. In many Canadian underground mines, the use of cemented rockfill (CRF) as backfill material is a common practice (Hassani and Archibald 1998, Parviz 1996). Cemented rockfill (CRF) allows for the full recovery of orebody while achieving global mine site stability (Brechtel et al. 1999, Grice 1989, Cordova et al. 2016, Emad et al. 2014b). To fulfill this, the exposed CRF masses require adequate compressive strength and stiffness to resist the forces and limit the displacement associated with movements in the rock mass surrounding the excavations (Potvin et al. 2008, Beck et al. 2010, Mercier et al. 2011). Also, the cemented rockfill (CRF) is a type of backfill with simple operation, moderate capital cost while acquiring good strength. Backfilling with controlled and rational specifications can improve ground support and pillar recovery effectively in underground mining (Reschke 1993, Shrestha et al. 2008, Yu et al. 2009).

To date, lots of work have been done to analyze the cemented rockfill (CRF) property with different component ratios in laboratory and backfilling effect of the stope stability under static and dynamic conditions, the relation between the backfilled CRF and the stope spans (Saw et al. 2011). Lingga (2018a, 2018b, 2019) conducted detailed laboratory experiments, including the measurement of compressive strength and stiffness and the shear properties, to achieve better ratios among the cement, water and aggregate to get proper backfilled CRF. Saw et al. (2011) and Stone (2007) studied the composition of different mix designations of water, waste rock, binder and their influences on the physical and mechanical properties of CRF at different curing times, temperature and humidity to achieve a target strength at different mining stages. Helinski et al. (2007, 2011),

Fahey et al. (2009), Gibson (1958) studied the curing process and the arching phenomenon of the backfilled CRF in the stopes by comparing field measured data and the back analysis based on laboratory measurements. In the blasthole stoping method, the backfilled CRF is prepared for the secondary stope blasting. Emad et al. (2012, 2014b, 2017) and Henning and Mitri (2010) examined and simulated different blast loads and profiles to assess the effects of blast vibrations on CRF backfilled stopes by monitoring vibration in a CRF stope. Thompson et al. (2009, 2012) quantified the evolution of total geo-pressures and pore pressures within the core of the backfilled CRF to assess the stability by conducting in-situ experiments in long-hole stopes. Kumar et al. (2016) conducted laboratory studies to characterize various mechanical properties of cemented rockfill (CRF) formulations and developed the relationship between the strength and the unit weight of CRF to better design and control the quality of CRF during its large scale application in underground cut-and-fill blasthole stopes. Cordova et al. (2016) undertook research to study the effect of particle size distribution upon the overall uniaxial compressive strength of the cemented rockfill (CRF). Seymour et al. (1998, 2018) and Tesarik et al. (2003, 2007) studied the long-term relationship between the compressive and tensile strength of CRF and the stability of CRF undercut spans by reading the monitoring data of the installed instruments in the test sites. Marlow et al. (2013) compared the shotcrete ribs and the cemented rock fill (CRF) in response to weaken the hazards and to control convergence and overbreak during the mining and backfilling process. Sainsbury et al. (2014,2017) developed a novel numerical modelling approach to accurately simulate the particulate nature of backfilled CRF and determined the stability of backfilled CRF exposures by conducting the novel numerical models that incorporate extraction, filling and the exposure sequence of the backfilled CRF filled stopes. All the mentioned above works have achieved an amount of significant and useful outcomes about the cemented rockfill (CRF) property

and backfilling effects on stope stability and mine global stability during the production of the whole mine site.

Backfilling with controlled specifications can be employed for improved ground support and pillar recovery in underground metalliferous mine workings (Parviz 1996). Where the fill is required to fill the extracted voids and to provide regional support (Helinski et al. 2007). Cemented rockfill (CRF) has proven to be of critical importance to the operation of many Canadian mines, primarily due to the rapid backfilling rate this method permits (Grabinsky, 2010). Cemented rockfill (CRF) is commonly used in conjunction with underhand cut-and-fill mining method to provide ground support in weak rock mass conditions, particularly in the underground mines. The cemented rockfill (CRF) supports the overlying material in the mine roof, also confines the surfaces of rock pillars and abutments (Brechetel et al. 1999, Cordova et al. 2016, Mitri 2007).

Underground mining involves the creation of voids that in many mining operations subsequently require backfilling to stabilize local stresses, minimize wall closure, and optimize ore recovery. Backfilling is a passive support and is used to prevent ore dilution from hanging wall and footwall, and it also enables good ground control (Doerner 2005). Backfill is used to fill the stope voids and serves basically as the working floor for the next slice, in addition to providing some degrees of confinement to the stope walls.

However, due to practical difficulties, it is impossible to conduct different backfilling scenario tests to study the influence of different backfilling scenarios on the stope stability in the in-situ field. With rapid developments in computer software and hardware, employing numerical modeling method to conduct various physical phenomena simulation in rock mechanics and rock engineering has achieved significant progress. Using numerical modeling method to model elastoplastic, non-linear, and post-yield behavior of rock masses and the effects of in-situ stresses

and excavation features on the mining works can help researchers to understand the “real world” in underground mining (Wang 2020). Thus, the application of the numerical simulation will be a good choice to investigate the influence of different backfilling scenarios on the stope stability. This part presents the investigations of five different backfilling scenarios in Diavik diamond mine by the full-size three-dimensional (3D) mine model to analyze the backfilling part length effects on the sidewall displacement, redistributed major principal stresses, and the stress concentration factor (SCF) on the stope sidewalls, and then decide the optimum backfilling scenario considering the consumed CPU time for running the simulation steps in numerical analysis finite element (FE) model.

### 3.2.2 Backfilling step scenarios

Continuing the previous PART-I, in which the excavation part length effect was investigated and analyzed, same with the PART-I, the six mining levels in mining pipe A154N were chosen to conduct the investigation, from mining level ML#8975 to level ML#9200, from the bottom to the top of the mining pipe, as shown in figure 3.26.

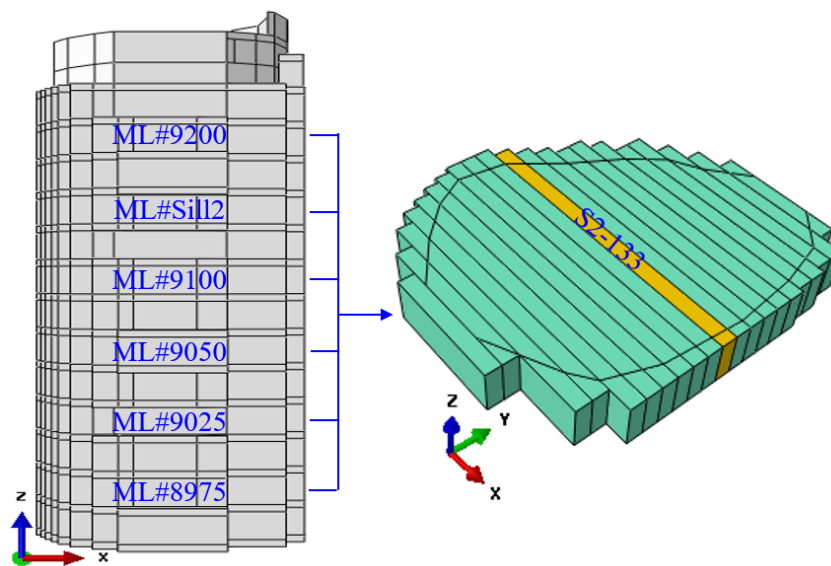


Figure 3.26 Profile of analyzed levels and stope S2-133

The elevation difference between two of the chosen levels is 30m, and the mining depths of these six mining levels are: -450m, -420m, -390m, -360m, -330m, -300m, from mining level ML#8975 to ML#9200, respectively.

Stope S2-133 was divided into several equal parts, from one part to five parts, as shown in figure 3.27. Five different backfilling scenarios were shown in figure 3.27, from backfilling scenario SCN#1 to SCN#5. For backfilling scenario SCN#1, it has one backfilling part, backfilling-1 (B1), and the length is 150 m. Backfilling scenario SCN#2 has two equal backfilling parts, B1 and B2, and each part is 75 m long. There are three equal backfilling parts for backfilling scenario SCN#3, B1, B2, and B3, and each part is 50 m long. Backfilling scenario SCN#4 has four equal parts, and backfilling scenario SCN#5 has five equal parts. Each part of backfilling scenario SCN#4 and SCN#5 are 37.5 m and 30 m long, respectively. The analyzed stope S2-133 has a size of 7.5m × 20m × 150m (width × height × length).

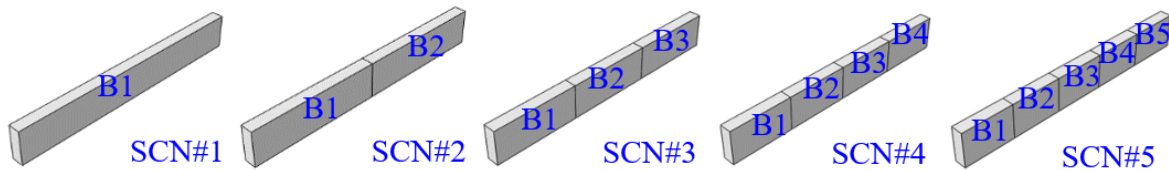


Figure 3.27 Five backfilling step scenarios

As shown in table 3.2, each backfilling scenario takes different steps to complete the simulation study of the excavation and backfilling process at the six mining levels in mining pipe A154N. In all five backfilling scenarios, the first simulation step Step1 (S1) is the geostatic step to calculate the initial state of stress before excavation, and the second simulation step Step2 (S2) is to excavate the whole stope S2-133. For backfilling scenario SCN#1, the third simulation step Step3 (S3) is to backfill the whole stope. In backfilling scenario SCN#2, it takes steps S3 and S4 to complete the backfilling the stope with the backfilling part B1 and B2. Following this logic, the backfilling

scenarios SCN#3 and SCN#4 take five and six steps in total, respectively, to complete the backfilling of stope S2-133. For backfilling scenario SCN#5, it takes five steps, S3, S4, S5, S6, S7, to finish the backfilling with backfilling part B1, B2, B3, B4 and B5, and in total, it takes seven steps to complete the simulation. Here, considering the actual technical limitations in field practice of backfilling, one assumption is made that once the CRF is backfilled, it takes into effect immediately with fully gained strength, and there will be no voids at the top of the backfilled CRF column and the whole stope voids will be fully backfilled with CRF.

Table 3.2 Five backfilling scenarios

Scenario	BF1	BF2	BF3	BF4	BF5	Step	Each part length(m)
SCN#1	Y	N	N	N	N	3	150
SCN#2	Y	Y	N	N	N	4	75
SCN#3	Y	Y	Y	N	N	5	50
SCN#4	Y	Y	Y	Y	N	6	37.5
SCN#5	Y	Y	Y	Y	Y	7	30

Note: Here, Y stands for yes, N stands for no. Step stands for the steps needed to complete simulation.

### 3.2.3 Results and discussion

Failure of underground openings in hard rocks is a function of the in-situ stress magnitudes, the characteristics of the rock mass, the intact rock strength, and the fracture network. In most scenarios, the failures are in the types of over-displacement in roof, swellings in the sidewalls, and over-heave in the floor. Same with the previous PART-I, in this part, the middle points of the sidewalls were chosen as the marked points to conduct the comparison and study.

### 3.2.3.1 Backfilling step effect on sidewall displacement

In the stope S2-133, for the roof and floor width, which is 7.5m, and the sidewalls are 20m high. Compared with the roof displacement and floor heave, the swellings of the sidewalls are more obvious and easier to monitor and measure in Diavik diamond mine.

As soon as the stope is excavated, the intact stress state around the stope surfaces changes, which causes stress release on the sidewall free surfaces resulting in the displacement in the sidewall free surfaces. The following figures show the sidewall displacement of the six mining levels, from mining level ML#8975 to ML#9200. Same with Part-I, here (a) and (b) represent the left and right sidewall, respectively. The dots on the represented curves are the steps.

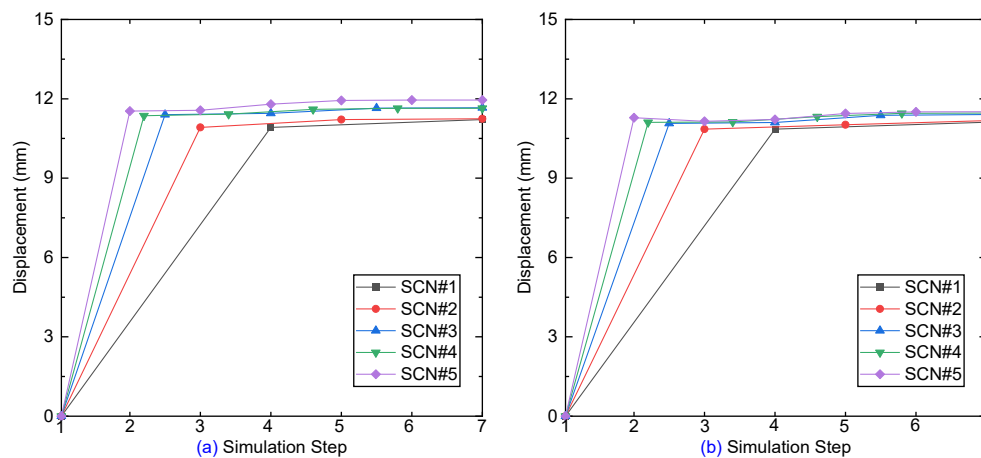


Figure 3.28 Displacement of two sidewall middle at level ML#8975

Figure 3.28 shows the sidewall displacement of mining level ML#8975, the changing trends of both left and right sidewall are similar. After step S2 of excavation of the whole stope, the displacement increases dramatically to the maximum values. With the process of backfilling, the displacement shows almost no more increase. For backfilling scenarios SCN#1 and SCN#2, the final displacement is about 10.5mm on both sidewalls. On the left sidewall, backfilling scenarios SCN#3, SCN#4 and SCN#5 have a larger displacement, which is about 12mm, while on the right

sidewall, it is about 11mm for these three backfilling scenarios. With the backfilled CRF taking into effect, it can effectively share the over layer load with the unmined stopes, which results in the slower increase of displacement on the sidewalls.

Similar with the changing trend in mining ML#8975, the sidewall displacement in mining level ML#9025 achieves the maximum value after the excavation of the whole stope, as shown in figure 3.29. Both sidewalls have a final displacement of 11mm among the five different backfilling scenarios. Different with mining level ML#8975, the five different backfilling scenarios show no difference at the final state of displacement at both sidewalls at mining level ML#9025, though for backfilling scenarios SCN#3, SCN#4 and SCN#5, which show the differences in the mining level ML#8975. Five backfilling scenarios present the same trend on both sidewalls of the stope S2-133, with the backfilled CRF taking into effect.

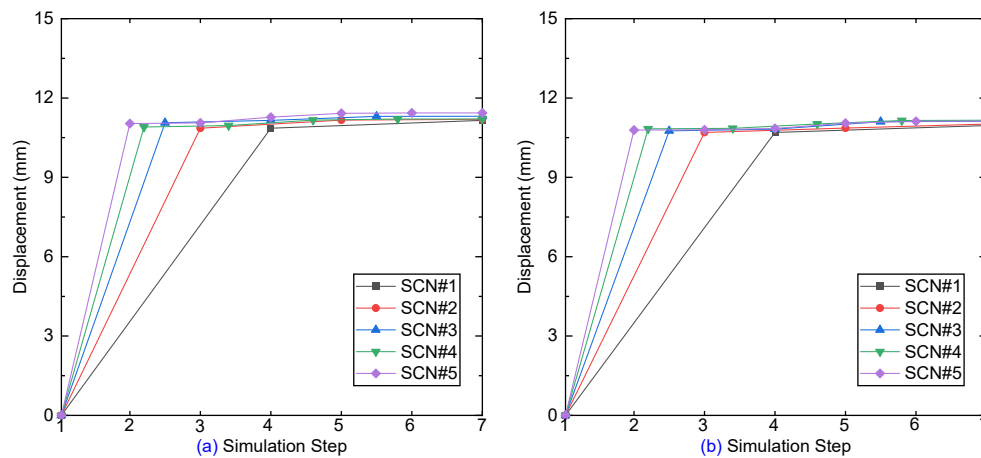


Figure 3.29 Displacement of two sidewall middle at level ML#9025

Following figure 3.30 illustrates the displacement changes during the excavation and backfilling process in stope S2-133 in mining level ML#9050. After step S2 of excavation of the whole stope, the displacement increases dramatically to the maximum values among all five backfilling scenarios. With the process of backfilling, the displacement shows almost no more increase. With

the mining depth going shallower, the final state of displacement on the sidewalls in stope S2-133 sees a decrease. As shown in figure 3.30, the final displacement on two sidewalls is about 10mm after the backfilled CRF taking into effect. Also, among the five different backfilling scenarios, after the backfilling steps were taken the difference of displacement was not shown. From backfilling scenario SCN#1 to SCN#5, after the backfilled CRF taking into effect, the displacement reaches a stable state, though for scenarios SCN#3, SCN#4 and SCN#5, which take several steps to backfill the stope S2-133.

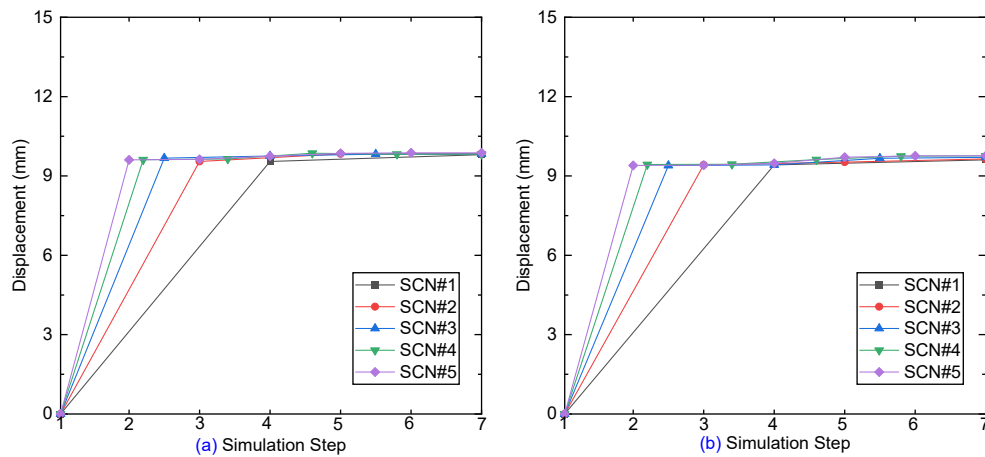


Figure 3.30 Displacement of two sidewall middle at level ML#9050

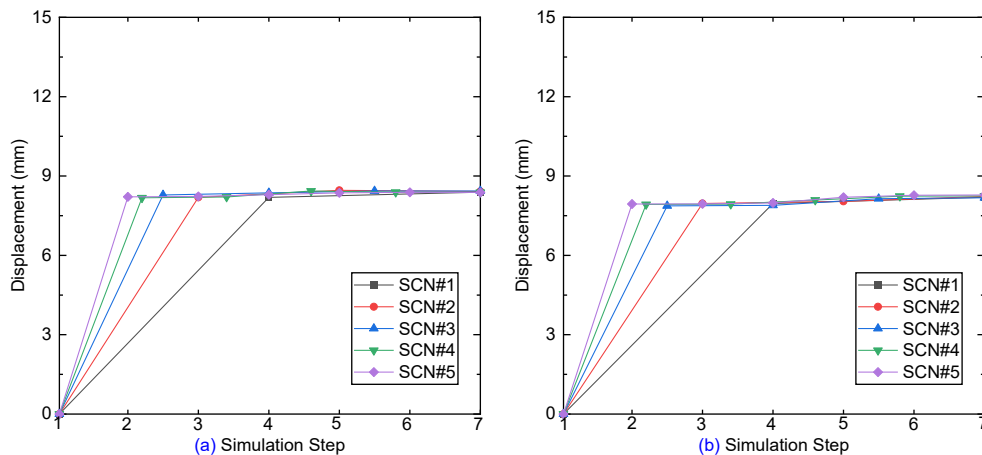


Figure 3.31 Displacement of two sidewall middle at level ML#9100

The displacement of sidewalls in mining level ML#9100 sees a final value of 8mm, as shown in figure 3.31. Among the five different backfilling scenarios, from the first step geostatic S1, the second step S2 excavated the whole stope S2-133, then the displacement on the sidewalls increases to its maximum value, especially for scenario SCN#1. For other four backfilling scenarios, before the backfilling part arrives at the monitored points, the displacement of the monitored points sees slight increases, from scenario SCN#2 to SCN#5.

As for the mining level ML#Sill2, it is close to the top surface of the mining pipe A154N, then the final displacement of the monitored points in ML#Sill2 is smaller compared to the deeper mining levels, and it is 7mm, compared with that of level ML#8975, it has a 42% decrease. Also, there is almost no difference of final displacement state among the five different backfilling scenarios.

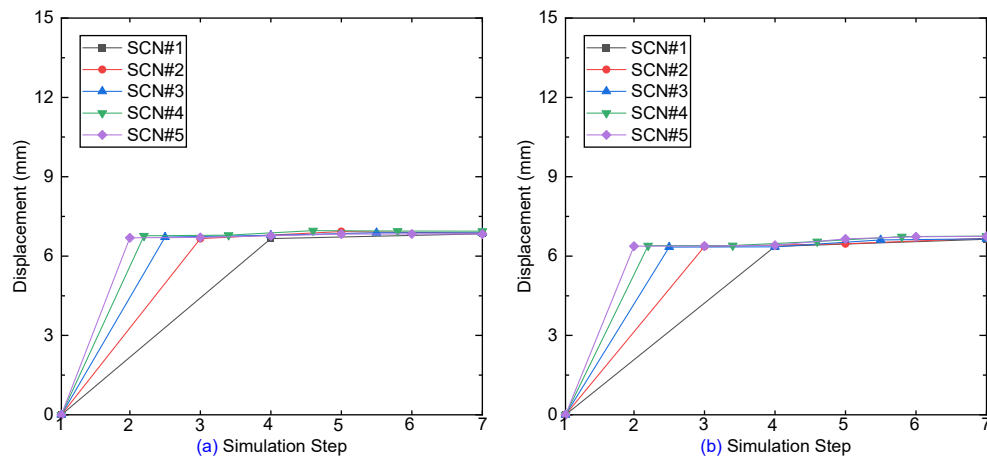


Figure 3.32 Displacement of two sidewall middle at level ML#Sill2

Among the six mining levels, stope S2-133 in mining level ML#9200 has the shallowest mining depth, then the final displacement state of two sidewalls in level ML#9200 is only 5mm, compared with the displacement of the other five mining levels, and it is the minimum one. Also, compared with the other five mining levels, the displacement change trend caused by the excavation step S2 is the slightest one. With the backfilled CRF taking into effect, the displacement shows no more

increase. Among these five different backfilling scenarios, scenario SCN#1 will provide the immediate support to the adjacent unmined stopes and improve the stability of the stopes for the next mining sequence.

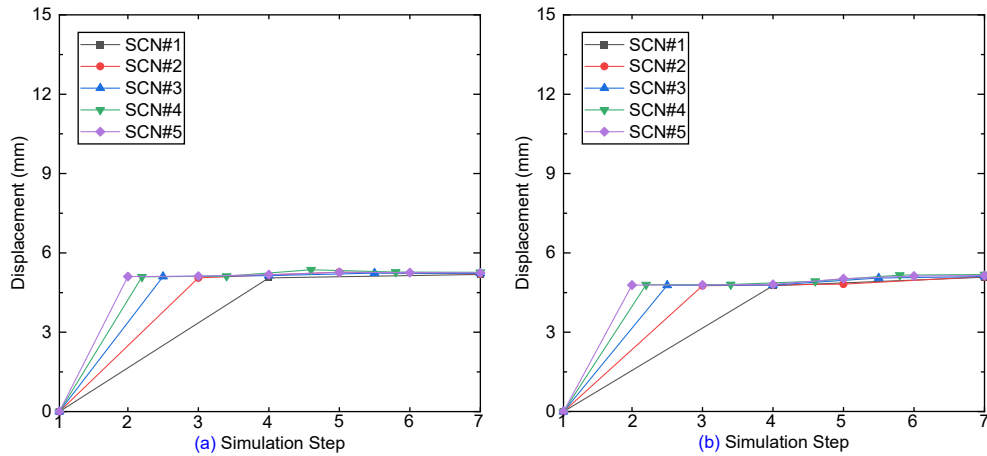


Figure 3.33 Displacement of two sidewall middle at level ML#9200

Comparing the displacement changes of backfilling scenario SCN#5 among the six mining levels, as shown in figure 3.34, with the increase of the mining depth, the displacement of the sidewall surface in stope S2-133 shows an increasing trend after the completion of the excavation step S2.

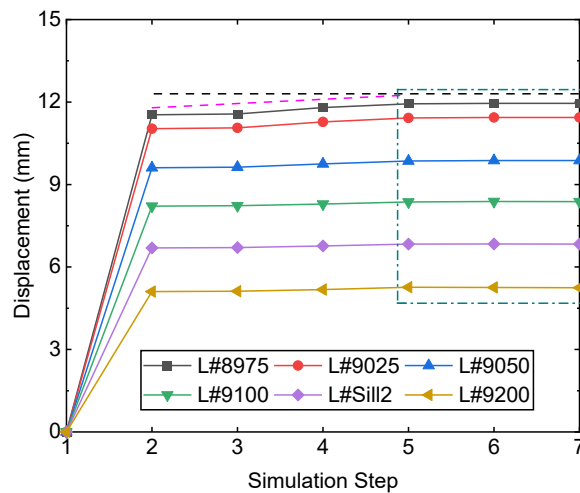


Figure 3.34 Comparison of displacement among six levels of scenario SCN#5

The deeper the mining level goes, the larger the displacement increases. After the backfilled CRF takes into effect, there is no more increase of sidewall displacement at these six different mining levels.

### 3.2.3.2 Backfilling step effect on major principal stress

Excavation in underground mining will disturb the intact stress state field around the mined stope openings and cause the stress to redistribute around the stope openings. The mining-induced stress redistribution may result in failures of the roof, sidewall and floor in the stope. Knowing the change path of the redistributed principal stress provides a reference base for the mining schedule and corresponding backfilling strategies.

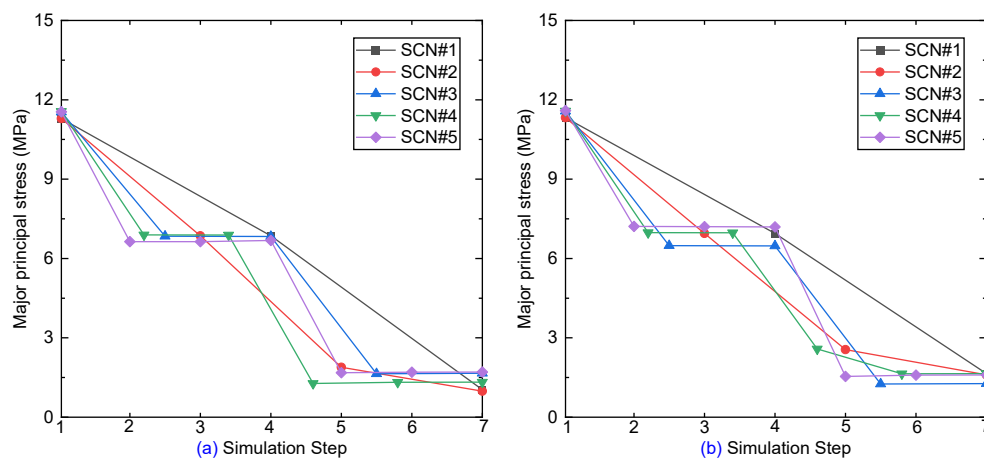


Figure 3.35 Major principal stress of two sidewall middle of level ML#8975

The major principal stress changes trends on the two sidewalls with the influence of the backfilled CRF of mining level ML#8975 are shown in figure 3.35. The excavation step S2 triggers the release of the major principal stress at the middle of the sidewalls to some degree at the first stage, then the major principal stress stays stable, after the backfilled CRF takes into effect, the major principal stress decreases swiftly at the monitored points. On both sidewalls, all the five different backfilling scenarios have almost the same final major principal stress. Mining level ML#8975 sees a decrease of 87% in the major principal stress from the state of before-excitation to the after-

backfilling, though the five backfilling scenarios have different changes during the several backfilling steps.

Following figure 3.36 presents the major principal stress changes on the sidewalls in stope S2-133 in mining level ML#9025. Both scenarios SCN#1 and SCN#2 see the constant decrease from the geostatic step S1 to the step the backfilling completion. For the other three scenarios, SCN#3, SCN#4 and SCN#5, after the step S2 of excavation of stope S2-133, the major principal stress stays stable at the monitored points till the backfilling steps commence one by one, then with the influence of the backfilled CRF, the major principal stress decrease to a minimum level. From initial 10.8MPa to the final 6.5MPa, the major principal stress of the sidewalls in the stope S2-133 in mining level ML#9025 sees a decrease of 39.8%, among all five backfilling scenarios.

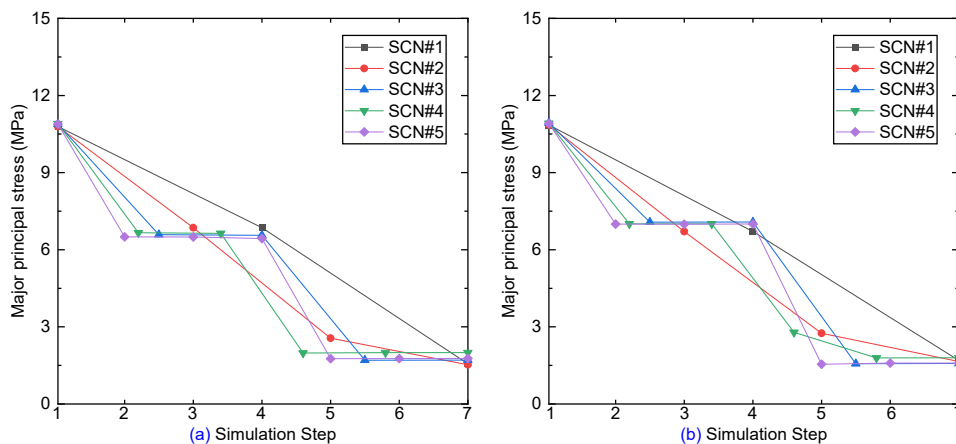


Figure 3.36 Major principal stress of two sidewall middle of level ML#9025

On the left sidewall of stope S2-133 in the mining level ML#9050, for backfilling scenario SCN#1, with the excavation step S2, the major principal stress sees a 32% decrease caused by the excavation stress release, from 9.8MPa to 6.6MPa. With the backfilled part P1 takes into effect at step S3, backfilling scenario SCN#1 sees another 77% decrease till the final stage of the major principal stress. For scenarios SCN#3, SCN#4 and SCN#5, the major principal stress keeps stable at the monitored points, till the backfilling parts take the place of the stope voids, as shown in

figure 3.37. Among the five backfilling scenarios, the major principal stress achieves an 85% decrease with the influence of backfilled CRF. The right sidewall sees a similar changes trend.

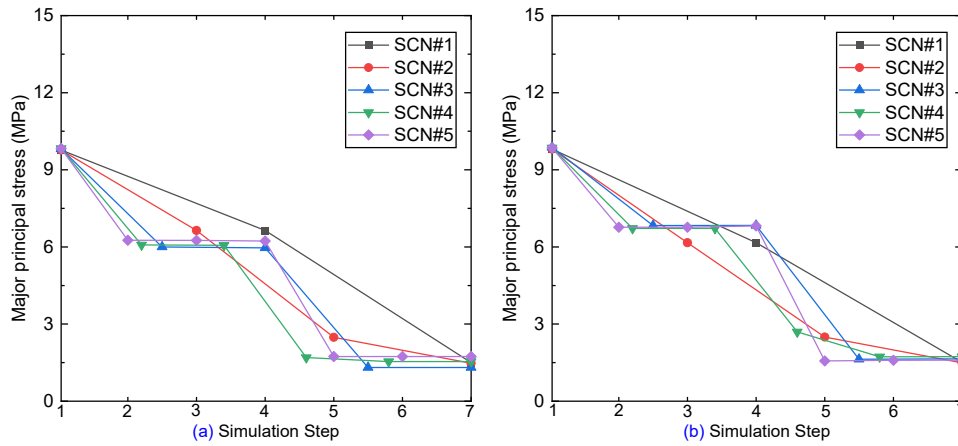


Figure 3.37 Major principal stress of two sidewall middle of level ML#9050

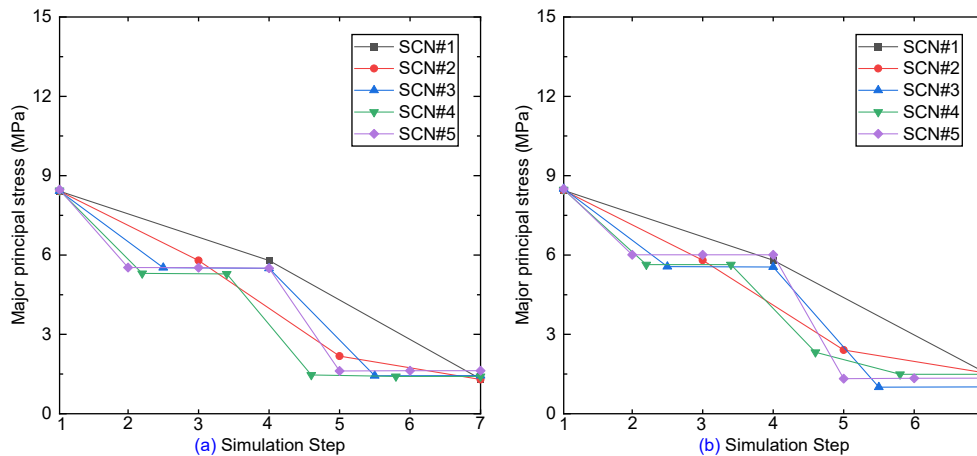


Figure 3.38 Major principal stress of two sidewall middle of level ML#9100

As the analyzed mining level going shallower, the initial major principal stress state decreases, as shown in figure 3.38, in the stope S2-133 in mining level ML#9100, the major principal stress at the geostatic step S1 is 8.5MPa, after the excavation and backfilling steps, it decreases to 1.4MPa, with a decrease of 84%. In backfilling scenario SCN#2, after the excavation of stope S2-133, the major principal stress has an 32% decrease, caused by the excavation stress release on the free

surfaces of the sidewalls, from 8.5MPa to 5.7MPa, after the first backfilling part P1 takes into effect, the decrease is 63%, after the backfilling part P2, the major principal stress achieves the final value of 1.4MPa. For backfilling scenarios, SCN#3 and SCN#5, the backfilling parts take into effect cause 74% and 71% decrease, respectively.

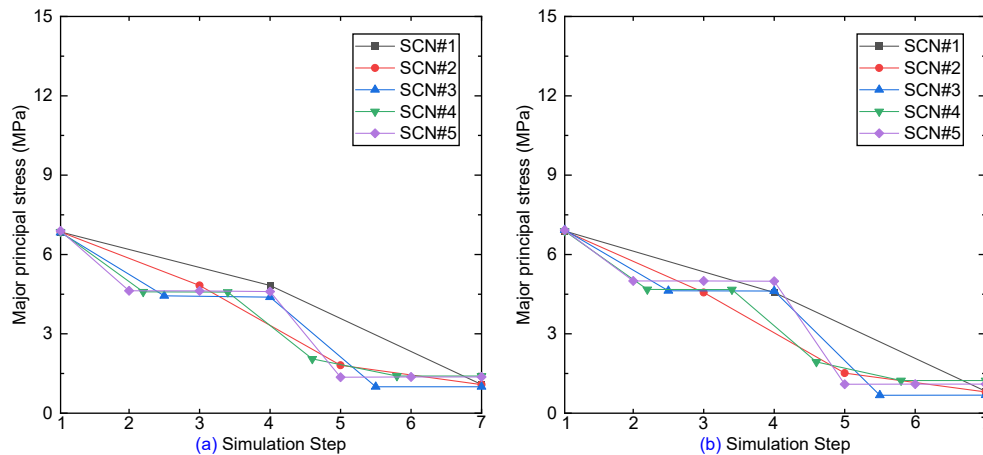


Figure 3.39 Major principal stress of two sidewall middle of level ML#Sill2

Starting at 6.8MPa and ends at 1.1MPa, the major principal stress in the stope S2-133 in mining level ML#Sill2 sees an 84% decrease during the process of excavation and backfilling of stope S2-133. Also, compared to the deeper mining levels, the change trend is slighter form the initial state to the final state. For the backfilling scenarios SCN#3 and SCN#5, the backfilling part at the monitored points takes into effect causing decrease of 74% and 72%, respectively. Compared with the total decrease of major principal stress, the backfilling step takes a major part of the total decrease, which proves that the backfilling parts can effectively share the stress with the adjacent unmined stopes and improve the stability of the unmined stopes.

As the shallowest mining levels among these six analyzed mining levels, mining level ML#9200 has the minimum initial stress state, compared with the other five mining levels, and it is 5.2MPa. With a final state of 1MPa, the major principal stress in the mining level ML#9200 witnesses an

80% decrease during the process of excavation and backfilling of the stope S2-133, as shown in figure 3.40. For backfilling scenarios SCN#3 and SCN#5, the major principal stress decrease amplitude is slighter than these of the other five mining levels. From mining level ML#8975 to ML#9200, with the influence of the backfilled CRF taking effect at each step, the final state of the major principal stress is not larger than 1.5MPa, though with the changes of mining depths.

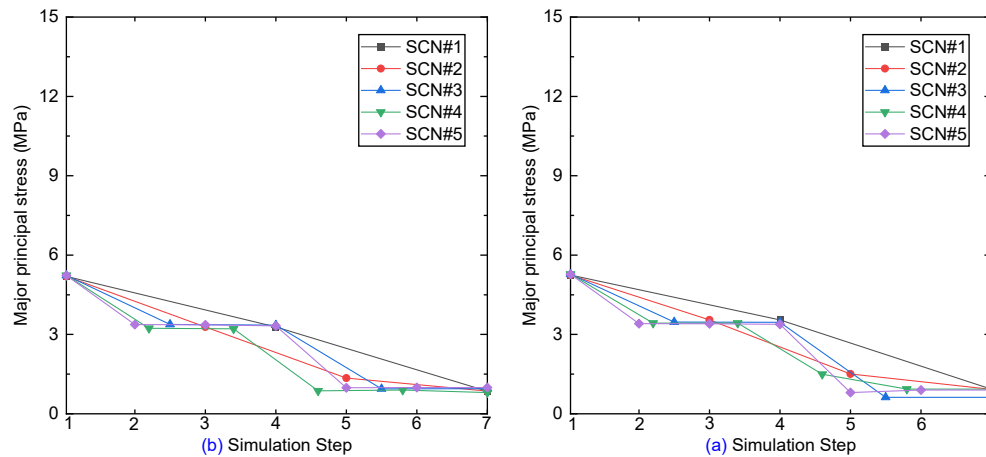


Figure 3.40 Major principal stress of two sidewall middle of level ML#9200

Figure 3.41 presents the changes of major principal stress in the backfilling scenario SCN#5 in all five analyzed mining levels during the process of excavation and backfilling the stope S2-133 at each mining level. With the mining levels getting close to the top surface of the mining pipe A154N, from mining level ML#8975 to ML#9200, the initial major principal stress level at geostatic step S1 decreases, as well as the final principal stress at the last step S7. At all six mining levels, when the backfilled CRF starts to take into effect, the body of the backfilled CRF will share the mining-induced redistributed stress with the adjacent unmined stopes. Backfilling scenario SCN#5 presents an obvious change trend to this at the monitored points, when the backfilled CRF body takes into effect, the principal stress sees a plunge from backfilling step S4 to step S5, and after that the principal stress achieves a stable status. The decreasing percentages of the major principal

stress from before-excavation to after-backfilling of the stope S2-133 of these four mining levels are very close, with a value over 80%, from mining level ML#8975 to ML#9200.

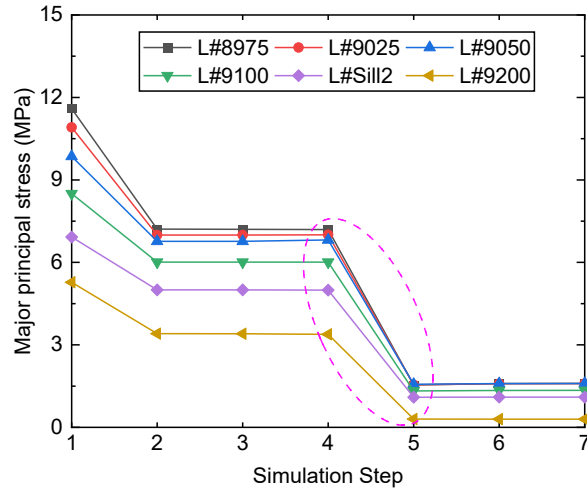


Figure 3.41 Comparison of major principal stress among six levels of scenario SCN#5

### 3.2.3.3 Backfilling step effect on sidewall stress concentration factor (SCF)

Mining the stopes in underground will cause stress redistribution as well as the stress concentration effect at the corners of the stopes with rectangular intersection. Wiseman (1979) found that the stability of tunnels in massive rocks can be assessed by comparing stresses on the boundary of essentially square openings to the laboratory uniaxial compressive strength. In 1979, he proposed the stress concentration factor (SCF) to assess the stability of the sidewalls according to his laboratory experiment and in-situ observations and measurements in South African mine tunnels [41].

$$SCF = (3\sigma_1 - \sigma_3) / \sigma_c \quad (3.2)$$

where  $\sigma_1$  and  $\sigma_3$  are the in-situ excavation-induced major and minor principal stress (MPa), respectively.  $\sigma_c$  is the laboratory uniaxial compressive strength (UCS) (MPa).

As a key factor, the sidewall stress concentration factor (SCF) is widely used to assess the sidewall stability in underground tunnels. In Diavik diamond mine, the excavated stope avoids in mining pipe A154N can be seen as the tunnels before the backfilling CRF takes the place of the stope voids. With the influence of the backfilling, the sidewall stress concentration factor (SCF) can also be used to assess the sidewalls in the stopes.

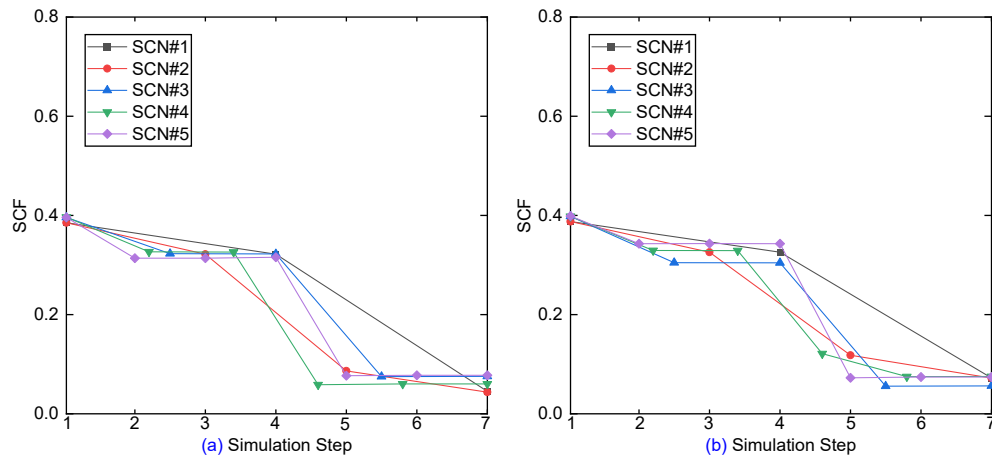


Figure 3.42 SCF of two sidewall middle at level ML#8975

At the starting geostatic step S1, the sidewall stress concentration factor has the maximum value in both sidewalls in mining level ML#8975, and it is 0.4, as shown in figure 3.42. After the excavation step S2, the stress concentration factor presents a slight decreasing trend among all the five backfilling scenarios. When the backfilling body takes into effect at different steps among the five backfilling scenarios, the stress concentration factor witnesses a sharp decrease and achieves a stable value of about 0.08. With the influence of the backfilled CRF, the sidewall stress concentration factor (SCF) sees an 80% decrease in mining level ML#8975, from the starting one of 0.4 to the final one of 0.08, from the initial state to the step the backfilling finished.

Similar with the trend of the major principal stress, the initial stress concentration factors of the sidewalls in mining level ML#9025 are smaller than those of mining level ML#8975, as shown in figure 3.43. For the backfilling scenarios SCN#1 and SCN#2, at both sidewalls, the sidewall stress

concentration factor witnesses a constant decrease, and the decreasing amplitude is larger when the backfilled CRF takes into effect. Before the backfilled CRF takes into effect, the sidewall stress concentration factor keeps almost constant in backfilling scenarios SCN#3, SCN#4 and SCN#5 at both sidewalls, after the backfilled CRF body takes into effect, the sidewall stress concentration factor sees a dramatic decrease and then keeps constant. Mining level ML#9025 has a 78% decrease from 0.37 to 0.08, from geostatic step S1 to the last backfilling step.

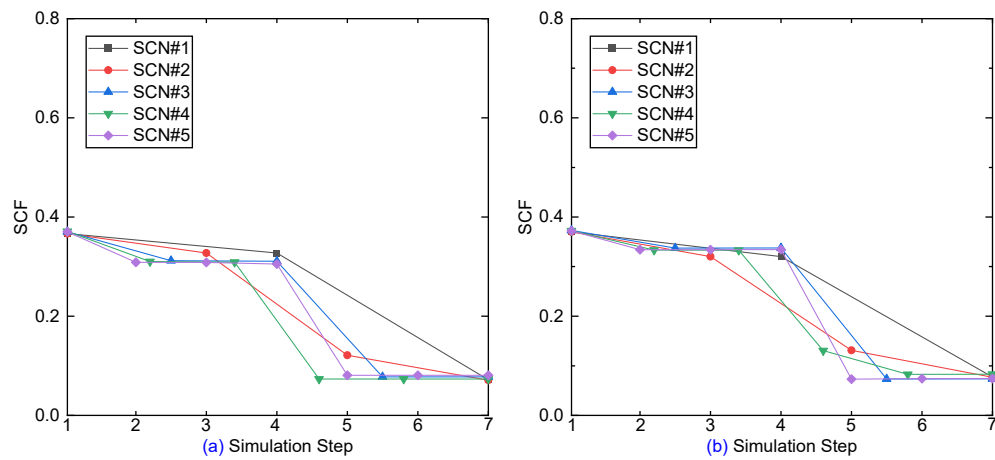


Figure 3.43 *SCF* of two sidewall middle of level ML#9025

Starting with a SCF of 0.33 and ending with a SCF of 0.04, mining level ML#9050 sees an 88% decrease of stress concentration factor (SCF) on both sidewalls, as shown in figure 3.44.

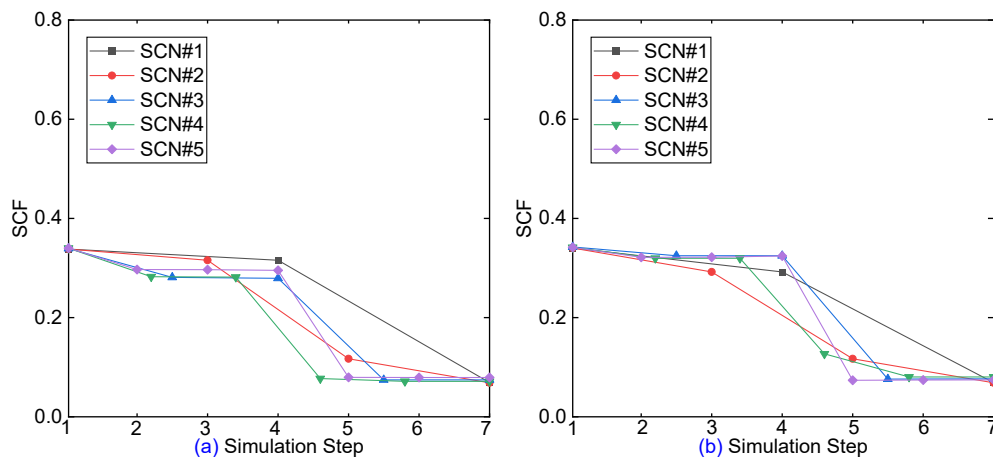


Figure 3.44 *SCF* of two sidewall middle of level ML#9050

With mining level ML#9050 getting close to the top surface of mining pipe A154N, the amplitude of the decrease of stress concentration factor (SCF) is getting smaller, though for backfilling scenario SCN#1, which backfills the stope S2-133 with backfilling step S3, compared with the deeper two mining levels, ML#8975 and ML#9025. On the left sidewall, after the excavation of stope S2-133, the stress concentration factor (SCF) of backfilling scenario SCN#1 is the highest, compared with that of other backfilling scenarios, on the right sidewall, the backfilling scenarios SCN#3 and SCN#5 have the highest SCF.

Figure 3.45 illustrates the stress concentration factor (SCF) on the sidewalls in the stope S2-133 in mining level ML#9100. The stress concentration factor (SCF) decreases from 0.3, at the initial stage at geostatic step S1, to 0.07 at the final stage with the backfilled CRF taking into effect, with an 76% of decrease. Similar with mining level ML#9050, on the left sidewall, after the excavation of stope S2-133, the stress concentration factor (SCF) of backfilling scenario SCN#1 is the highest, compared with that of other backfilling scenarios. On the right sidewall, the backfilling scenarios SCN#3 and SCN#5 have the highest SCF. Backfilling scenarios SCN#3, SCN#4 and SCN#5 see almost the same decrease amplitude starting from the step of backfilling at the monitored points on the sidewalls.

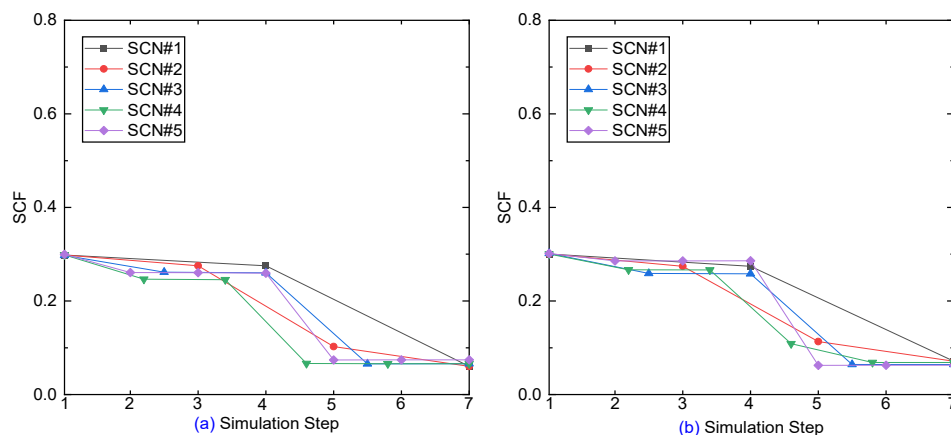


Figure 3.45 SCF of two sidewall middle of level ML#9100

Mining level ML#Sill2 starts the stress concentration factor (SCF) at 0.26, and it ends at 0.06, with an 77% of decrease from geostatic step S1 to the step of backfilling completion, among all five backfilling scenarios. The decrease amplitude of SCF on the left sidewall is smaller than that on the right sidewall in each backfilling scenario. From backfilling scenario SCN#2 to SCN#5, as soon as the excavation of stope S2-133 at the step S2, the stress concentration factor (SCF) sees slight decrease. When the backfilled part arrives at the monitored points and the backfilled CRF takes into effect, the SCF decrease swiftly from a value over 0.2 to a value around 0.06, as presented in figure 3.46. On both sidewalls, the stress concentration factor (SCF) follows the similar trend, which is that after the excavation of stope S2-133, the SCF decreases slightly, when the CRF takes into effect, the SCF decreases quickly, and reaches a stable state. The backfilled CRF provides immediate support to the sidewalls for the adjacent unmined stopes.

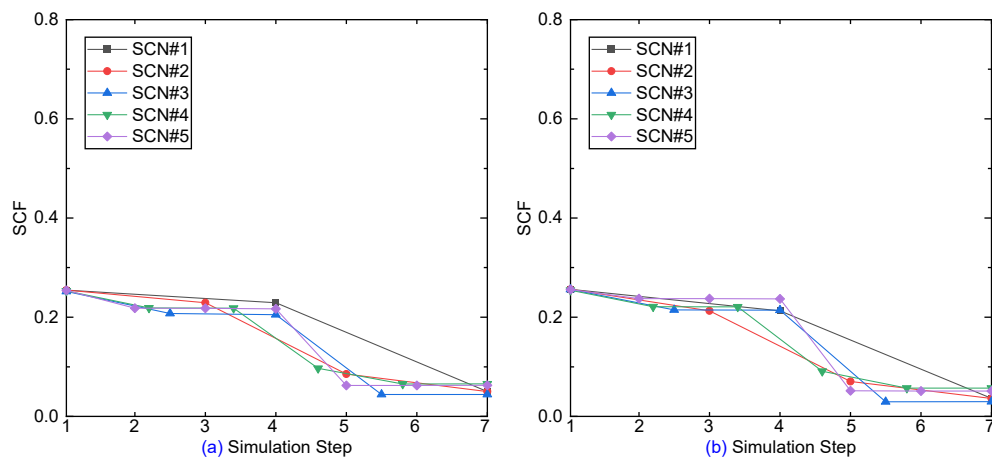


Figure 3.46 SCF of two sidewall middle of level ML#Sill2

For mining level ML#9200, it is close to the top surface of the mining pipe A154N, then the stress concentration factor (SCF) on the sidewalls in the stope S2-133 has the minimum starting stress concentration factor, which is 0.2, as shown in figure 3.47. On the left sidewalls, with the backfilled CRF taking into effect, the stress concentration factor (SCF) stops at 0.05, with a 75% decrease,

from the geostatic step S1 to the last backfilling step. On the right sidewall, the stress concentration factor (SCF) can be as low as zero for backfilling scenario SCN#5 with the backfilled CRF column taking into effect in the stope voids. And other four backfilling scenarios have a final state of stress concentration factor (SCF), which is lower than 0.05.

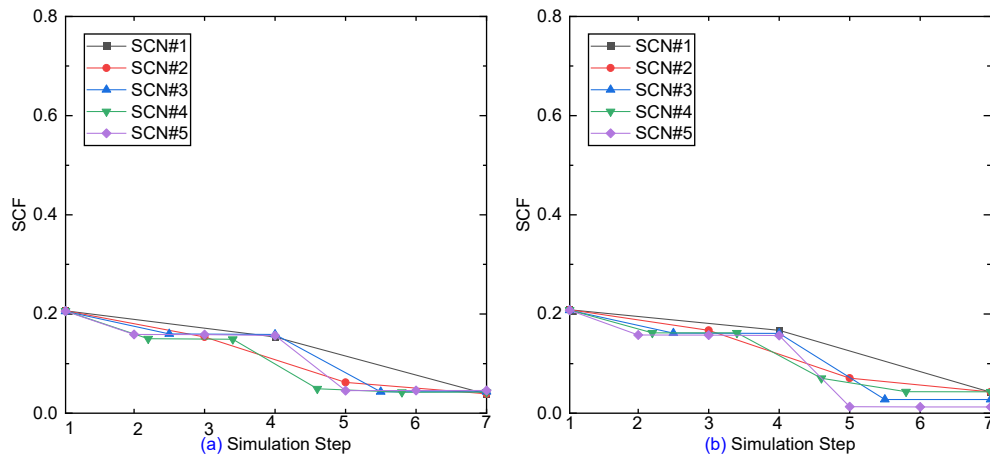


Figure 3.47 *SCF* of two sidewall middle of level ML#9200

According to the above results of the sidewall stress concentration factor (SCF) in the six different mining levels during the process of excavation and backfilling of stope S2-133, the backfilling bodies can effectively reduce the stress concentration effect on the surface of the stope sidewalls. After the backfilled CRF column bodies take into effect, the stress concentration factor (SCF) will decrease to a value under 0.1, which means the backfilled CRF column bodies can effectively prevent the possible failure of the sidewall and improve the stability in the adjacent unmined stopes. The decreasing amplitude of the sidewall stress concentration factor (SCF) has an increasing trend when the mining level becomes shallower, though the differences of decreasing amplitude among the four mining levels are very close.

An example comparison of the stress concentration factor of backfilling scenario SCN#5 among the six mining levels was conducted, as illustrated in figure 3.48. The stress concentration factor

(SCF) has a strong relation with the mining level depth before the backfilling bodies take into effect, the shallower the mining level, the smaller the sidewall stress concentration factor. While, after the backfilling bodies take into effect at step S4, the relation between the stress concentration factor and the mining level depth shows no more relation.

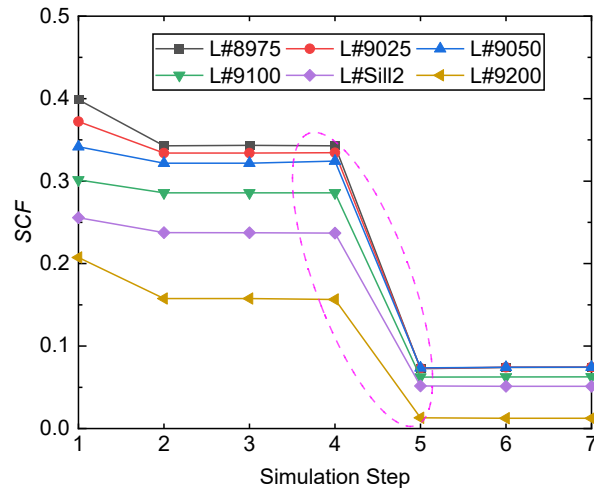


Figure 3.48 Comparison of *SCF* of SCN#5 among six mining levels

All six mining levels see a sharp decrease of the sidewall stress concentration factor (SCF) at the monitored points when the backfilling process is finished at backfilling step S4. All the six sidewall stress concentration factors (SCFs) will be under 0.1 and keep constant after the completion of backfilling step, which means the backfilled CRF is taking into effect and share the over layers weight and mining induced redistributed stress with the adjacent unmined stopes. From figure 3.48, one conclusion can be made that using the backfilling CRF of same strength at different mining depths is acceptable and feasible to improve the stability of the stopes.

### 3.2.3.4 Discussions

From the above analysis of the sidewall displacement, mining-induced major principal stress, and the sidewall stress concentration factor (SCF) at the monitored points in the sidewalls in the stope

S2-133 in mining pipe A154N, backfilling scenario SCN#1 is the optimum option among these five different backfilling scenarios. Considering the final status of sidewall displacement, redistributed major principal stress, and the sidewall stress concentration factor (SCF), the backfilling process of backfilling scenario SCN#1 can be done in the shortest time compared with the other four backfilling scenarios, which will save time for the following mining activities and release the tension between the preparation and blasting.

Meanwhile, compared with the other four backfilling scenarios, scenario SCN#1 can immediately provide immediate and adequate support to the adjacent unmined stopes and prevent the possible failure caused by the delayed-parted backfilling, thereby improving the stope stability.

From the decreasing percentages of the major principal stress from before-excavation to after-backfilling of these six mining levels, the same kind of backfilling CRF can achieve almost the same effect in lowering the redistributed major principal stress in the sidewalls, though at different mining depths.

In the aspect of decreasing the sidewall stress concentration factor (SCF), the same type of backfilled CRF with same strength and elastic properties achieves very close decreasing amplitude, though with the changes of the mining depths. Combined with the decrease percentage of displacement, major principal stress and stress concentration factor (SCF), using the same type of backfilled CRF at different mining depths can result in the same effect in the aspect of decreasing the stress concentration factor and then improving the stability of the stopes.

### **3.2.3.5 Conclusions**

By comparing the displacement, redistributed major principal stress and sidewall stress concentration factor (SCF) caused by the excavation, the backfilling is an effective method to prevent possible failures and improve the safety in the mining stopes.

With the backfilling bodies taking into effect, the sidewall displacement sees no more increases, compared with the sharp increases caused by the excavation step. The five different backfilling scenarios result in almost the same final displacement results. By stopping the increase of the sidewall displacement, the backfilling bodies prevent the possible sidewall failure, which provides better conditions for the next stope mining sequence schedule.

The sidewall major principal stress release caused by the excavation sees a dramatic plunge with the effect of the backfilling bodies. The backfilling bodies share the mining induced redistributed stresses with the adjacent unmined stopes. Compared with the other four backfilling scenarios, backfilling scenario SCN#1 sees a constant decreases of the sidewall major principal stress with the process of excavation and backfilling and arrives at a very low value status at the six different mining levels.

As a key factor to assess the stope sidewall stability, the stress concentration factors (SCF) of each mining level proves that the backfilling bodies are effective to reduce the stress concentration effect on the sidewalls. By lowering the sidewall stress concentration factor (SCF), the backfilling bodies improve the stability of the adjacent unmined stopes for the next stope mining scheme.

Among the five different backfilling scenarios, the backfilling scenario SCN#1 is the optimum method among these five scenarios. By applying the SCN#1 backfilling scenario, the displacement will keep constant and has no more increase, which can prevent the possible failure on the sidewalls. For the major principal stress, compared with other four backfilling scenarios, though after the excavation, it shows a decreasing trend, scenario SCN#1 will achieve the minimum status quickly. Moreover, the usage of the same type of backfilled CRF with the strength achieves good results at the six different mining levels.

### 3.3 Chapter summary

In this chapter, two investigations were conducted. The first one was presented in the PART-I, which investigated the excavation part length effect on the stope stability in numerical analysis. The second one was about the backfilling part length effect on the stope stability, and it was presented in PART-II. And the stope S2-133 of the six different mining levels was analyzed for conducting the study. Five different excavation scenarios and five backfilling scenarios were proposed to conduct the study.

For the investigation of the excavation part length effect, three indicating factors were analyzed for the study, displacement, major principal stress and damage initiation (DI). The comparison of the three indicating factors caused by the five different excavation scenarios was conducted. Also, the consumed CPU time for running the simulation steps of different excavation scenarios was compared and analyzed. Based on the comparison results of displacement, major principal stress, damage initiation, consumed CPU time, among the five proposed excavation scenarios, excavation scenario SCN#1, which excavated the whole stope S2-133 by one step, was the optimum option. From excavation scenario SCN#1, excavation the whole length of the stope at once is a rational and feasible alternative excavation scheme compared to the scheme of excavation one whole stope in two or three steps, when conducting the numerical study of excavation effect on the ground surface and mine site stability based on a full mine size three-dimensional (3D) finite element model.

As a continuing study, in PART-II, the investigation of backfilling part length effect on the stope stability was conducted. According to PART-II, the proposed backfilling scenario SCN#1 was an alternative option when conducting the analysis of finite element modelling, especially conducting the numerical simulation of a whole mine size model focusing on the global mine site stability.

Backfilling scenario SCN#1 could backfill the stope voids in the shortest time, in which the immediate support will be provided to the adjacent unmined stopes.

The conclusions from this chapter prove that in numerical modelling analysis, especially focusing on the full size mine model, the alternative options are feasible and reliable to conduct the study.

The alternative option, in this chapter, it is scenario SCN#1 for both investigations of excavation part length and backfilling part length effect on the stope stability, can achieve an optimum balance of analysis accuracy and consumed CPU time to make the numerical analysis more productive and efficient. This chapter pays the foundation to the following Chapter 5 and Chapter 6.

## **CHAPTER 4: OPTIMUM LOCATION OF THE LAST-MINED STOPE IN MINING LEVEL DURING MINING AND PILLAR RECOVERING WITH THE INFLUENCE OF BACKFILLING**

*In this chapter, investigation will be conducted to locate the optimum location of the last-mined stope in both mining and sill pillar recovery. Mining of the last stope at the mining level can be more dangerous, especially with high mining-induced redistributed stress. The two-dimensional (2D) numerical analysis will be processed, and the detailed three-dimensional (3D) numerical analysis will be conducted in the following Chapter 5 and Chapter 6.*

## 4.1 Optimum location of the last-mined stope with the influence of backfilling

### 4.1.1 Stope configuration at mining levels

As shown in following figure 4.1, the stopes arrangement in mining level N9050 and level N9075 are the same. In the simulation steps, after the completion of the excavation of one stope in the mining level, the mined stope voids will be backfilled with cemented rockfill (CRF) at the next simulation step. For example, stope P1-95 in mining level N9050 is excavated at step S40, and it will be backfilled with CRF at step S41. The stopes S2-193 are the last stopes that are mined at both mining levels N9050 and N9075.

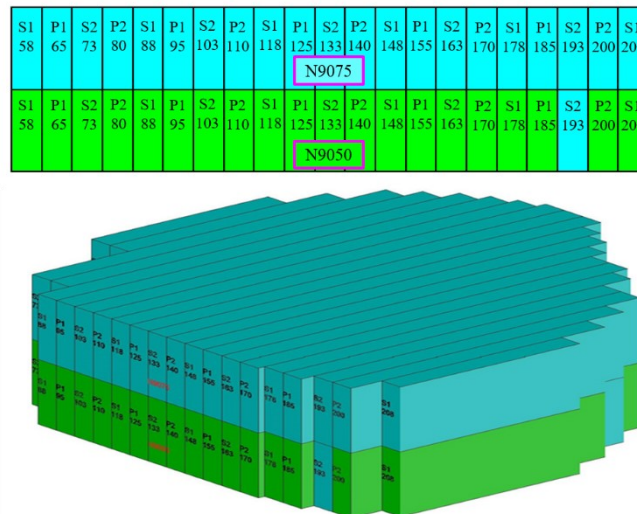


Figure 4.1 Stope mining and backfilling in level N9050 and N9075

In figure 4.1, the color cyan represents the kimberlite rock mass, all the stopes in mining level N9075 and the stope S2-193 in mining level N9050. The green color stands for the backfilled CRF. The excavation process starts from stope P1-65 in level N9050, after excavation of stope S2-193 in level N9050, the mining process moves to the upper level N9075. When all stopes in level N9075 are excavated, the mining process moves to upper levels.

The laboratory tested backfilled CRF samples collected at Diavik diamond mine (DDM) were cored in the already backfilled stopes. The backfilled CRF was fully cured, and the samples were

shipped to the university of Alberta. In the rock mechanics lab, both ends were trimmed according to the ASTM standards to make cylindrical samples for laboratory strength tests.

According to the laboratory test results, the backfilled CRF is much weaker than the kimberlite, as shown in table 2.4 in chapter 2. In this case, it is a practical question that whether the backfilled CRF surrounding the stope S2-193 in level N9050 can hold the kimberlite rock mass in upper level N9075 within a small subsidence of the upper layers to keep stope S2-193 safe during the mining process in stope S2-193. Is stope S2-193 the optimum location of the last mined stope in the level N9050? The stability of the last mined stope S2-193 is a priority problem.

#### **4.1.2 Literature review**

Stopes, as the basic excavation elements of sublevel open stoping mining method in underground mining, play key role in the whole production process. Mathews et al. (1981) initially proposed stability graph to predict the open-stope stability, and this method based on a limited number of cases. Chen et al. (1983) showed that the stope height was the critical design parameter. Bai et al. (2013) presented a new algorithm to optimize stope design for the sublevel stoping mining method with two parameters: (i) the maximum distance of a block from the raise and (ii) the horizontal width required to bring the farthest block to the raise. Cai et al. (1998) assumed tensile cracking as the dominant fracture mechanism for brittle rocks under compressive pressure. Diederichs et al. (1999) explored the influence of residual tensile strength and boundary parallel relaxation on the failure process by using crack and rock-bridge analogues, and updated the empirical stability assessment techniques for underground tunnels and for mining stopes. Martin et al. (2003) provided examples to illustrate how the philosophy of observational design method can be used to infer the in situ stress state. Zhang and Mitri (2007) presented that previous beneath mining activities significantly affected the stability of stope walls by the method based on yield zone

distribution. Cepuritis et al. (2010) back-analyzed hanging wall over-break data from longhole open stopes, and established global relationships between velocity and plastic strain and marked increases in over-break. Idris et al. (2011a, 2011b, 2012) studied the stability of open stopes considering the variability in the rock mass properties and divided rock mass into six strength classes. Cai (2011) presented a systematic assessment of uncertainty in rock mass characterization in rock engineering. Kurlenya et al. (2012) presented the estimation of stability of stopes in the bottom-up slice mining by modelling the stress-strain state and in situ observations. Urli and Esmaili (2016) presented the ore-skin design approach, and showed that the minimum ore-skin thickness required depends on the quality of governed rock mass and could be a function of stope lifetime. Heidarzadeh et al. (2018) evaluated the individual and interactive effects of open stope geometrical parameters related to brittle damage of the surrounding rock mass.

For stope stability assessment, many works were done on displacement prediction, mining induced stress assessment, protect supporting design. While the location optimization of the last-mined stope was rarely discussed, especially with the influence of the CRF backfilling mining method. The location of the last-mined stope plays a key role in mining safety and resource recovery rate in each level. Rational location of the last-mined stope can not only improve the resource recovery rate but also with lower instability of overcuts and undercuts. Then, the influence of the backfilled CRF is considered to optimize the location of the last mined stope.

Blasthole stoping (BHS) mining method includes two sublevels and amount of preparation of the stopes before production commence. One sublevel is on the top of the stope, it is for drilling and called overcut, and another is at the bottom of the stope, it is for production and called undercut. Usually, both overcut and undercut have the same width as the stope, as shown in figure 4.2. Hustrulid (2001) classified the features of the mines which apply BHS mining method, and the

three main features are: i) host rock and orebody are competent, ii) orebody dip is steep, iii) boundaries of orebody are regular. The case study mine Diavik diamond mine (DDM) meets all three features. The host rock granite and the orebody kimberlite are competent. All the three mining pipes, A418, A154S and A154N are located steeply, as shown in figure 2.2 and figure 2.15. The boundary between the host rock granite and orebody kimberlite is regular, as shown in figure 2.28.

In the blasthole stoping mining method, the mining level is excavated by each single stope block, and the excavated stope void is backfilled immediately after the excavation. Compared with the backfilled cemented rockfill (CRF), the strength of the kimberlite is stronger. Due to the special structure of the kimberlite pipe, according to the numerical analysis results and in-situ reported failure cases, observation and measurement, the kimberlite unmined stopes in the mining level provides more support to the upper kimberlite mining levels, then the location of the last mined stope in each mining level is a key factor to keep the stability of the mining levels.

#### **4.1.3 Last-mined stope location scenarios**

To achieve a quick assessment and analysis, the simulation method in this chapter applies a global-to-local method. Firstly, the primary studies are run in the three-dimensional (3D), shown in figure 2.20. After the completion of the first simulation step S1 of geostatic, the stress field of the researched levels are extracted from the three-dimensional (3D) model and applied to a simplified two-dimensional model. By extracting the stress field of level N9050 and N9075 in the three-dimensional (3D) model, the extracted stress is applied to the simplified two-dimensional (2D) model of stopes in level N9050 and N9075. The simplified two-dimensional (2D) models are shown in the following figure 4.2, figure 4.3 and figure 4.4.

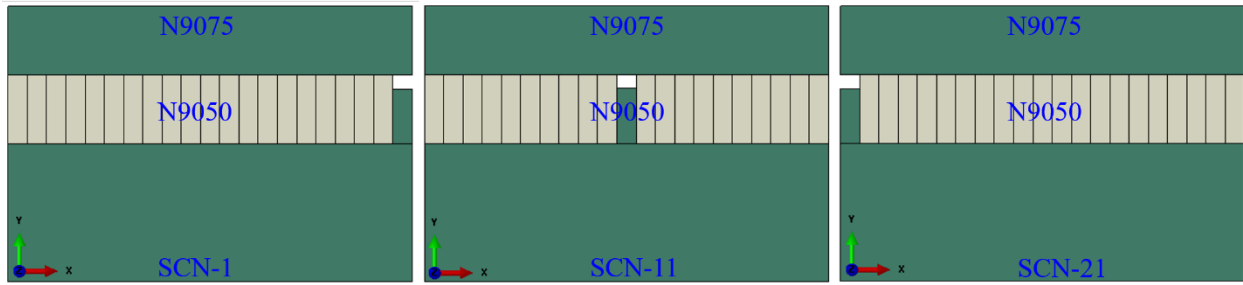


Figure 4.2 Example scenarios with overcut of Case-1

For the Case-1 (C1), it means that there are only overcuts in the stopes in level N9050, figure 4.2 shows three representative locations of the last mined stope in the level N9050. Scenario SCN-1 means that the last mined stope is at the right edge of the level. Location 21 means the last mined stope is at the left edge of the level. During the simulation process, the location of the last mined stope changes the location from the right edge to the left edge, from scenario SCN-1 to scenario SCN-21. For the scenario SCN-11, it means that the last mined stope is in the middle of the level. The void area in the figure is the overcut.

For the Case-2 (C2), it only has undercuts in the stopes in level N9050, figure 4.3 presents the locations of the undercut in each stope. The simulation process begins from the SCN-1 and ends at SCN-21. The void area at the bottom of the stope is the undercut.

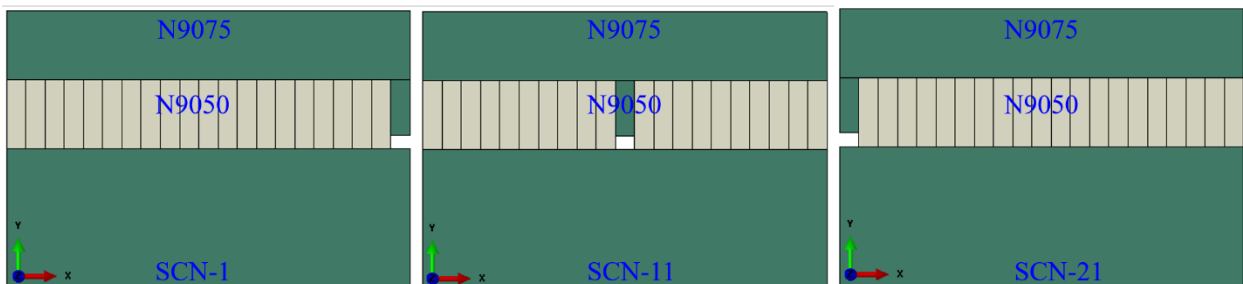


Figure 4.3 Example scenarios with undercut of Case-2

For the Case-3 (C3), it has both overcuts and undercuts in the stopes at the same location scenario with cases C1 and C2. Figure 4.4 shows the locations of last mined stopes with both overcut and undercut. Moreover, Case-3 (C3) has the same simulation process with cases C1 and C2.

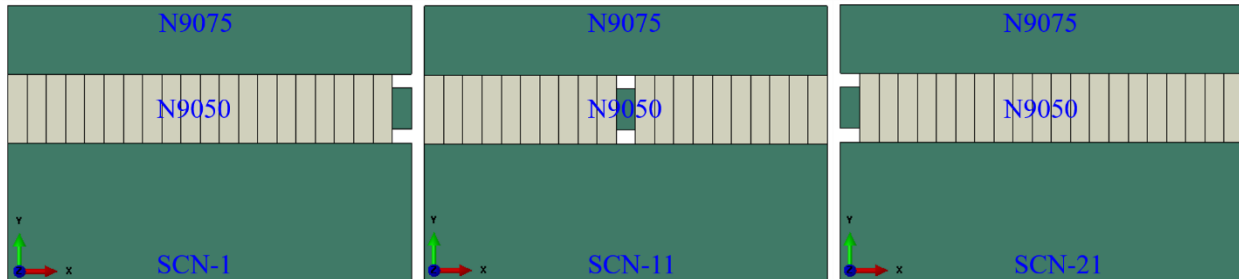


Figure 4.4 Example scenarios with overcut of Case-3

All three cases have the same boundaries condition, also the same stress condition fields are applied to the three cases. In figure 4.2, figure 4.3 and figure 4.4, the dark green represents the unmined kimberlite orebody, the white represents the backfilled CRF. And the size of the 2D model is  $157.5\text{m} \times 150\text{m}$  (width  $\times$  height), the height of both levels N9050 and N9075 is 30m. The kimberlite block under level N9050 is 90m in height. Both undercut and overcut have the same size,  $7.5\text{m} \times 5\text{m}$  (width  $\times$  height).

In underground mining, roof displacement, floor heave and sidewall swelling are the commonly seen in the overcuts and undercuts. Also, excavation in the shape of rectangular easily causes the stress concentration effect at the four corners of the openings. Then monitoring and measuring the displacement at these locations can provide indication of the possible failure in the openings. From the overcut and undercut layouts, eight locations are selected for the comparison. Node1 and node3 represent the roof corners of the overcut and undercut, and node2 and node6 represent the middle points of the roof and floor, respectively. Node4 and node8 are the middle points of both sidewalls, node5 and node7 are the floor corners, as shown in figure 4.5. Similarly, the locations chosen from

the undercut are also marked with eight nodes. The displacement of these eight locations are significant factors to indicate the safety of the crosscuts.

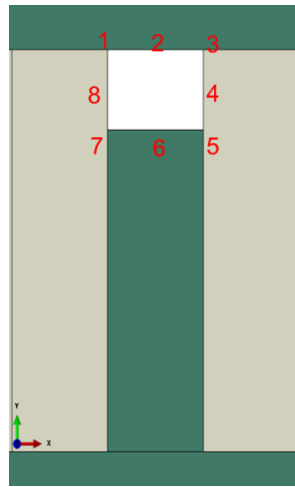


Figure 4.5 Chosen comparison location in overcut

#### 4.1.4 Displacement of chosen location in the overcut

The displacement of node1 and node3 in the overcut in both cases C1 and C3 is shown in figure 4.6. In both cases, the minimum displacement of the overcut corners is over 4 cm, while most of the maximum displacement is less than 5 cm, especially in the overcut in case C3.

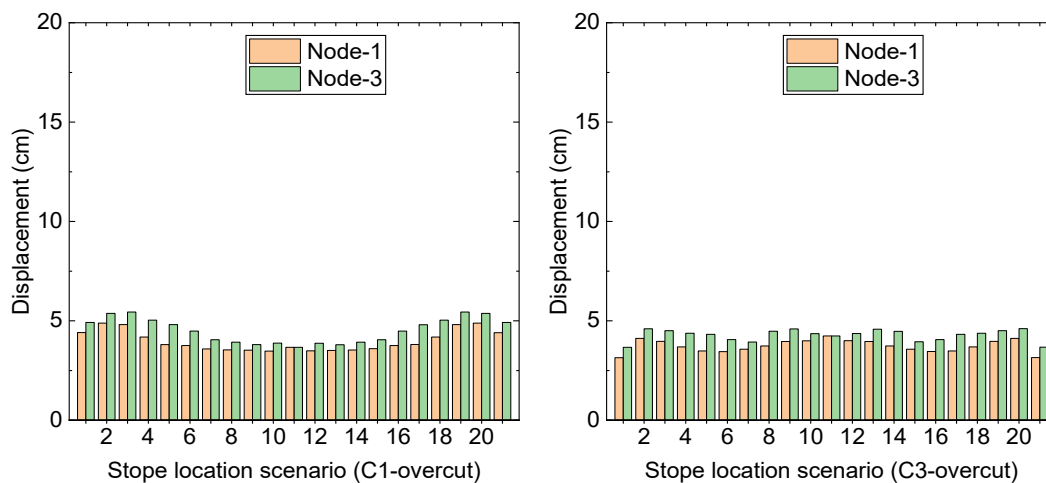


Figure 4.6 Overcut displacement at node1, node3 of cases C1 and C3

From figure 4.6, there is no significant difference among different location scenarios of the last mined stope. Each location of the last mined stope has small and similar displacement in both cases C1 and C3; though case C3 has the undercut at the bottom of the stope, while case C1 only has the overcut.

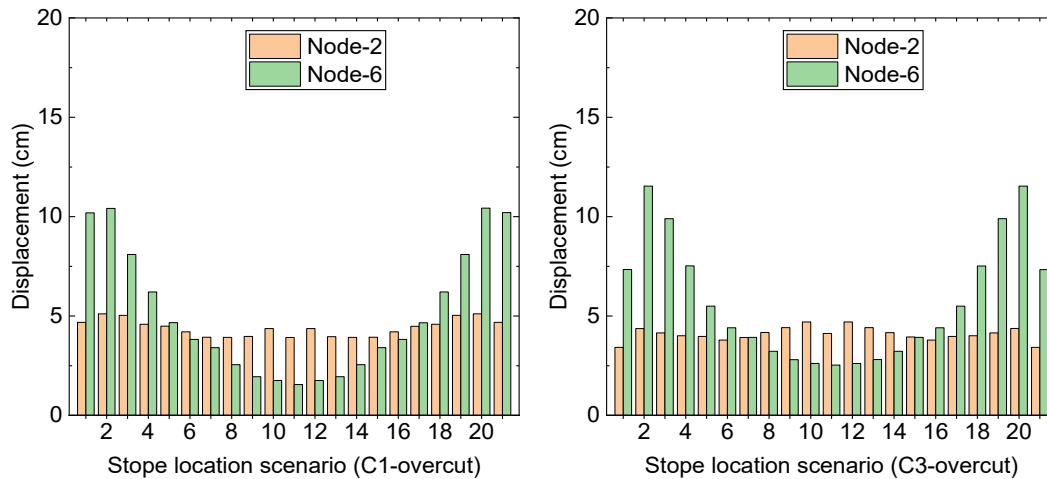


Figure 4.7 Overcut displacement at node2, node6 of cases C1 and C3

Figure 4.7 presents the displacement of the middle point of the roof and floor. In both cases, the displacement of the roof is small, and it is under 5cm, as it is shown with node2. For the heave of the floor center, it is larger than the displacement of the roof center when the location of the last mined stope is away from the vertical center axis of the level. Both the two corners and middle point of the roof has almost the same displacement, shown in figure 4.6 and figure 4.6. Whereas for the locations around the center axis, the displacement of the roof center is larger than the heave of the floor center in both cases C1 and C3. For the heave of the floor, from each side to the center of the level, the displacement decreases gradually for both cases C1 and C3, and the floor center heave at location scenario SCN-11 is the minimum. The displacement of the roof center shows no obvious effect by the last mined stope locations.

Excavation in the crosscuts makes the free surfaces of the sidewalls, also with the stress release on the sidewalls. Figure 4.8 shows the sidewall swellings caused by the stress release. Similar with the change trend of roof displacement and floor heave, the central location of the level has the minimum sidewall swellings, which is around 3 cm.

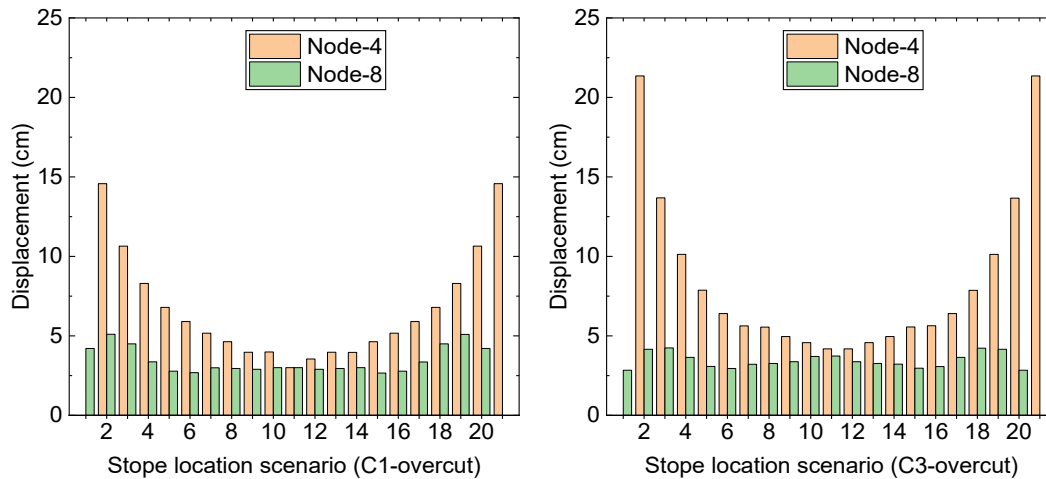


Figure 4.8 Overcut displacement at node4, node8 of cases C1 and C3

At the same location of the last mined stope in both cases of C1 and C3, the swelling in case C3 is larger than that in case C1. For example, in location No.2, case C3 has a 22 cm swelling and case C2 has a 15 cm swelling, which are also the maximum sidewall swelling at the same location in each case. The swelling of the sidewall middle in cases C1 and C3 presents a different trend. In case C1, the right sidewall has larger swellings, while in case C3, it is the left sidewall that has larger swellings.

As shown in figure 4.9, the heave of the two floor corners at the same location of the level is almost the same, and for most of them, it is less than 10 cm. From the edge to the center of the level, the heave of the floor corners decreases gradually, and the central location has the minimum value of the floor heave. The heave of the overcut of the floor corners in case C3 is slightly larger than that in case C1 except for the furthest locations at the level edges.

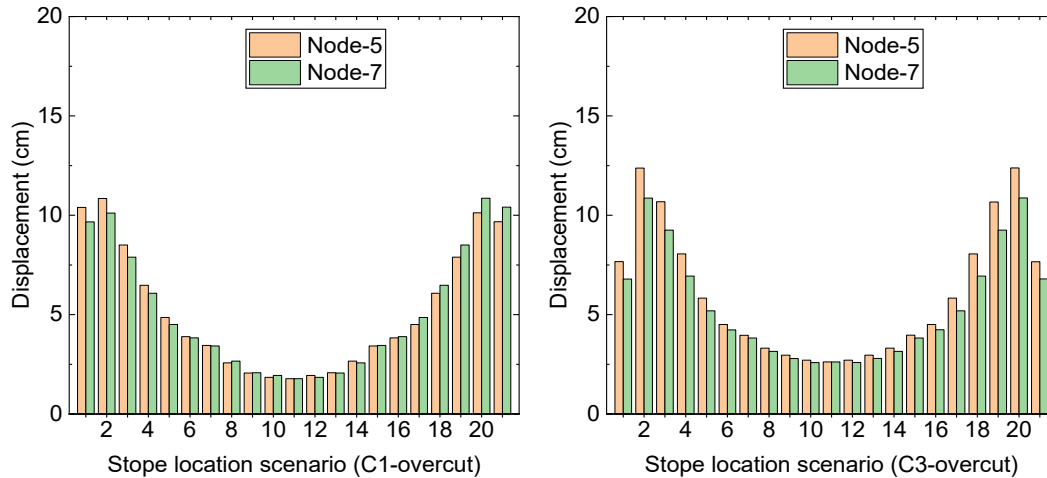


Figure 4.9 Overcut displacement at node5, node7 of cases C1 and C3

#### 4.1.5 Displacement of chosen location in undercut

A comparison of the displacement at node1 and node3 in the undercut in both cases C2 and C3 shows the same trend. Different with the trend in the overcut in cases C1 and C3, the displacement of node1 and node3 in the undercut decreases from the level edge to the center of the level, as shown in figure 4.6 and figure 4.10.

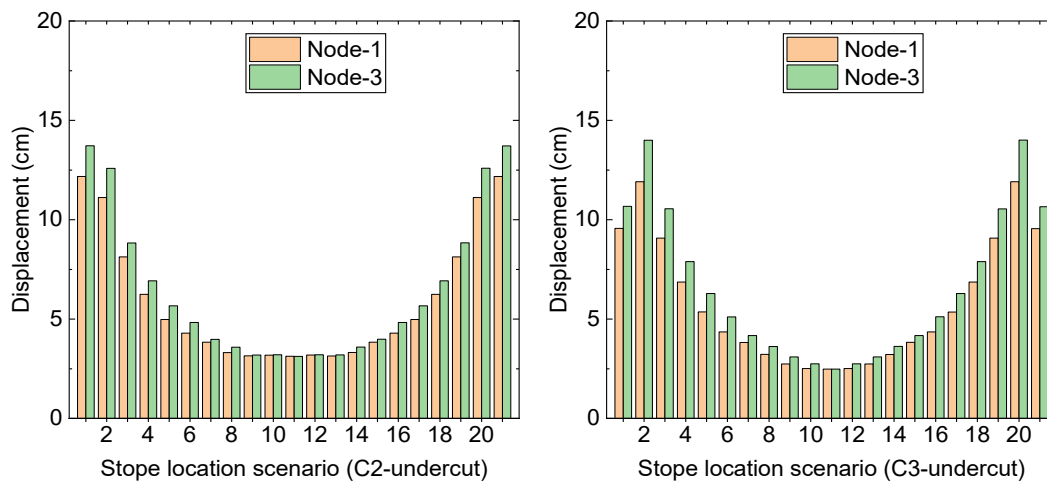


Figure 4.10 Undercut displacement at node1, node3 of cases C2 and C3

The minimum displacement at node1 and node3 in case C2 is around 3 cm, while the maximum displacement can be 13 cm. For case C3, the minimum displacement is about 2.5 cm, and the

maximum one is about 13 cm, same as that in case C2. The displacement of node1 and node3 in the undercut is more sensitive to the influence of the backfilled CRF and the location of the last mined stope than that in the overcut.

As shown in figure 4.11, for the displacement of node2 and heave of node6 in the undercut in cases C2 and C3, the heave of node6 is very small compared with the displacement of node2. The displacement of the roof is more obvious than the heave of the floor in the undercut in both cases C2 and C3. The maximum displacement of the roof can be 13 cm, while the heave of the floor is less than 2 cm in both cases C2 and C3.

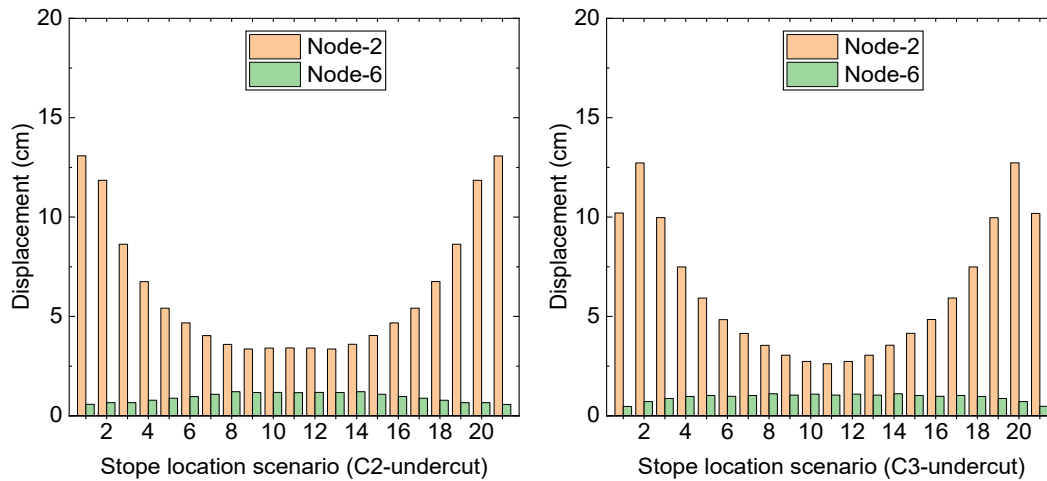


Figure 4.11 Undercut displacement at node2, node6 of cases C2 and C3

Different from the change trend of the displacement of the roof, shown in figure 4.8, the heave of the floor increases from the level edge to the central location of the level, though the maximum floor heave is less than 2 cm, as shown in figure 4.11. Then, the displacement of the roof is an indicator that is more reliable than the heave of the floor in the undercuts.

Figure 4.12 shows the sidewall swellings in the undercut of cases C2 and C3. Compared with the swellings of the right sidewall, the swelling of the left sidewall presents a different trend though the sidewall swellings are very small. The maximum sidewall swelling on the right side is less

than 2.5 cm, while the maximum sidewall swelling on the left side can be 18 cm and 22 cm in case C2 and case C3, respectively.

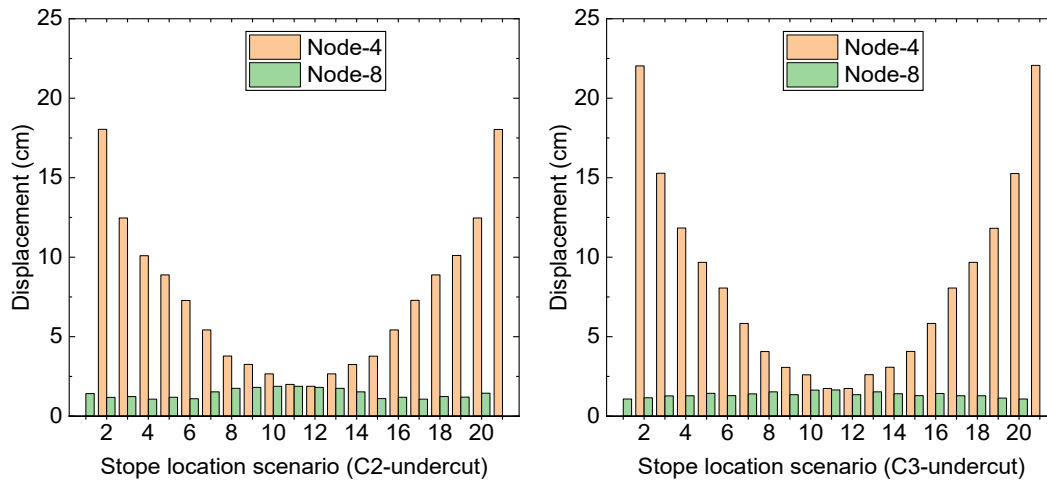


Figure 4.12 Undercut displacement at node4, node8 of cases C2 and C3

According to figure 4.8 and figure 4.12, the sidewall swelling of the left sidewall in the overcut is larger than that of the undercut, while the change trend of the left sidewall swelling in the undercut is sharper than that in the overcut, especially when the locations are close to the edge of the level, according to figure 4.8 and figure 4.12. The sidewall swelling on the right sidewall sees almost no changes from the edge to the center of the level in both cases C2 and C3, shown in figure 4.12.

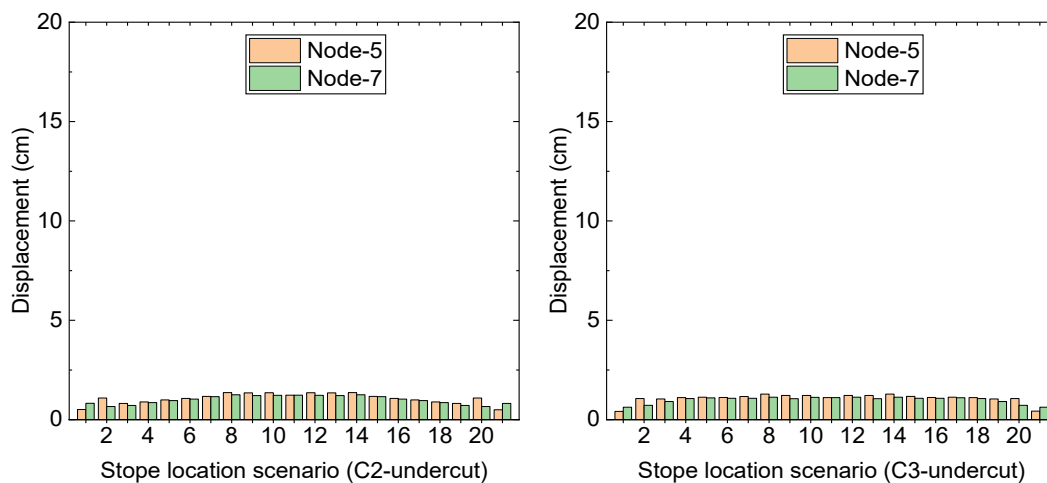


Figure 4.13 Undercut displacement at node5, node7 of cases C2 and C3

Figure 4.13 shows the floor corner heave in the undercut in both cases C2 and C3. Different from the situations in the overcut shown in figure 4.9, the floor corner heave in the undercut is very small, and there is no obvious difference among different location scenarios of the last mined stope from the edge to the center of the level. The maximum floor heave of the floor corners is less than 1.5 cm, and the left corner and the right corner has almost the same heave, in both cases C2 and C3.

#### 4.1.6 Discussions and Conclusions

The above figures present the roof displacement, sidewall swelling and floor heave at the analyzed locations in both overcuts and undercuts among the three cases, C1, C2 and C3. Compared with undercut, the displacement of the roof corners in overcut is smaller, which means the roof in the overcut is more stable than that in undercut. As for the displacement of the roof middle in the overcut, there is no obvious difference in both cases of C1 and C3, and the heave of the floor middle is larger than the displacement of the roof middle. Different with the overcut, the floor middle heave in undercut is tiny, the maximum floor heave of the floor corners is less than 1.5 cm, which means the floor in the undercut is more stable than the floor in overcut, as well the floor corners.

The sidewalls in both undercuts and overcuts are the backfilled CRF, and according to table 2.6, the strength of the CRF is lower than the kimberlite strength, then the supporting system of sidewalls should be stronger than that of the roofs in to improve the safety of the working areas in both overcuts and undercuts.

In overcuts, more attention of supporting should be paid on the roof than on the floor. While in the undercuts, more attention should be paid on the floor than on the roof. Based on the comparison study of the displacement at different locations in the undercuts and overcuts, such as the roof and

floor middle, the corners of roof and floor, the optimum location of the last mined stope should be close to the central area of the level. In this case, the location scenario #10, #11 and #12 can be the location for the last-mined stope.

#### **4.2. Optimum location for the last-mined stope in sill pillar recovery**

Pillar recovery is the practice of forming a series of pillars and then partially or totally extracting some or all of the pillars (Mark et al. 2013). Pillar recovery is considered the most hazardous form of underground mining and is thought to be an art as much as a science (Mark 2017). Sill pillars are initially left in place to support the great weight of the overburden in underground mining. Pillar recovery is an important step in mining operations, specifically in maximizing resource recovery (Darling 2011). During the process of pillar recovery, it is possible to induce risks, such as overlaying rock subsidence, stope failure and pillar failure. Researchers initiated and proposed empirical, analytical theories and numerical technical methods to assess the stability and guarantee the safety of miners and mining equipment. Hudyma and Mining (1994), Potvin and Hudyma (2000) studied microseismics, conventional ground control instruments, numerical modelling and visual observations to understand the mechanisms of pillar failures. Mark (2003, 2017) and Iannacchione (2009) analyzed the strengths and weaknesses of MHRA techniques and assessed the major hazard risks to evaluate sill pillar recovery in two room-and-pillar mines. Zhukova et al. (2018) used monitored underground seismic registrations and mathematical models to improve the safety operations in pillar recovery. Langston et al. (2006) designed the stope layout, extraction procedure and ground support, which were applied to successively recover a pillar. Ghasemi et al. (2010, 2012) assessed the risk of pillar recovery operations and classified that risk into four categories by using indicators. Beruar et al. (2011) developed proper stope sequencing to avoid the highly stressed area during pillar recovery. Valley et al. (2012) optimized the mining sequence

and suggested new directions for the different methods and the potential shortcomings. Townend and Sampson (2014) proposed five mitigation strategies to mitigate the high stress concentration while mining sill pillars. To determine the strength of concrete, an Artificial Neural Network (ANN) was applied to establish the relationship between the various input parameters and the compressive strength of normal concrete and High-Performance Concrete (HPC) (Nguyen et al. 2010). To reduce the cost of the concrete production, laboratory tests were conducted to replace some percent of cement in the concrete with the by-product materials of power plant without reducing the strength of the concrete (Rodvinij and Ratchakrom 2021). Studying the structures of concrete gives a better understanding of how the concrete works. Kropacek et al. (2020) studied the interaction between the concrete structure and the subsoil and presented the experiments that showed the concrete mixed with steel fibers had a positive effect on reducing volume changes at the early stages of setting and hardening process.

With the completion of the excavation of the mineral stopes, the already excavated stopes are backfilled with the cemented rockfill (CRF). However, the strength of the backfilled cemented rockfill (CRF) is not as strong as the blocks of the minerals, also the mining-induced stress conditions has changed. Then, in the process of sill pillar recovery, to recover the stopes in the sill pillar to the most, the location of the last mined stope plays a significant role in the stability aspect of the whole mining level.

#### **4.2.1 Last mined stope location scenarios**

Under the A154 open pit, there are mining pipe 154S and A154N, in the mining pipe A154N, there are two sill pillars according to the updated exploration geology data from Diavik diamond mine. Figure 4.14 shows the one of the two sill pillars which is located between the mining level N9125 and N9150.

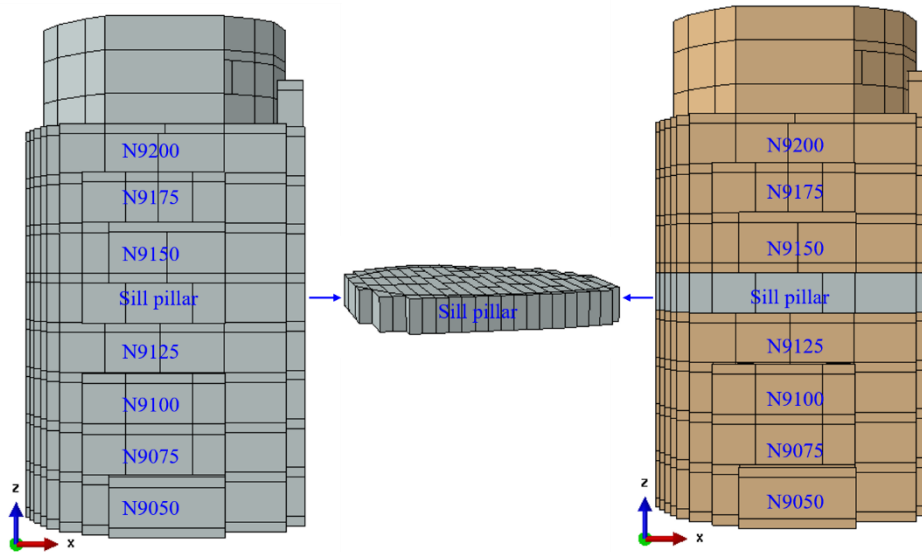


Figure 4.14 Profile of sill pillar location

Sill pillars are intentionally kept between the two mining blocks to prevent the transfer of the mining induced redistributed stress from block-A to block-B, then the mining activities can proceed in both blocks simultaneously. In figure 4.14, the yellow color represents the backfilled CRF, and the white color represents the kimberlite orebody. Recovery of the sill pillar can prolong the mine life and achieve more interests. While recovering the sill pillar can cause stability problems in the stopes, especially with the blasthole stoping (BHS) mining method and the influence of the backfilled CRF, which has not been widely discussed.

As discussed in previous parts, the location of the last mined stope in the process of the pillar recovery is a technical issue that worth analysis and discussion. Different from the production process, in which the upper and lower levels to level N9050 are the kimberlite orebody, in the process of the sill pillar recovery, the upper and lower levels to the sill pillar are the backfilled CRF. Whether these backfilled CRF can provide sufficient support in the process of sill pillar recovery, where is the optimum location of the last mined stope in the process in recovering the sill pillar? Assessment of the recovery process will be made in the following content.

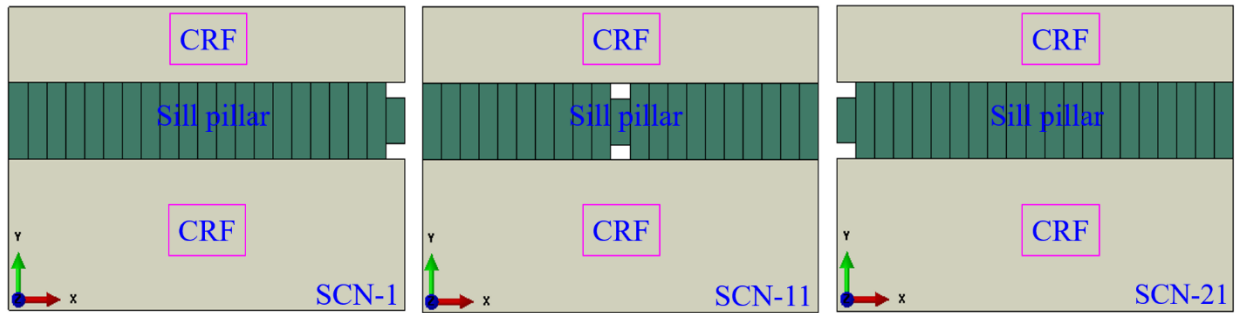


Figure 4.15 Example stope location layout of sill pillar

Similar with the previous, the two-dimensional (2D) model is used to make this study. After the completion of the production of block A and block B, the redistributed stress field was extracted from the three-dimensional (3D) model and applied on the two-dimensional (2D) model. Figure 4.15 shows three examples of stope locations in the sill pillar with both overcuts and undercuts. In figure 4.15, the white color stands for the backfill CRF, as marked in the figure, and the dark green stands for the kimberlite orebody in the sill pillar. Both the upper and lower areas to sill pillar were backfilled with CRF already. The size of the two-dimensional (2D) model is  $157.5\text{m} \times 150\text{m}$  (width  $\times$  height), the height of the sill pillar is 30m, same as levels N9050 and N9075. The backfilled CRF block under sill pillar is 90m in height, and the backfilled CRF block over the sill pillar is 30m in height. Both undercut and overcut have the same size,  $7.5\text{m} \times 5\text{m}$  (width  $\times$  height) in the stope.

Scenario SCN-1 means that the last mined stope in the sill pillar is at the right edge of the sill pillar. SCN-21 means the last mined stope is at the left edge of the sill pillar. During the simulation process, the location of the last mined stope in the sill pillar changes from SCN-1 to SCN-21, from the right edge to the left edge of the sill pillar.

### 4.2.2 Results and discussion

Same with the previous part, eight locations are chosen for the analysis, as shown in figure 4.5.

Both undercuts and overcuts have the same labeled locations.

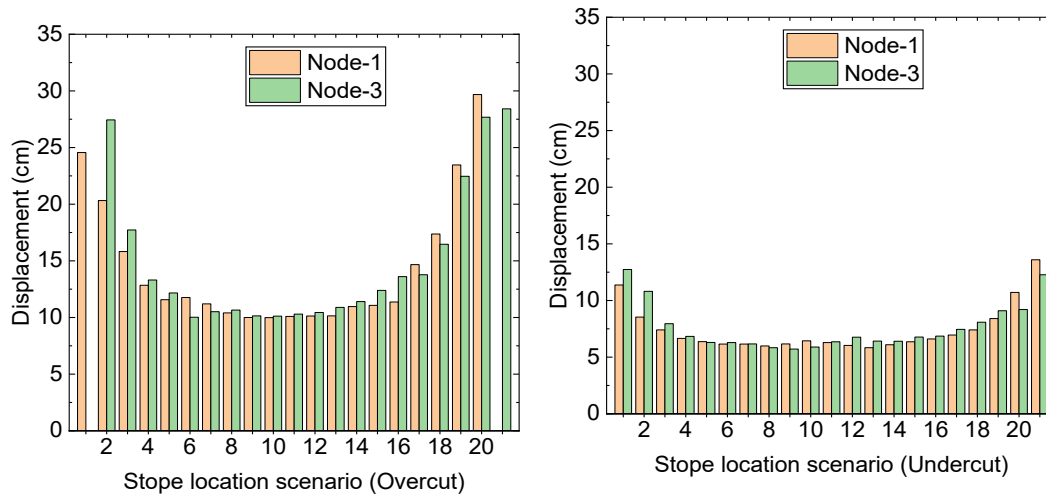


Figure 4.16 Displacement at Node-1, Node-3 in both overcut and undercut

As shown in figure 4.16, compared with the displacement of the roof corners in the overcut, the displacement in the undercut is much smaller at the same location scenarios from SCN-1 to SCN-21. For the undercut, except for the locations close to the two edges of the sill pillar, there is almost no difference in displacement between different stope location scenarios. For most of the displacements, at the same location number, the overcut is about two times that of the undercut. For example, at location scenario No.3, the displacement of node3 in the overcut is 17.4 cm, and that in the undercut is about 8.57 cm. From location scenario SCN-4 to SCN-18, at each location scenario, the two roof corners have almost the same displacement in both overcut and undercut. There is a high possibility that the roof corners in the overcut will fail at the two edges of the sill pillar if the last stope is located at the two edges of the sill pillar.

Figure 4.17 shows the roof displacement and floor heave in both the undercut and overcut. Unlike the roof corners displacement in figure 4.16, the roof displacement in both the undercut and overcut

is much larger than the floor heave. Similar with the roof corners, the roof displacement and floor heave in the overcut are much larger than those in the undercut.

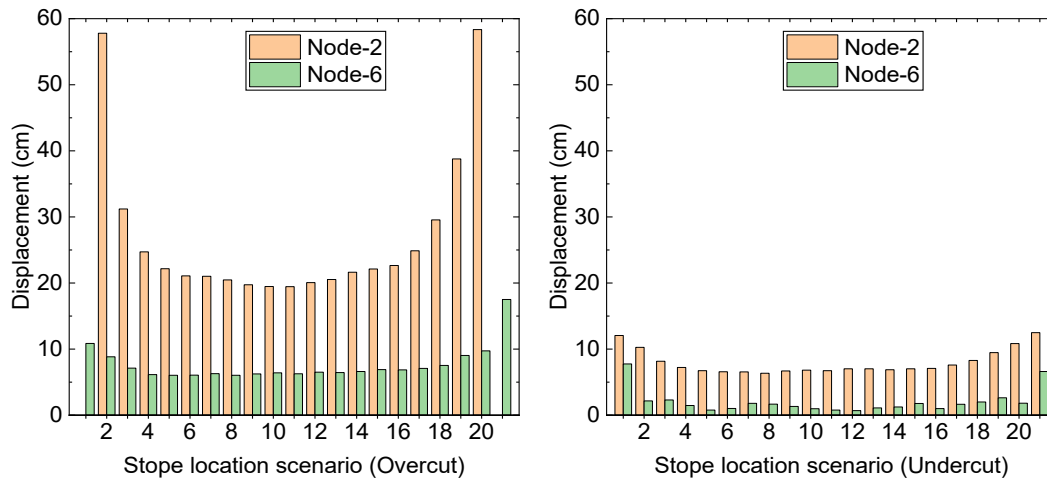


Figure 4.17 Displacement at Node-2, Node-6 in both overcut and undercut

At the same location scenario, the roof displacement in the overcut is about three times of that in the undercut. For example, at scenario SCN-6, the displacement of roof in the overcut is more than 24 cm, while in the undercut, it is about 7.8 cm. In the undercut, there is almost no floor heave, and the roof displacement is under 10 cm. The roof displacement in the overcut shows a slight difference except for the two edge location scenarios. For the floor heave in the overcut, no significant difference among various locations, and the floor heave is less than 10 cm. For the sake of safety, more supports should be installed in the roof and floor in the overcut.

Figure 4.18 shows the comparison of the sidewall swellings in both overcut and undercut. Similar with the roof corners displacement, the swellings show a gradual changing trend from the edges of the sill pillar to the center of the sill pillar. In the undercut, the sidewall swellings are very close at same stope location scenarios, and the swellings are considerably low, most of them is around 5 cm. While the sidewall swellings in the overcut are almost twice the size of those in the undercut at the same stope location scenarios, and most of them are about 10 cm. For example, at SCN-6,

in overcut, it is 9.5cm, in undercut, it is 4.9 cm. More attention should be paid on the safety of sidewalls in the overcut.

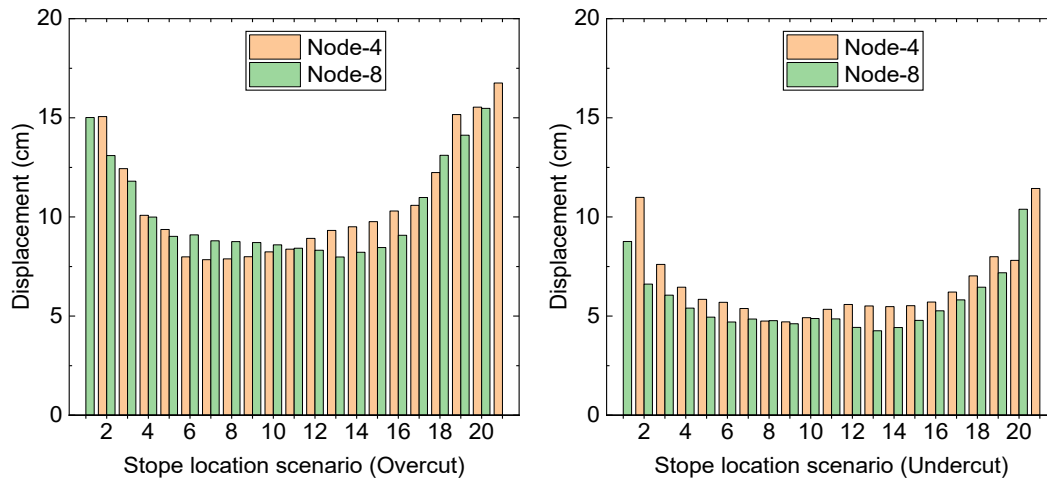


Figure 4.18 Displacement at Node-4, Node-8 in both overcut and undercut

Floor heave is an important indicator of roadway safety in mining engineering. Figure 4.19 shows the heave of the two floor corners. The heave of the two floor corners at the same stope location in the sill pillar is almost the same, except the locations close to the two edges of the sill pillar.

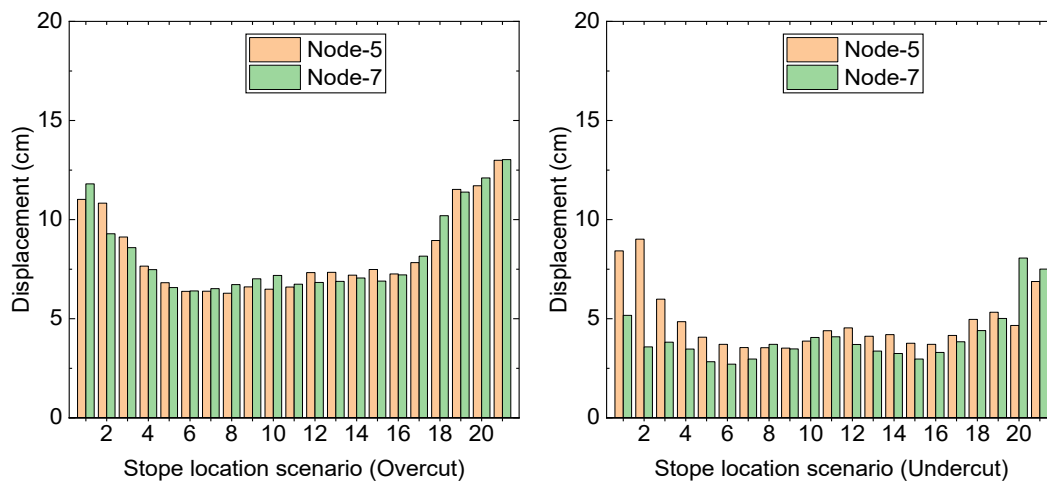


Figure 4.19 Displacement at Node-5, Node-7 in both overcut and undercut

Most of the floor heaves are less than 5 cm in the undercut. For the overcut, the floor corners are in the granite; and for the undercut, the floor corners are in the backfilled CRF. The floor corner

heave in the overcut is much larger than that in the undercut, which means the sill pillar takes most of the redistributed stresses and plays a key role in maintaining the safety in the mining process in both above and underneath mining blocks.

### **4.2.3 Conclusions**

The following conclusions can be reached regarding the comparison of roof displacements, floor heaves and sidewall swellings of different locations in the undercuts and overcuts in various stope location scenarios in the process of sill pillar recovery.

From the roof displacements, floor heaves and sidewall swellings in both undercuts and overcuts, the sill pillar in the mining pipe A154N plays a key role in maintaining the safety of the mining pipe throughout the mining and backfilling processes in the two mining blocks above and under the sill pillar.

In the same stope location scenario, compared with overcut, the displacement of the roof corners in undercut is smaller, and most of the roof corner displacements in undercuts are less than 10 cm, while in the overcuts, all the displacements in roof corners are over 10 cm, which means the roof in the undercut is more stable than that in the overcut, and more protective measures should be taken in the roof of the overcut.

The floor heave in the undercut is tiny, and at the same location scenarios, the values of the floor heave in the overcuts are more than 7 times of that in the undercuts, which means the floor in the undercut is more stable than the floor in the overcut. Also, the roof displacements in the overcuts are more than 2 times of that in the undercuts. The sidewall swellings in the undercuts are about half of that in the overcuts at each same location scenario.

Roofs in the overcuts and floors in the undercuts are the backfilled CRF. The strength of the CRF is lower than the kimberlite blocks in the sill pillar, then the roof displacement in overcuts is much

larger than that in undercuts. In both undercuts and overcuts, more attention should be paid to the supports on the roof than on the floor.

Based on the above conclusions, for the optimum location of the last mined stope in sill pillar recovery, the last mined stope can be any location between No.5 to No.17 in the sill pillar, and at least four-stope-width away from the edges of the sill pillar.

### **4.3 Chapter summary**

In this chapter, the study of the optimum location of the last mined stope in the mining level during the process of normal mining production and the sill pillar recovery was conducted. The comparison of roof displacement, floor heave and sidewall displacement/ swelling among different proposed location scenarios of the last mined stope was conducted to proceed the investigation of the optimum location for the last mined stope. The full size three-dimensional (3D) model was developed to extract the redistributed stress field, and the extracted stress field from the 3D model was applied on the simplified two-dimensional (2D) model to proceed the quick assessment.

More mined orebodies, more interests for the mine company. Recovering the sill pillar can also prolong the mine life. Finding the optimum location of the last mined stope in the mining levels is a good way to improve the stability of the stopes during the mining production, though with the influence of the backfilled CRF. In the process of normal mining production, compared with undercut, the displacement of the roof corners in overcut is smaller, which means the roof in the overcut is more stable than that in undercut. Different with the overcut, the floor middle heave in undercut is tiny, which means the floor in the undercut is more stable than the floor in overcut, as well the floor corners. The supporting system of sidewalls should be stronger than that of the roofs in to improve the safety of the working areas in both overcuts and undercuts. In overcuts, more attention of supporting should be paid on the roof than on the floor. While in the undercuts, more

attention should be paid on the floor than on the roof. The optimum location of the last mined stope in the mining level N9050 should be close to the center of the mining level.

For the optimum location of the last mined stope in the process of sill pillar recovery, in the same stope location scenario, compared with overcut, the displacement of the roof corners in undercut is smaller, and the roof in the undercut is more stable than that in the overcut, and more protective measures should be taken in the roof of the overcut. In both undercuts and overcuts, more attention should be paid to the supports on the roof than on the floor. The location should be at least four-stope-width away from the two edges of the sill pillar.

It is notable that the above analysis is a quick assessment to determine the optimum location of the last mined stope by using the two-dimensional (2D) numerical model instead of the real three-dimensional (3D) numerical model, and it therefore still provides useful suggestions about the supporting system to improve the safety of mining zones in overcuts and undercuts. However, with the simulation of the three-dimensional (3D) model moving forward, the detailed changes of stresses and strains of the last mined stope and the haulage drifts will be discussed in detail, and more reliable results will be achieved. The detailed three-dimensional (3D) numerical analysis will be conducted in the following Chapter 5 and Chapter 6.

---

## CHAPTER 5: ASSESSMENT OF THE STABILITY OF STOPE ACCESSES AND HAULAGE CONNECTIONS

*In underground mining, stope access and haulage drifts are the arteries of an underground mine which are used to transport the valuable mineral out of the mining zone to ground surface. Compared with other structures in underground mining, stope access and haulage drift serve a longer time for the production process. Then the stability of stope access and haulage drift play a significant role in the whole underground mining. This chapter presents the assessment of the stability of stope access and haulage drift based on several criteria, such as: tangential stress criterion, energy based rockburst potential. And the results show that the boundary of the mining pipe A154N has higher possibility of failure compared with the central area of the mining pipe. The stope access and haulage drift around the two edges of the mining pipe 154N should be paid more attention to improve the stability during the mining process.*

## 5.1 Introduction

Stope accesses are the tunnels that connect the haulages and stopes. The mined ore materials and supplementary materials are transported by the loading trucks in-and-out the stopes between the underground working area and the ground surface through the stope accesses and haulage drifts. The stability of the stope accesses and haulage drift accesses is as equal important as the stopes and haulages. Then keeping the safety of the stope and haulage drift accesses is a significant and challenging job. Assessment of the stability of stope and haulage drift access during the period of the service time will be conducted in this part. In underground mining, stope and haulage accesses are excavated to connect the stopes and haulages. The stope access intersection is the key part of stope access, and in many cases, it is located at the boundary of orebody and host rock mass. Stope and haulage drift accesses, as the arteries of an underground mine which are used to transport the valuable mineral out of the mining zone to ground surface. Therefore, it is crucial to keep the functions of stope and haulage drift accesses. As mines continue to reach deeper deposits, stope and haulage accesses are expected to experience higher pre-mining stress conditions, thus suffering from more instability problems. Arjang and Herget (1997) suggested that most mining excavations were subjected to high stress conditions. Stope access failure and instability could lead to serious consequences such as injuries, production delays and higher operational cost. Significant effort is put into understanding the stability of stope accesses and reinforcing them with suitable supports during the mine life.

To better understand the instability and failure mechanism of stope access, many scholars have done lots of studies by various research methodologies. Sjöberg et al. (2003, 2012) identified the failure mechanisms, and quantified the controlling factors governing failure of stope accesses. Zhang et al. (2007, 2008) and Abdellah et al. (2015) defined the stability indicators: displacement,

---

stresses and the extent of yield zones to examine the stability of the stope accesses through a two-dimensional nonlinear numerical model parametric study. Musunri et al. (2010) used random variables to determine the stability of underground stope access. Abdellah et al. (2011, 2013) proved that the same-level mining has stronger influence on the stability of the stope access intersection than lower-level mining. Then he examined the haulage drift safety with indicators: extent of yielding, and brittle shear failure, and defined a minimum strength-to-stress ratio as failure criterion and modified the “point-estimate method” (PEM) to study the drift instability at the intersections. Yao and Wang (2014) combined site observations, conceptual analysis to investigate the reasons for the poor rock-mass conditions in essential crossing cuts. Raju et al. (2015) found that same-level mining of nearby stopes has a more severe effect on the stope access intersection support system than lower-level mining. Li and Guo (2018) showed that gangue-backfilling mining method reduced the overlaying ground subsidence at the stope access intersection. Shnorhokian et al. (2014, 2015, 2018) compared the extent of unstable rock mass using shear, compressive, and tensile instability criteria; and determined that shear criterion and tensile instability were the two main decided criteria. Basarir et al. (2019) used the extracted stresses from 3D global model into 2D local model of the gateway to analyze the stability of the gateway in the mine. Most of the researchers have not taken the influence of backfilled cemented rockfill (CRF) into consideration, this research will consider the CRF influence.

Rockburst is a dynamic rock failure phenomenon usually marked by instantaneous and violent ejection of rock blocks at the underground openings. The ejected rock block is a result of the rapid release of large amounts of accumulated energy. Due to the unpredictability and high intensity, rockburst is one of the most hazardous geological underground engineering disasters. Rockburst can cause damages of equipment, facilities and even fatalities (MSHA 1984, Wang 2020, Sepehri

2016). According to rockburst source mechanism, rockbursts can be classified into three types: fault-slip burst, strainburst and pillar burst (Hedley 1992, Blake and Hedley 2003, Kaiser and Cai 2012, Cai 2013, Mazaira and Konicek 2015). Fault-slip burst is due to the slip along pre-existing faults or along newly generated shear ruptures. When the normal and shear stress along a fault or a shear rupture exceeds the normal and shear strength, the fault or shear rupture will slip and cause a fault-slip burst. Strainbursts are the most common type of rockburst and triggered by the local high excavation-induced stress concentration at the edges of underground openings (Zhang et al. 2012a, Cai 2013). The existence of a relatively “soft” loading environment in the rock mass surrounding the fractured rock contributes to the strainbursts (Kaiser and Cai 2012). The strainburst can cause local rock mass failure at excavation boundaries in an unstable and violent manner. Pillar burst is a violent failure in the pillar core or the complete collapse of a pillar when the excavation-induced stress and accumulated elastic strain energy on pillars exceeds the pillar strength. A large amount of failed rocks can be released and the magnitude is usually larger than that of strainbursts (Ortlepp and Stacey 1994). A schematic representation of three types of rockburst is shown in following figure 5.1.

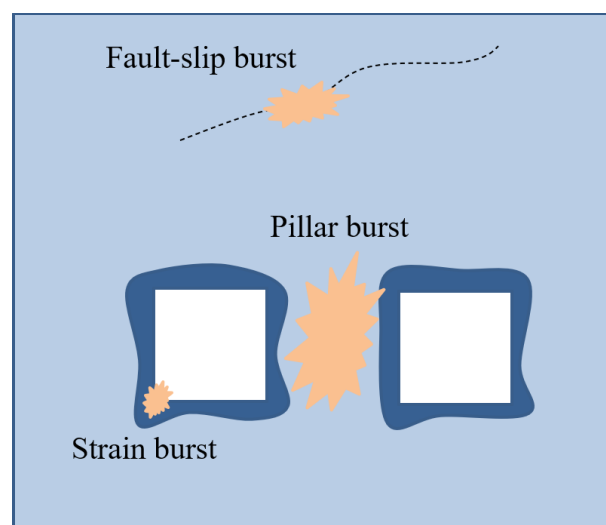


Figure 5.1 Schematic three rockburst potentials (after Castro et al. 2012)

At Diavik Diamond Mine (DDM), the three main mining pipes, A154S, 154N and A418, contain millions of tons of kimberlite, and the host rock is granite. According to Leveille (2015, 2016), Sepehri (2016, 2019) and Pu (2019), the kimberlite at DDM is prone to rockburst. There were several reported rockburst occurrences at different locations in various mining levels at DDM during the mining process, and even the preparation schedule. The reported rockburst cases are shown in figure 5.2. Some of the reported rockburst cases at DDM occurred very close to the stope access intersection. To improve the safety and stability of the stope access during the mining process and the two sill pillars recovery process, assessment of the possible rockburst at the stope access intersection is necessary and important. In this chapter, the assessment of the rockburst potential at the stope access intersection and haulage drift access only includes the process of mining and backfilling the three mining blocks, block-A, block-B and block-C, from simulation step S1 to step S83 in the developed numerical model. The assessment of the stope access intersection and haulage drift access intersection will be conducted in the following chapter 6.

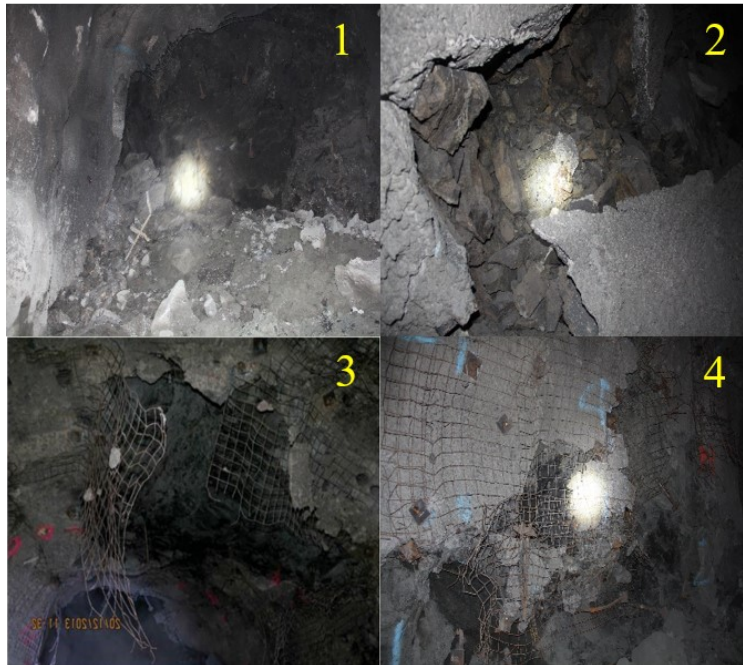


Figure 5.2 Rockburst cases at Diavik Diamond Mine

This chapter presents both the stress and strain related possible failure by applying tangential stress method ( $T_s$ ) and strain energy-based burst potential index (BPI), and comparing the key factors indicating the rockburst proneness at the haulage drift intersection and stope access intersection.

## 5.2 Rockburst potential criteria

### 5.2.1 Criterion of tangential stress (CTS)

The criterion of tangential stress (CTS) method considers the strength property of the intact rock and mining-induced redistributed tangential stress (major principal stress) (Kaiser and Cai 2012) in the rock mass. Therefore, both conditions required for a rockburst to occur can be evaluated.

The tangential stress ( $T_s$ ) criterion can be estimated using equation (5.1) below:

$$T_s = \sigma_\theta / \sigma_c \quad (5.1)$$

where,  $\sigma_c$  is the uniaxial compressive strength (UCS) (MPa) of the rock and  $\sigma_\theta$  is the tangential stress (MPa) around the underground opening (i.e. stopes, haulage drifts). According to Park (1994), Wang and Park (2001), the rockburst tendency can be evaluated using  $T_s$  criterion as presented in table 5.1.

Table 5.1 Rockburst tendency prediction based on CTS (Wang and Park, 2001)

Tangential stress criterion ( $T_s$ )	Rockburst tendency
$T_s \geq 0.7$	Violent
$0.5 \leq T_s < 0.7$	Strong
$0.3 \leq T_s < 0.5$	Weak
$T_s < 0.3$	No rockburst

### 5.2.2 Energy-based burst potential index

To better assess and predict rockburst tendency, Mitri et al. (1999) proposed an energy-based burst potential index (BPI). The basic assumption in this method is that violent failure (rockburst) will occur when the energy stored in the rock mass exceeds the critical energy value ( $e_c$ ). The  $e_c$  is the

maximum capacity of the rock mass to store energy, and it can be obtained from the uniaxial compressive strength (UCS) test or from the UCS hysteresis looping test curve with equation (5.2).

$$e_c = \sigma_c^2 / 2E \quad (5.2)$$

where  $\sigma_c$  is the UCS (MPa) and  $E$  is the Young's modulus (GPa) achieved from the UCS test.

It should be noted that using equation (5.2) is a conservative approach to estimate  $e_c$ , because the energy dissipated by fracturing and plastic deformations is neglected. However, in the absence of the detailed UCS hysteresis looping stress-strain curve, it can be used for providing an approximate value.

Therefore, the burst potential index (BPI) can be defined as:

$$BPI = ESR / e_c \times 100\% \quad (5.3)$$

where  $ESR$  is the energy storage density (also called the energy storage rate) ( $\text{kJ/m}^3$ ) in the rock mass and  $e_c$  is the critical elastic strain energy density (SED) ( $\text{kJ/m}^3$ ) of the rock.

The larger the value of the BPI, the higher the probability of a rockburst occurring. Equation (5.2) can be used to calculate the value of  $e_c$ .

### 5.2.3 Criterion of elastic strain energy

The stored elastic strain energy per unit volume of the rock mass is called the elastic strain energy density (SED). The elastic strain energy density (SED) is an important factor to identify the potential for rockburst phenomenon in underground mining (Jaeger et al. 2008).

For rock samples under the UCS test, using the principle of conservation of energy and the linear elasticity theory, the storage elastic strain energy density (SED) can be calculated using equation (5.4).

$$SED = \sigma_c^2 / 2E_s \quad (5.4)$$

where  $\sigma_c$  is the uniaxial compressive strength (UCS) (MPa) and  $E$  is the Young's modulus (GPa) in the unloading curve.

According to the study by Miao et al. (2016), based on the value of the strain energy density (SED), the rockburst intensity in a rock mass can be classified into four categories. The result of this rating system is presented in table 5.2.

Table 5.2 Rockburst rating system based on SED (Miao et al., 2016)

<b><i>SED</i> (KJ/m<sup>3</sup>)</b>	<b>Rockburst hazard</b>
$SED \geq 200$	Extra strong
$100 \leq SED < 200$	Strong
$40 \leq SED < 100$	Moderate
$SED < 40$	Low

According to the laboratory tests conducted by Leveille (2015) and Sepehri (2016, 2020), in the mining pipe A154N, the kimberlite rock mass has proneness to rockburst, and the calculated strain energy density (SED) of kimberlite from equation (5.4) is 119.7 KJ/m<sup>3</sup>. According to the rockburst category in table 5.2, the rockburst hazard in the kimberlite in mining pipe A154N has a strong level of hazard caused by the rockburst in kimberlite. However, during the mining production in mining pipe A154N, the redistributed stresses present the dynamic changing trends. Then, only knowing that the kimberlite in mining pipe A154N has strong rockburst tendency is not sufficient for the in-situ mining engineers to propose the corresponding support strategies to improve the safety of underground mining activities.

By applying the tangential stress criterion (Ts) (Wang and Park 2001) and energy based burst potential index (BPI) (Mitri et al. 1999), the real time rockburst tendency caused by the mining activities during the process of production in mining pipe A154N can be assessed by the in-situ engineers and the potential rockburst areas can be located. In the following part of assessment of

the stability of stope accesses and haulage drift accesses in this chapter, both tangential stress criterion (Ts) and burst potential index (BPI) will be used to conduct the assessment in the mining pipe A154N during the process of mining the three mining blocks, block-A, block-B and block-C.

### 5.3 Stability assessment of stope access intersection

Ground caving in the stope access intersection can have serious consequences from injuries to delayed production and increased operational cost. Several factors may influence the stability of stope access intersection such as the strength and quality of the rock masses and mining depth.

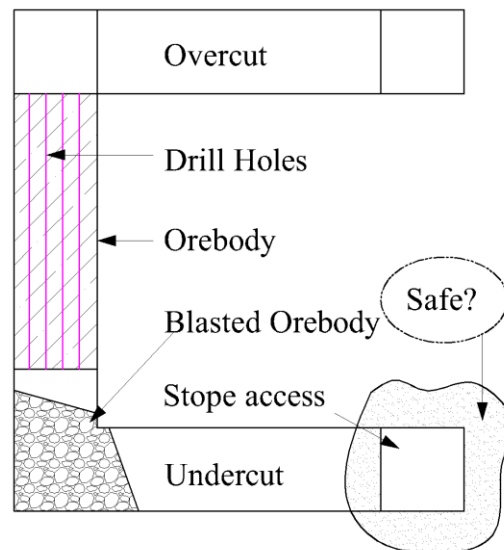


Figure 5.3 Profile of stope access and intersection

As mines continue to reach deeper deposits, stope accesses and haulage drifts are expected to experience higher pre-mining stress conditions, thus suffering from more instability problems. The intersections shown in figure 5.3 attract special attention. Figure 5.3 presents the profile of the blasthole stoping (BHS) mining method in the mining pipe A154N. Blastholes are drilled from the overcut in the stope, vertically to the undercut. The blasted minerals will be moved and transported by mining trucks in the undercut and stope access to the ground surface. Usually, compared with the stopes, the stope access and haulage access will serve a longer time during the whole process

of mining production, and the intersection area causes instability due to the large open zones from the roofs and ribs. To improve the stability of this zone, it is essential to better understand the overstressed zones induced by the mining process, and the degree of reduction of stresses and strain induced by the backfilled CRF.

### 5.3.1 Assessment of the rockburst potential of stope access intersection

According to the Diavik diamond mine report, there were rockburst cases and other types of rock mass failures, and some failures occurred in the stope access intersections. Following figure 5.4 presents the failure case that in the stope access intersection. The access roof failed and the ventilation tubes fell down to the floor, also the sidewall swell at the left floor corner was obvious.



Figure 5.4 Rock failures in the stope access at Diavik diamond mine

The failures in these areas will halt the mining production in the specific stopes, or even the whole mining level if the failure close to the haulage drift. Assessment of the stability of these areas plays a significant role in the mining transportation schedule and the blastholes drills schedule in the failures related mining levels. The stability of this area is a result of the combined effect of over stresses caused by the mining process and a reduction of stress-strain induced by the backfilled CRF.

By applying the above-mentioned criteria, tangential stress ( $T_s$ ) and burst potential index (BPI), the assessment of the rockburst potential of the stope and haulage access intersection was conducted. According to Chapter 4, three stope accesses at three representative locations in the mining level were chosen to conduct the assessment. Figure 5.5 presents the outlines of the stope, stope access, and haulage drift between N9050 and N9075 levels.

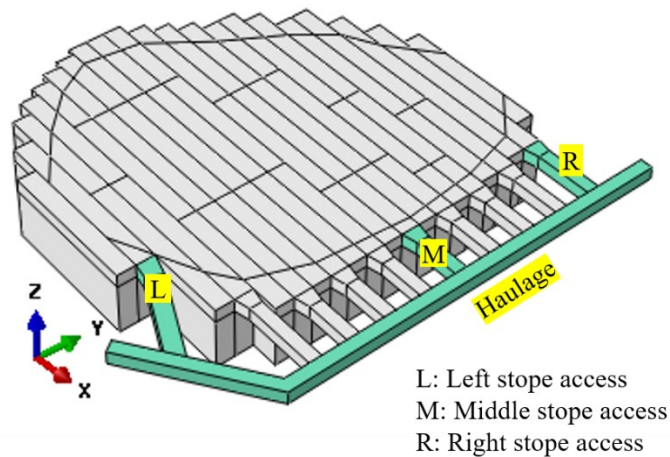


Figure 5.5 Stope access and haulage drifts between level N9050 and N9075

Mining levels are chosen from the mining pipe A154N. In total, there are 15 levels of haulage drifts and stope accesses from the bottom to the top of the mining pipe A154N. However, the two levels above the mining level N9200 have less stope accesses than the other 13 levels, then these two levels will not be in the selection range for the analyzed levels. The accesses to the stopes in mining levels, N8950, N9000, N9050, NSill2, N9200, are chosen as the analyzed examples for the assessment. Three stope accesses are chosen in each of the chosen mining levels, these accesses have the same X-Y coordinates in X-Y plane, and elevation difference among them is 75m. Figure 5.5 shows the chosen stope accesses at mining level N9050. L stands for the chosen stope access is at the left-edge of the mining level, M means the chosen stope access is around the middle in

the mining level, and R means the chosen stope access is at the right-edge of the mining level. And this selection arrangement works for the haulage drifts.

### 5.3.1.1 Energy based burst potential index (BPI) of the stope accesses

The burst potential index (BPI) can be calculated by equation (5.2) and equation (5.3), as a conservative estimation method (Mitri et al. 1999, Sepehri 2020), the BPI will not predict the rockburst occurrence directly, however it can predict the rockburst tendency based on the computed energy storage rate (ESR) from the developed model. Due to the rectangular section shape, the four corners in the stope access will easily generate the stress concentration, also cause the high density of stress-strain energy.

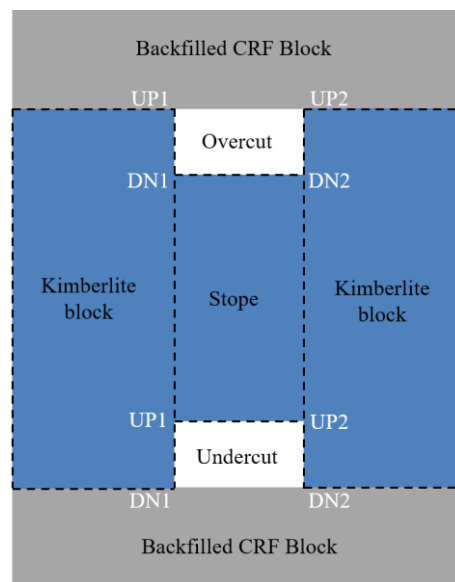


Figure 5.6 Analyzed four corners in undercut and overcut

Moreover, as the reported stope access failure case shown in figure 5.4, then the four corners in the stope access are chosen to conduct the assessment, and they are: left roof corner UP1, right roof corner UP2, left floor corner DN1 and right floor corner DN2, as shown in above figure 5.6.

Figure 5.7 presents the BPI values of the four corners in the stope accesses in the right-edge stopes in five analyzed mining levels. For the left roof corner UP1, mining level L#8950 sees huge

increase, from 5% to 15%, caused by the excavation at the step of excavation, and the BPI decreases to 7% with the backfilled CRF taking into effect and achieving a stable stress-strain level.

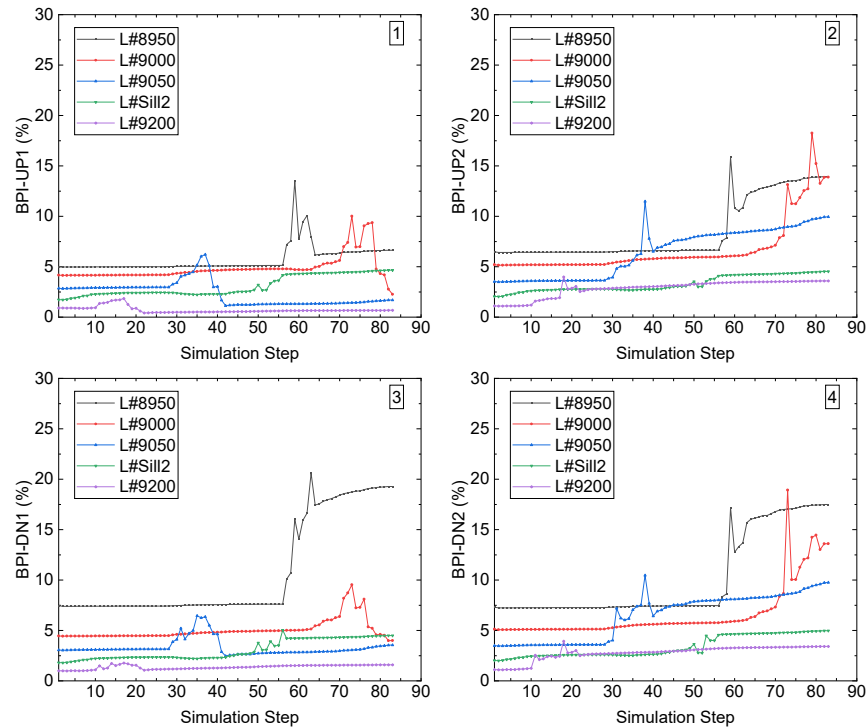


Figure 5.7 BPI of the stope access at right-edge stope in five mining levels

For the level L#9000, the excavation of the adjacent stopes causes the BPI increases gradually, and at the step of excavation it achieves the peak value of 10%, then with the following step backfilling, the BPI decreases to 2.5%. Mining level L#9050 has a twice increase from 2.5% to 5%, caused by the excavation, and the BPI decreases to a value of 1%, with the backfilled CRF taking into effect. Level L#9200 sees tiny changes during the process of excavation and backfilling. At the right roof corner UP2, three levels, L#8950, L#9000, L#9050, see quick increase of BPI caused by the step of excavation, through with the following backfilled CRF taking into effect, the BPI at the right roof corner in these three levels still present an increasing trend. While, in the mining level L#9200, the changes of the BPI at UP2 are small, and it is under 4%.

In the third picture in the figure 5.7, the left floor corner DN1 in the mining level L#8950 achieves significant increase from 7.5% to 20% caused by the excavation. Similar with the right roof corner UP2, the backfilling does not change the increasing trend of BPI. For other four levels, the BPI experiences little changes during the steps of excavation and backfilling, and all the BPI values are under 10%. The trends of the BPI at the right floor corner DN2 are similar with the right roof corner UP2, the excavation causes the BPI of level L#8950 and L#9000 a significant increase, from 7.5% to 17.5% and 5% to 20%, respectively. The BPI of other three mining levels is under 10%, though level L#9050 achieves a dramatic increase caused by the excavation.

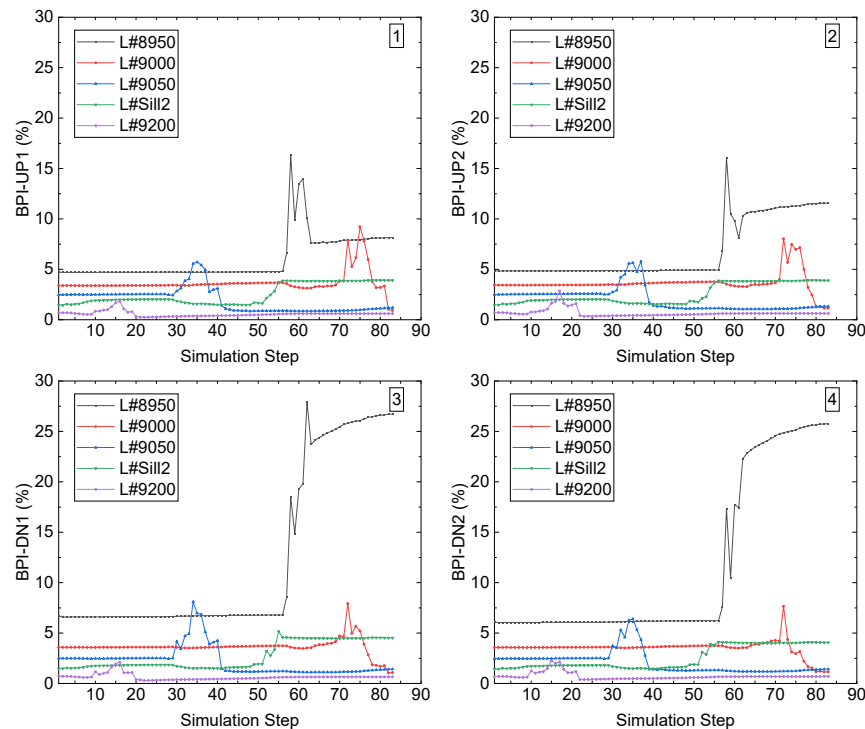


Figure 5.8 BPI of the stope access at middle stope

The BPI values of the stope access in the middle stopes in the six mining levels present different changes trend with the right edge-located stopes, as shown in figure 5.8. For the left roof corner UP1, only the BPI of the level L#8950 sees a significant increase, from 5% to 15%, though is decreases to 8% with the influence of the following backfilled CRF. The BPI values of the other

four mining levels are all under 10%, though for level L#9000 and L#9050, the excavation step causes increase of BPI. The right roof corner UP2 presents a similar changes trend as the left roof corner, as shown in the second picture in figure 5.8. The BPI in the level L#8950 achieves huge increases from 5% to 17%, though it decreases to 11% with the flowing step of backfilling.

Both the floor corners, DN1 and DN2 at the mining level L#8950 achieve dramatic increase caused by the excavation, and the backfilled CRF is unable to reduce the value of BPI, which indicates a violent rockburst tendency when excavates the adjacent stopes close to the middle stopes. In mining level L#8950, both corners present an increasing trend of BPI. For the other mining levels, the BPI values experience no big changes, the maximum one is 7%, indicating no rockburst tendency.

The BPI values of the four corners in the stope access to the left edge-located stopes are illustrated in the following figure 5.9. As shown in the first picture, for the left roof corner UP1, at the step of the excavation, the BPI increase from 5% to 12% in level L#8950, and from 4% to 11% in level L#9000, both are more than twice. For the other three levels, the BPI values of the left roof corner are less than 5%, though increase and decrease are caused by the excavation and backfilling. For the right roof corner UP2, only the deepest level L#8950 sees a significant increase caused by the excavation, and then the BPI decreases to 6% with the backfilled CRF taking into effect. Other four levels see small changes, and the BPI values are under 5%, though the excavation causes the BPI in level L#9000 increases to 7%, and it decreases to 2% with the following step of backfilling. The third and fourth pictures in the figure 5.9 present the changes of BPI at the left floor corner DN1 and right floor corner DN2, respectively. At both floor corners, the BPI of the level L#8950 achieves significant increases, even after the backfilling, the BPI still presents an increasing trend. Both floor corners, DN1 and DN2, achieve a 10% increase, from 7.5% to 17.5%. The left floor

corner DN1 in the level L#9000 achieves twice increase, from 4% to 10%. For the other three mining levels, the BPI values of both floor corners are under 5%.

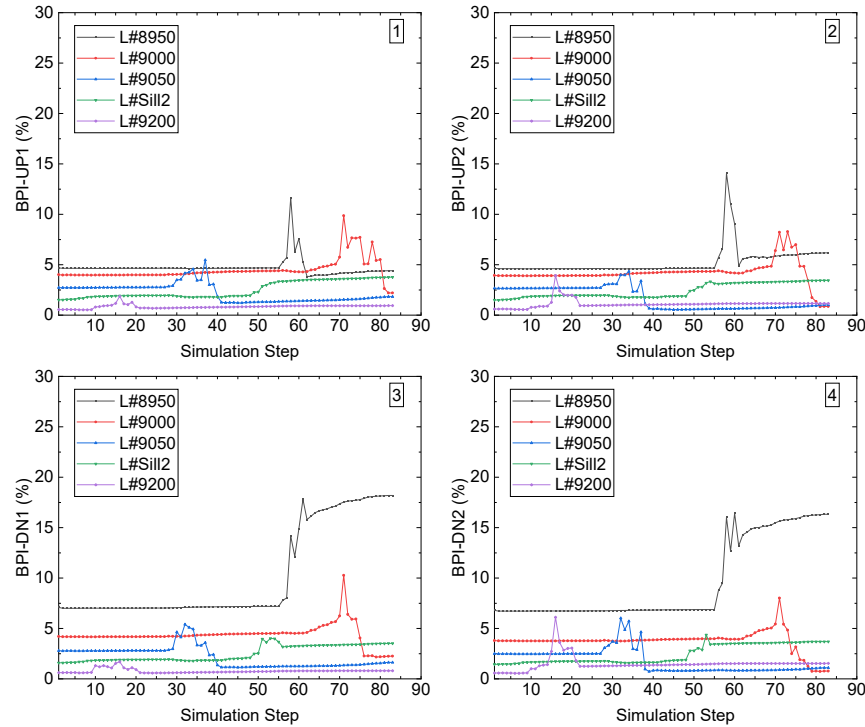


Figure 5.9 BPI of the stope access at left-edge stope

### 5.3.1.2 Tangential stress criterion (Ts) of the stope accesses

Different from burst potential index (BPI), the tangential stress criterion (Ts) can assess the rockburst tendency into four categories, as shown in table 5.1. The rockburst tendency assessed by the tangential stress criterion of the four corners in the stope assess in the right-edge stopes in the five mining levels is shown in figure 5.10. For the left roof corner UP1, when the excavation simulation step occurs at the stopes, the Ts values of the mining level L#8950 and L#9000 are over 0.3 and under 0.5, indicating a weak tendency of rockburst, while after the backfilled cemented rockfill (CRF) takes into effect, the Ts values of these two mining levels decrease to the values under 0.3, with no rockburst tendency. For other three mining levels, L#9050, L#Sill2 and L#9200,

there is no rockburst tendency, though the excavation at these stopes causes the increase of the  $T_s$ , after the backfilled CRF takes into effect, the  $T_s$  decreases to a value under 0.05.

For the right roof corner UP2, as shown in the second picture in figure 5.10, different from the left roof corner UP1, three mining levels, L#8950, L#9000 and L#9050 show weak rockburst tendency caused by the excavation. Though after the backfilled CRF takes into effect, the  $T_s$  values of these three mining levels are still over 0.3, indicating the weak tendency of rockburst, which may cause failures when the mining activities in the adjacent stopes. For the right roof corner UP2, in other mining levels, L#Sill2 and L#9200, the  $T_s$  values show no tendency of rockburst.

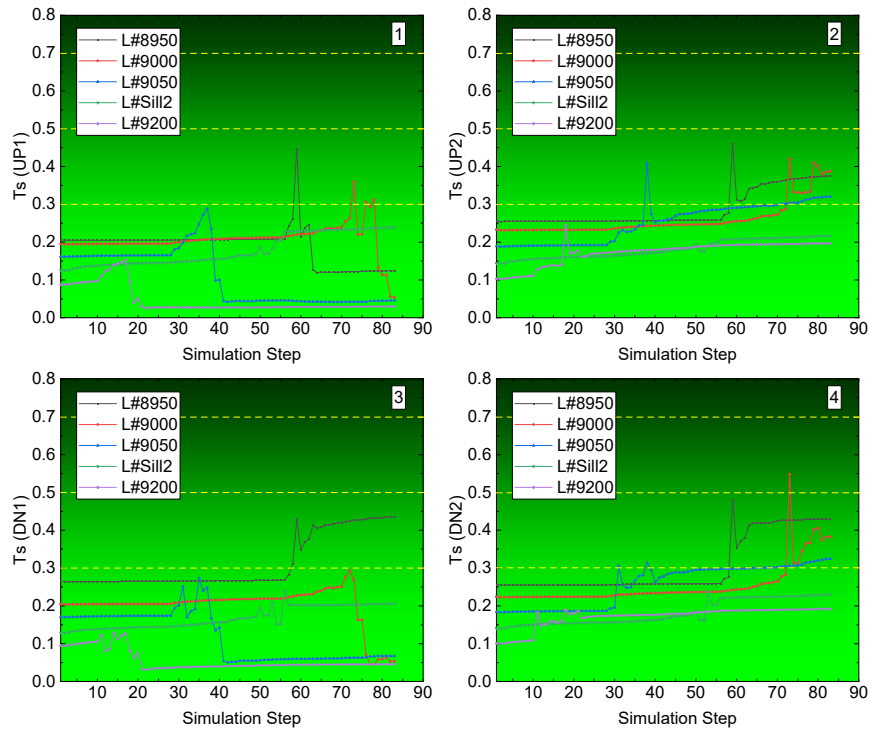


Figure 5.10  $T_s$  of the stope access at right-edge stope in five mining levels

For the left floor corner DN1, only the mining level L#8950 shows the weak tendency of rockburst even after the backfilling of CRF, as shown in the third picture in figure 5.10. The left floor corner DN1 in other four mining levels shows no rockburst tendency, and the  $T_s$  decreases to a value under 0.05, though with some increases caused by the excavation of the stope access in particular

mining simulation step. Similar with the right roof corner, the right floor corner DN2 in the mining levels L#8950, L#9000 and L#9050 show the weak tendency of rockburst after the completion of the excavation and the backfilling of the stope access. The right floor corner in the mining level L#9000 even sees a  $T_s$  value over 0.5, indicating a strong tendency of rockburst caused by the excavation. For the other mining levels L#Sill2 and L#9200, the  $T_s$  values of the right floor corner DN2 show no tendency of rockburst.

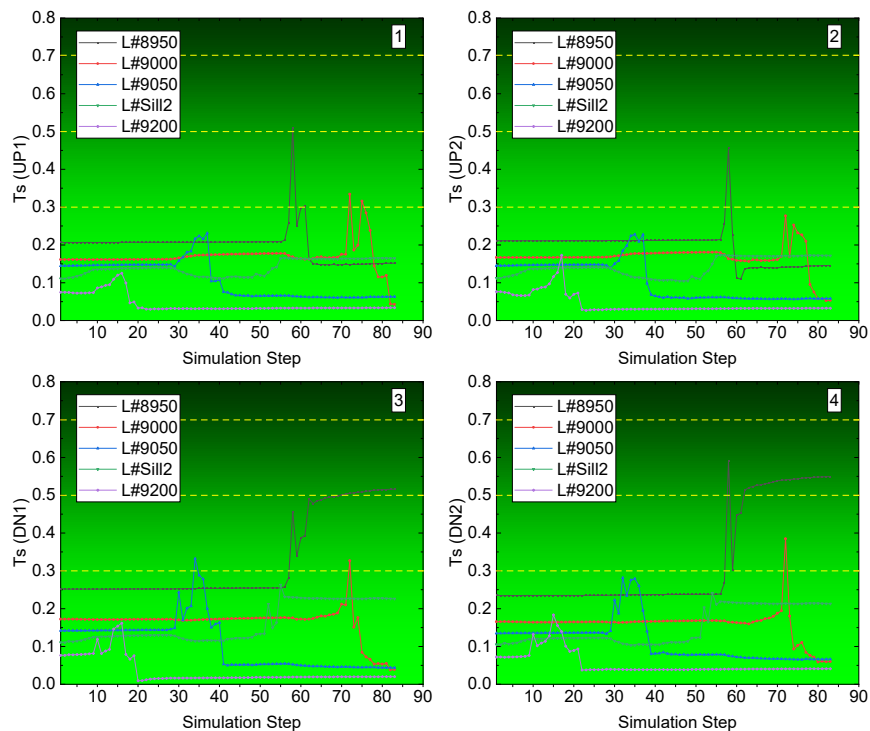


Figure 5.11  $T_s$  of the stope access at middle stope in five mining levels

For the  $T_s$  values of the stope access in the middle stopes in the five mining levels, figure 5.11 illustrates the changes during the process of excavation and backfilling. The left roof corner UP1 in mining level L#8975 sees the dramatic increase of  $T_s$  caused by the excavation. from no rockburst tendency to violent tendency, and after the backfilled CRF takes into effect, the  $T_s$  decreases to a value under 0.3, indicating no tendency of rockburst anymore. For other four mining levels, only level L#9000 shows the weak tendency of rockburst when the excavation occurs at the

stope access, with the backfilled CRF, the  $T_s$  decreases to value under 0.05, same as the mining levels L#9050 and L#9200. And level L#Sill2 shows no significant changes of  $T_s$  during the whole process, as shown in first picture in figure 5.11. The right roof corners UP2 in the five mining levels show similar trend as the left roof corner, approximately symmetry. Only the mining level L#8950 shows weak tendency of rockburst caused by the excavation and  $T_s$  decreases to a value has no tendency. The right roof corners in the other mining levels show the same changes trend as the left roof corner UP1.

While the two floor corners present different trends. For the left floor corner DN1 in mining level L#8950, when the excavation occurs, the  $T_s$  increases from 0.25 to 0.45, from no tendency to weak tendency of rockburst. After the backfilled CRF takes into effect, the  $T_s$  shows decrease, then  $T_s$  increases again to a value over 0.5, indicating violent tendency of rockburst. The huge mining induced redistributed stress contributes to this tendency. For mining level L#900 and L#9050, the excavation does cause the  $T_s$  to a value of weak tendency of rockburst, the flowing backfilled CRF decreases it to a value under 0.05. For mining level L#Sill2 and L#9200, though the  $T_s$  values show different trend, both are under 0.3, especially for L#9200, it is under 0.03, as shown in the third picture.

For the right floor corner DN2, the changes trend is similar with the left floor corner DN1 during the process of excavation and backfilling, as shown in the fourth picture. The excavation at the stope access causes the  $T_s$  of the right floor corner DN2 has an increase from 0.24 to 0.6, from no tendency to violent tendency of rockburst. After the backfilling, the  $T_s$  of the right floor corner decreases to a value indicating weak tendency, and then it grows up again to the value over 0.5, indicating the violent tendency of rockburst. The right floor corner DN2 in mining level L#9000 also shows a weak tendency caused by the excavation at simulation step S71, and the following

backfilling step S72 decreases it to a value under 0.1. For the mining level L#9050, the  $T_s$  sees a significant increase, it is still under 0.3, same as the scenarios in mining levels L#Sill2 and L#9200, which show no tendency of rockburst at the right floor corner from the geostatic step S1 to the step S83 with the completion of mining and backfilling three blocks in the mining pipe A154N.

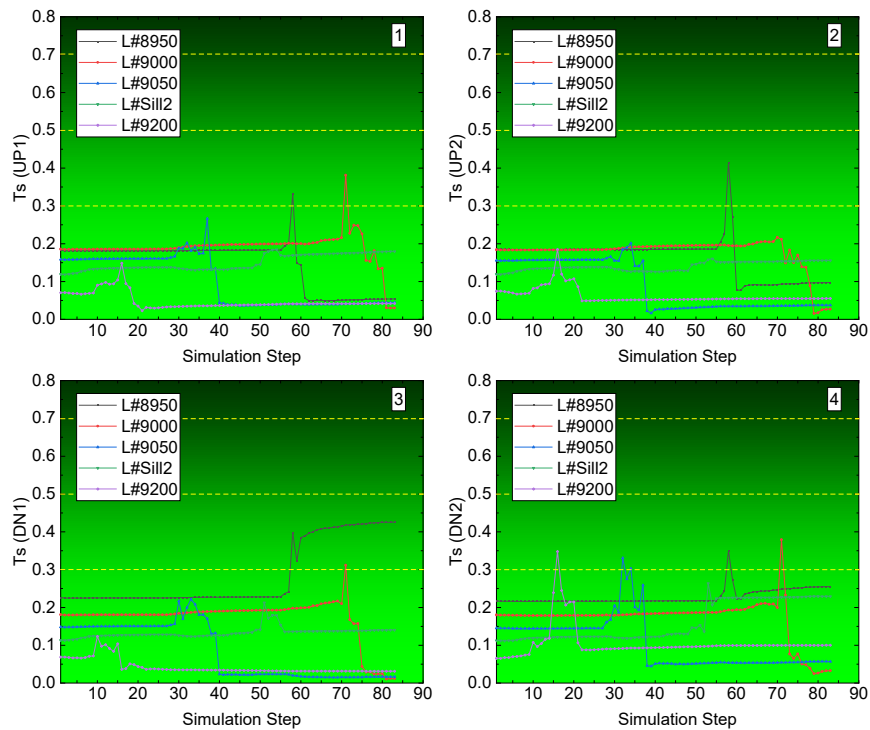


Figure 5.12  $T_s$  of the stope access at left-edge stope in five mining levels

The  $T_s$  changes trend of the four corners in the left-edge stope access in the five mining levels are illustrates in figure 5.12. The first picture shows the  $T_s$  changes trend in the left roof corner UP1, the mining levels L#8950 and L#9000 present a weak tendency of rockburst caused by the excavation, and  $T_s$  value in level L#9000 is higher than that in level L#8950. With the following backfilling step, both left roof corners show no more rockburst tendency, and the  $T_s$  decreases to a value about 0.05. For the other mining levels L#9050, L#Sill2 and L#9200, the excavation steps at each level cause no tendency of rockburst, and with the influence of the backfilled CRF, the  $T_s$  values of the mining level L#9050 and L#9200 decrease to a value under 0.05. For the right roof

corner UP2, as shown in the second picture, only the mining level L#8950 has the weak tendency of rockburst caused by the excavation, and then decreases to a value about 0.1 by the following step of backfilling. For the level L#Sill-2, the Ts value experiences no significant changes during the process of excavation and backfilling in the adjacent stopes, and it changes between 0.1 and 0.15. For the other two levels L#9050 and L#9200, though with increases at the excavation step, the Ts value is under 0.3 from the step S1 to step S3, indicating no tendency of rockburst.

At the floor corners DN1 and DN2, the Ts changes trend is different with that of roof corners, as shown in the third and fourth pictures. In the left floor corner DN1, the mining level L#8950 shows weak rockburst tendency, though with the following step of backfilling, and the step of excavation causes the Ts increases from 0.22 to 0.4, with a quick decrease, it increases back to 0.4, indicating a weak tendency of rockburst. For the other four mining levels, though the level L#9000 has a peak value over 0.3, then it decreases to 0.03, same with the levels of L#9050 and L#9200. For the right floor corner DN2, four mining levels, L#8950, L#9000, L#9050 and L#9200, show a peak value of Ts over 0.3, then it decreases with the following step of backfilling, through L#8950 has a Ts value over 0.2 after the backfilling.

From the above figure 5.10 and figure 5.11, figure 5.12 the mining level of Sill-2 has a final Ts value at the four analyzed corners, UP1, UP2, DN1 and DN2, at the three locations of the stopes. The unmined kimberlite rock mass contributes to the higher values of Ts, and the Ts will decrease with the completion of the recovery of the two sill pillars, Sill-1 and Sill-2, which will be analyzed in detail in following Chapter 6.

#### 5.4 Stability assessment of haulage accesses

Different from the stope accesses, which locate in the kimberlite rock mass, the haulage drift accesses parts locate in the host rock granite. The average distance between the haulage and stopes in each mining levels in mining pipe A154N is about 15m.

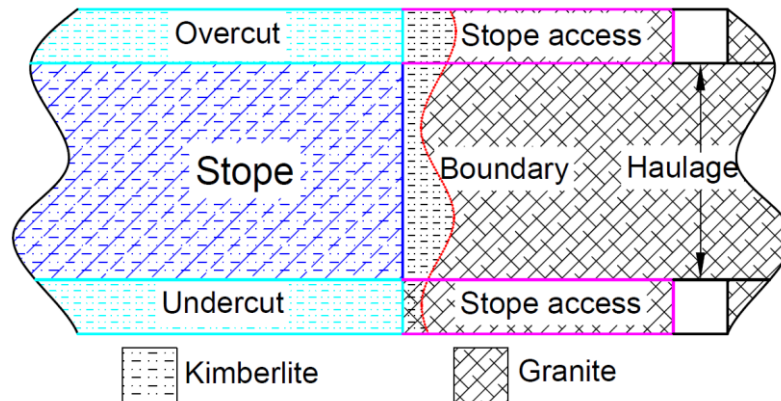


Figure 5.13 Profile of stope and haulage access

Figure 5.13 illustrates the side view of the haulage/stope accesses in mining pipe A154N. There was a boundary between the mining pipe A154N and the host rock mass of granite, as shown in figure 2.28 in Chapter 2 and figure 5.13. The haulage/stope accesses were excavated in part-part of kimberlite and granite, and the accesses get cross the boundary. One end of the stope access locates in kimberlite, and another end locates in the granite, connecting the stopes and haulages. The haulages and the haulage/stope accesses have the same section and size,  $5\text{ m} \times 5\text{ m}$ , in height and width, respectively.

According to the properties of granite, shown in table 2.6, and Leveille (2015), the critical strain energy density (SED) is  $402.5\text{ KJ/m}^3$ , calculated by the equation (5.4). The BPI values of the four corners in the haulage access located in the granite were calculated by equation (5.3), and the following figures present the results of the BPI.

### 5.4.1 Energy based burst potential index (BPI) of the haulage drift accesses

Duo to the higher critical strain energy density (SED), the BPI values of the four corners in the haulage access are much smaller than that of the stope access, which locate in the kimberlite. Figure 5.14 illustrates the BPI values changes in the right edge-located haulage access. For all four corners, UP1, UP2, DN1 and DN2, the BPI values are under 3% in all five mining levels, from the bottom to the top of the mining pipe A154N, through the BPI values of the mining level L#8950 are larger than all the other four mining levels at all four corners.

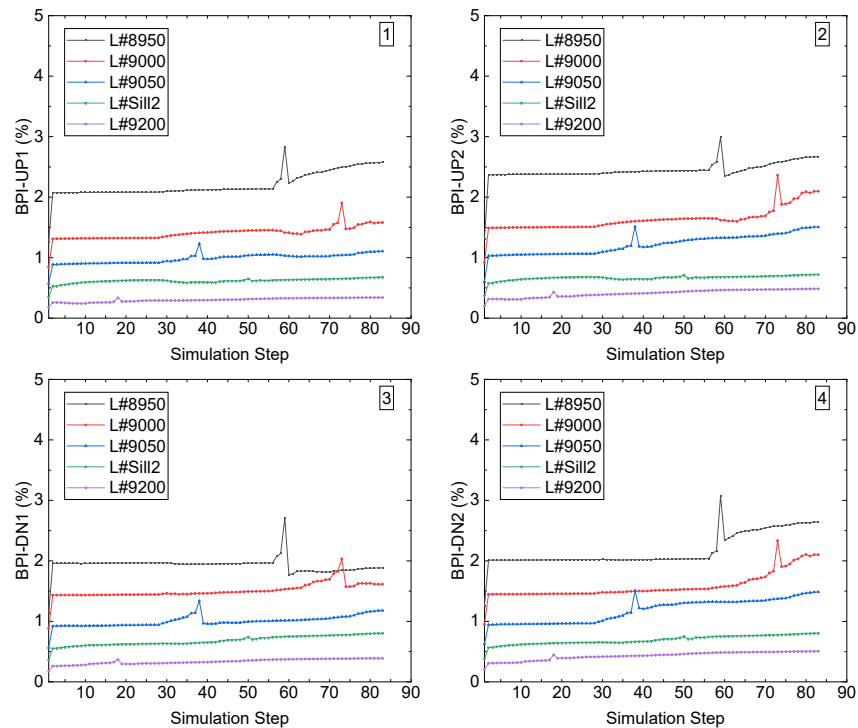


Figure 5.14 BPI of the stope access at right-edge haulage drift

For the left roof corner UP1, the step excavation of the haulage access causes the BPI increases from 2% to 3%, then with the following step of backfilling, the BPI decreases to 2.3% and with an increasing trend. For the other four levels, the increase of BPI caused by the excavation decreases with the mining depth going shallower, from level L#9000 to level L#9200. For the right roof corner UP2, in level L#8950, L#9000, and L#9050, after the step of backfilling, the BPI values

present an increasing trend, though it is still under 3%. For level L#Sill2 and L#9200, the changes are tiny, and the BPI is under 5%. For the left floor corner DN1, the BPI value sees increase at the step of excavation and then it decreases back to the initial value in all five levels. For the right floor corner DN2, the BPI changes trend is similar with that of the right roof corner.

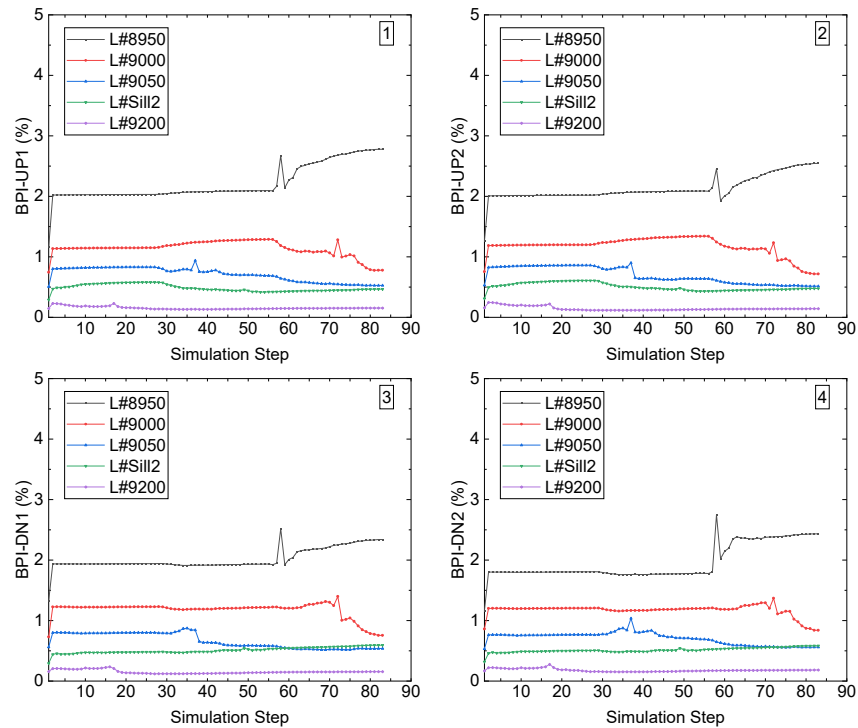


Figure 5.15 BPI of the stope access at middle haulage drift

The changes of the BPI values in the four corners in the middle-located haulage access are presented in figure 5.15. At all for corners, the BPI of the level L#8950 presents a similar trend, increase by the excavation then decrease by the following backfilling, and with a whole increasing trend. For other four levels, though with changes of BPI, it is under 1.5%. For level L#9000 and L#9050, with backfilled CRF taking into effect, it presents a decreasing trend, and level L#9200, the BPI almost keeps the same, and it is under 0.2%.

For the left edge-located haulage access, the BPI values of the four corners are presented in figure 5.16. Same with the right edge-located and middle-located haulage accesses, the BPI values at the

mining level L#8950 are larger than that of the other four mining levels. After the increase caused by the excavation, the BPI of the four corners in mining level L#8950 decreases back to almost the initial value with the backfilled CRF taking into effect. The four corners in the mining level L#9000 present the similar trend except the left roof corner UP2. For levels, L#9050 and L#9200, the changes of the BPI values at the four corners are negligible.

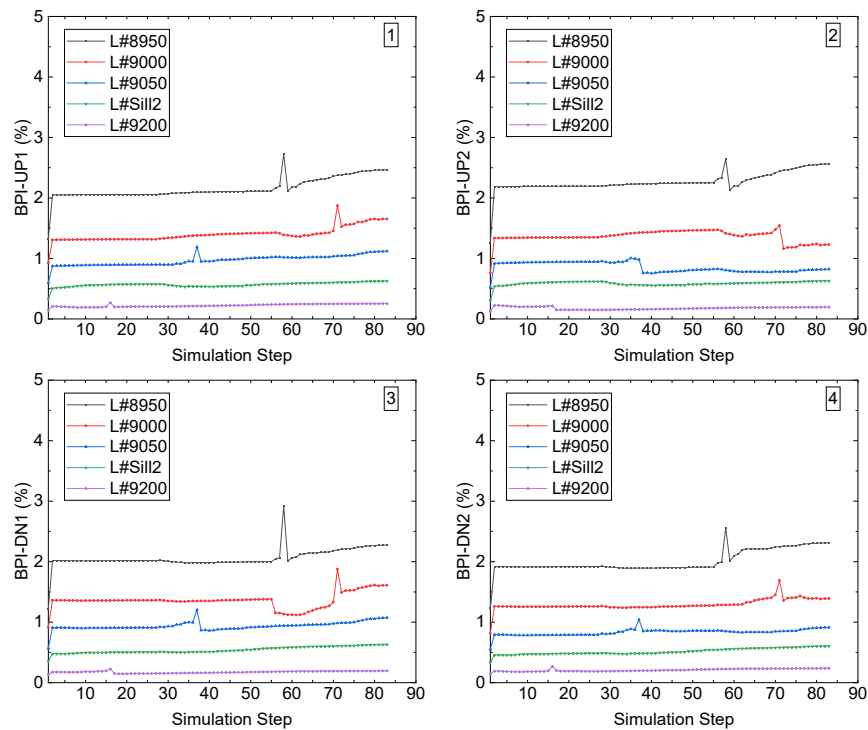


Figure 5.16 BPI of the stope access at left-edge haulage drift

According to the above three figures, the BPI values of the four corners in the haulage access are quite low compared with that of the stope access, indicating not rockburst tendency. Even at the mining level L#8950, which locates at the bottom of the mining pipe A154N, the BPI values are still lower than that of the stope access, indicating that the haulage access is safer than the stope access.

### 5.4.2 Tangential stress criterion (Ts) of the haulage drift accesses

According to the table 2.6, compared with the kimberlite, the host rock granite has stronger strength in Young's modulus and uniaxial compressive strength, which indicates that it needs higher level of tangential stress to cause the rockburst in the granite. Following figures present the Ts results in the haulage drift accesses. Same with the scenarios of assessment of the stope access intersections, the same stope accesses were chosen from the five mining levels at the same three locations, but another end of the stope access was takes for analysis.

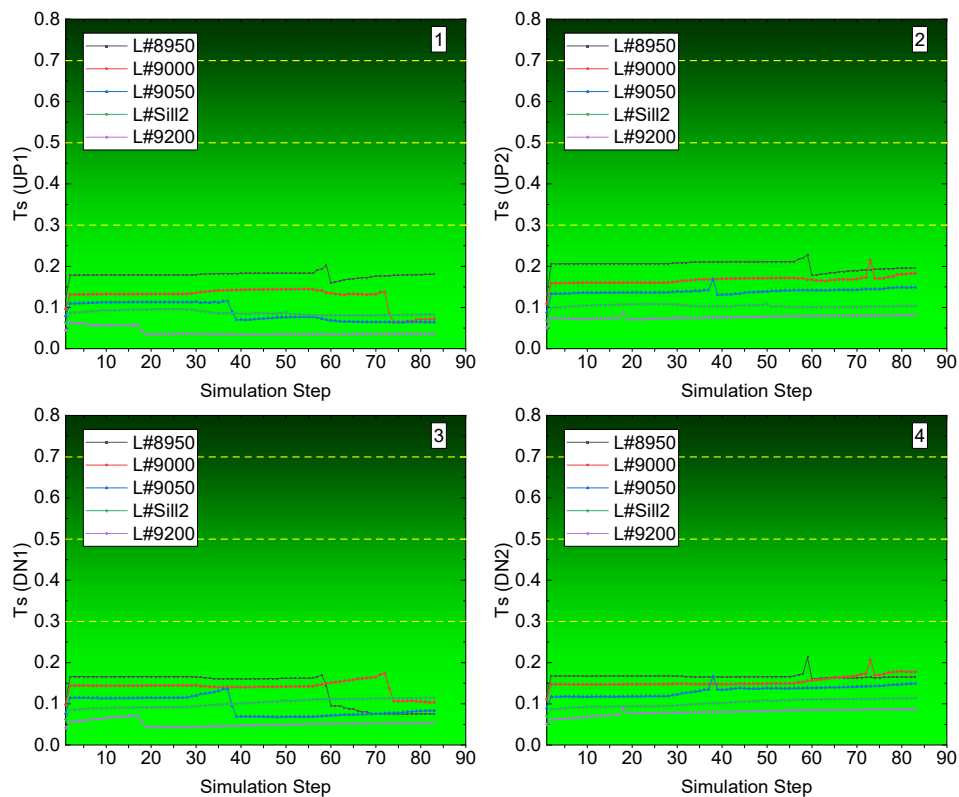


Figure 5.17 Ts of the stope access at right-edge haulage drift access

Figure 5.17 presents the Ts values of the four corners in the haulage drift access in five mining levels, from level L#8950 to L#9200. All the four corners, UP1, UP2, DN1, DN2, in the haulage drift accesses from the five mining levels have a value of Ts under 0.3, indicating no rockburst tendency in these areas. For the level L#8950, at the left roof corner UP1, the excavation causes

the  $T_s$  a small increase, then it decreases to the initial value of 0.18. For the other three levels, L#9000, L#9050 and L#9200, the  $T_s$  value is under 0.15 from the simulation step S1 to step S83, though the excavation step causes changes to  $T_s$ . The right roof corner UP2 presents a similar trend with that of the left roof corner UP1 for each specific mining level. For both floor corners, DN1 and DN2, the steps of excavation cause no significant changes, as shown in the third and fourth pictures in figure 5.17.

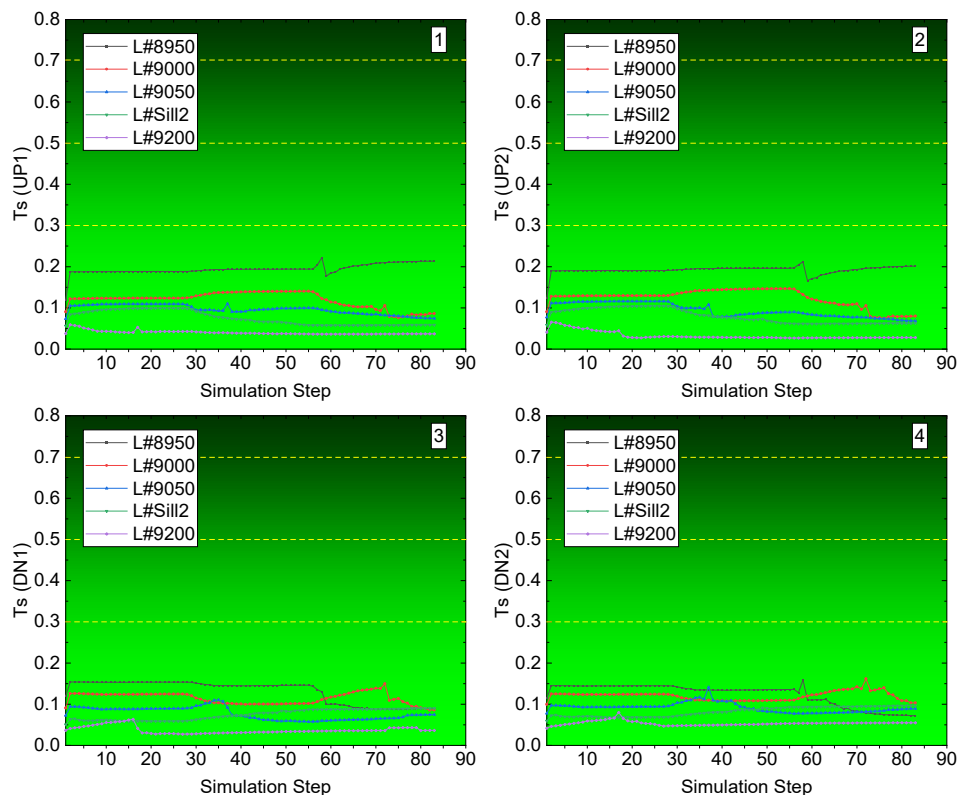


Figure 5.18  $T_s$  of the stope access at middle haulage drift access

For the  $T_s$  at the four corners in the haulage drift access in the middle haulage in each mining level, figure 5.18 illustrates the changes during the mining and backfilling process. For the two roof corners, UP1 and UP2, the mining level L#8950 has higher value of  $T_s$ , though all the  $T_s$  value of the five mining levels are under 0.3. The changes trends of both roof corners are the same, the step of excavation causes a little increase, then the backfilling step makes it back to the initial one. In

the other four levels, the  $T_s$  experiences no significant changes from the starting simulation step S1 to step S83. For the two floor corners, DN1 and DN2, the  $T_s$  value in the five mining levels shows no significant difference, all the  $T_s$  values are under 0.15, though with the process of excavation and backfilling at the particular simulation step in each mining level.

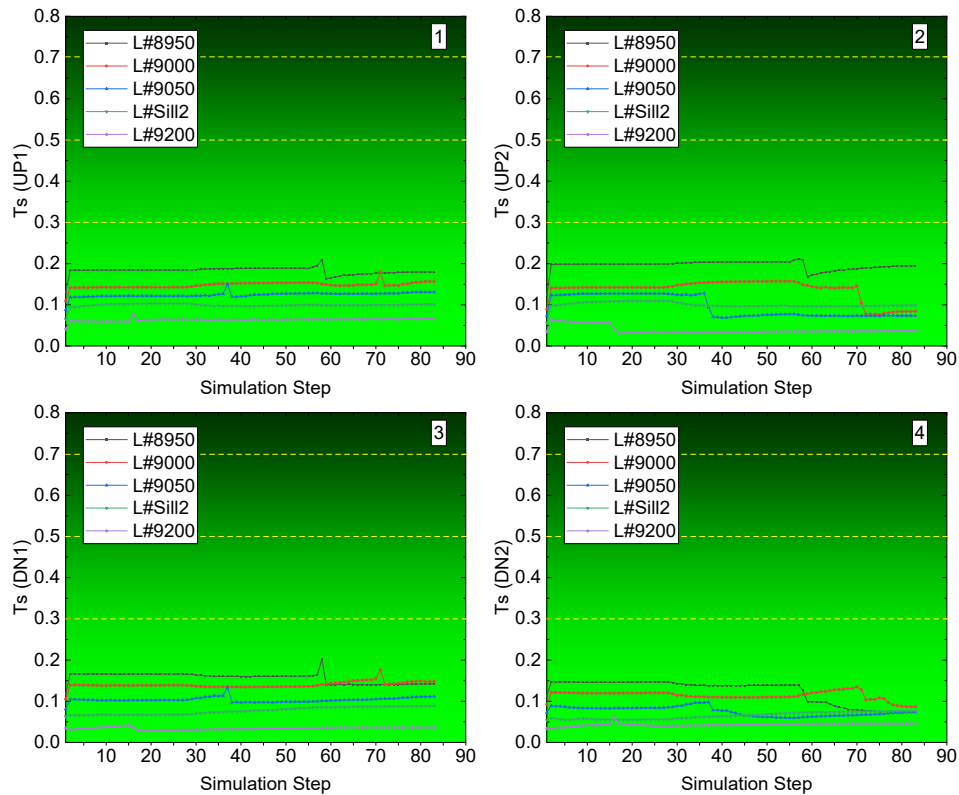


Figure 5.19  $T_s$  of the stope access at left-edge haulage drift access

In the left-edge haulage drift accesses, as shown in figure 5.19, same with the scenarios in the right-edge and middle haulage drifts, the  $T_s$  values of the four corners in each haulage drift access in each mining levels are under 0.3, indicating no tendency of rockburst. For the left roof corner UP1, all the  $T_s$  values from the five mining levels are less than 0.2, through the excavation causes the changes, and in each level, the  $T_s$  almost keeps the initial value. For the right roof corner UP2, level L#8950 has a  $T_s$  value of 0.2 from the starting simulation step S1 to the completion step S83, with changes caused by the step of excavation. In the other four levels, the right roof corner UP2

only sees decrease of the Ts. The left floor corner DN1 has a Ts value under 0.18 for all five levels, and the right floor corner DN2 has a Ts value under 0.15 from the whole mining and backfilling process of the three mining blocks.

### 5.5 Comparison of the stability of stope accesses to the stopes at three locations

In Chapter 4, the optimum location of the last mined stope was analyzed by the displacement based on a simplified two-dimensional (2D) model, and the conclusions suggested that compared with the two edges of the mining level, the middle of the mining level could be the optimum location of the last mined stopes, and in the process of the sill pillar recovery, the last mined stope should be four-stope-width away from the two edges of the mining levels in mining pipe A154N. This part presents the comparison of the BPI in the three locations in mining level L#9000 and L#9050.

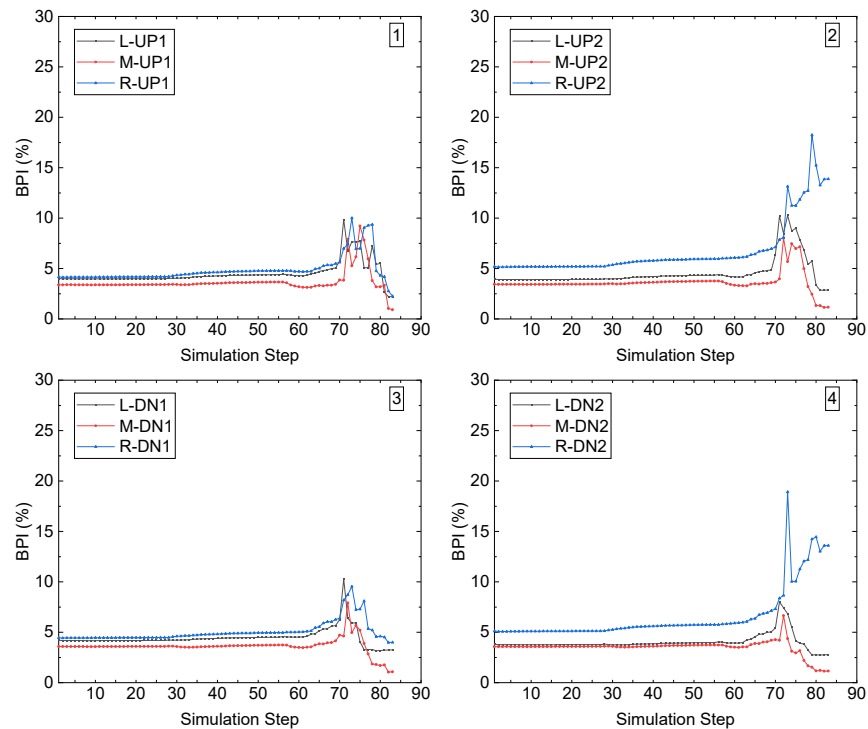


Figure 5.20 Comparison of BPI of three stope accesses in L#9000

The BPI values of the four corners in the stope access in three stope locations in the mining level L#9000 are presented in figure 5.20. At the left roof corner UP1, the BPI values among the three

stope locations show little difference during the process of excavation and backfilling in this mining level. For the right roof corner UP2, the BPI values of the two edge-located stopes are larger than that of the middle stope, as shown in the second picture, and the eight-edge has the largest value of BPI. For the right floor corner DN1, before the excavation occurs, the BPI values of the two edge-located stopes are larger than that of the middle-located stope, through with the influence of the backfilled CRF, the difference between the middle-located and left edge-located stopes decreases. The BPI value of the right floor corner DN2 presents the similar trend as the right roof corner UP2, both the edge-located stopes have larger values than that in the middle-located stope.

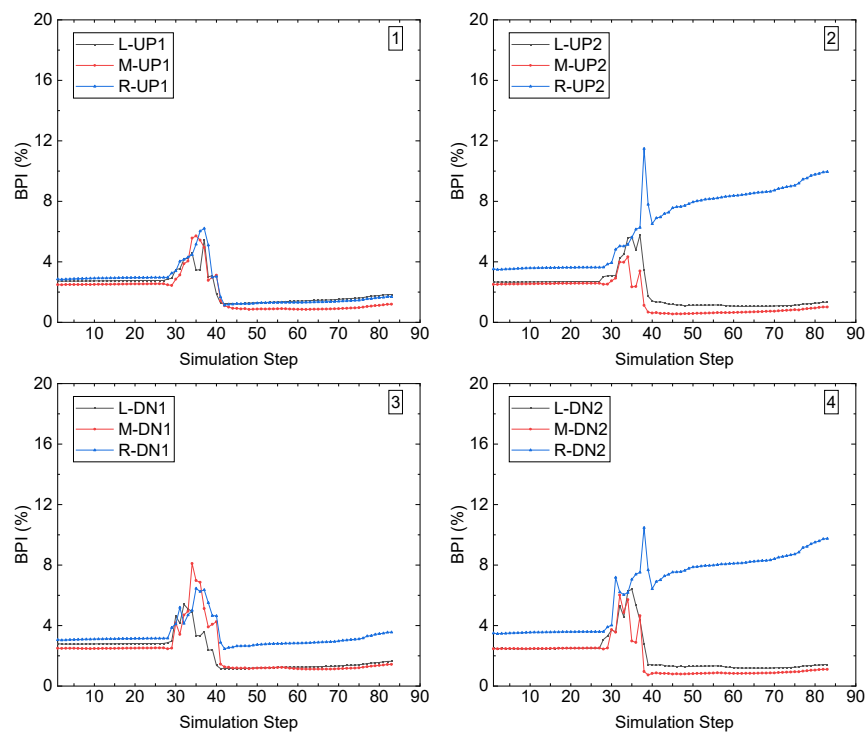


Figure 5.21 Comparison of BPI of three stope accesses in L#9050

For mining level L#9050, the mining depth is shallower than that of the level L# 9000, the BPI presents smaller values than that in level L#9000, as shown in figure 5.20 and figure 5.21. At the left roof corner UP1, similar with that in level L#9000, the stopes from the three locations show

almost no difference and present the same change trend. For the right roof corner UP2, before the excavation, the difference among three locations is small and middle-located and left edge-located stopes are almost the same, while after the excavation and backfilling, the right edge-located stope has larger BPI than the middle-located and left edge-located stopes, and the left edge-located stope has larger BPI than the middle-located stope, though the difference is small. For the left floor corner DN1, the middle-located and left edge-located stope have almost the same BPI at each simulation step, and it is smaller than that in the right edge-located stope. The right floor corner presents a similar trend, and with larger difference between the right edge-located stope and the other two locations, compared to the left floor corner DN1.

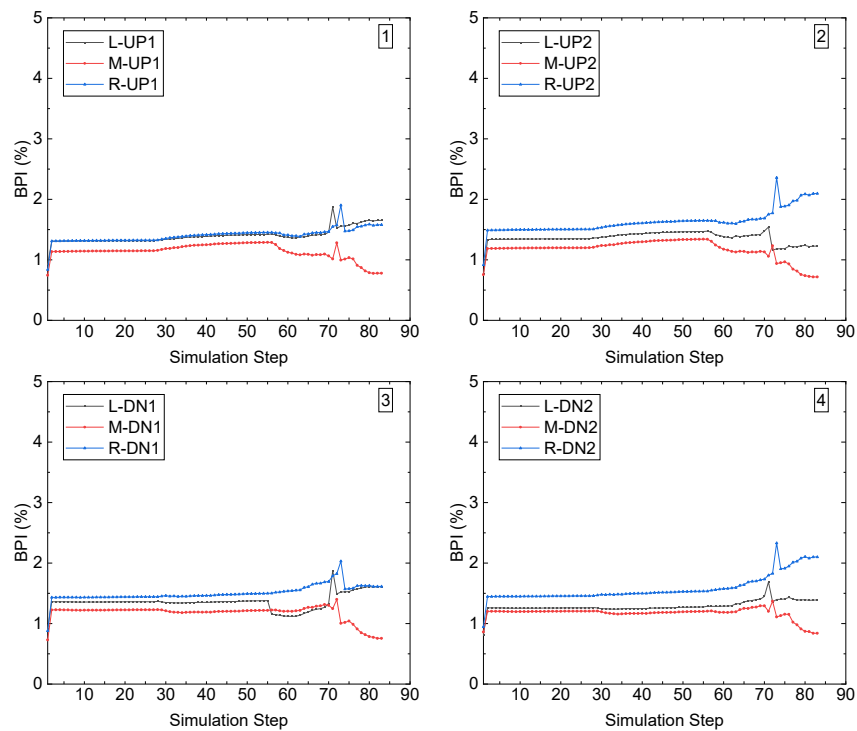


Figure 5.22 Comparison of BPI of three haulage accesses in L#9000

Figure 5.22 presents the BPI of the four corners in the haulage drift access from three locations in mining level L#9000, compared with the stope accesses locating in kimberlite, the haulage drift accesses locate in the granite, and the granite has a critical energy value ( $e_c$ ) of  $402.15\text{KJ/m}^3$ , then

the BPI values are much smaller than that of the stope access. While, in all four corners in the five mining levels, from level L#8950 to L#9200, the two edge-located haulage drift accesses have larger BPI than the middle-located one. At the left roof corner UP1 and floor corner DN1, after the step of backfilling the two edge-located haulage drift accesses have almost the same BPI and it is larger than the middle-located one. For the right roof corner UP2 and floor corner DN2, though they have differences, both are larger than that of the middle-located one.

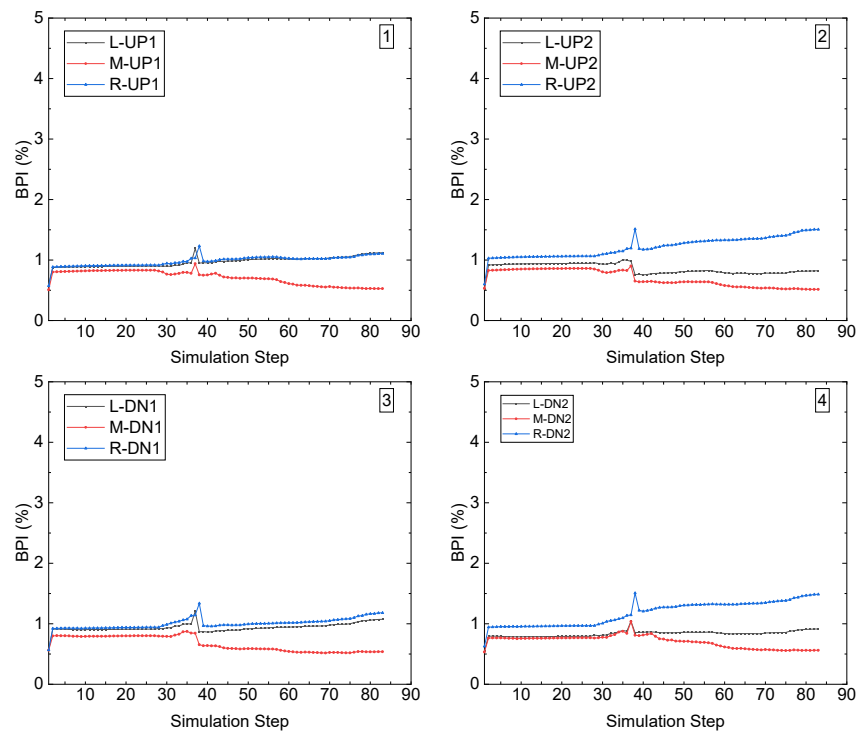


Figure 5.23 Comparison of BPI of three haulage accesses in L#9050

For the mining level L#9050, at the left roof corner UP1 and left floor corner DN1, the trends are the same, as shown in figure 5.23. Before the excavation, there is almost no difference among three locations, after the excavation and backfilling, the two edge-located haulage drift accesses increase the value of BPI, and have almost the same values, while the BPI of the middle-located one decreases constantly. For the right roof corner UP2 and floor corner DN2, the right edge-located haulage drift access presents an increasing trend, and the value of BPI is larger than the other two

locations. For the left edge-located haulage drift access, it keeps a stable value of BPI, though with little changes caused by excavation and backfilling, and the BPI is also larger than that of the middle-located haulage drift access.

From the above figure 5.20, figure 5.21, figure 5.22, and figure 5.23, the same conclusions can be achieved as the conclusions in Chapter 4 that the two edges of each mining level should be avoided to be the location of the last mined stopes. The failures presented in the figure 5.4 occurred in the stope access is a proof of the conclusion in Chapter 4, this stope access locates in stope S2-193, which is three stope-width away from the edge of the mining level.

### **5.6 Chapter summary and conclusions**

In this chapter, the assessment of the rockburst tendency of the stope accesses and haulage accesses to the stopes and haulages at three locations in each mining level from the five analyzed mining levels was conducted by the usage of the tangential stress criterion (Ts) and energy based burst potential index (BPI). For the stope accesses, the four corners in the access were analyzed due to the in-situ reported failures were in these locations. In the right edge-located stope access, the BPI and the Ts values of the two floor corners are higher than that of the roof corners. The corners of UP2, DN1 and DN2 present an increasing trend of BPI and Ts even with the backfilled CRF taking into effect, indicating the possible failure at the left floor corner DN1 and right roof corner UP2, when the adjacent stopes are mining out. At the stope access to the middle-located stope in each mining level, the two floor corners at the mining level L#8950 has higher BPI and Ts values than other four mining levels, indicating violent tendency of rockburst at the excavation process of the adjacent stopes in the next mining sequence. For the other four levels, there was no tendency of rockburst. At the left edge-located stope access, the values of the BPI and Ts are higher at the left

floor corner DN1 in the mining level #8950, for other corners among the other four mining levels, the BPI and Ts values are relatively low, indicating no rockburst tendency.

For the stability assessment of the haulage access, which locate in the rock mass of granite, due to the higher critical strain energy density compared with the kimberlite, no rockburst tendency was shown in all three chosen analyzed haulage accesses in each mining level among the five mining levels, L#8950, L#9000, L#9050, L#Sill2, L#9200, from the bottom to the top of the mining pipe A154N. Though in mining level L#8950, it has higher values of BPI and Ts, while the BPI value is under 4%, and the Ts value is under 0.3. Both values of the two criteria indicate no tendency of rockburst in the haulage access, even mining level L#8950 is the deepest one with mining depth of -473m.

Compared with the stope access and haulage access located at the two edges of the mining level, the middle-located stope access and haulage access have lower values of BPI, especially for the haulage access, except the level L#8950, which shares the boundary with the host rock granite at the four edges of the mining level. Then for other mining levels, the middle-located stopes are safer than the stopes close to the two edges of the mining level, which has good agreement with the conclusions from Chapter 4.

## **CHAPTER 6: ASSESSMENT OF FEASIBILITY OF RECOVERING SILL PILLAR AND COMPARATIVE STUDY OF THREE SCHEMES OF SILL PILLAR RECOVERY**

*Sill pillars are the mineral blocks that initially kept between different mining block to improve stability in the mining block. Recovery sill pillars can cause failures in the stopes in the sill pillar being recovered. In this chapter, three different proposed sill pillar recovery schemes are studied to assess the feasibility of the sill pillar recovery. In Diavik diamond mine, there are two sill pillars. By comparing the stability, such as the mining induced ground subsidence, rockburst potential around the stope access, etc., of the stope access during the process of recovery, the proposed scheme SBS is the optimum one among these three recovery schemes.*

### 6.1 General background of sill pillars at Diavik diamond mine

As one of the valuable and precious mineral materials, diamond has a large market all around the world (Yip and Thompson 2015). For the mining company, the more material that can be mined out, the more profits can be obtained. According to the updated mining design plan from Diavik diamond mine (DDM), there is one newly explored and planned mining block in mining pipe A154N. Then, combined with the other two primary mining blocks, there are three planned mining blocks in mining pipe A154N, namely block-A, block-B, and block-C, as shown in figure 6.1. Between the mining blocks, there are two initially kept sill pillars, Sill-1 and Sill-2. The two sill pillars work as the protective pillars, which can effectively prevent the transfer of stress from one block to another when the mining activities are in production in the three mining blocks.

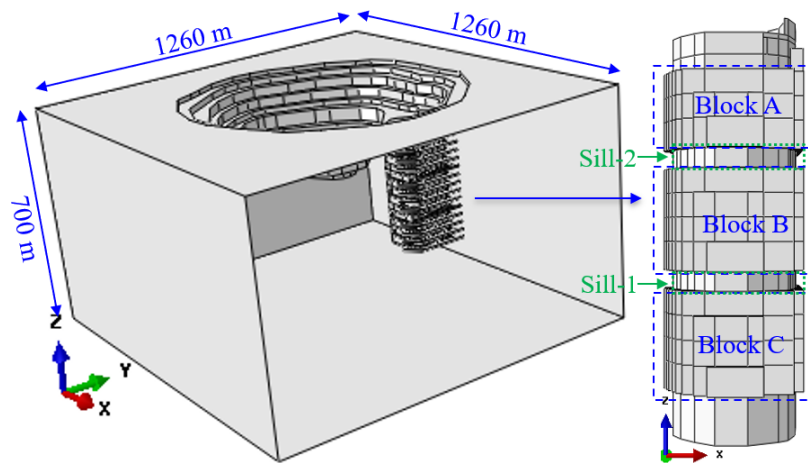


Figure 6.1 Profile of two sill pillars in pipe A154N

The total bulk volume of Sill-1 and Sill-2 in total is approximate 2 million tons. According to the Diavik mine, this volume of kimberlite rock mass can recover approximately 4 million carats worth of diamonds, this is a significantly high yield (Yip and Thompson 2015). After the completion of mining the three blocks, the possibility of excavation of the two sill pillars is of great interest to the engineers of the mine. The feasibility of recovery of these two sills then plays a significant role

in the resource development plan and prolonging the mine life, then it is challenging and interesting to propose the recovery schemes of the two sill pillars.

According to Sepehri (2016) and the monitored data from Diavik mine (Yip and Thompson 2015), when mining out and backfilling the kimberlite rock mass in block-A and block-B, the benches in open pit A154 stay safe. After the completion of block-A, block-B and block-C, these three blocks will be backfilled with cemented rockfill (CRF) and the strength of the backfilled blocks is weaker compared with the kimberlite rock masses and the host rock granite. Also, the location of Diavik diamond mine is surrounded by lakes, the waters are blocked by the dikes between the lakes and the open pit, as shown in figure 6.2. There is a high possibility that the subsidence of the open pit benches can cause the collapse of the dikes, which can cause catastrophic results. As a result, the assessment of sill pillar recovery feasibility is critical.

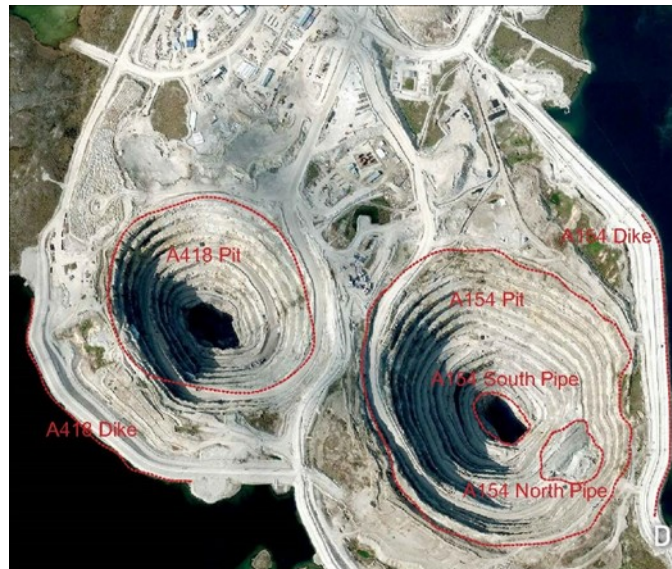


Figure 6.2 Aerial view of Diavik diamond mine (after Diavik, 2016)

## 6.2 Literature review

Pillar recovery is the practice of forming a series of pillars and then partially or totally extracting some or all of the pillars (Mark et al. 2003, 2007). Pillar recovery is considered the most hazardous

form of underground mining and is thought to be an art as much as a science (Mark and Gauna 2017). Sill pillars are initially left in place to support the great weight of the overburden in underground mining. Pillar recovery is an important step in mining operations, specifically in the aspect of maximizing resource recovery. During the process of pillar recovery, it is possible to induce risks, such as overlaying rock subsidence, stope failure and pillar failure (Henning et al. 1992). Researchers initiated and proposed empirical, analytical theories and numerical technical methods to assess the stability and guarantee the safety of miners and mining equipment. Hudyma and Potvin (1994, 2000) studied microseismic, conventional ground control instruments, numerical modelling, and visual observations to understand the mechanisms of pillar failures. Mark et al. (1995, 1997a, 1997b, 2001, 2003, 2005) and Iannacchione et al. (2009) analyzed the strengths and weaknesses of MHRA techniques and assessed the major hazard risks to evaluate sill pillar recovery in two room-and-pillar mines. Zur et al. (2004) used the enhanced cemented rock-fill for pillar recovery, and the pillars took advantage of the passive confinement effect of CRF to increase the post-peak load bearing ability. Zhukova et al. (2018) used monitored underground seismic registrations and mathematical models to improve the safety operations in pillar recovery. Langston et al. (2006) designed the stope layout, extraction procedure, and ground support, which were applied to successfully recover a pillar. Sainsbury et al. (2002, 2014) examined the stability and failure mechanisms of undermined stabilized rockfill and simulated pillar recovery by replacing the orebodies with laboratory tested stabilized rockfill, which solved the technical risks associated with the proposed extraction method. Ghasemi et al. (2010, 2012) assessed the risk of pillar recovery operations and classified that risk into four categories by using indicators. Beruar et al. (2011) developed proper stope sequencing to avoid the highly stressed area during pillar recovery. Valley et al. (2012) optimized the mining sequence and suggested new

directions for the different methods and the potential shortcomings. Townend et al. (2014) proposed five mitigation strategies to mitigate the high-stress concentration while mining sill pillars. Zhou et al. (2018) investigated the instability of large mined-out areas triggered by dynamic disturbance resulting from residual pillar recovery. Kyei et al. (2018) analyzed the fragmentation sizes of blasted rocks and selected the suitable rock particle size which was used for backfilling the mined-out stopes for the sake of sill pillar recovery.

In underground mining, to improve the production, generally, several mining levels are active in mining process at different mining depths, simultaneously. The mining process will cause the redistributed stresses, and the redistributed stress could make transfers horizontally and vertically. The transferred stress may contribute to failures of the stopes and damages to the mining equipment. For the sake of the safety of the mining zones, sill pillars are commonly reserved to prevent the vertical transfer of the redistributed stress, especially in the steeply dipping orebodies. As discussed in previous chapter 3, chapter 4, and chapter 5, using the CRF to backfill the mined stopes voids provides an effective way to improve the mining stability. While, as mentioned above, the strength of the CRF is not as strong as the kimberlite, when recover the two sill pillars in the mining pipe A154N, the influence of the backfilled CRF should be taken into consideration.

## **6.3 Calibration and verification of the finite element (FE) model**

### **6.3.1 Initial stress state of geostatic step**

As a powerful tool to study the underground engineering, finite element (FE) numerical analysis model is capable to conduct the general study and help the engineer to better understand the “real world” of the underground space. The initial in-situ stress state corresponds to the geostatic simulation in the developed FE analysis model. At the beginning of the simulation process, the FE model was calibrated by comparing the theoretical calculated initial maximum stress by equation

(2.11) with the computed initial maximum stress in the FE model. The computed initial maximum stress in the FE model is -27.2 MPa, as shown in figure 6.3, and the theoretically calculated initial maximum is 27.2 MPa, in ABAQUS, the compressive stress is assigned to be negative.

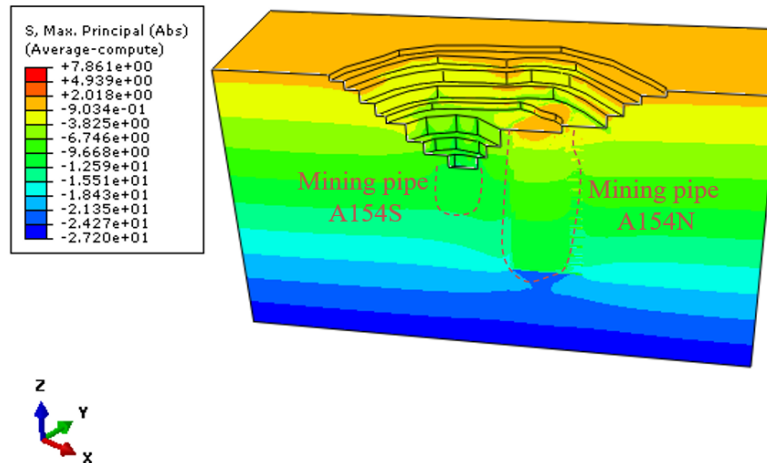


Figure 6.3 Initial computed maximum stress in FE model at geostatic step

### 6.3.1 Mining induced ground displacement at monitoring zones

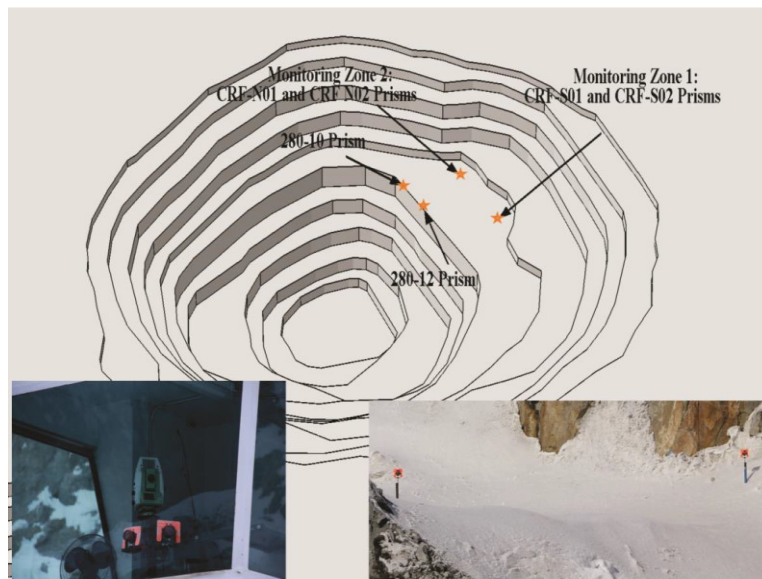


Figure 6.4 Monitor prisms on open pit bench (after Sepehri, 2016)

To calibrate the developed FE model, several monitor prisms were installed on the A154 pit benches to measure the ground surface subsidence induced by the mining activities in the mining

pipe A154N and A154S. Above figure 6.4 presents the location of the installed monitor prisms on the benches. Monitoring zone 1 has two prisms: CRF-S01 and CRF-S02. Monitoring zone 2 has two prisms: CRF-N01 and CRF-N02. Both monitoring zone 1 and monitoring zone 2 are on the boundary of the top surface of the mining pipe A154N. Meanwhile, another monitoring zone 3 also has two prisms: 280-10 and 280-12. These two prisms are on the edge of the A154 open pit bench.

Before conducting the simulation of the recovery process of the sill pillars, the verification and validation of the numerical with the monitored and measured data from the in-situ filed is significant to check whether the developed model really representing the real world in underground spaces. Before starting the assessment of the sill pillar recovery feasibility by the developed FE model, checking the validation and calibration of the model is a primary problem to be solved.

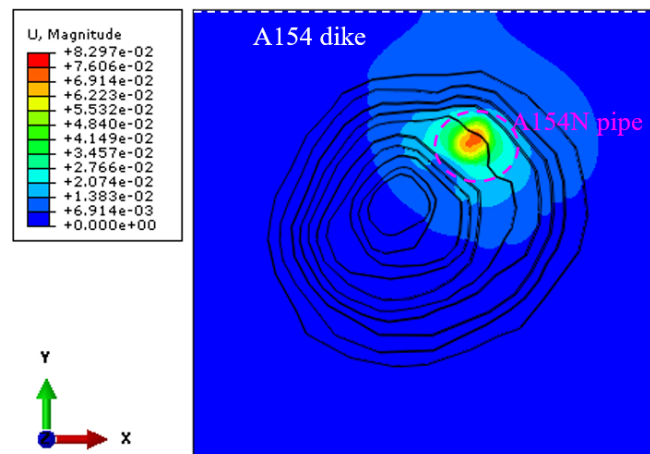


Figure 6.5 Computed displacement in FE model before sill pillar recovery

The computed displacement in the FE model is shown in figure 6.5. The main areas that have large displacement are over the mining pipe A154N, where the mining activities are in active. Though the three mining blocks are backfilled with cemented rockfill (CRF), the boundary of the model, which is also the A154 dike, still sees a tiny increase of displacement after the completion of the

excavation of the three mining blocks. Whether the recovery the two sill pillars will cause larger displacement of the A154 dike is a key question to be answered, and it will be analyzed in the following parts.

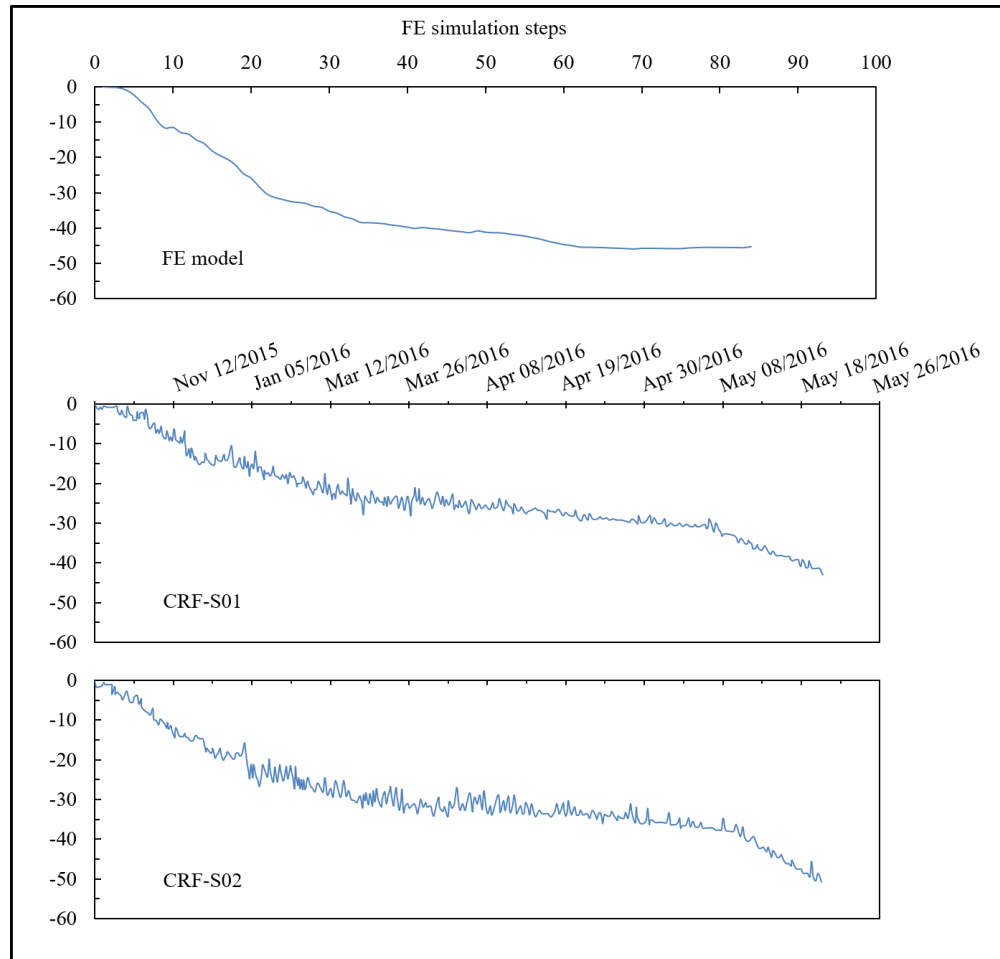


Figure 6.6 Displacement comparison between in-situ data and FE model at CRF-S

The simulation steps in the FE model were assigned based on the actual mining schedule of A154N mining pipe. The mining induced ground surface displacement of each excavation step was recorded by the model, also the accumulated ground surface displacement was computed. Then, it is reasonable and rational to compare the computed displacement in the FE model with the recorded in-situ data. The displacement of the location of the prisms were presented for the calibration of the model with the recorded data from Diavik diamond mine.

Figure 6.6 and figure 6.7 present the comparison of the displacement trend between the in-situ recorded data and the computed results in the FE model. In-situ data from both monitoring zone 1 and monitoring zone 2 are presented, and the results of the FE model are the average results from the FE model at each monitoring zone, respectively. The computed results in the FE model are the displacement from the simulation step S1, the geostatic step, the simulation step S83, at which all the three mining blocks are excavated and backfilled already.

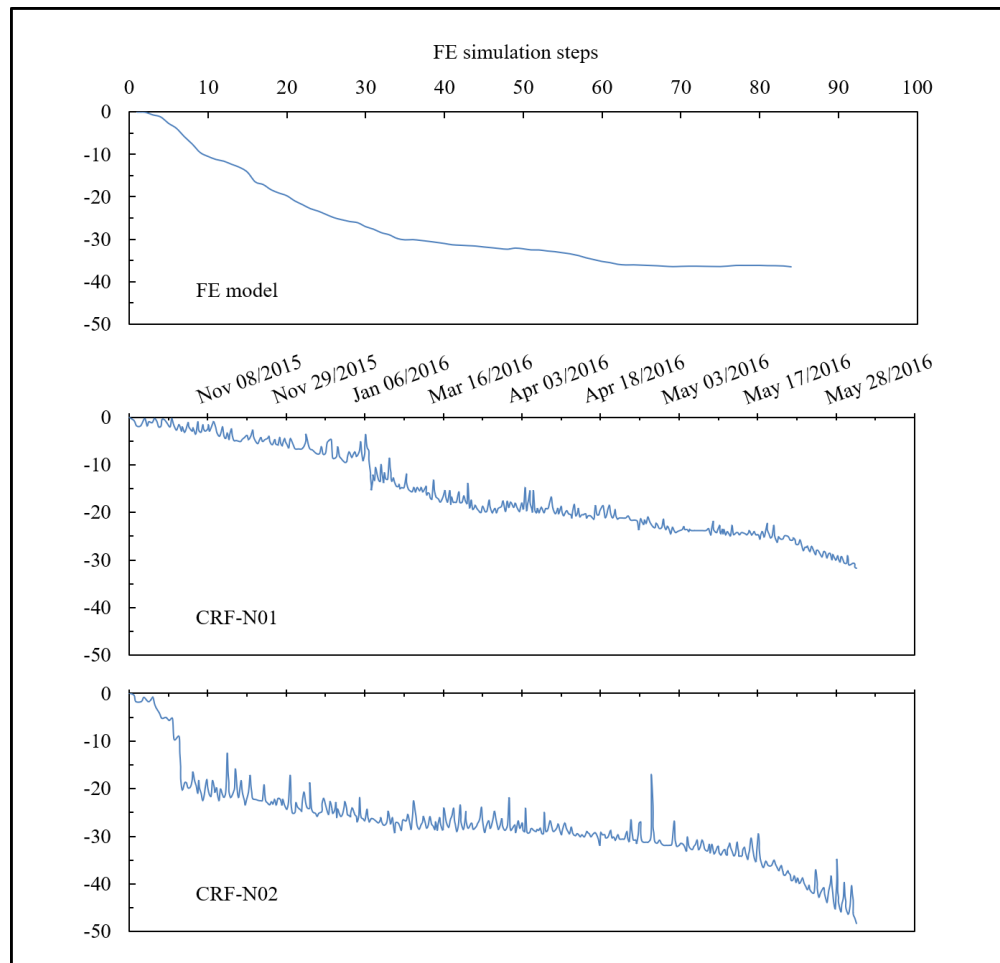


Figure 6.7 Displacement comparison between in-situ data and FE model at CRF-N

The accumulated displacement comparison between the in-situ recorded data and the computed FE model results is shown in table 6.1. The relative errors at different zones are: -2.57%, -8.01%,

5.51%, 10% from zone 1 to zone 3, respectively. The average relative error is 4.83%, which is acceptable (Kalenchuk, et al., 2014,2021; Sepehri, 2016; Kang, et al., 2019).

Table 6.1 Comparison of the displacement between in-situ data and the FE model computation

Monitoring prism location	FE model computed (mm)	In-situ data (mm)	Relative error (%)
Monitoring zone 1 (Ave-S01 & S02)	45.50	46.7	-2.57
Monitoring zone 2 (Ave-N01 & N02)	36.38	39.55	-8.01
Monitoring zone 3 (280-10)	20.47	19.4	5.51
Monitoring zone 3 (280-12)	18.15	16.5	10
Average relative error			6.52

#### 6.4 Schemes of sill pillar recovery

From the above FE model calibration by comparison of the initial maximum stress between the theoretical calculation and the computed geostatic, and the in-situ recorded displacement and the computed displacement in the FE model, the developed FE model is capable and precise to conduct the numerical simulation analysis of the topics in this research. Then the assessment of the feasibility of the recovery of the two sill pillars can be conducted by this developed FE model.

##### 6.4.1 Stress condition around the mining pipe A154N pre-sill-pillar-recovery

The reserved sill pillar consists of several mining stopes, and each stope can contain thousands of tons of materials. Compared with the backfilled CRF in the mined voids, the unmined stopes in the sill pillar will provide more support than the backfilled CRF. Figure 6.8 presents the yield zone around the mining pipe A154N. As shown in figure 6.8, the yellow areas are the two sill pillars, and the other zones in the mining pipe A154N were already backfilled with the CRF. Compared with the backfilled CRF, the possibility of the sill pillar prone to yield is higher. And this causes the concerns that whether it is safe to recover the two sill pillars.

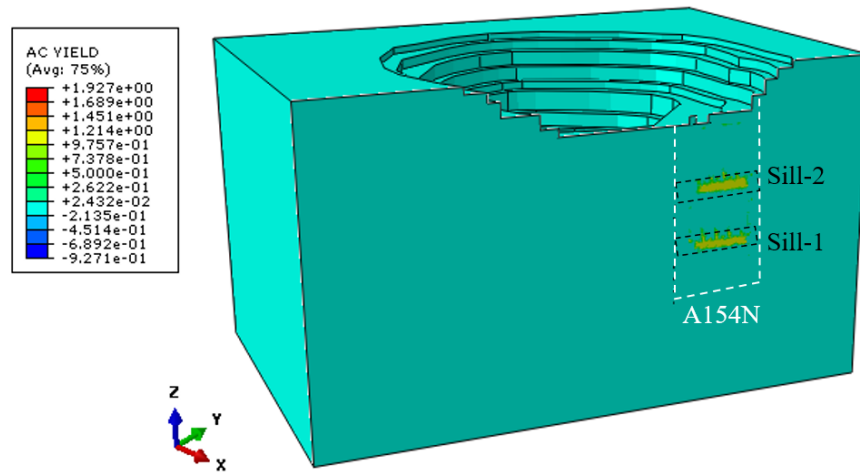


Figure 6.8 Yield zones before the recovery of the two sill pillars

The mining induced redistributed stress field around the mining pipe A154N is another concern. According to the studies done by Leveille (2015), Sepehri (2016) and Pu (2019), the kimberlite and granite in Diavik diamond mine has the potential of rockburst. The over tangential stress contributes to the rockburst in the rockburst prone rock mass.

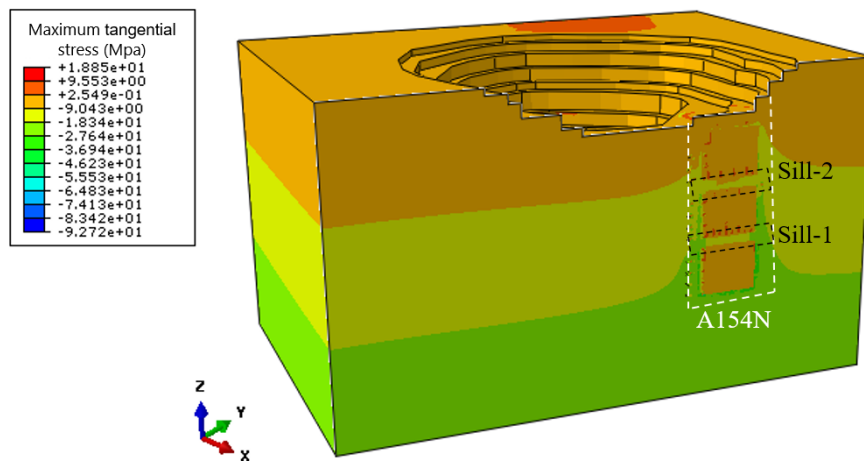


Figure 6.9 Maximum tangential stress before the recovery of the two sill pillars

Above figure 6.9 presents the tangential stress field around the mining pipe A154N after the completion of the excavation and backfilling of the three mining blocks, block-A, block-B and block-C. Similar with the scenario of yield zones, the tangential stress around the mining pipe

A154N is higher than other areas, especially around the two sill pillars. The boundaries between the mining pipe A154N and the host rock has higher degree of tangential stress.

#### 6.4.2 Proposed three sill pillar recovery schemes

Knowing the stress field around the mining pipe A154N, where the two sill pillars are located, is the first step to propose the recovery schemes. To recover the two sill pillars, three sill pillar recovery schemes are proposed. To keep the mining sequence is consistent with the designed sequence schedule at Daivik diamond mine, here, the mining sequence to recover the two sill pillars follows the sequence of mining and backfilled the three mining blocks in mining pipe A154N.

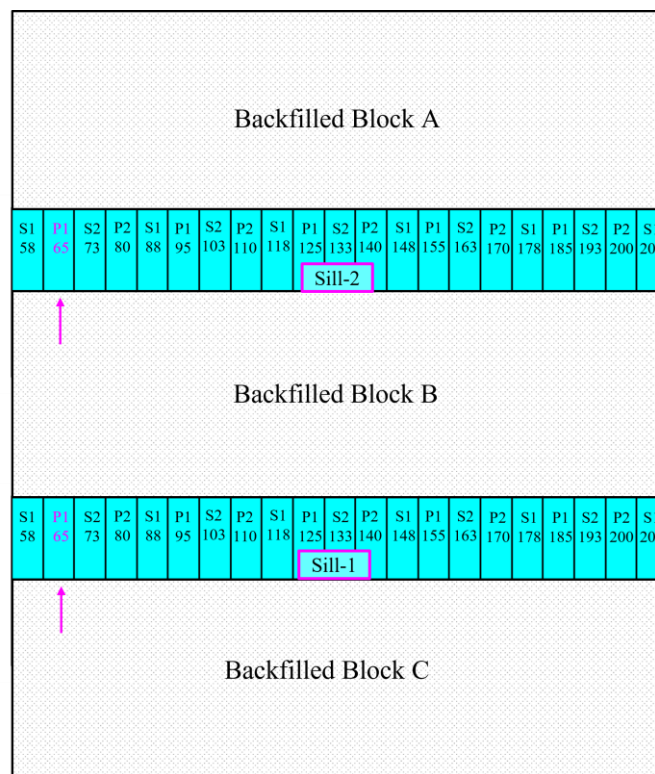


Figure 6.10 Profile of sill pillar recovery scheme of SBS

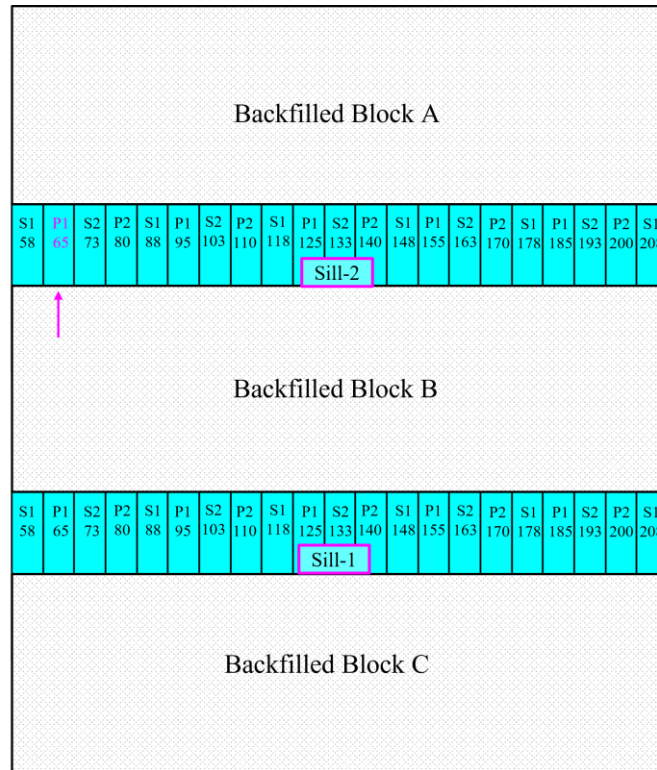


Figure 6.11 Profile of sill pillar recovery scheme of SS1

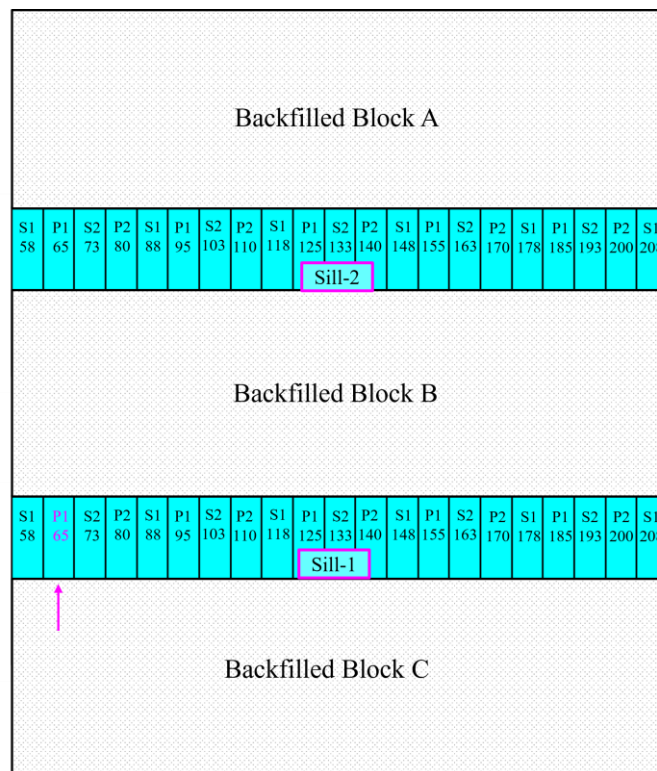


Figure 6.12 Profile of sill pillar recovery scheme of SS2

The first mined stopes in the three recovery schemes of the two sill pillars are labelled with color of magenta, as shown in figure 6.10, figure 6.11 and figure 6.12. The first proposed scheme of recovery process starts at both sill pillars (SBS), as shown in figure 6.10, from the stope P1-65, till the two sill pillars are excavated and backfilled. The second proposed scheme of recovery process starts at Sill-1 (SS1), as shown in figure 6.11, from the stope P1-65, when all the stopes are excavated in Sill-1, then the mining process moves to Sill-2, till the two sill pillars are recovered and backfilled. The third proposed scheme of recovery process starts at Sill-2 (SS2), as shown in figure 6.12, from the stope P1-65, when all the stopes in Sill-2 are excavated, the mining process moves to Sill-1, till all the two sill pillars are recovered and backfilled. All three sill pillar recovery schemes follow the primary and secondary mining sequence mentioned in chapter 2. The primary sequence stopes will be excavated firstly, then the secondary sequence stopes will be excavated.

### 6.5 Comparison of displacement at four prisms among the three sill pillar recovery schemes

When conducting the recovery of the two sill pillars, the open pit benches are still in function for the transportation of the orebodies from the sill pillars in mining pipe 154N to the ground surface, then the stability of the benches is still a key issue to be considered.

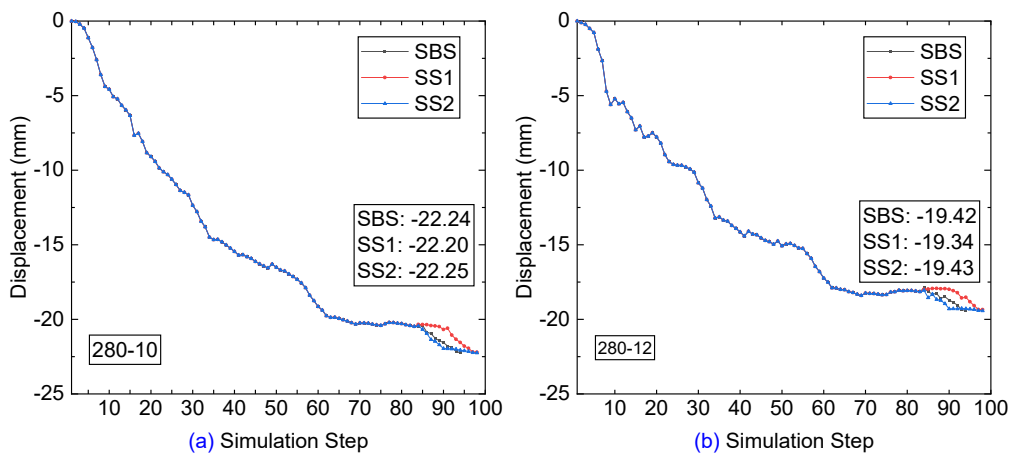


Figure 6.13 Comparison of displacement at monitored prism 280-12 and 280-10

From the simulation step S84, the recovery process starts. Scheme SBS takes 11 simulation steps to recover the two sill pillars and backfill the two sill pillars, the simulation step ends at step S94. Both schemes SS1 and SS2 take 15 steps to recover and backfill the two sill pillars, and the simulation step ends at step S98. Though, it takes different simulation steps to recover and backfill the two sill pillars, the mining induced displacement during the recovery process are almost the same. Figure 6.13 presents the computed displacement from FE model at the location of prisms 280-10 and 280-12. The final displacements at prism 280-10 are: -22.24 mm, -22.20 mm and -22.25mm, for schemes SBS, SS1 and SS2, respectively. For the prism 280-12, the final three displacements are: -19.42 mm, -19.34 mm and -19.43 mm, for schemes SBS, SS1 and SS2, respectively.

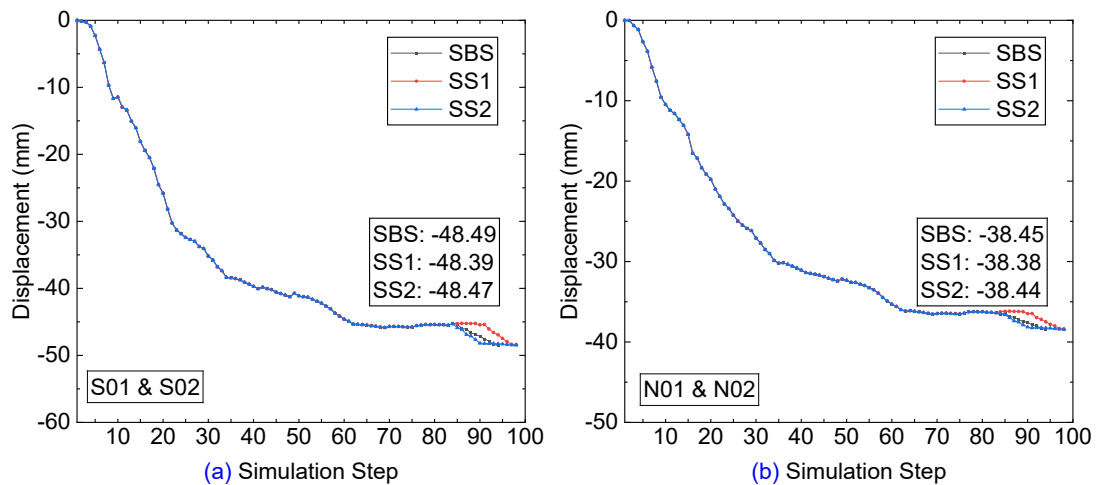


Figure 6.14 Comparison of displacement at monitored site S01-02 and N01-02

The displacements at the monitoring zone 1 and zone 2 are shown in figure 6.14. Similar with the displacement at monitoring zone 3, the final displacements of three different recovery schemes are very close, at both monitoring zone 1 and zone 2. At the prism CRF-S, the three displacements are: -48.49mm, -48.39mm and -48.47mm, for schemes SBS, SS1 and SS2, respectively. At the

monitoring prism CRF-N, the displacements are: -38.45mm, -38.38mm and -38.44mm, for schemes SBS, SS1 and SS2, respectively.

During the mining and backfilling of the three mining blocks, the mining induced displacement at the three monitoring zones reach a value of 46.7mm (CRF-S), 39.55mm (CRF-N), 19.4mm and 16.5mm (280-10, 280-12), respectively. From the view of the mining induced displacement, the three different schemes of sill pillar recovery have very close results at the three monitoring zones. Also, the displacement induced by the process of sill pillar recovery sees a slight increase at all three monitoring zones. Following table 6.2 present the displacement induced by the process of sill pillar recovery.

Table 6.2 Sill pillar recovery induced displacement at monitoring zones

Monitoring zone	Recovery scheme		
	SBS (mm)	SS1 (mm)	SS2 (mm)
280-10	1.77	1.73	1.78
280-12	1.27	1.19	1.28
CRF-S	2.99	2.89	2.97
CRF-N	2.07	2.00	2.06

All displacement induced by the three sill pillar recovery schemes is not more than 3 mm. The backfilled CRF in the three mining blocks provide sufficient support for the process of sill pillar recovery. And all three schemes of sill pillar recovery can be implemented.

Figure 6.15 presents the displacement profile of the A154 open pit benches after the completion of the recovery of two sill pillars by the recovery scheme SS1, compared with figure 6.5, which shows the displacement before the two sill pillars recovery process, the displacement induced by the process of two sill pillar recovery is tiny, as shown in table 6.2, around the top surface of the mining pipe A154N.

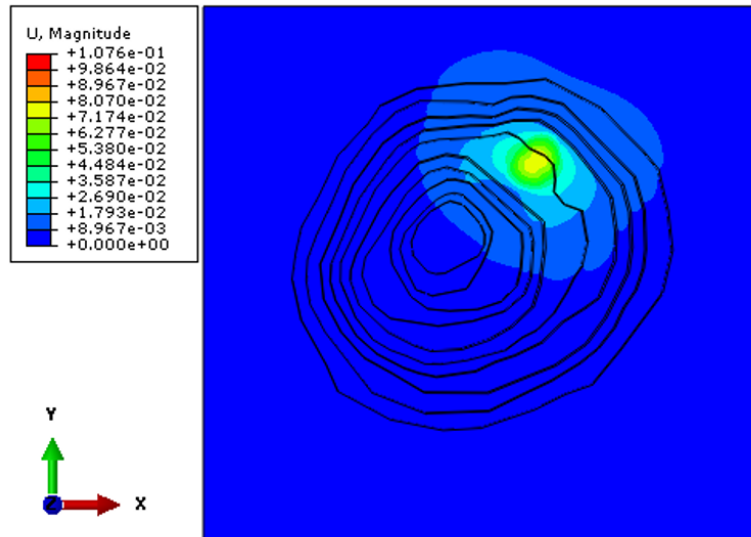


Figure 6.15 Displacement after the recovery of two sill pillars (by scheme SS1)

### 6.6 Displacement of the upper levels caused by sill pillars

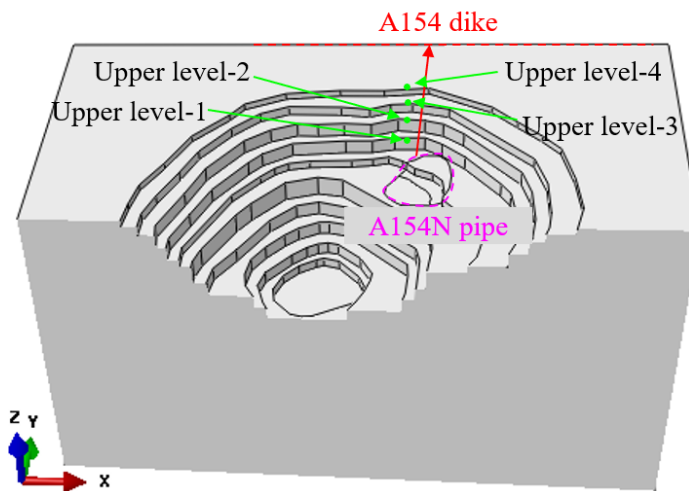


Figure 6.16 Chosen monitored location on upper bench levels

In Diavik diamond mine, the A154 pit is surrounded and protected by the A154 dike from the waters in the lake, as shown in figure 6.2. The stability of the dike is key to the mining area in A154 pit.

Upper the A154N mining pipe, there are four levels of open pit benches, as shown in figure 6.16. Several locations are chosen on each bench level in the numerical model to monitor the

displacement on the benches caused by the mining activities and sill pillar recovery process in the mining pipe A154N. Starting from the upper level closest to the mining pipe A154N, following the direction of the red arrow to the dike boundary, the four chosen upper levels are marked with, upper level-1 (UL1), upper level-2 (UL2), upper level-3 (UL3) and upper level-4 (UL4), as shown in figure 6.16. Here, the upper level-4 is the ground surface at Diavik diamond mine, the elevation between the top surface of mining pipe A154N and the ground surface is 94m. The depths of the four bench levels are: 0m, -14m, -34m, -64m, from upper level-4 to upper level-1, from the ground surface to the top surface of bench level-1.

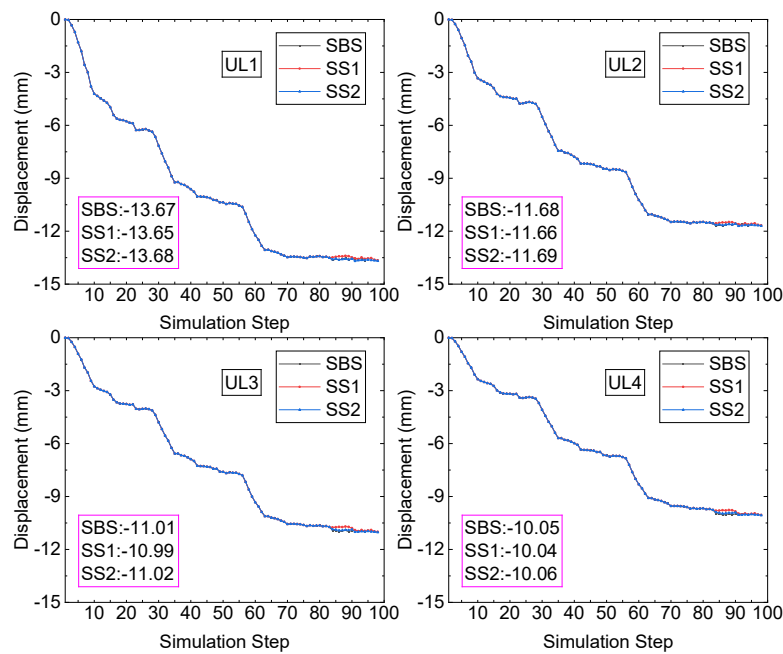


Figure 6.17 Displacement comparison at monitored location

The average displacement at the chosen locations on the four upper bench levels in the numerical model caused by the mining activities and the three sill pillar recovery schemes process are presented in figure 6.17. From the beginning of the mining production in mining pipe A154N to the state of three mining blocks were all mined and backfilled, the process of mining and backfilling in pipe A154N caused displacement of -13.50mm, -11.56mm, -10.73mm, and -9.76mm,

from upper bench level-1 to upper bench level-4. Compared with the displacement of the monitored prisms at the monitoring zones around top surface of pipe A154N, the displacements at the upper bench levels caused by the mining activities in pipe 154N are much smaller. From upper bench level-1 to upper bench level-4, the displacement at the bench level decrease constantly.

From the simulation step S84, the sill pillar recovery process commences. Following table 6.3 presents the average displacement at the upper bench levels of the chosen locations from the beginning simulation step S84 of the sill pillar recovery to the completion of the backfilling step in the two sill pillars.

Table 6.3 Sill pillar recovery induced displacement at upper levels

Chosen location	Recovery scheme		
	SBS (mm)	SS1 (mm)	SS2 (mm)
UL-1	0.168	0.147	0.180
UL-2	0.128	0.111	0.139
UL-3	0.284	0.294	0.294
UL-4	0.294	0.282	0.303

From figure 6.17 and table 6.3, the displacements of the chosen locations at the upper bench levels caused by the process of sill pillar recovery conducting by the three sill pillar recovery schemes have slight increase, the maximum one is 0.303mm at the upper level-4 from sill pillar recovery scheme SS2. In the view of displacements of the chosen locations in the numerical model and monitoring prisms at the in-situ field, the three sill pillar schemes are feasible. All three sill pillar recovery schemes will not trigger the huge displacement of the upper bench levels.

## 6.7 Assessment of the stope and haulage accesses stability among three pillar recovery schemes

In underground mining, stope access and haulage drift are excavated for the transportation of the minerals and the supplementary materials in-and-out the stopes from the ground surface. Compared with other underground mining structures, stope access and haulage drift serve the longest time for the production in the mine. Then, the stability of the stope access and the haulage drift is a key issue to be assessed.

### 6.7.1 Assessment of the stope access stability among three pillar recovery schemes

#### 6.7.1.1 Tangential stress criterion ( $T_s$ )

For a rockburst to occur, the rock mass must have the ability to store a considerable amount of strain energy which could be released violently at failure and there must be an environment for stress concentration and energy accumulation (Wang and Park, 2001). Here, the tangential stress criterion was used to conduct the comparison of the stability assessment among the three sill pillar recovery schemes: SBS, SS1 and SS2. According to Wang and Park (2001), the rockburst tendency can be evaluated using  $T_s$  criterion as presented in table 6.4.

Table 6.4 Rockburst tendency prediction based on CTS

Tangential stress criterion ( $T_s$ )	Rockburst tendency
$T_s \geq 0.7$	Violent
$0.5 \leq T_s < 0.7$	Strong
$0.3 \leq T_s < 0.5$	Weak
$T_s < 0.3$	No rockburst

According to Chapter 4 and Chapter 5, the stope access and haulage drift from three representative locations of left-edge, middle line and right-edge, are chosen to conduct the assessment. Both the stope access and haulage drift access have a section size of  $5\text{m} \times 5\text{m}$  (height  $\times$  width).

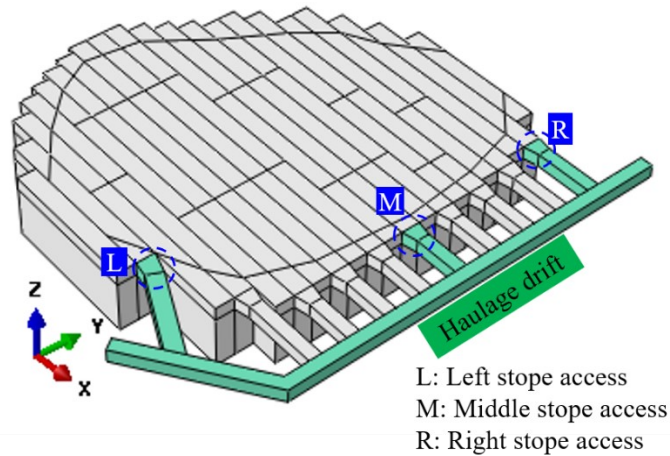


Figure 6.18 Stope access and Haulage drifts to Sill-1

According to the Chapter 5, the boundaries of the mining pipe A154N have higher tangential stress than the center of the mining pipe. Then, the stope accesses to the undercuts of stopes in Sill-1 from the three locations are chosen to check whether the tangential stress around Sill-1 has the same stress status.

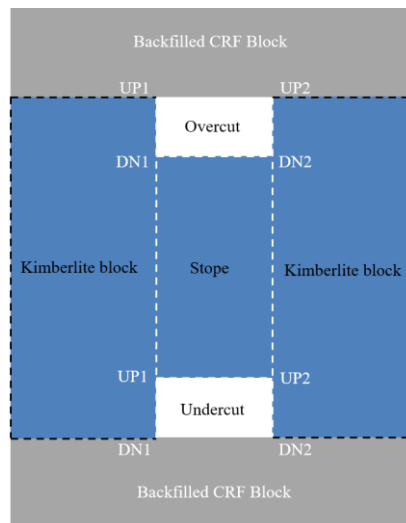


Figure 6.19 Profile of chosen corners in overcut and undercut

In underground rectangular openings, the four corners will easily generate the stress concentration effect, which may cause failures at these locations. Four corners in the overcut and undercut are chosen to conduct the comparison among the three sill pillar recovery schemes, UP1 is the left

roof corner, UP2 is the right roof corner, DN1 is the left floor corner, DN2 is the right floor corner, the gray parts are the already backfilled CRF block in the mined stope voids, as shown in figure 6.19.

All three sill pillar recovery schemes start at simulation step S84, the following present figures start at simulation step S83, which is the end step of excavation and backfilling the three mining blocks, and simulation step 84 is the first step to recover the sill pillars by three recovery schemes. Following figure 6.20, figure 6.21 and figure 6.22, present the comparison of the Ts among three sill pillar recovery schemes at the four corners in the stope access section at three stope locations. The three sill pillar schemes present the similar trend at each chosen corner in the three stope locations.

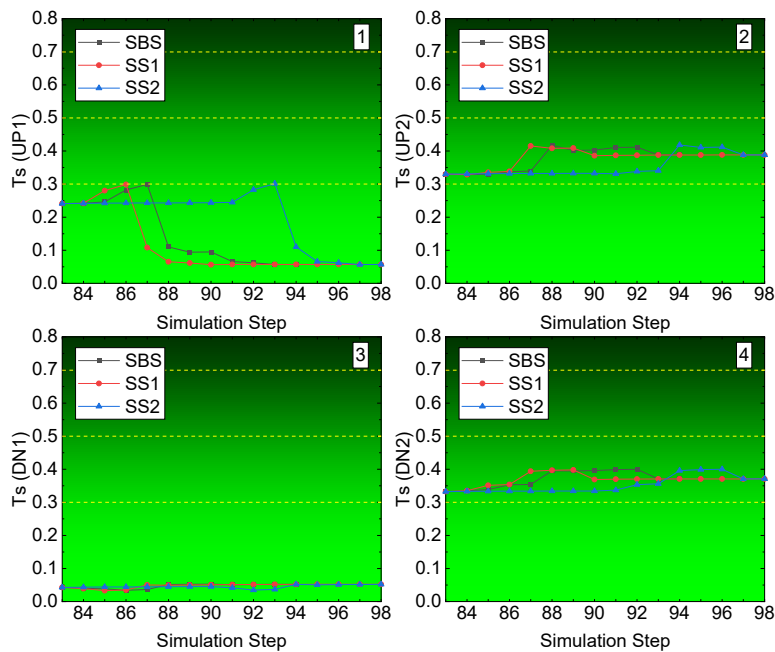


Figure 6.20 Ts of right-edge stope access to undercuts in Sill-1

The Ts of the four corners at the undercut access in the right-edge stope in Sill-1 is shown in figure 6.20. For the left roof corner UP1, the Ts value is less than 0.3, though through at some step it reaches to 0.3, with the backfilling taking into effect at the flowing step, it goes down to a value

under 0.1, then it is safe for this corner based on the  $T_s$  value, and according to table 6.4, there is no rockburst tendency. For the right roof corner UP2, from the beginning of the recovery, it is over 0.3, which means it is not stable as the left roof corner, according to table 6.4, with a  $T_s$  value between 0.3 and 0.5, there is a rockburst tendency, though it is weak. For the left floor corner DN1, the  $T_s$  value is always under 0.1, which means there is no tendency of rockburst. For the right floor corner DN2, similar with the right roof corner, the value of  $T_s$  is between 0.3 and 0.5, presenting a weak tendency of rockburst. Comparing the  $T_s$  value at the four corners in the stope access to undercut of the right-edge in the Sill-1, the right side of the undercut access is more unstable than the left side. Both right roof corner and floor corner present weak rockburst tendency, while the left side has no rockburst tendency.

The rockburst tendency at the four corners in the middle stope undercut access in Sill-1 is shown in figure 6.21. Different from the right-edge stope access to undercut, the four corners in the middle stope access to undercut show no rockburst tendency.

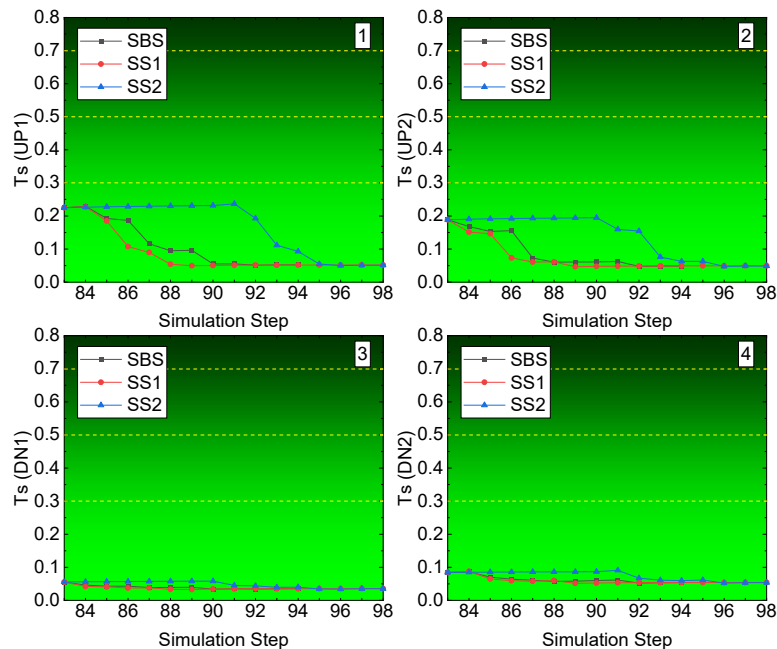


Figure 6.21  $T_s$  of middle stope access to undercuts in Sill-1

Both the corners of the floor have a value of  $T_s$  less than 0.1, while the roof corners have larger  $T_s$  value, through it is under 0.3. according to figure 6.19, the roof corners are in the unmined kimberlite rock mass, while the floor corners are in the backfilled CRF block. According to the introduction of rock mechanics properties parameters in-put in the developed FE model in table 2.6 in Chapter 2, the backfilled CRF has lower strength and elastic properties than the kimberlite block, when the backfilling finishes, the backfilled CRF could fail, but not in the type of rockburst.

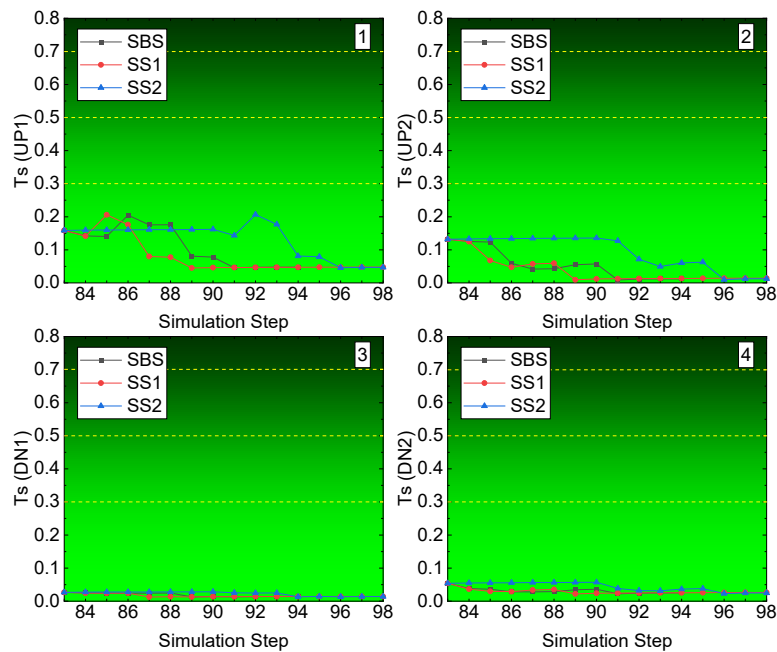


Figure 6.22  $T_s$  of left-edge stope access to undercuts in Sill-1

The rockburst tendency of the four corners in the left-edge stope access to undercut is illustrated in following figure 6.22. Similar with the middle stope access to undercut, there is no rockburst tendency in the four corners. While compared with the floor corners, the roof corners have high values of  $T_s$ . Both the floor corners have a  $T_s$  value under 0.05 among the three sill pillar recovery schemes. For the roof corners, UP1 and UP2, though the three sill pillar recovery schemes cause difference value of  $T_s$ , the  $T_s$  is under 0.2, and after the completion of the recovery and backfilling

of the two sill pillars, the  $T_s$  values of the three sill pillar recovery schemes reach the same final state of  $T_s$ .

Referring to figure 6.18, in which the locations of the three analyzed stope accesses were marked, based on the results presented in figure 6.10, figure 6.21 and figure 6.22, the right-edge stope access has higher value of  $T_s$ , indicating the rockburst tendency at the right side of the right-edge stope access is higher than any other location in other two stope accesses, the left-edge one and the middle one, shown in figure 6.18. Then, in the following parts, only the results of right-edge stope accesses are presented for the analysis, considering they have the higher rockburst tendency compared with the other two stope accesses during the process of excavation and backfilling the two sill pillars among three recovery schemes.

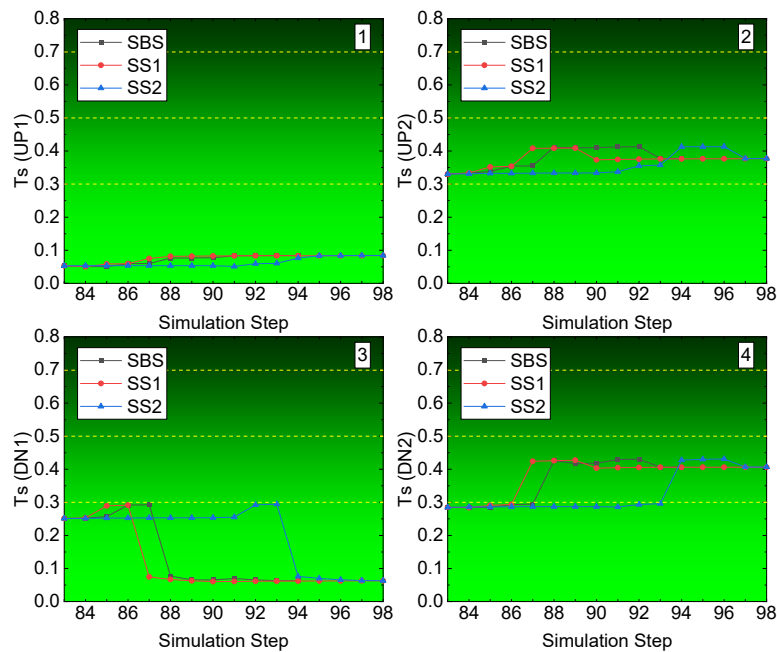


Figure 6.23  $T_s$  of right-edge stope access to overcuts in Sill-1

The stope access to overcut in the right-edge stope in Sill-1 has similar rockburst tendency, though the roof corners are in the backfilled cemented rockfill (CRF) and floor corners are in the kimberlite in contrast with that in the undercut, as shown in figure 6.19 and figure 6.23. The left

roof corner UP1 has a  $T_s$  value under 0.1 during the whole process of excavation and backfilling of two sill pillars, indicating no rockburst tendency. For the right roof corner UP2, the  $T_s$  value is between 0.3 and 0.5 among all three schemes during the whole process, indicating a weak tendency of rockburst, though after the completion of the backfilling, and the excavation of the stope access to overcut causes a slight increase of  $T_s$  in the right roof corner. On the two floor corners, they present a contrary trend, when the stope access to overcut was excavated, the  $T_s$  value of the right floor corner DN1 increases slightly, while when the backfilled CRF taking into effect, it decreases swiftly. For the right floor corner DN2, the excavation of the stope access to overcut causes a swift increase of  $T_s$ , from 0.28 to 0.45, from no rockburst tendency to weak rockburst tendency, and it keeps the  $T_s$  though with the completion of the backfilling in Sill-1. All three recovery schemes present the same increase after the excavation of the stope access, through it occur at different simulation steps, as shown in the fourth picture in figure 6.23.

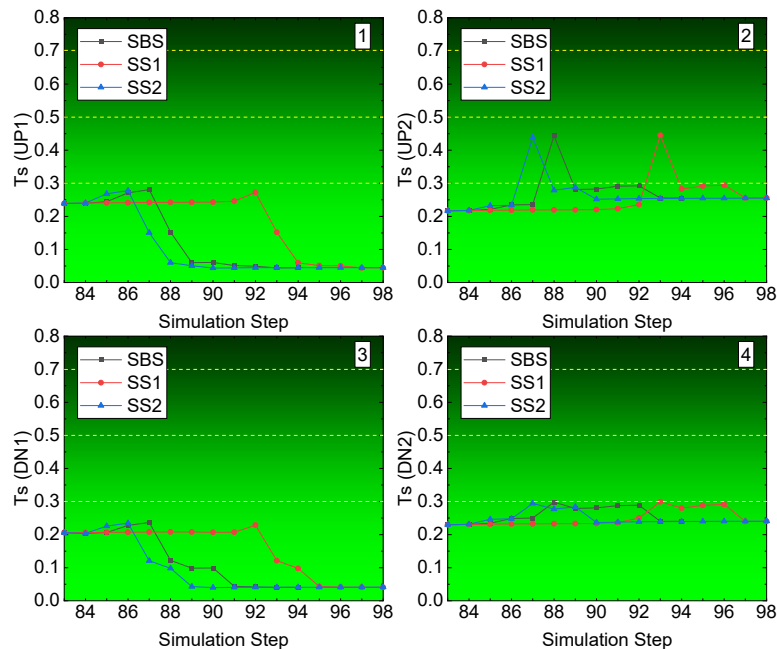


Figure 6.24  $T_s$  of right-edge stope access to undercuts in Sill-2

Going up to Sill-2, figure 6.24 illustrates the  $T_s$  tendency at the four corners of stope access to the undercut in right edge-located stope in Sill-2. With the mining depth decrease, the value of  $T_s$  shows a lower trend. Except the right roof corner UP2, for all the other three corners, there is not rockburst tendency during the process of the excavation and backfilling of right edge-located stope. Both the left roof corner UP1 and left floor corner DN1 present the same trend of  $T_s$ , with a slight increase caused by the excavation of the stope access, it decreases swiftly to 0.05 with the backfilled CRF taking into effect. For the right roof corner UP2, as shown in the second picture, the excavation of the stope access does cause the increase of  $T_s$  to the value of 0.45, indicating the weak tendency of rockburst, while with the completion of backfilling, it decreases to a  $T_s$  value under 0.3 indicating no tendency of rockburst. For the right floor corner DN2, there is almost no changes of  $T_s$  during the process of excavation and backfilling in the right-edge stope among the three recovery schemes.

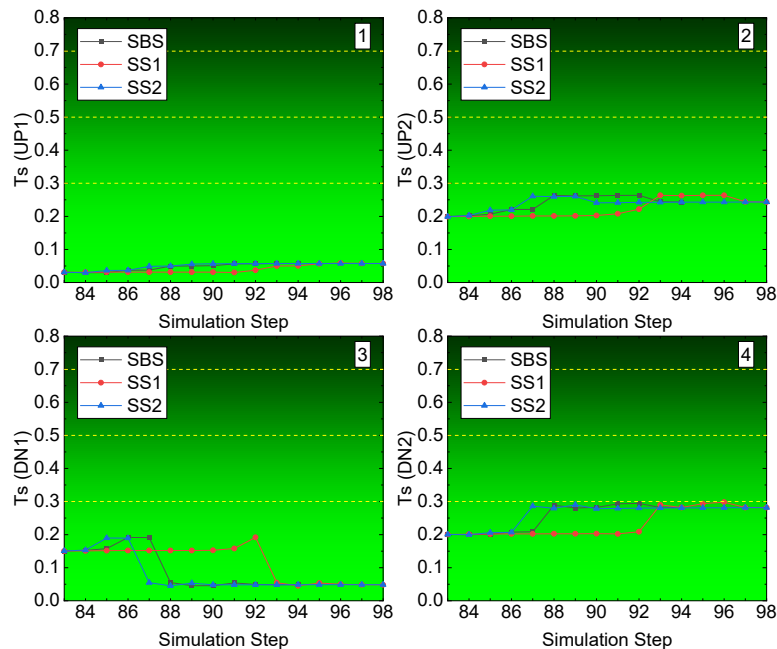


Figure 6.25  $T_s$  of right-edge stope access to overcuts in Sill-2

For the stope access to the overcut in the right-edge stope in Sill-2, figure 6.25 presents the  $T_s$  changes during the process of recovery the Sill-s among three recovery schemes. At the left roof corner UP1, the  $T_s$  keeps stable though experiencing the excavation and backfilling of the stope access to the overcut, and it is under 0.05 indicating no tendency of rockburst. For the right roof corner UP2, the excavation of the stope access causes slight increase of  $T_s$ , the  $T_s$  sees tiny increase from 0.2 to 0.25, still under 0.3. For the left floor corner DN1, similar with that in the undercut, excavation caused increase percentage is much less than the decrease percentage by backfilling, shown in the third picture. For the right floor corner DN2, the excavation causes the increase of  $T_s$  and the backfilling causes no decrease of  $T_s$ , which is different from that in the undercut.

From the above results and analysis, combined with the figure 6.18, which shows the location of the three analyzed stope accesses, the boundary of kimberlite and host rock granite has higher rockburst tendency than the boundary of kimberlite and backfilled CRF. All the right roof corners UP2 and right floor corners DN2 in the four stope accesses to overcuts and undercuts in Sill-1 have weak tendency of rockburst, while for Sill-2, there is no rockburst tendency though the right roof corners UP2 and right floor corners DN2 have higher  $T_s$  value than that of the left side, among the three sill pillar recovery schemes. Through the immediate backfilled CRF will provide support to the unmined stopes, considering the long-serving time of the stope accesses to undercuts and overcuts, more support should be paid at these sections.

#### **6.7.1.2 Energy based burst potential index criterion (BPI)**

In the previous part, the rockburst tendency of the four corners at the stope accesses were assessed based on the criterion of stress. According to Leveille (2015), Sepehri (2016) and Pu (2019), the rockburst occurred at Diavik diamond mine was classified to strainburst. To better conduct the assessment and prediction of the rockburst in underground rock mass, Mitri et al. (1990) proposed

the energy-based burst potential index (BPI). Violent failure (rockburst) will occur when the energy stored in the rock mass exceeds the critical energy value ( $e_c$ ). The  $e_c$  is the maximum capacity of the rock mass to store energy, and it can be obtained from the uniaxial compressive strength (UCS) test or from the UCS hysteresis looping test curve with the following equation:

$$e_c = \sigma_c^2 / 2E \quad (6.1)$$

where  $\sigma_c$  is the UCS and  $E$  is the Young's modulus in the UCS test. It should be noted that estimating  $e_c$  using equation (6.1) is a conservative approach, because the energy dissipated by fracturing and plastic deformations is neglected. Therefore, the BPI can be defined as:

$$BPI = ESR / e_c \times 100\% \quad (6.2)$$

where  $ESR$  is the energy storage rate ( $\text{kJ/m}^3$ ) in the rock mass and  $e_c$  is the critical elastic strain energy density (SED) ( $\text{kJ/m}^3$ ) of the rock. The larger the value of the BPI, the higher the probability of a rockburst occurring. According to Leveille (2015), the average critical energy ( $e_c$ ) value for kimberlite in mining pipe A154N is  $119.7 \text{ kJ/m}^3$ .

Based on the computed ESR from the FE analysis model, the burst potential index (BPI) of the four corners of stope accesses to the undercuts and overcuts in the Sill-1 and Sill-2 during the process of recovery of two sill pillars conducting by the three recovery schemes can be calculated, and following figures present the results. Following figure 6.26, figure 6.27 and figure 6.28 present the BPI of the stope accesses to undercuts at three locations in Sill-1.

At the right-edge stope access, all four corners have low value of BPI, as shown in figure 6.26. For left roof corner UP1, during the whole process of recovery, among the three recovery schemes, the BPIs are less than 10%, though with a slight increase caused by the excavation. For the right roof corner UP2, the BPIs see a swift increase caused by the excavation of the stope access at the specific simulation steps among the three recovery schemes.

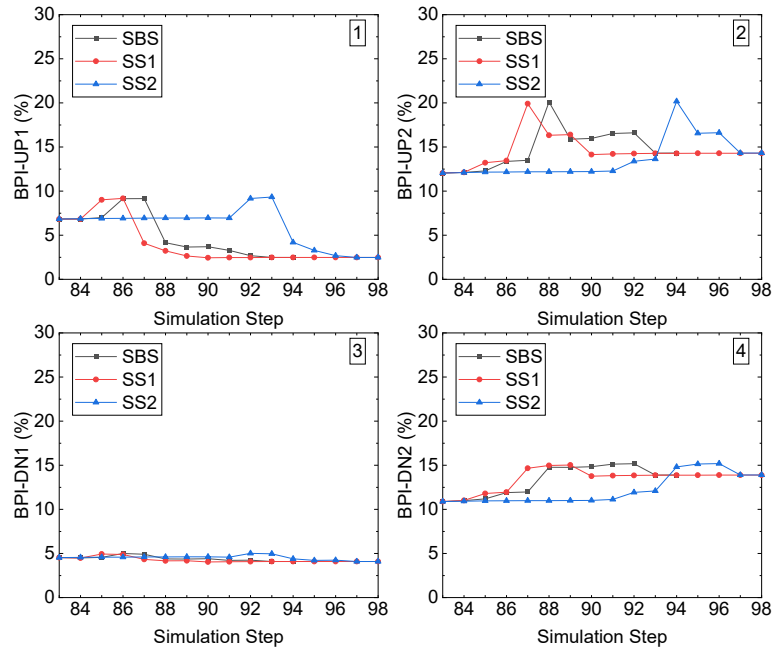


Figure 6.26 BPI of right-edge stoep access to undercut in Sill-1

Before the excavation occurs, the BPIs stay a stable value of 12.5%, due to the excavation, it increases to 20%, after the backfilling, it comes down to initial value of 12.5%, which proves the backfilled CRF can effectively lower the BPI by providing the immediate support. The left floor corner DN1 has the lowest BPI among these four corners in the stoep access, and it is 5% and it keeps stable. For the right floor corner, with an increase of 4.5% from 10.5% to 15%, and all three recovery schemes end at 14%.

For the middle stoep access to undercut in Sill-1, compared with the right-edge one, the BPIs are much smaller, as shown in figure 6.27. For the two roof corners, UP1 and UP2, which have the highest BPI compared to the floor corners, the BPIs are not larger than 5%, and the excavation simulation step causes decrease at both roof corners, as shown in first and second pictures. On the two floor corners, DN1 and DN2, as shown in the third and fourth pictures, the BPIs are even much smaller, both are less than 2%, though with the process of excavation, among the three recovery schemes, for recovery schemes SS2, before the excavation occurs, the BPI keeps stable as 2%.

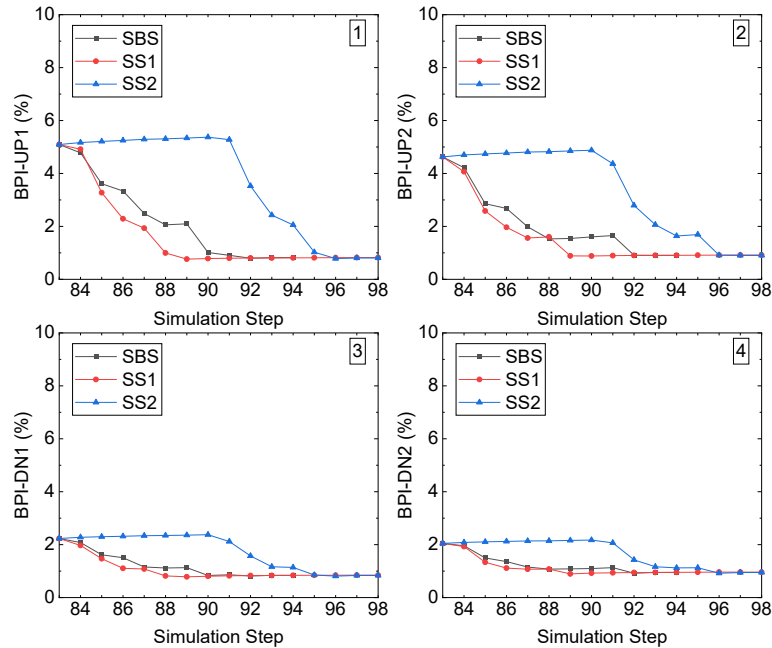


Figure 6.27 BPI of middle stope access to undercut in Sill-1

Following figure 6.28 illustrates the BPI of the four corners in stope access to undercut in the left-edge stope in Sill-1. Similar with the right-edge stope access, the left roof corner UP1 sees an increase, caused by the excavation, and the following decrease, caused by the taking effect backfilled CRF, among the three recovery schemes. All the BPIs of the three recovery schemes are less than 9%, though with the excavation caused increase. The right roof corner, UP2, sees the constant decrease during the excavation and backfilling sill pillar recovery, and it is under 6% the whole process. For the two floor corners, DN1 and DN2, the BPIs are under 3%, for DN2, the BPI is even under 1.5%.

Similar with the results of tangential stress criterion ( $T_s$ ), compared with the stope accesses to the undercuts in left edge-located stope and middle stope in Sill-1, the right-edge stope access has higher value of BPI, due to the contact boundary of kimberlite and granite. Then, in the following part of BPI results, the right-edge stope accesses will be presented for the analysis, considering their higher BPI values.

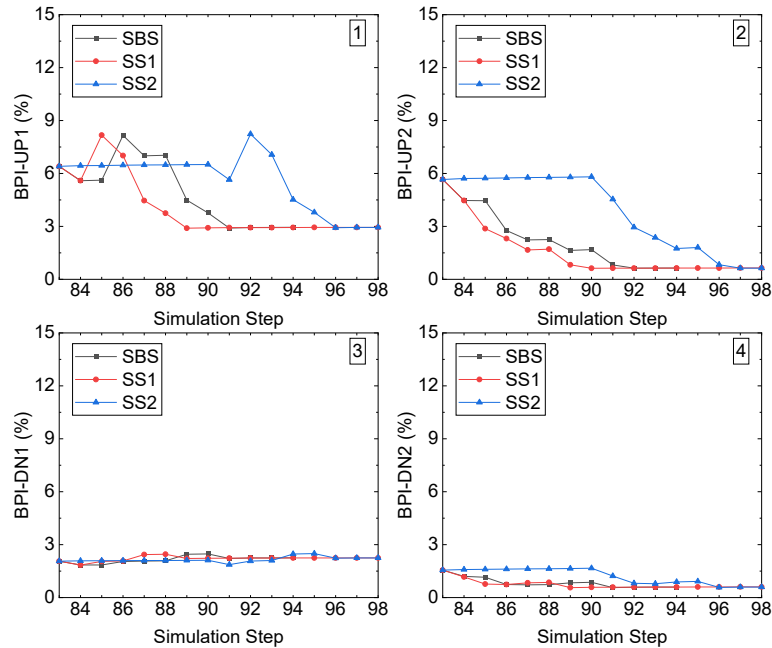


Figure 6.28 BPI of left-edge stope access to undercut in Sill-1

Going up to the stope access to the overcut in the right-edge stope in Sill-1, for the left roof corner, UP1, the BPI is about 2.5%, and it keeps stable at this value during the process of recovery of the sill pillars, as shown in figure 6.29. For the right roof corner, UP2, the BPI sees an increase, caused by the excavation, from 10% to 14%, with the backfilled CRF taking into effect, it decreases down to 12.5%, much larger than that of the left roof corner UP1.

For the left floor corner, DN1, the excavation causes the increase, from 7.5% to 10%, then immediately decreases to a value of 4.5% with the backfilled CRF. The right floor corner DN2 sees the largest increase among these four corners, from 9% to 17% with the influence of excavation among the three recovery schemes, with the backfilled CRF takes into effect, the BPI decreases gradually to a value of 14%, which is higher than the initial 9%.

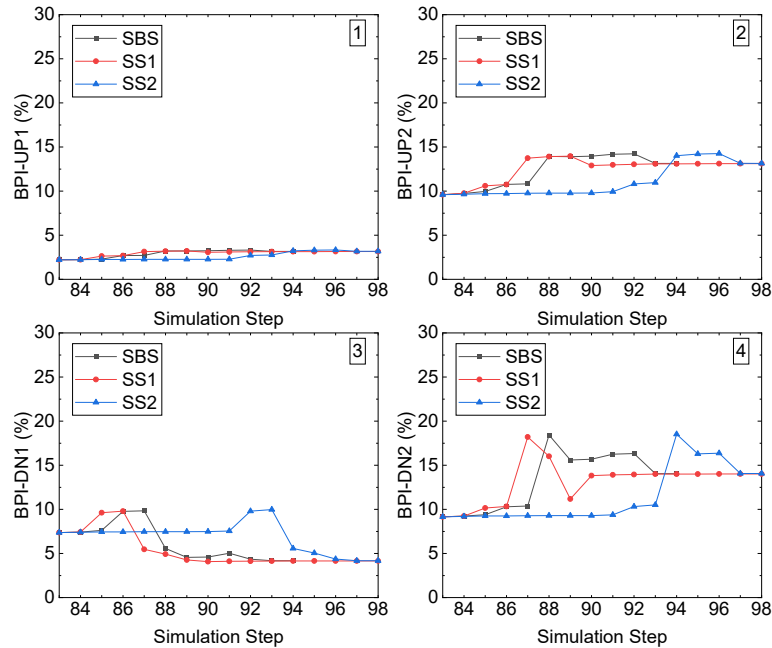


Figure 6.29 BPI of right-edge stope access to undercut in Sill-1

Following figure 6.30 and figure 6.31 present the BPI of the four corners at the stope accesses to the undercut and undercut in Sill-2, respectively. For the left corner UP1 in the stope access to undercut, the BPI is under 6%, though the excavation causes an increase at simulation step S85 for SS2, step S86 for SBS and step S92 for SS1, respectively, the following backfilling step in each recovery scheme contributes the decrease of BPI. The final state of BPI at the left roof corner is under 4%.

The right roof corner UP2 sees a significant increase from 5% to 12% of the BPI, also the following step of backfilling makes the BPI decreases to 8%, and final state of BPI in all three recovery schemes are 6.3%. The left floor corner DN1 sees a tiny increase caused by the excavation, and immediate decrease at the following step, and the final BPI has a value of 2%. Similar with the right roof corner UP, the right floor corner DN2 has a swift increase, from 5% to 10% of the BPI, and the final value of BPI is 5%, which is same with its initial one.

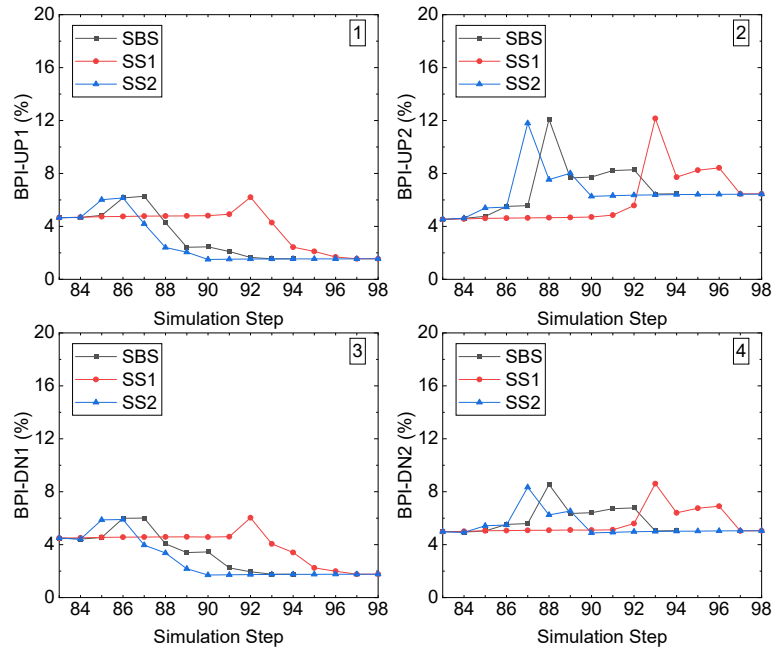


Figure 6.30 BPI of right-edge stope access to undercut in Sill-2

For the BPI of the four corners in the stope access to the undercut in Sill-2, figure 6.31 illustrates the changes during the recovery process of sill pillars. Compared the four corners in the undercut access, the BPI of the four corners in the undercut is much smaller.

For the left roof corner UP1, the BPI almost has no changes, and it is about 2%, though with the process of excavation. The right roof corner sees significant increases from 4.55 to 6.5% caused by the excavation step, with the backfilled CRF taking into effect, the BPI keeps the value of 6.5% among the three recovery schemes.

For the left floor corner DN1, the excavation step of stope access causes the immediate increase, and the following backfilling step contributes the decrease, the final state of BPI is little smaller than the starting state. The right floor corner DN2 sees the maximum increase, from 4% to 9%, and the backfilled CRF makes the BPI some decreases, while the final state of BPI is still higher than the initial value, from initial value of 4% to the final value of 7%.

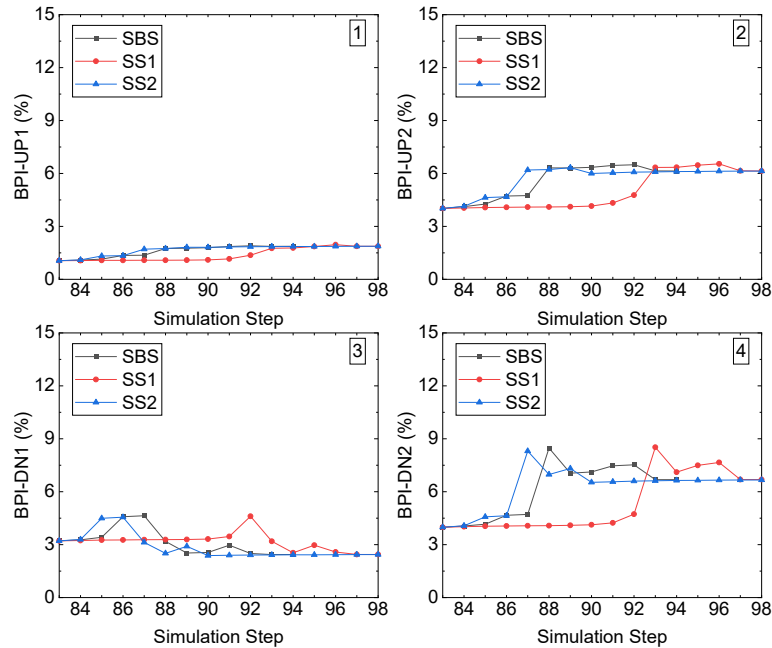


Figure 6.31 BPI of right-edge stope access to undercut in Sill-2

From the above results of BPI of the four corners in the stope accesses to the undercuts and overcuts in the two sill pillars, the right side of the stope access, right roof corner and right floor corner, has higher BPI values. According to Leveille (2015) and Sepehri (2016), when the BPI of the kimberlite is over 20%, the kimberlite rock mass has a weak tendency of rockburst. The above results at the four corners are all less than 20%, though the BPI at right roof corner in the stope access to undercut in the right-edge stope in Sill-1 once reaches 20% caused by the excavation, then the following backfilling step takes it back to a value under 20%. From the analysis, in the view of the BPI, all the corners have very low tendency of rockburst during the process of recovery sill pillars among the three recovery schemes.

## 6.7.2 Assessment of the haulage drift stability among three pillar recovery schemes

### 6.7.2.1 Tangential stress criterion (Ts)

At the Diavik diamond mine, in the mining pipe 154N, different from the stope accesses which was developed in the kimberlite rock mass, the haulage drift accesses were developed in the host

rock mass granite. According to table 2.6 in Chapter 2, the granite has higher strength and elastic mechanics property parameters, such as Young's modulus  $E$  is 24GPa, and uniaxial compressive strength  $\sigma_c$  is 130MPa, both are larger than that of kimberlite. Same with stope access, the haulage drift access will serve the mine production the mine-life long, then the stability of the haulage drift access is vital for the mine.

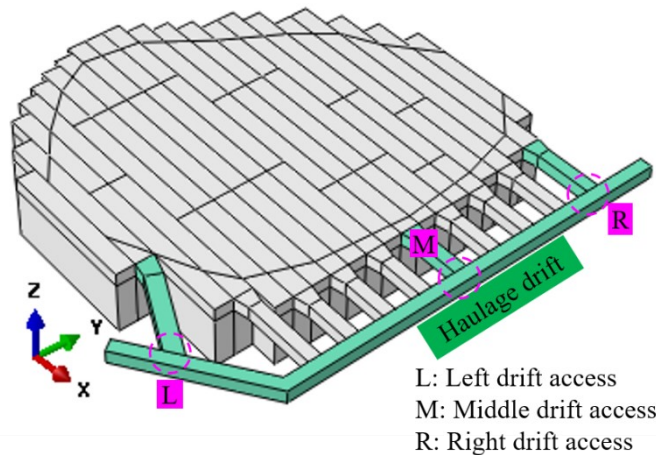


Figure 6.32 Chosen haulage drift access locations in Sill-1

Similar with the scenarios for stope accesses, three haulage drift access locations, which were corresponding to the three stope accesses, were chosen to conduct this study, as shown in figure 6.32. All the haulage drift were excavated in the host rock granite, when applying the tangential stress criterion (Ts), the property parameters of granite were introduced into the equation (5.1) to conduct the assessment of the rockburst tendency in the haulage drift accesses during the process of sill pillars recovery among the three recovery schemes.

Based on the analysis of Ts results of stope accesses in Sill-1, which shows that the rockburst tendency is weak in the stope access to the undercut of the right-edge stope. For the other stope accesses to the left-edge stopes and middle stopes to both undercuts and overcuts in both sill pillars Sill-1 and Sill-2 have no rockburst tendency, then the assessment of the rockburst tendency of the

haulage drift accesses only present the analysis of the haulage drift access to the undercut in the right-edge stope in Sill-1.

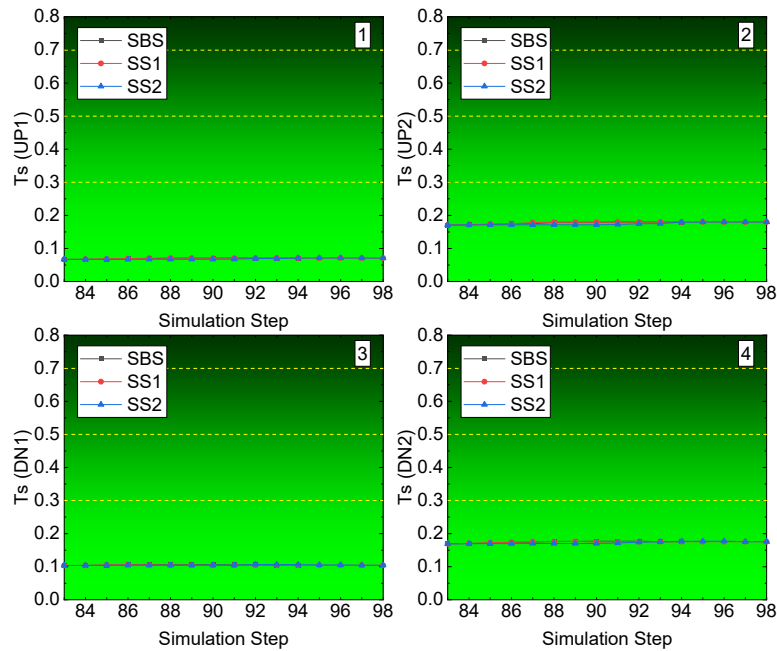


Figure 6.33 Ts of right-edge haulage drift access to undercuts in Sill-1

The rockburst tendency in the haulage drift access to the right-edge stope undercut in Sill-1 is presented in figure 6.33. Due to the high uniaxial compressive strength  $\sigma_c$  and the small section size of the haulage drift access, the Ts values of the four corners in the access are all under 0.2, indicating no rockburst tendency in the haulage drift access at the right-edge haulage.

For the left roof corner UP1, the Ts value is 0.06 from the initial state to the final state, and for the left floor corner DN1, the Ts is 0.1 and it keeps stable as 0.1, during the process of recovery the two sill pillars among the three recovery schemes. For the right side of the haulage drift access, right roof corner UP2 and right floor corner DN2, though both Ts values are larger than that on the left side, the two values of the right side are under 0.2, though with tiny changes during the process of sill pillar recovery.

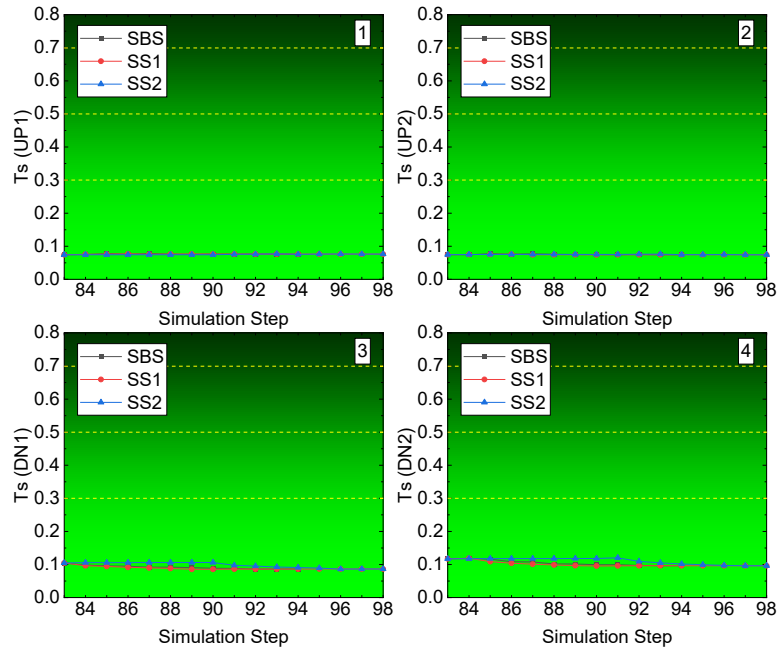


Figure 6.34 Ts of middle haulage drift access to undercuts in Sill-1

The Ts values of the four corners at the haulage drift access to the middle haulage drift are illustrated in figure 6.34. For the left side of the access, the left roof corner UP1 and left floor corner DN1, the Ts values are under 0.1, though at the left floor corner DN1 with tiny changes caused by the excavations. The Ts value of UP1 keeps stable under 0.1. For the right side, the right roof corner UP2 and right floor corner DN2, the values are as small as that of the left side. Right roof corner UP2 shows the same value as left roof corner UP1, and right floor corner DN2 has same changes as the left floor corner DN1. In the haulage drift access to the middle haulage drift, there is no rockburst tendency, same as the right-edge haulage drift access.

About the left-edge haulage drift access, the Ts values keep small. The left roof corner UP1 has a Ts value of 0.15 and keeps it stable during the process of sill pillar recovery. For the right roof corner UP2, the Ts value is smaller than that of left roof corner UP1 at the same simulation step, and it is 0.1. The left floor corner DN1 is almost the same as left roof corner UP1, and it is also 0.15 and keeps it stable from the initial state to the final state. The right floor corner DN2 sees the

minimum  $T_s$  value compared with the other three corners, and it keeps a  $T_s$  value of 0.08 from the beginning to the end of the sill pillar recovery. And there is no rockburst tendency in the left-edge haulage drift access.

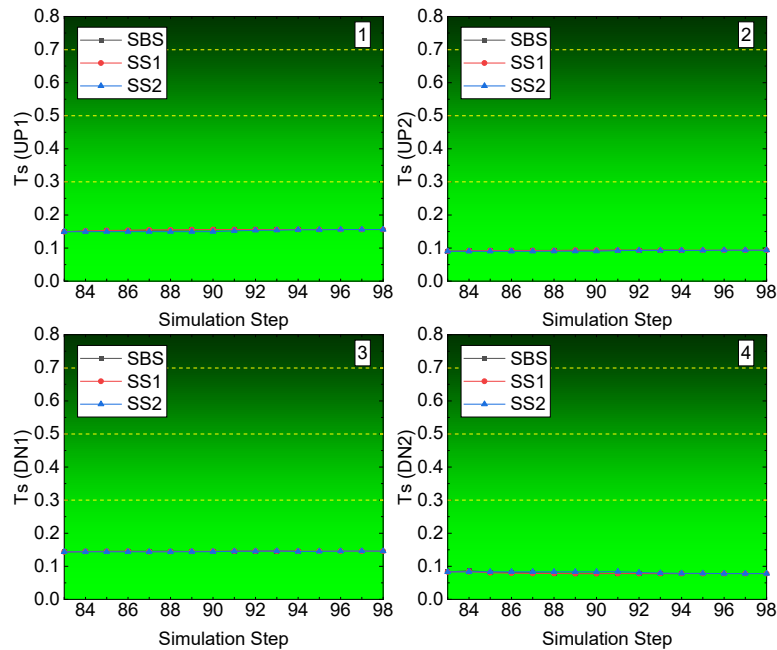


Figure 6.35  $T_s$  of left-edge haulage drift access to undercuts in Sill-1

### 6.7.2.2 Energy based burst potential index criterion (BPI)

Granite has the property to store strain energy in the rock mass. According to Sepehri (2016), the granite has rockburst tendency, especially around the boundary between the kimberlite mining pipes, A154N and 154S, and the host rock granite. By the laboratory tests conducted by Leveille (2015) and equation (6.1), the average critical strain energy value of granite is  $402.38 \text{ kJ/m}^3$ . Following figure 6.36, figure 6.37 and figure 6.38 present the BPI value at the four corners in the haulage drift access in Sill-1.

For the left roof corner UP1, the BPI value is about 1.5% throughout the whole process of the sill pillar recovery among all three recovery schemes, and the three recovery schemes show almost no differences. The left floor corner DN1 also experiences no changes during the process of the

excavation and backfilling of the two sill pillars, and the BPI value keeps constant with a value of 1.5%, same with that of left roof corner UP1.

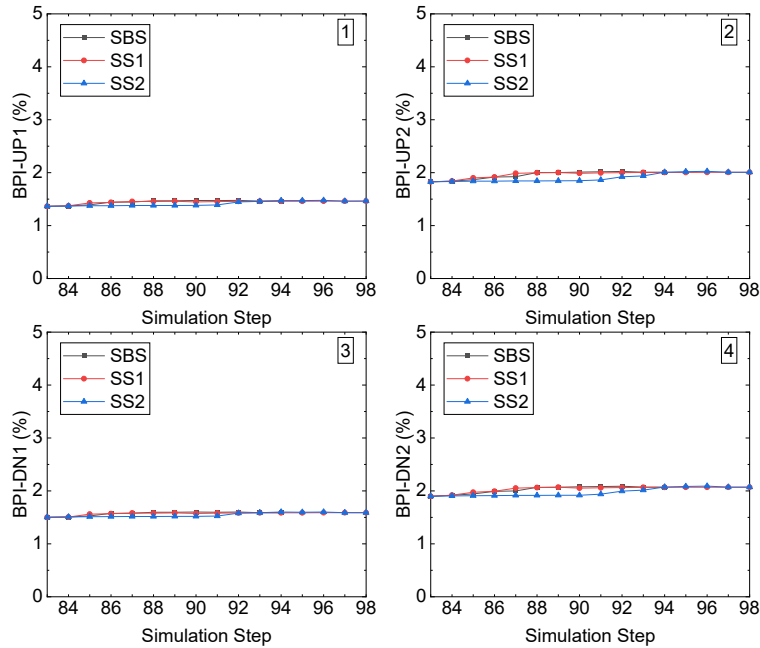


Figure 6.36 BPI of right-edge haulage access in Sill-1

Different with the left side, the right side has higher value of BPI, though the difference is tiny. On the right roof corner UP2, with tiny increase caused by the excavation step, the BPI increases from 1.8% to 2%, and among the three recovery schemes with tiny differences. For the right floor corner DN2, the BPI starts from 1.8% and ends at 2%, the same changes with the right roof corner UP2. With differences during the process of recovery, the three recovery schemes reach the same final state with BPI, as shown in figure 6.36.

The BPI changes trends of the middle haulage drift access during the process of sill pillar recovery is illustrated in figure 6.37. Similar with the trend of Ts, the BPI of the middle haulage drift access is smaller than that of the right-edge haulage drift access. The left roof corner UP1, the BPI has a value of 0.08% from the beginning to the end, among the three recovery schemes. For the other three corners, the left floor corner DN1, right roof corner UP2 and right floor corner DN2, the BPI

presents almost the same changes trend during the process of two sill pillars recovery, and all three corners have a value of BPI of 0.08%, seeing tiny changes during the whole recovery process.

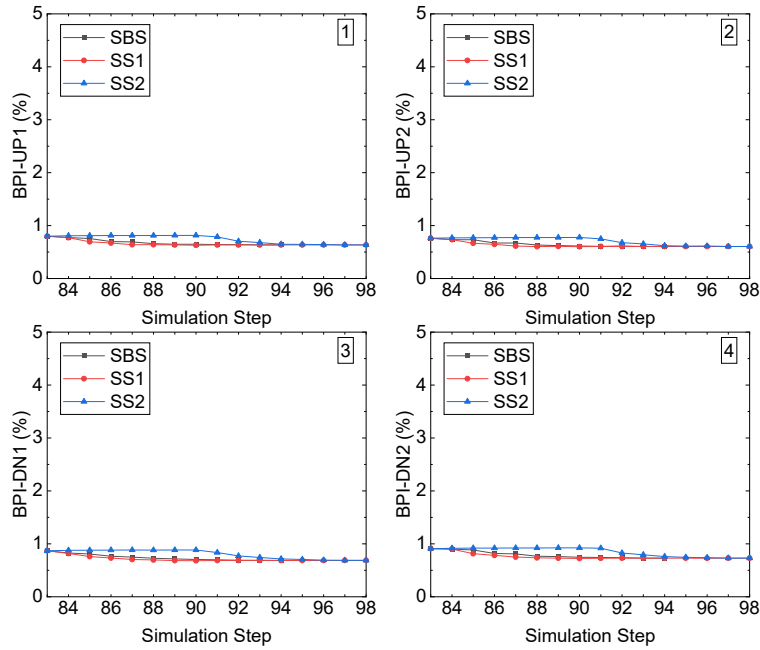


Figure 6.37 BPI of middle haulage access in Sill-1

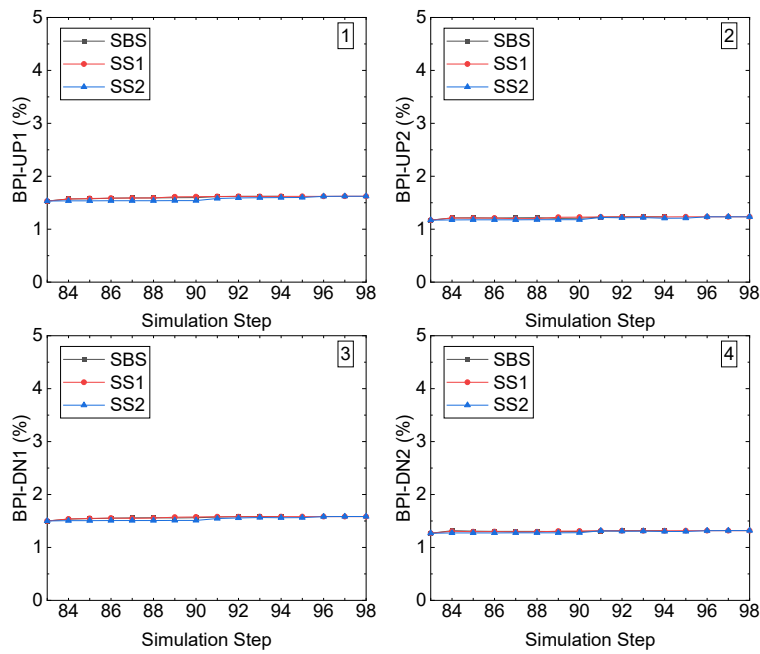


Figure 6.38 BPI of left-edge haulage access in Sill-1

For the left-edge haulage drift access, the BPI values at all four corners are larger than that of the middle haulage drift access, as shown in figure 6.37 and figure 6.38. For the left roof corner UP1, the BPI value starts at 1.5%, with tiny differences among the three recovery schemes, and it ends at 1.5%, though the excavation and backfilling process causes the changes. For the right roof corner UP2, the BPI starts at 1.2%, smaller than that of left roof corner UP1, and ends at 1.3% when the sill pillar recovery process completes. For the left floor corner DN1, the changes of the BPI are almost the same with that of the left roof corner UP1. For the right floor corner DN2, it has the same changes of BPI as the right roof corner UP2, and the value of BPI is about 1.3% from the beginning to the end of the sill pillar recovery process.

From the above assessment of the stability of the haulage drift accesses to the three locations of the haulage drifts in Sill-1 based on the results of tangential stress criterion (Ts) and burst potential index (BPI), the three schemes of sill pillar recovery will not cause rockburst in the haulage drifts in the granite. The distances between the stopes and the haulages, the small haulage drift access section size and the high energy storage ratio may protect the haulage drifts from failures caused by the rockburst.

## **6.8 Chapter summary and conclusions**

In this chapter, the study of the feasibility of recovering the two sill pillars was conducted. To investigate the feasibility of two sill pillars recovery, three sill pillar recovery schemes, SBS, SS1 and SS2, were proposed to conduct the recovery of the two sill pillars, Sill-1 and Sill-2. Based on the developed conclusions, the recovery scheme SBS was the optimum one among the three schemes.

Firstly, to assess the feasibility of the two sill pillars recovery, the developed finite element (FE) analysis model was calibrated and verified. To calibrate and verify the FE model, the comparison

of the initial maximum stress between the theoretically calculated one and the FE model computed geostatic one was conducted, and the results of these two methods were identical. Also, to calibrate and verify the FE model, the monitoring prisms were installed on the in-situ filed open pit benches at Diavik diamond mine. The in-situ filed recorded data of ground displacement was compared with the computed displacement from the FE model, the recorded in-situ displacements of four prisms location and the computed FE model displacement showed small differences, which were acceptable in mining engineering. By the comparison of the initial stress state and the final displacement caused by the mining and backfilling in the mining pipe A154N from both in-situ recorded and FE model, the developed FE model in this thesis was rational and credible.

After the calibration and verification of the developed FE model, the three sill pillar recovery schemes were proposed to conduct the assessment of the feasibility of two sill pillars recovery. The displacement of the installed prisms caused by the process of the sill pillar recovery was presented and compared among the three recovery schemes, and the three recovery schemes showed no big difference from the final displacement values. Considering the A154 pit was surrounded and protected by the A154 dike, then the displacement of the upper benches above the 154N mining pipe were chosen to investigate the possible failure caused by the recovery of the sill pillars. According to the results of the displacement of the four upper bench levels, the three sill pillar recovery schemes had an extremely low possibility to cause failures of the four upper bench levels and the A154 dike.

By completing the assessment of the stability of the upper bench levels and A154 dike above the A154N mining pipe, the assessment work went down to the stability of the stope accesses and haulage drifts to the underground two sill pillars in mining pipe A154N. Stope accesses and haulage drifts are mine-life long serving structures, then the stabilities of these structures are vital

for the production at Diavik diamond mine. Due to the rockburst proneness of the kimberlite and granite, the tangential stress criterion (Ts) and energy based burst potential index (BPI) criterion were applied to assess the stability of the stope accesses and haulage drifts during the two sill pillars recovery by the three recovery schemes. According to the results of Ts criterion, in Sill-1, the stope accesses to the right-edge stope had weak rockburst tendency, compared with the left-edge and middle stope accesses, which had no tendency of rockburst during the process of sill pillar recovery. No rockburst tendency showed at the stope accesses at all three analyzed locations in Sill-2. Similar with the scenarios of Ts criterion, the results of BPI showed that, only the right-edge stope access in Sill-1 has possible rockburst tendency at the right roof corner and the right floor corner. And no rockburst tendency at the stope accesses showed in Sill-2.

For the assessment of the stability of the haulage drift accesses in granite rock mass, due to the small section size of haulage drift access, which is  $5\text{m} \times 5\text{m}$  (height $\times$ width), and the high energy storage ratio of granite, the disturb caused by the excavation of the access will not cause rockburst in the haulage drift access in granite. For all three sill pillar recovery schemes, there will be not rockburst caused by the sill pillar recovery process.

Considering the displacement of the monitoring prisms and the upper bench levels above A154N pipe, the stability of the stope accesses and haulage drift accesses in the two sill pillars, Sill-1 and Sill-2, all the three sill pillar recovery schemes are feasible and rational, and scheme SBS, starting the sill pillar recovery process from both sill pillars, is the optimum one among the three schemes, in the view of the technical aspects.

## **CHAPTER 7: SUMMARY, CONCLUSION AND RECOMMENDATIONS**

*This chapter presents the summary and conclusions of this thesis. The contributions and significance of this thesis study are presented. In addition, this chapter also recommends the future work in the assessment of the stabilities of underground mining structures.*

### 7.1 Summary of the research

For underground mining, the excavation activities in the mining pipe areas will disturb the initial pre-mining stress state and cause the in-situ stresses to redistribute according to the scale and duration time of the excavation. Usually, the failures or even disasters at the stopes, haulages and other structures are caused by the over-stress effect on the structures. Knowing the changes of the redistributed stress field at each mining step and period is vital for the safety of mining. The assessment of the stabilities of the underground structures based on the measured in-situ data and the developed finite element analysis model can provide the reference to plan the mining activities for next step. By applying the numerical analysis method, the engineer can better understand what is going on in the “real world” of the underground mining zones and conduct the “rehearsal” of the planned mining activities and predict the possible failures at the specific locations at the specific mining activities steps, then provide the corresponding method and strategies to solve or eliminate the potential problems.

By the literature review of the stress redistribution caused by excavation and underground stability design, the major shortcomings revealed by the literature review include: i) in mining practice, it is difficult and costly to estimate and measure the direction and magnitude of the pre-excavation stress state at the key locations; ii) a predictive assessment and design method and tool to properly conduct the “rehearsal” simulation of the whole mining activities in the mine domain throughout the mine life is needed.

This research conduct the i): Investigation of excavation part length effect on the stope stability and Investigation of the backfilling part length effect on the stope stability, ii): Optimum location of the last mined stope with the influence of backfilling and Optimum location of the last mined stope in the process of sill pillar recovery, iii): Assessment of the stability of the stope accesses

and haulage drift accesses during the process of excavation and backfilling, iv): Assessment of the feasibility of recovering the two sill pillars, Sill-1 and Sill-2, by three proposed sill pillar recovery schemes by applying the numerical analysis method by a case study mine Diavik diamond mine.

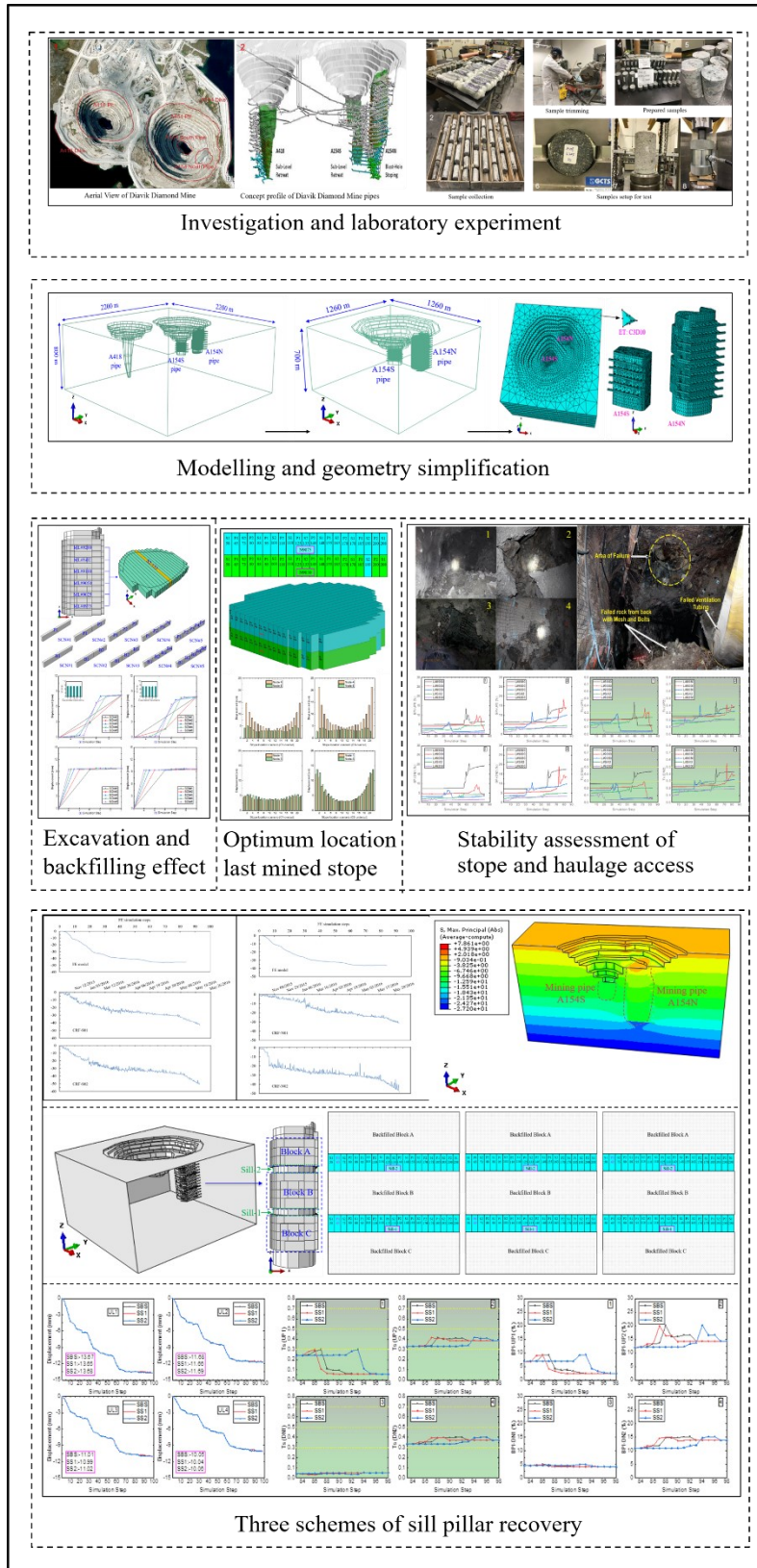


Figure 7.1 Visual summary of the research methods

## 7.2 Conclusions of this research

Throughout this research, an integrated methodology has been developed using the laboratory tests and finite element methods to assess the stope stabilities and optimize the mining sequence. Laboratory tests were conducted to achieve the rock mechanics properties of the research topic rock mass in the mine domain. The finite element (FE) model was developed to conduct the assessment and prediction of the possible failures during the mining activities in the mining pipe. Some conclusions are drawn from this research, and the conclusions will be exhibited in the specific chapter here.

Chapter 1 presents the overview and introduction of this research thesis. Firstly, it provides the general background of this study. Then, it presents a comprehensive literature review based on the stated problems and objectives. The problems studied in this research are stated. Finally, the methodology to study the stated problems are proposed.

Chapter 2 presents the basic background of the case study Diavik Daimond Mine. The mining methods, blasthole stoping (BHS), used at Diavik diamond mine was introduced. A basic introduction of the numerical finite element method applied in this study was presented. To conduct the numerical analysis study, the laboratory rock mechanics tests, Brazilian test, uniaxial compressive strength (UCS) test, triaxial test, were conducted to achieve the parameters of the rock samples, such as the Young's modulus  $E$ , Poisson's ratio  $\nu$ , internal friction angle  $\phi$ , uniaxial compressive strength  $\sigma_c$ , etc. for the input parameters for the developed FE model. To make the numerical model more productive, the simplification and modification of the geometry and mining activities of the finite element model was conduct. Also, a study of mesh density convergence on the accuracy of the FE model and the consumed CPU time for running the simulation steps was

conducted. Finally, the numerical simulation steps based on the real mining activities in the finite element model was proposed.

Chapter 3 presents the study of the effect of both excavation part length effect on the and backfilling part length effect on the stope stability. Firstly, the investigation of the excavation part length effect on the stope stability was conducted. The stopes S2-133 of six mining levels were analyzed by the proposed five excavation scenarios with different part length at each excavation step in the simulation process. By comparing the excavation-induced displacement, redistributed major principal stress, excavation-induced damage initiation (DI), the excavation scenario SCN#1 achieved almost the same results of the three analyzing indicators as the other four excavation scenarios. Excavation scenarios SCN#1 was a rational and reliable alternative excavation scenario to conduct the prediction of the possible failures caused by the underground mining activities, especially for the prediction of the ground displacement of the whole mine site with a full mine size finite element model. As a continuing study, the backfilling part length effect on the stope stability was conducted. Similar with the excavation scenarios study, five backfilling scenarios with different backfilling part length were proposed. The comparison of, sidewall displacement, redistributed major principal stress and stress concentration factor (SCF) among the five backfilling scenarios was conducted. In the aspects of eliminating the sidewalls displacement, reducing the major principal stress on the sidewalls and the stress concentration factor (SCF) on the sidewalls, the backfilling scenario SCN#1 achieved almost the same results as the other four backfilling scenarios. Scenario SCN#1 provided the immediate support to the adjacent unmined stopes and improved the stability of the adjacent unmined stopes. These two investigations pave the foundation of the study in the following chapters, Chapter 4, Chapter 5 and Chapter 6.

Chapter 4 presents the study of the optimum location of the last-mined stopes in each mining level during the normal mining production with the influence of backfilled CRF, and the optimum location of the last-mined stope in the process of the sill pillar recovery with the influence of backfilled CRF. Firstly, the study of optimum location of the last mined stope in the normal mining production was conducted. Based on the conclusions of Chapter 3 and the geometry of the mining pipe A154N, the mining level N9050 was analyzed for this research topic. There were 21 stopes in mining level N9050, and 21 locations of the last mined stope were proposed. The stress field around the mining level N9050 was extracted from the three-dimensional (3D) developed finite element (FE) model and applied to the simplified two-dimensional (2D) finite element (FE) analysis model through a global-to-local method to make a fast assessment. The results proved that, in the normal mining activities, the last mined stopes should be located close to the center of the mining level. For the optimum location for the last mined stope in the process of the sill pillar, the basic method followed the previous one. The results showed that the last mined stope during the sill pillar recovery should be located at least four-stope width from the two edges of the mining level in the mining pipe A154N.

Chapter 5 presents the study of the assessment of the stability of the stope accesses and haulage drifts accesses during the process of excavation and backfilling of the three mining blocks, block-A, block-B and block-C. The investigation of the rockburst potential tendency was conducted by applying the tangential stress criterion ( $T_s$ ), energy-based burst potential index (BPI). Four corners are chosen in both stope access and haulage access at each analyzed mining level in the mining pipe A154N. In the haulage accesses at different mining levels, due to the high critical strain energy density, no rockburst tendency was shown in all five analyzed mining levels, including the deepest level L#8950, with a mining depth of -473m, at the bottom of the mining pipe A154N. For the

stope accesses, the rockburst tendency is higher than the haulage access, especially in the mining level L#8950, the high density of stored strain energy in this level will cause failures when the adjacent stopes are mined out. For other mining levels, the immediate backfilled CRF will eliminate the tendency of rockburst to no tendency level. The stope access and haulage access to the middle-located stopes and haulages present lower value of BPI and Ts, compared with the stope access and haulage access to the two edge-located stopes and haulages, indicating middle stopes are safer than the stopes close to the edges of the mining level. In each mining level, the stopes close to the right edge should be paid more support since the higher values of BPI and Ts are shown in this edge side, and the last mined stope should not be located close to the two edges, especially the right edge.

Chapter 6 presents the assessment of the recovery feasibility of the two sill pillars by the three proposed recovery schemes, SBS, SS1 and SS2. Firstly, before the recovery of the two sill pillars, the verification and validation of the developed finite element (FE) model by comparing the FE model computed results to the actual field data and site observations were conducted, and the developed FE model was rational and reliable for this research thesis. Then this chapter presents the comparative study of the three different proposed recovery schemes of the two reserved sill pillars. By comparing the sill-pillar-recovery-induced displacement of the upper bench levels up to the surrounding A154 dike and monitored prisms on the open pit benches, the three sill pillar recovery schemes caused not much displacement at the chosen locations of the upper bench levels and the monitoring prisms, which proved that it was feasible to recover the two sill pillars by the proposed recovery schemes. Then, the assessment of the stability of stope accesses and haulage drift accesses to the overcuts and undercuts in Sill-1 and Sill-2 was conducted. By applying the tangential stress criterion (Ts) and the energy based burst potential index (BPI) criterion, only the

right-edge stope access showed weak rockburst tendency among the chosen stope locations, other stope accesses and haulage drift accesses had no rockburst tendency. Compared with the other two recovery schemes, the scheme SBS, starting the sill pillar recovery from both sill pillars, shown in figure 6.10, was optimum among these three recovery schemes, in the view of technical aspect.

From this research thesis, some main contributions to both scientific and industrial aspects can be listed as following:

- i): Find that for a volcanic-eruption-developing kimberlite mining pipe with boundaries with the other type of rock mass (e.g. granite), the mining pipe boundary has higher possibility of instability compare with the center of the mining pipe.
- ii): Prove that in full size numerical modelling analysis of underground mining engineering, the excavation and backfilling schedules can be made some combination to make the numerical analysis more productive, especially for the prediction of the ground surface settlement caused by the process of excavation and backfilling.
- iii): Prove that some type of cemented rockfill (CRF) can be used as the backfilled material at different mining levels in underground cut-and-fill mining engineering.
- iv): Create a database for the in-situ engineers to better understand the changes of mining-induced displacement, field of mining-induced redistributed stresses and stress-strain for each mining structure such as stope, haulage, crosscut and access, and to predict the possible failure during the whole mining process.
- v): Provide the reference to the mine by conducting the feasibility assessment of sill pillar recovery in the scenario containing open-pit-to-underground mining and protective dike with blasthole stoping (BHS) mining method.

Among these four main contributions from this research thesis, the first three contributions are for the scientific aspects and the other two are the industrial contributions.

### **7.3 Recommendations for future work**

In this research thesis, the developed FE model and the proposed methods provided the engineering methodology to assess the stope stability and the stope mining sequence considering the mining-induced stress regimes. However, based on the case study engineering background, some more continued studies can be done in usage of this methodology in a mine environment.

- i). The disturbs of the blast in cross cuts, caused by the blasthole stoping mining method, on the in-situ fractures initiation and development of the kimberlite rock mass and the backfilled cemented rockfill (CRF).
- ii). The properties of kimberlite and open pit slope stability considering the weaken strength of the rock mass in the open pit benches after several cycles of freezing and thawing at Diavik diamond mine.
- iii). Curing time effect of the backfilled CRF on the stability of the adjacent unmined stopes during the mining and backfilling sequences.

These continued studies can make the finite element analysis model more accurate to make predictions on the mining-induced ground displacement and assessment of the underground stope stabilities during the whole mining and backfilling process.

## BIBLIOGRAPHY

- ABAQUS/Standard User's Manual (2015), Dassault Systemes Simulia Corp.
- Abdellah, W. R. E. (2015a). Numerical modelling stability analyses of haulage drift in deep underground mines. *JES. Journal of Engineering Sciences*, 43(1), pp.71-81.
- Abdellah, W. R. E. (2015b). Parametric stability analysis of room and pillar method in deep coal mines. *JES. Journal of Engineering Sciences*, 43(2), pp.253-262.
- Abdellah, W., Mitri, H. S., & Thibodeau, D. (2011). Assessment of mine haulage drift safety using Probabilistic Methods of Analysis. *Procedia Engineering*, 26, pp.2099-2111.
- Abdellah, W., Mitri, H. S., Thibodeau, D., & Moreau-Verlaan, L. (2013). Stability of mine development intersections—a probabilistic analysis approach. *Canadian Geotechnical Journal*, 51(2), pp.184-195.
- AC10520925, A. (Ed.). (2008). Standard test method for splitting tensile strength of intact rock core specimens. ASTM International.
- Adeeb S., (2018). Introduction to Finite Element Analysis, Course notes, University of Alberta.
- Amoah-Kyei, A., Amoako, R., & Dumakor-Dupey, N. K (2018). Fragmentation Analysis of Backfill Material for Paboase Modified Sublevel Caving (MSLC). 5<sup>th</sup> UMaT Biennial International Mining and Mineral Conference.
- Apel, D., Sepehri, M. (2017). Geomechanical mine design at underground diamond mines. SOMP Conference-Society of Mining Professors. Torino, Italy.
- Arjang, B., & Herget, G. (1997). In situ ground stresses in the Canadian hardrock mines: an update. *International Journal of Rock Mechanics and Mining Sciences*, 34(3-4), pp.652.
- ASTM Committee D-18 on Soil and Rock. (2008). Standard practices for preparing rock core as cylindrical test specimens and verifying conformance to dimensional and shape tolerances. ASTM International.
- ASTM Committee D-18 on Soil and Rock. (2010). Standard Test Method for Compressive Strength and Elastic Moduli of Intact Rock Core Specimens Under Varying States of Stress and Temperatures. ASTM International.

ASTM D4623-08, (2008). Standard Test Method for Determination of In Situ Stress in Rock Mass by Overcoring Method—USBM Borehole Deformation Gauge.

Aydan, ö. (2014). Methods of In-situ Stress Measurements and its Applications to Turkey. *Yer mühendisliği*, No. 2, 46-51.

Aydan, ö. and Kawamoto, T. (1997) The general characteristics of the stress state in the various parts of the earth's crust. In Sugawara, K., and Obara, Y. (Eds.). *Rock Stress, Proc. Int. Symp.*, Kumamoto, Balkema: Rotterdam, 369–73.

Bai, X., Marcotte, D., & Simon, R. (2013). Underground stope optimization with network flow method. *Computers & geosciences*, 52, pp.361-371.

Barla, G. (2001). Tunnelling under squeezing rock conditions. *Eurosummer-school in tunnel mechanics*, Innsbruck, pp.169-268.

Barla, G., Bonini, M., & Debernardi, D. (2010). Time dependent deformations in squeezing tunnels. *ISSMGE International Journal of Geoenineering Case Histories*, 2(1), pp.40-65.

Barla, G., Debernardi, D., & Sterpi, D. (2012). Time-dependent modeling of tunnels in squeezing conditions. *International Journal of Geomechanics*, 12(6), pp.697-710.

Basarir, H., Sun, Y., & Li, G. (2019). Gateway stability analysis by global-local modeling approach. *International Journal of Rock Mechanics and Mining Sciences*, 113, pp.31-40.

Beck, D. A., Kassbohm, S., & Putzar, G. (2010, April). Multi-scale simulation of ground support designs for extreme tunnel closure. In *Proceedings of the Second International Symposium on Block and Sublevel Caving* (pp. 441-453). Australian Centre for Geomechanics.

Beruar, O., Forsythe, A. S., & Yao, M. (2011, January). Sill Pillar Mining In the Main Orebody at Vale's Coleman Mine. In *45th US Rock Mechanics/Geomechanics Symposium*. American Rock Mechanics Association.

Bieniawski, Z. (1988). The rock mass rating (RMR) system (geomechanics classification) in engineering practice. In *Rock Classification Systems for Engineering Purposes*. ASTM International.

- Bieniawski, Z. T., & Hawkes, I. (1979). Suggested methods for determining tensile strength of rock materials. *International Journal of Rock Mechanics and Mining Sciences & Geomechanics Abstracts*, 16(2), pp.138-140.
- Blake, W., & Hedley, D. G. (2003). *Rockbursts: case studies from North American hard-rock mines*. SME.
- Bobet, A., Fakhimi, A., Johnson, S., Morris, J., Tonon, F., & Yeung, M. R. (2009). Numerical models in discontinuous media: review of advances for rock mechanics applications. *Journal of geotechnical and geoenvironmental engineering*, 135(11), pp.1547-1561.
- Brady, B., and Brown, E. (2004) *Rock mechanics for underground mining*, Kluwer Academic Publishers, pp.628.
- Brechtel, C. E., Struble, G. R., & Guenther, B. (1999, January). The evaluation of cemented rockfill spans at the Murray mine. In *Vail Rocks 1999, The 37th US Symposium on Rock Mechanics (USRMS)*. American Rock Mechanics Association.
- Cai, M. (2008). Influence of stress path on tunnel excavation response—numerical tool selection and modeling strategy. *Tunnelling and Underground Space Technology*, 23(6), pp.618-628.
- Cai, M. (2011). Rock mass characterization and rock property variability considerations for tunnel and cavern design. *Rock mechanics and Rock Engineering*, 44(4), pp.379-399.
- Cai, M. (2013). Principles of rock support in burst-prone ground. *Tunnelling and Underground Space Technology*, 36, 46-56.
- Cai, M., Kaiser, P. K., & Martin, C. D. (1998). A tensile model for the interpretation of microseismic events near underground openings. In *Seismicity Caused by Mines, Fluid Injections, Reservoirs, and Oil Extraction*. pp.67-92. Birkhäuser, Basel.
- Castro, L. A. M., Bewick, R. P., & Carter, T. G. (2012). An overview of numerical modelling applied to deep mining. *Innovative numerical modelling in geomechanics*, pp.393-414.
- Castro, L. A., Grabinsky, M. W., & McCreath, D. R. (1997). Damage initiation through extension fracturing in a moderately jointed brittle rock mass. *International Journal of Rock Mechanics and Mining Sciences*, 34(3-4), 110-e1.

Cepuritis, P. M., Villaescusa, E., Beck, D. A., & Varden, R. (2010). Back analysis of over-break in a longhole open stope operation using non-linear elasto-plastic numerical modelling. In 44th US Rock Mechanics Symposium and 5th US-Canada Rock Mechanics Symposium. American Rock Mechanics Association.

Chen, D. W., Chen, J. Y., & Zavokni, Z. M. (1983). Stability analysis of sublevel open stopes at great depth. In The 24th US Symposium on Rock Mechanics (USRMS). American Rock Mechanics Association.

Cook R.D, Malkus D.S, Plesha M.E, Witt R.J, (2001). Concepts and applications of finite element analysis. Fourth Edition, John Wiley and Sons Inc.

Cordova, M., Saw, H., & Villaescusa, E. (2016). Laboratory testing of cemented rock fill for open stope support. In Proceedings of the Seventh International Conference & Exhibition on Mass Mining (pp. 755-762).

Coulomb, C.A, (1773), Application of the rules of maxima and minima to some problems of statics related to architecture, Acad. Roy. Sci. Mem. Math. Phys., Vol. 7, pp.343-382.

Darling, P. (Ed.). (2011). SME mining engineering handbook (Vol. 1). SME.

Dassault Systèmes Simulia Corp., "Analysis User's Manual Volume 1: Introduction, Spatial modeling, execution and output," Abaqus 6.12, vol. I, 2012.

Diavik Dialogue, (2011), Diavik Diamond Mine Inc., Volume 14, 4th quarter, pp:1-8.

Diavik Diamond Mine (2012). Fact Book, RioTinto.

Diederichs, M. S., & Kaiser, P. K. (1999). Tensile strength and abutment relaxation as failure control mechanisms in underground excavations. International Journal of Rock Mechanics and Mining Sciences, 36(1), pp.69-96.

Doerner, C. A. C. (2005). Effect of Delayed Backfill on Open Stope Mining Methods. Master of science, THE UNIVERSITY OF BRITISH COLUMBIA, Canada.

Eberhardt, E. (2001). Numerical modelling of three-dimension stress rotation ahead of an advancing tunnel face. International Journal of Rock Mechanics and Mining Sciences, 38(4), pp.499-518.

Emad, M. Z., Mitri, H. S., & Henning, J. G. (2012). Effect of blast vibrations on the stability of cemented rockfill. *International Journal of Mining, Reclamation and Environment*, 26(3), pp.233-243.

Emad, M. Z., Mitri, H., & Kelly, C. (2014). Effect of blast-induced vibrations on fill failure in vertical block mining with delayed backfill. *Canadian Geotechnical Journal*, 51(9), pp.975-983.

Emad, M. Z., Mitri, H., & Kelly, C. (2015). State-of-the-art review of backfill practices for sublevel stoping system. *International Journal of Mining, Reclamation and Environment*, 29(6), pp.544-556.

Emad, M. Z., Mitri, H., & Kelly, C. (2017). In-situ blast vibration monitoring in cemented rockfill stope—a case study. *International Journal of Mining, Reclamation and Environment*, 31(2), pp. 119-136.

Fahey, M., Helinski, M., & Fourie, A. (2009). Some aspects of the mechanics of arching in backfilled stopes. *Canadian Geotechnical Journal*, 46(11), pp.1322-1336.

Feng, X. T., & Hudson, J. A. (2010). Specifying the information required for rock mechanics modelling and rock engineering design. *International Journal of Rock Mechanics and Mining Sciences*, 47(2), pp.179-194.

Funatsu, T., Hoshino, T., Sawae, H., & Shimizu, N. (2008). Numerical analysis to better understand the mechanism of the effects of ground supports and reinforcements on the stability of tunnels using the distinct element method. *Tunnelling and Underground Space Technology*, 23(5), pp.561-573.

Ghaboussi, J., & Gioda, G. (1977). On the time-dependent effects in advancing tunnels. *International Journal for Numerical and Analytical Methods in Geomechanics*, 1(3), pp. 249-269.

Ghasemi, E., Ataei, M., Shahriar, K., Sereshki, F., Jalali, S. E., & Ramazanzadeh, A. (2012). Assessment of roof fall risk during retreat mining in room and pillar coal mines. *International Journal of Rock Mechanics and Mining Sciences*, 54, pp.80-89.

Ghasemi, E., Ataei, M., Shahriar, K., Sereshki, F., Jalali, S. E., & Ramazanzadeh, A. (2012). Assessment of roof fall risk during retreat mining in room and pillar coal mines. *International Journal of Rock Mechanics and Mining Sciences*, 54, pp.80-89.

- Ghasemi, E., Shahriar, K., & Sharifzadeh, M. (2010). A new method for risk assessment of pillar recovery operation. *Safety science*, 48(10), pp.1304-1312.
- Gibson, R. E. (1958). The progress of consolidation in a clay layer increasing in thickness with time. *Geotechnique*, 8(4), pp.171-182.
- Gioda, G., & Cividini, A. (1996). Numerical methods for the analysis of tunnel performance in squeezing rocks. *Rock mechanics and rock engineering*, 29(4), pp.171-193.
- Golshani, A., Oda, M., Okui, Y., Takemura, T., & Munkhtogoo, E. (2007). Numerical simulation of the excavation damaged zone around an opening in brittle rock. *International Journal of Rock Mechanics and Mining Sciences*, 44(6), pp.835-845.
- Goodman R. (1989). *Introduction to rock mechanics*, 2nd ed. John Wiley & sons, New York.
- Grabinsky, M. W. (2010, May). In situ monitoring for ground truthing paste backfill designs. In *Proceedings of the Thirteenth International Seminar on Paste and Thickened Tailings* (pp. 85-98). Australian Centre for Geomechanics.
- Grice, A. G. (1989). Fill research at Mount Isa mines limited. *Innovations in Mining Backfill Technology*, pp.15-22.
- Hart, R. (2003). Enhancing rock stress understanding through numerical analysis. *International journal of rock mechanics and mining sciences*, 40(7-8), pp.1089-1097.
- Hassani, F.; Archibald, J. (1998). *Mine backfill*. Canadian Institute of Mining, Metallurgy, and Petroleum.
- Hedley, D. G. (1992). *Rockburst handbook for Ontario hardrock mines* (Vol. 92, No. 1). Canmet.
- Heidarzadeh, S., Saeidi, A., & Rouleau, A. (2018). Assessing the effect of open stope geometry on rock mass brittle damage using a response surface methodology. *International Journal of Rock Mechanics and Mining Sciences*, 106, pp.60-73.
- Helinski, M., Fahey, M., & Fourie, A. (2007). Numerical modeling of cemented mine backfill deposition. *Journal of Geotechnical and Geoenvironmental engineering*, 133(10), pp.1308-1319.
- Helinski, M., Fahey, M., & Fourie, A. (2011). Behavior of cemented paste backfill in two mine stopes: measurements and modeling. *Journal of geotechnical and geoenvironmental engineering*, 137(2), pp.171-182.

- Henning, J., & Mitri, H. (2010). Production blast-induced vibrations in longhole open stoping: a case study. *International Journal of Geotechnical Earthquake Engineering (IJGEE)*, 1(2), pp.1-11.
- Hoek E. (1994). Strength of rock and rock masses. *ISRM News Journal*, 2(2), pp.4–16.
- Hoek, E., & Brown, E. T. (1997). Practical estimates of rock mass strength. *International journal of rock mechanics and mining sciences*, 34(8), pp.1165-1186.
- Hoek, E., Brown, E.T, (1980). Empirical strength criterion for rock masses. *J. Geotech. Engng Div., ASCE 106 (GT9)*, pp.1013-1035.
- Hoek, E., Carranza-Torres, C., & Corkum, B. (2002). Hoek-Brown failure criterion-2002 edition. *Proceedings of NARMS-Tac*, 1(1), pp.267-273.
- Hoek, E., Kaiser, P. K., & Bawden, W. F. (1995). Support of underground excavations in hard rock. *Balkema, Rotterdam*. p.215.
- Hoek, E., Wood, D., & Shah, S. (1992). A modified Hoek–Brown failure criterion for jointed rock masses. In *Rock Characterization: ISRM Symposium, Eurock'92, Chester, UK*, pp.209-214. Thomas Telford Publishing.
- Hudson, J. A., & Feng, X. T. (2007). Updated flowcharts for rock mechanics modelling and rock engineering design. *International Journal of Rock Mechanics and Mining Sciences*, 44(2), pp.174-195.
- Hudyma, M. R., Potvin, Y., Grant, D. R., Milne, D., Brummer, R. K., & Board, M. (1994). Geomechanics of sill pillar mining. In *1st North American Rock Mechanics Symposium*. American Rock Mechanics Association.
- Hustrulid, W.A and Bullock, R.L. (2001). *Underground mining method: engineering fundamentals and international case studies*. Society of Mining, Metallurgy, and Exploration (SME), USA.
- Iannacchione, A. T., & Mark, C. (2009). Major hazard risk assessment applied to pillar recovery operations. In *Proceedings of the 28th international conference on ground control in mining*. Morgantown, West Virginia University, USA; pp.261-70.
- Idris, M. A., Saiang, D., & Nordlund, E. (2011a). Probabilistic analysis of open stope stability using numerical modelling. *International Journal of Mining and Mineral Engineering*, 3(3), pp.194-219.

- Idris, M. A., Saiang, D., & Nordlund, E. (2011b). Numerical analyses of the effects of rock mass property variability on open stope stability. In 45th US Rock Mechanics/Geomechanics Symposium. American Rock Mechanics Association.
- Idris, M. A., Saiang, D., & Nordlund, E. (2012). Consideration of the rock mass property variability in numerical modelling of open stope stability. In Bergmekanikdag. pp.111-123.
- J. G. Henning, T. R. Yu & D. H. Zou. (1992). Rock mechanics aspects of sill pillar recovery at Kidd Creek Mine, 16th Canadian Rock Mechanics Symposium, Sudbury, Ontario.
- Jaeger, J. C., Cook, N. G., & Zimmerman, R. (2009). Fundamentals of rock mechanics. John Wiley & Sons.
- Jing, L. (2003). A review of techniques, advances and outstanding issues in numerical modelling for rock mechanics and rock engineering. International Journal of Rock Mechanics and Mining Sciences, 40(3), pp.283-353.
- Jing, L., Hudson, J. A. (2002). Numerical methods in rock mechanics. International Journal of Rock Mechanics and Mining Sciences, 39(4), pp.409-427.
- Kaiser, P. K., & Cai, M. (2012). Design of rock support system under rockburst condition. Journal of Rock Mechanics and Geotechnical Engineering, 4(3), pp.215-227.
- Kaiser, P. K., Diederichs, M. S., Martin, C. D., Sharp, J., & Steiner, W. (2000, November). Underground works in hard rock tunnelling and mining. In ISRM international symposium. International Society for Rock Mechanics and Rock Engineering. pp.841–926.
- Kalenchuk, K. S., Crockford, A. M., Hume, C. D., Milner, N., & Watson, J. (2014, June). Application of numerical modelling to predicted seismic probability and mitigate associated risks during the Craig pillar extraction at Morrison Mine, KGHM International. In 48th US Rock Mechanics/Geomechanics Symposium. OnePetro.
- Kalenchuk, K. (2021). 2019 Canadian Geotechnical Colloquium: Mitigating a fatal flaw in modern geomechanics: understanding uncertainty, applying model calibration, and defying the hubris in numerical modelling. Canadian Geotechnical Journal, (ja).

- Kang, Y., Liu, H., Aziz, M. M. A., & Kassim, K. A. (2019). A wavelet transform method for studying the energy distribution characteristics of microseismicities associated rock failure. *Journal of Traffic and Transportation Engineering (English Edition)*, 6(6), pp.631-646.
- Kasper, T., & Meschke, G. (2004). A 3D finite element simulation model for TBM tunnelling in soft ground. *International journal for numerical and analytical methods in geomechanics*, 28(14), pp.1441-1460.
- Kielbassa, S., & Duddeck, H. (1991). Stress-strain fields at the tunnelling face—Three-dimensional analysis for two-dimensional technical approach. *Rock mechanics and rock engineering*, 24(3), pp.115-132.
- Kishida, K., Kikumoto, M., Cui, Y., & Kimura, M. (2012). Advanced numerical simulation of tunnel excavation and its application to the shallow overburden tunnel on unconsolidated ground.
- Kropacek, M., Mynarcik, P., & Cajka, R. (2020). Concrete structures interacting with subsoil depending on the use of sliding joint. *International Journal*, 18(69), pp.136-142.
- Kumar, D., Singh, U. K., & Singh, G. S. P. (2016). Laboratory characterization of cemented rock fill for underhand cut and fill method of mining. *Journal of The Institution of Engineers (India): Series D*, 97(2), pp.193-203.
- Kurlenya, M. V., Baryshnikov, V. D., & Gakhova, L. N. (2012). Experimental and analytical method for assessing stability of stopes. *Journal of Mining Science*, 48(4), pp.609-615.
- Labrie, D., Boyle, R., Anderson, T., Conlon, B., & Judge, K. (2007). Monitoring the behavior of a sill pillar at failure in a narrow vein mine. In 1st Canada-US Rock Mechanics Symposium. American Rock Mechanics Association.
- Labuz, J. F., & Zang, A. (2012). Mohr–Coulomb failure criterion. In *The ISRM Suggested Methods for Rock Characterization, Testing and Monitoring: 2007-2014* (pp. 227-231). Springer, Cham.
- Langston, R., Kirsten, H. A., Niemi, E., & Marjerison, J. (2006). Extraction of a Remnant Sill Pillar Under Challenging Ground Conditions at the Stillwater Mine, Nye, MT. In *Golden Rocks 2006, The 41st US Symposium on Rock Mechanics (USRMS)*.

- Leveille, P. (2016). Rockbursting Properties of Kimberlite-Diavik Diamond Mine Case Study. University of Alberta, Canada.
- Leveille, P., Sepehri, M., & Apel, D. B. (2017). Rockbursting potential of kimberlite: a case study of Diavik diamond mine. *Rock Mechanics and Rock Engineering*, 50(12), pp.3223-3231.
- Li, H., & Guo, G. (2018). Surface subsidence control mechanism and effect evaluation of gangue-backfilling mining: a case study in China. *Geofluids*, 2018.
- Li, Q., Chen, L., Xiao, Y., Qiao, L., & Wang, Y. (2017). Energy characterization based assessment of pillar recovery. *Arabian Journal of Geosciences*, 10(16), pp.1-12.
- Lingga, B. A., & Apel, D. B. (2018b). Shear properties of cemented rockfills. *Journal of Rock Mechanics and Geotechnical Engineering*, 10(4), pp.635-644.
- Lingga, B. A., (2018a) "Investigation of Cemented Rockfill Properties Used at a Canadian Diamond Mine," University of Alberta, Canada.
- Lingga, B. A., Apel, D. B., Sepehri, M., & Pu, Y. (2019). Assessment of digital image correlation method in determining large scale cemented rockfill strains. *International Journal of Mining Science and Technology*, 29(5), pp.771-776.
- Malan, D. F. (1999). Time-dependent behaviour of deep level tabular excavations in hard rock. *Rock Mechanics and Rock Engineering*, 32(2), pp.123-155.
- Malan, D. F. (2002). Manuel Rocha medal recipient simulating the time-dependent behaviour of excavations in hard rock. *Rock Mechanics and Rock Engineering*, 35(4), pp.225-254.
- Manh, H. T., Sulem, J., Subrin, D., & Billiaux, D. (2015). Anisotropic time-dependent modeling of tunnel excavation in squeezing ground. *Rock Mechanics and Rock Engineering*, 48(6), pp.2301-2317.
- Mark, C. (2009). Deep cover pillar recovery in the US. In *Proceedings of the 28th International Conference on Ground Control in Mining*. pp.1-9.
- Mark, C., & Gauna, M. (2017). Preventing roof fall fatalities during pillar recovery: a ground control success story. *International Journal of Mining Science and Technology*, 27(1), pp.107-113.
- Mark, C., & Tuchman, R. J. (1997a). *Proceedings: New Technology for Ground Control in Retreat Mining*.

Mark, C., & Zelanko, J. C. (2001). Sizing of final stumps for safer pillar extraction. In Proceedings of the 20th international conference on ground control in mining, Morgantown, West Virginia University, USA; pp.59-66.

Mark, C., Chase, F. E., & Campoli, A. A. (1995). Analysis of retreat mining pillar stability (No. CONF-950811-). Morgantown, West Virginia University, USA; pp.17–37.

Mark, C., Chase, F. E., & Pappas, D. M. (2007). Analysis of multiple seam stability. In: Proceedings of the 26th international conference on ground control in mining, Morgantown, West Virginia University, USA; pp.5–18.

Mark, C., Chase, F., & Pappas, D. (2003). Reducing the risk of ground falls during pillar recovery. Transactions-Society for Mining Metallurgy and Exploration Incorporated, 314, pp.153-160.

Mark, C., McCall, F. E., & Pappas, D. M. (1997b). A statistical overview of retreat mining of coal pillars in the United States. In Proceedings-New Technology for Ground Control in Retreat Mining. Pittsburgh, PA: US Department of Health and Human Services, Public Health Service, Centers for Disease Control and Prevention, National Institute for Occupational Safety and Health, DHHS (NIOSH) Publication (No. 97-122), pp.2-16.

Marlow, P., & Mikula, P. A. (2013, May). Shotcrete ribs and cemented rock fill ground control methods for stoping in weak squeezing rock at Wattle Dam Gold Mine. In Proceedings of the Seventh International Symposium on Ground Support in Mining and Underground Construction (pp.133-147). Australian Centre for Geomechanics.

Martin, C. D., Kaiser, P. K., & Christiansson, R. (2003). Stress, instability and design of underground excavations. International Journal of Rock Mechanics and Mining Sciences, 40(7-8), pp.1027-1047.

Martino, J. B., & Chandler, N. A. (2004). Excavation-induced damage studies at the underground research laboratory. International Journal of Rock Mechanics and Mining Sciences, 41(8), pp.1413-1426.

Mathews, K. E., Hoek, E., Wyllie, D. C., & Stewart, S. (1981). Prediction of stable excavation spans for mining at depths below 1000 m in hard rock. CANMET DSS Serial No: 0sQ80-00081., Ottawa.

- Mazaira, A., & Konicek, P. (2015). Intense rockburst impacts in deep underground construction and their prevention. *Canadian Geotechnical Journal*, 52(10), pp.1426-1439.
- Mercier-Langevin, F., & Hadjigeorgiou, J. (2011). Towards a better understanding of squeezing potential in hard rock mines. *Mining Technology*, 120(1), pp.36-44.
- Miao, S. J., Cai, M. F., Guo, Q. F., & Huang, Z. J. (2016). Rock burst prediction based on in-situ stress and energy accumulation theory. *International Journal of Rock Mechanics and Mining Sciences*, 100(83), pp.86-94.
- Mine Safety and Health Administration, (1984). Hearing on Proposed Standards for Ground Control Metal/Nonmetal Mines, United States Department of Labor, Spokane, WA, June.
- Mitri, H. S. (2007). Assessment of horizontal pillar burst in deep hard rock mines. *International Journal of Risk Assessment and Management*, 7(5), pp.695-707.
- Mitri, H. S., Tang, B., & Simon, R. (1999). FE modelling of mining-induced energy release and storage rates. *Journal of the Southern African Institute of Mining and Metallurgy*, 99(2), pp.103-110.
- Mohr, O. (1900). Welche Umstände bedingen die Elastizitätsgrenze und den Bruch eines Materials. *Zeitschrift des Vereins Deutscher Ingenieure*, 46(1524-1530), pp.1572-1577.
- Musunuri, A., Mitri, H., & Thibodeau, D. (2010). Stochastic Analysis of Haulage Drift Stability Using Numerical Modelling. In *ISRM International Symposium-6th Asian Rock Mechanics Symposium*. International Society for Rock Mechanics and Rock Engineering.
- Nguyen, T. T., Ngoc, L. T., Vu, H. H., & Thanh, T. P. (2021). Machine learning-based model for predicting concrete compressive strength. *International Journal of Geomate*, 20(77), pp.197-204.
- Ortlepp, W. D., & Stacey, T. R. (1994). Rockburst mechanisms in tunnels and shafts. *Tunnelling and Underground Space Technology*, 9(1), pp.59-65.
- Park, H. D. (1994). Tensile rock strength and related behaviour revealed by hoop tests, Doctoral dissertation, Department of Geology, Imperial College.
- Parviz N. F. (1996). IMPROVING CEMENTED ROCKFILL DESIGN IN OPEN STOPING. Doctor of Philosophy, McGill University, Canada.

- Pellet, F., Roosefid, M., & Deleruyelle, F. (2009). On the 3D numerical modelling of the time-dependent development of the damage zone around underground galleries during and after excavation. *Tunnelling and Underground Space Technology*, 24(6), pp.665-674.
- Perras, M., Langford, C., Ghazvinian, E., & Diederichs, M. (2012, May). Numerical delineation of the excavation damage zones: from rock properties to statistical distribution of the dimensions. In *ISRM International Symposium-EUROCK 2012*. International Society for Rock Mechanics and Rock Engineering.
- Potvin, Y., & Hadjigeorgiou, J. (2008). Ground support strategies to control large deformations in mining excavations. *Journal of the Southern African Institute of Mining and Metallurgy*, 108(7), pp.397-404.
- Potvin, Y., & Hudyma, M. (2000). Open stope mining in Canada. *Procc MassMin 2000*.
- Potvin, Y., Hudyma, M. R., & Miller, H. D. S. (1989). Design guidelines for open stope support. *CIM bulletin*, 82(926), pp.53-62.
- Pu, Y. (2019). *Machine Learning Approaches for Long-term Rock Burst Prediction*. Doctor of Philosophy, University of Alberta, Canada.
- Raju, G. D., Mitri, H., Thibodeau, D., & Moreau-Verlaan, L. (2015). Numerical modelling and in situ monitoring of drift support performance with respect to mining sequence. *International Journal of Mining, Reclamation and Environment*, 29(2), pp.83-95.
- Reschke, A. E. (1993). The use of cemented rockfill at Namew Lake mine, Manitoba, Canada. In *Minefill*, Vol. 93, pp.101-108.
- ROCLAB (2002). *User's Manual*, Rocscience INC.
- Rodvinij, P., & Ratchakrom, C. (2021). Effect of Cement Replacement By Fly Ash and Fgd Gypsum on Strength of Subbase. *International Journal*, 20(80), pp.9-16.
- Sainsbury, B. A., Sainsbury, D. P., Western, J., Petrie, P. E., & Mutton, V. (2014). Pillar recovery adjacent to stabilised rockfill at the Ballarat Gold Project. In *AusRock 2014: Proceedings of the Third Australasian Ground Control in Mining Conference*. pp.1-18. AUSIMM.

Sainsbury, D. P., & Sainsbury, B. L. (2014, January). Design and implementation of cemented rockfill at the Ballarat Gold Project. In Proceedings of the 11th International Symposium on Mining with Backfill, Australian Centre for Geomechanics, Perth (pp. 205-216).

Sainsbury, D. P., Cai, Y., & Hebblewhite, B. K. (2002). Numerical investigation of crown pillar recovery beneath stabilized rockfill. In Numerical Modeling in Micromechanics via Particle Methods: International PFC Symposium, Gelsenkirchen, Germany, CRC Press, pp.225.

Saw, H., Prentice, S., & Villaescusa, E. (2011, September). Characterisation of cemented rock fill materials for the Cosmos nickel mine, Western Australia. In Proceedings International Conference on Advances in Construction Materials through Science and Engineering (pp.907-914).

Sepehri, M. (2016). Finite Element Analysis Model for Determination of In-situ and Mining Induced Stresses as a Function of Two Different Mining Methods Used at Diavik Diamond Mine, Doctor of Philosophy, University of Alberta, Canada.

Sepehri, M., Apel, D. B., & Hall, R. A. (2017). Prediction of mining-induced surface subsidence and ground movements at a Canadian diamond mine using an elastoplastic finite element model. International Journal of Rock Mechanics and Mining Sciences, 100, pp.73-82.

Sepehri, M., Apel, D. B., Adeb, S., Leveille, P., & Hall, R. A. (2020). Evaluation of mining-induced energy and rockburst prediction at a diamond mine in Canada using a full 3D elastoplastic finite element model. Engineering Geology, 266, 105457.

Seymour, B., Tesarik, D., Larson, M., & Shoemaker, J. (1998, August). Stability of backfilled cross-panel entries during longwall mining. In Proceedings of the seventeenth international conference on ground control in mining, Morgantown (pp. 4-6).

Seymour, J. B., Raffaldi, M. J., Warren, S. N., Martin, L. A., & Sandbak, L. A. (2018, August). Long-term stability of a large undercut span beneath cemented rockfill at the Turquoise Ridge Mine. In 52nd US Rock Mechanics/Geomechanics Symposium. American Rock Mechanics Association.

Shnorhokian, S., MacNeil, B., & Mitri, H. S. (2018). Volumetric analysis of rock mass instability around haulage drifts in underground mines. Journal of Rock Mechanics and Geotechnical Engineering, 10(1), pp.60-71.

- Shnorhokian, S., Mitri, H. S., & Moreau-Verlaan, L. (2015). Stability assessment of stope sequence scenarios in a diminishing ore pillar. *International Journal of Rock Mechanics and Mining Sciences*, 74, pp.103-118.
- Shnorhokian, S., Mitri, H. S., & Thibodeau, D. (2014). A methodology for calibrating numerical models with a heterogeneous rockmass. *International Journal of Rock Mechanics and Mining Sciences*, 70, pp.353-367.
- Shrestha, B. K., Tannant, D. D., Proskin, S., Reinson, J., & Greer, S. (2008). Properties of cemented rockfill used in an open pit mine. *GeoEdmonton*, 8, pp.609-616.
- Singh R, Ghose A. (2006). *Engineering Rock Structures in Mining and Civil construction*, Taylor & Francis, London.
- Singiresu S.R, (2004). *The Finite Element Method in Engineering*, Fourth Edition. Elsevier Science & Technology Books, December.
- Sjöberg, J., Christiansson R., Hudson J.A., (2003). ISRM Suggested Methods for rock stress estimation – Part 2: Overcoring methods, *International Journal of Rock Mechanics & Mining Sciences* 40, pp.999-1010.
- Sjöberg, J., Perman, F., Quinteiro, C., Malmgren, L., Dahner-Lindkvist, C., & Boskovic, M. (2012). Numerical analysis of alternative mining sequences to minimise potential for fault slip rockbursting. *Mining Technology*, 121(4), pp.226-235.
- Stone, D. M. R. (2007, August). Factors that affect cemented rockfill quality in Nevada mines. In *Minefill 2007: The 9th International Symposium on Mining with Backfill* (pp. 1-6). Canadian Institute of Mining and Metallurgy, Montreal, QC, Canada.
- Sulem, J., Panet, M., & Guenot, A. (1987, June). An analytical solution for time-dependent displacements in a circular tunnel. In *International journal of rock mechanics and mining sciences & geomechanics abstracts* (Vol. 24, No. 3, pp. 155-164). Pergamon.
- Sun, Q., Zhang, J., & Zhou, N. (2018). Study and discussion of short-strip coal pillar recovery with cemented paste backfill. *International Journal of Rock Mechanics and Mining Sciences*, 104, pp.147-155.

- Sun, Y., Chen, Y. N., & Wang, Z. Y. (2012). Numerical Simulation of Inner Support for Excavation Based on FEM Software ABAQUS. In *Applied Mechanics and Materials* (Vol. 236), pp.632-635. Trans Tech Publications.
- Taherynia, M. H., Agha S., and Fahimifar A., (2016). In-Situ Stress State and Tectonic Regime in Different Depths of Earth Crust. *Geotech. Geol. Eng.*, Springer, 34, pp.679-687.
- Tang, S., Yu, C., & Tang, C. (2018). Numerical modeling of the time-dependent development of the damage zone around a tunnel under high humidity conditions. *Tunnelling and Underground Space Technology*, 76, 48-63.
- Terzaghi K., Richart F.E., (1952). Stress in rock about cavities. *Geotechnique* 3, 57-90.
- Tesarik, D. R., Seymour, J. B., & Jones, F. M. (2003, September). Determination of in situ deformation modulus for cemented rockfill. In 10th ISRM Congress. OnePetro.
- Tesarik, D. R., Seymour, J. B., Martin, L. A., & Jones, F. M. (2007, April). Numeric model of a cemented rockfill span test at the Turquoise Ridge Mine, Golconda, Nevada, USA. In *Proceedings of the ninth international symposium on mining with backfill (Minefill 2007)*, Montreal (Vol. 29).
- Thompson, B. D., Bawden, W. F., & Grabinsky, M. W. (2012). In situ measurements of cemented paste backfill at the Cayeli Mine. *Canadian Geotechnical Journal*, 49(7), 755-772.
- Thompson, B. D., Grabinsky, M. W., Bawden, W. F., & Counter, D. B. (2009, May). In-situ measurements of cemented paste backfill in long-hole stopes. In *Proceedings of the 3rd CANUS rock mechanics symposium*, Toronto (pp. 197-198).
- Townend, S., & Sampson-Forsythe, A. (2014). Mitigation strategies for mining in high stress sill pillars at Coleman Mine—a case study. In *Proceedings of the Seventh International Conference on Deep and High Stress Mining*. pp.65-77. Australian Centre for Geomechanics.
- Urli, V., & Esmaili, K. (2016). A stability-economic model for an open stope to prevent dilution using the ore-skin design. *International Journal of Rock Mechanics and Mining Sciences*, 82, pp.71-82.
- Valley, B., Milkereit, B., Pun, W., Pilz, M., Hutchinson, J., Delaloye, D., & Forsythe, A. (2012). Rock mass change monitoring in a sill pillar at Vale's Coleman mine, Sudbury, Canada. *Proceedings of the CMI*, 8p.

- Wang, J. A., & Park, H. D. (2001). Comprehensive prediction of rockburst based on analysis of strain energy in rocks. *Tunnelling and Underground Space Technology*, 16(1), pp.49-57.
- Wang, J., Apel, D. B., Pu, Y., Hall, R., Wei, C., & Sepehri, M. (2020). Numerical modeling for rockbursts: A state-of-the-art review. *Journal of Rock Mechanics and Geotechnical Engineering*.
- Wang, T. T., & Huang, T. H. (2011). Numerical simulation on anisotropic squeezing phenomenon of New Guanyin Tunnel. *Journal of GeoEngineering*, 6(3), pp.125-133.
- Weng, M. C., Tsai, L. S., Liao, C. Y., & Jeng, F. S. (2010). Numerical modeling of tunnel excavation in weak sandstone using a time-dependent anisotropic degradation model. *Tunnelling and underground space technology*, 25(4), pp.397-406.
- Wiles, T. D. (2006). Reliability of numerical modelling predictions. *International Journal of Rock Mechanics and Mining Sciences*, 43(3), pp.454-472.
- Wiseman, N. (1979). Factors affecting the design and condition of mine tunnels. *Chamb Mines S Afr*, Pretoria, 22.
- Yao, G. H., Wang, Y. M., & Hu, K. J. (2014). Stability analysis of central haulage in Baluba copper mine. In *Applied Mechanics and Materials* (Vol. 638), pp.822-828. Trans Tech Publications.
- Yip, C. G., and Thompson, K. S. (2015). Diavik Diamond Mine – Technical Report NI43-101. Diavik Diamond Mine Corporation, Yellowknife, Canada
- Yu, T. R., & Counter, D. B. (1983). Backfill practice and technology at Kidd Creek Mines. *CIM bulletin*, 76(856), pp.56-65.
- Zelanko, J. C., & Mark, C. (2005). Reducing roof fall accidents on retreat mining sections: Developing and following a mining plan, and using equipment properly could reduce miner exposure to ground falls. *Coal age*, 110(12), pp.26-31.
- Zhang, C., Feng, X. T., Zhou, H., Qiu, S., & Wu, W. (2012). Case histories of four extremely intense rockbursts in deep tunnels. *Rock mechanics and rock engineering*, 45(3), pp.275-288.
- Zhang, Q., Wang, J., Wang, W., Bai, S., & Lin, P. (2019). Study on slope stability due to the influence of excavation of the high-speed rail tunnel. *Geomatics, Natural Hazards and Risk*.

Zhang, Y., & Mitri, H. S. (2007). Stability Assessment of Non-entry Stopes Using Nonlinear Finite Element Analysis. In 1st Canada-US Rock Mechanics Symposium. American Rock Mechanics Association.

Zhang, Y., & Mitri, H. S. (2008). Assessment of mine haulage drift stability using nonlinear analysis. In The 42nd US Rock Mechanics Symposium (USRMS). American Rock Mechanics Association.

Zhou, Z., Zhao, Y., Cao, W., Chen, L., & Zhou, J. (2018). Dynamic response of pillar workings induced by sudden pillar recovery. *Rock Mechanics and Rock Engineering*, 51(10), pp.3075-3090.

Zhukova, S., Korchak, P., Streshnev, A., & Salnikov, I. (2018). Geodynamic rock condition, mine workings stabilization during pillar recovery at the level+ 320 m of the Yukspor deposit of the Khibiny Massif. In *E3S Web of Conferences* (Vol. 56, p. 02022). EDP Sciences.

Zur, K. J., & Apel, D. (2004). Use of cemented rock fill for enhanced pillar recovery in area 1 of the Doe Run Company. *5<sup>th</sup> International Conference on Case Histories in Geotechnical Engineering*.26.

## Appendix I: Laboratory Test Results Plots

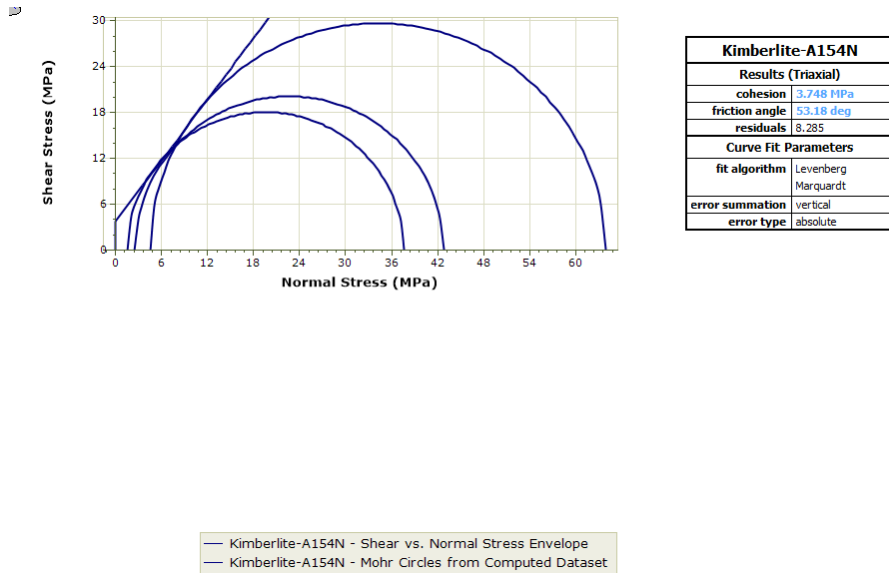


Figure AI-1 Mohr-Coulomb curve of Kimberlite sample of A154N pipe



Figure AI-2 Mohr-Coulomb curve of Kimberlite sample of A154S pipe

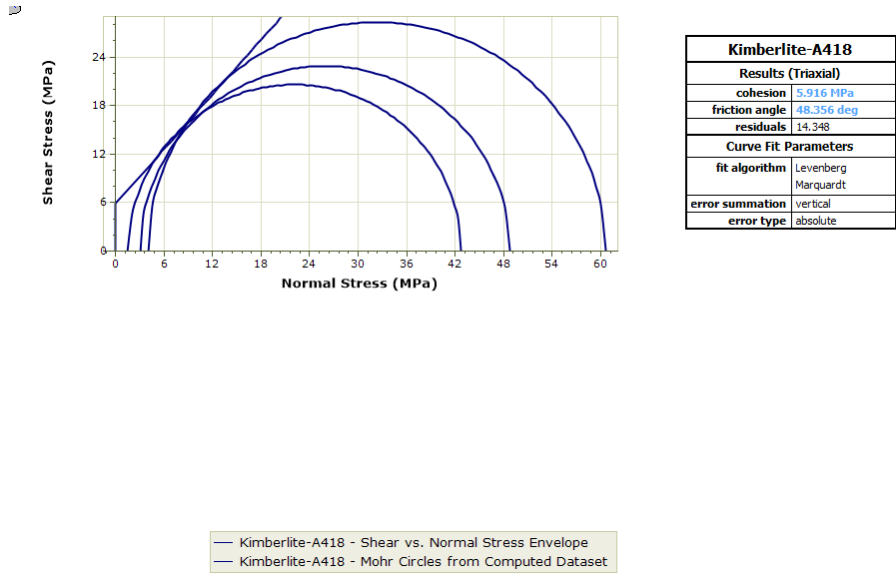


Figure AI-3 Mohr-Coulomb curve of Kimberlite sample of A418 pipe

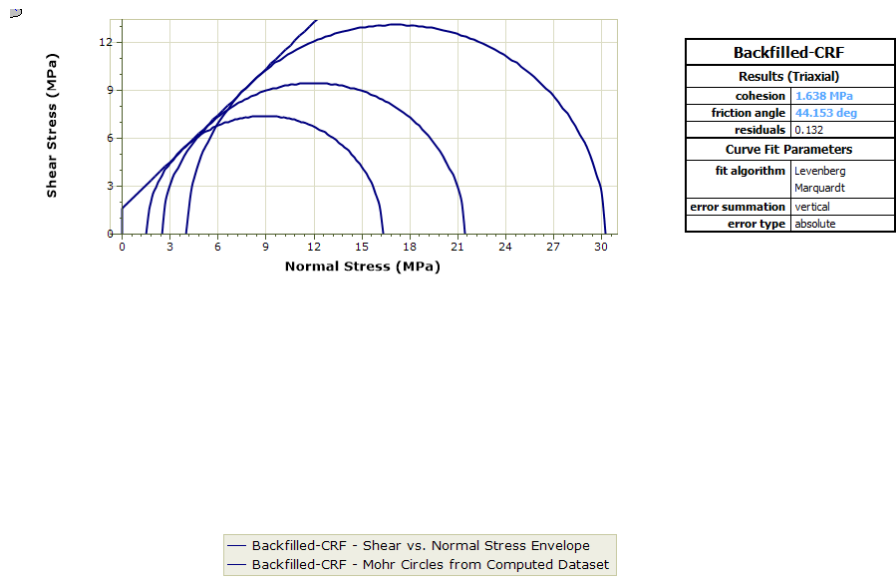


Figure AI-4 Mohr-Coulomb curve of backfilled CRF of A154N pipe

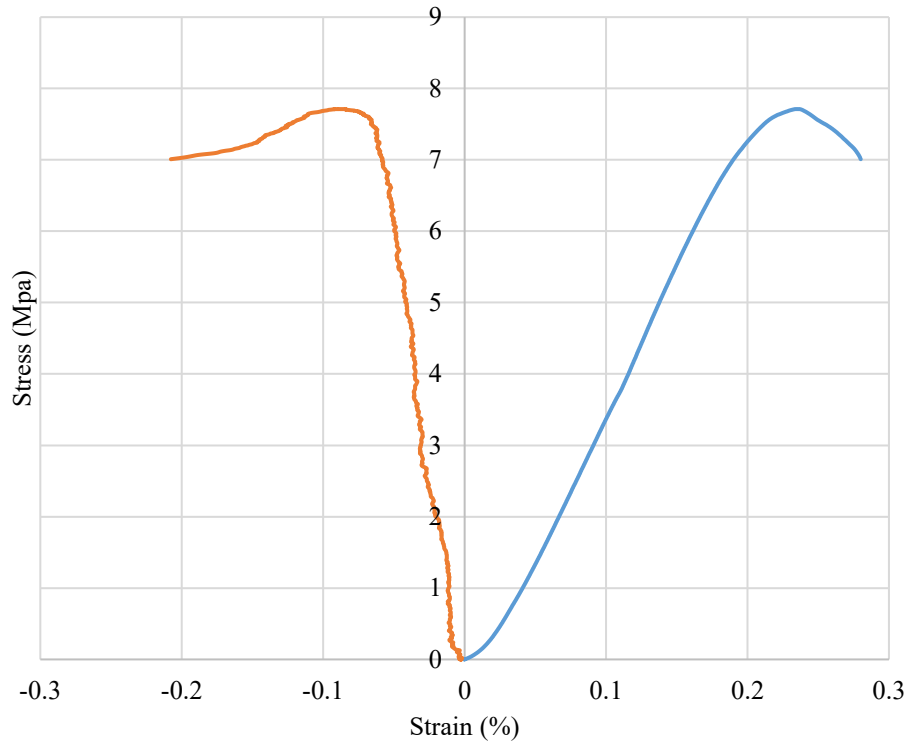


Figure AI-5 UCS test of backfilled CRF of A154N pipe

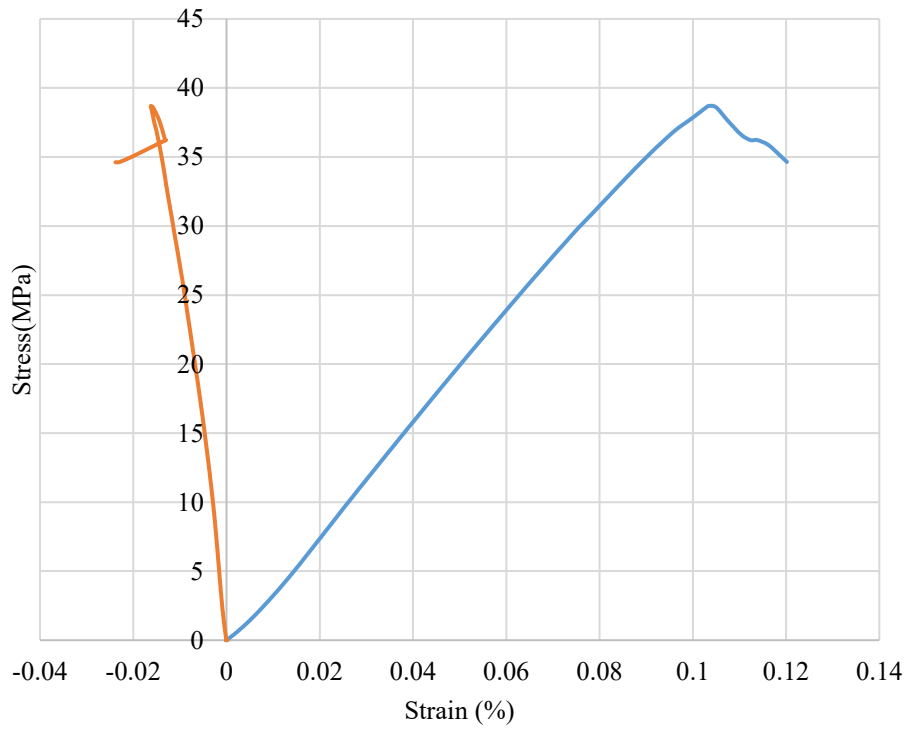


Figure AI-6 UCS test of Kimberlite of A154N pipe

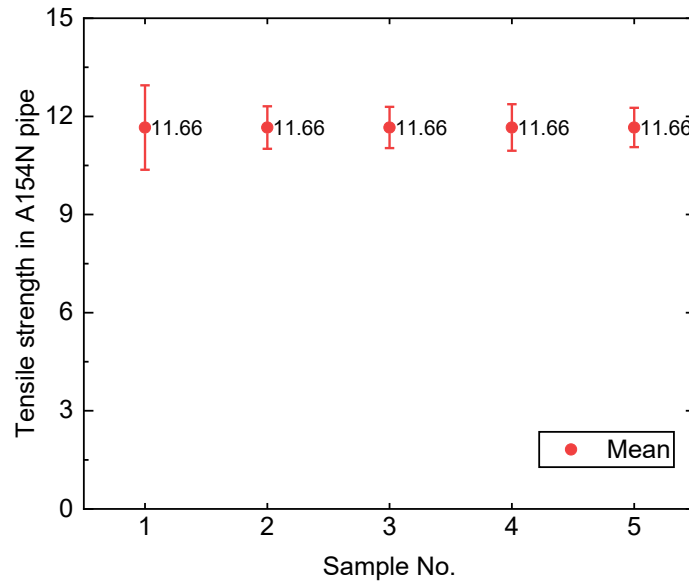


Figure AI-7 Tensile strength estimation of Kimberlite of A154N pipe

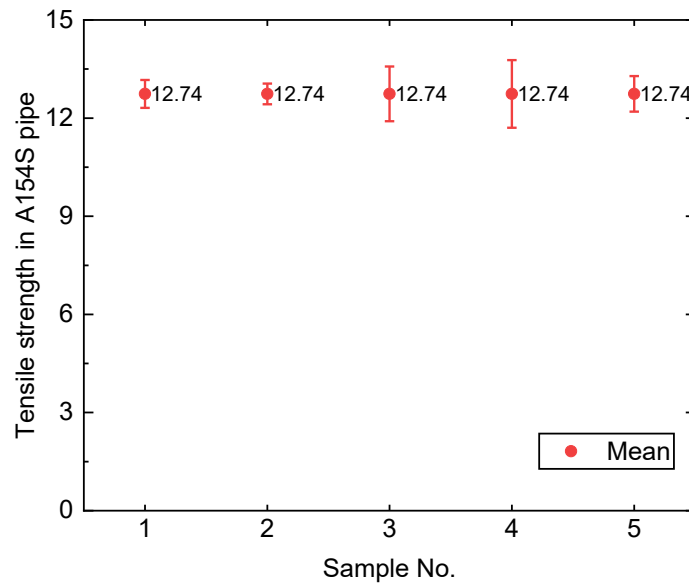


Figure AI-8 Tensile strength estimation of Kimberlite of A154S pipe

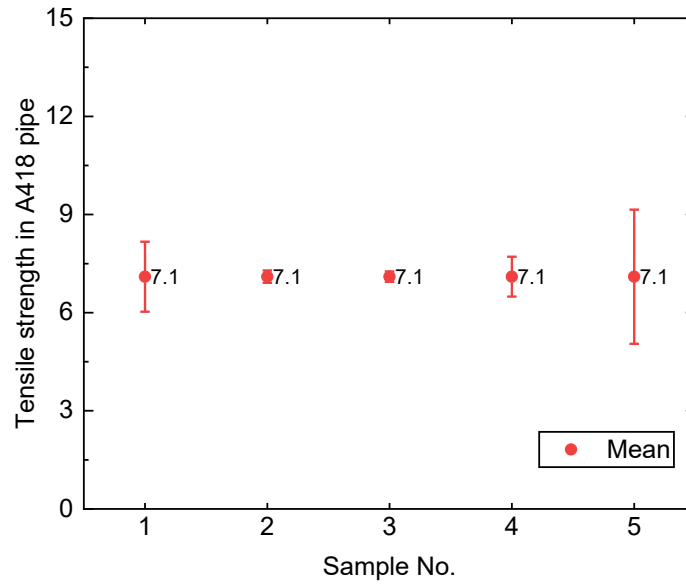


Figure AI-9 Tensile strength estimation of Kimberlite of A418 pipe

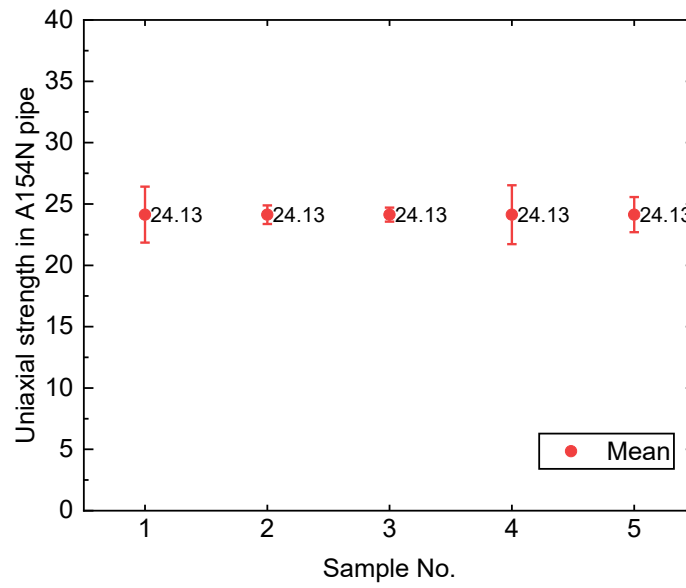


Figure AI-10 Uniaxial strength estimation of Kimberlite of A154N pipe

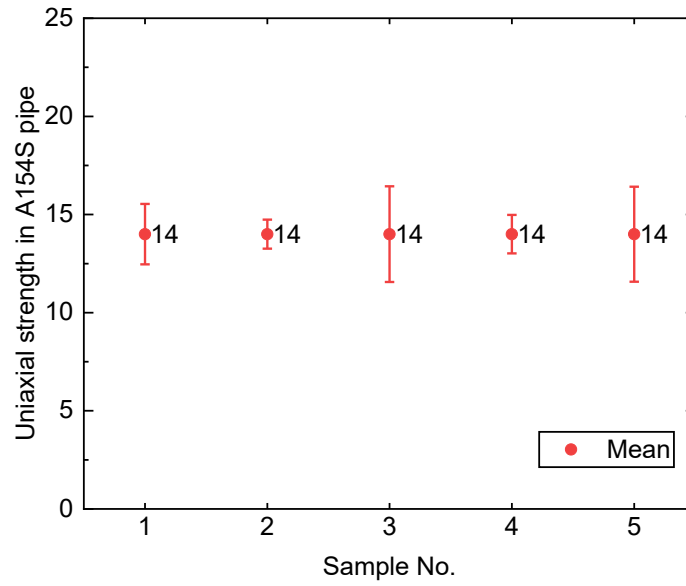


Figure AI-11 Uniaxial strength estimation of Kimberlite of A154S pipe

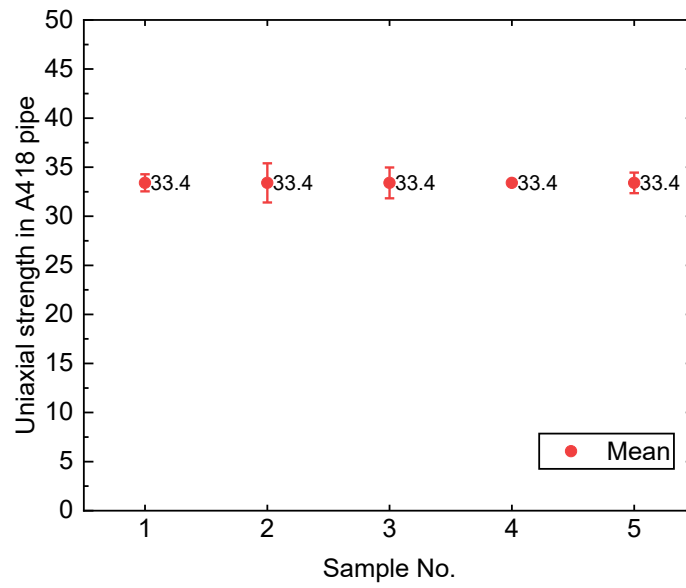


Figure AI-12 Uniaxial strength estimation of Kimberlite of A418 pipe

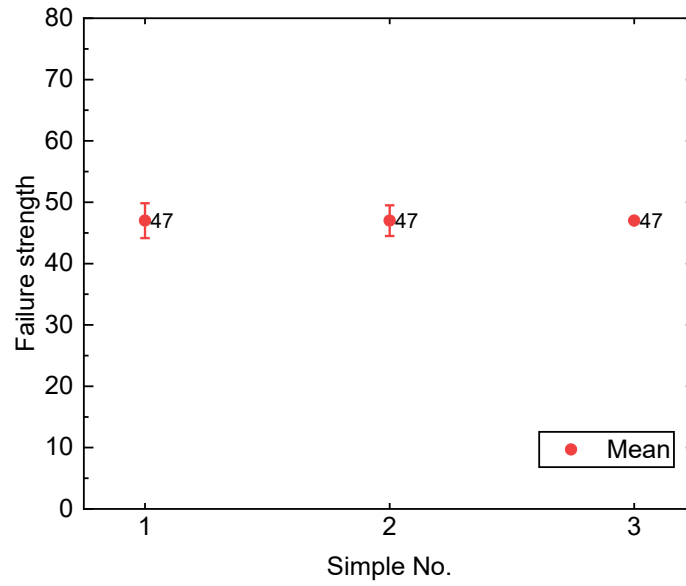


Figure AI-13 Triaxial failure strength estimation of Kimberlite of A418 pipe with 1.5MPa confinement

## Appendix II: Numerical Simulation Steps

<pre> ** STEP: Step-3 ** *Step, name=Step-3, nlgeom=YES, inc=200, unsymm=YES Excavation of the STOPEN9175P1C95B1, STOPEN9175P1C125B1, STOPEN9175P1C155B1 *Static 0.1, 1., 1e-07, 1. *CONTROLS, ANALYSIS=DISCONTINUOUS *MODEL CHANGE, REMOVE STOPEN9175P1C95B1, STOPEN9175P1C125B1, STOPEN9175P1C155B1 ** ** OUTPUT REQUESTS ** *Restart, write, frequency=0 ** ** FIELD OUTPUT: F-Output-2 ** *Output, field *Element Output, directions=YES ELEDEN, ELEN, ENER, PEEQMAX, PEEQT *Contact Output EFENRRTR, ENRRT ** ** FIELD OUTPUT: F-Output-1 ** *Output, field, variable=PRESELECT ** ** HISTORY OUTPUT: H-Output-1 ** *Output, history, variable=PRESELECT *End Step ** ----- ** ** STEP: Step-4 ** *Step, name=Step-4, nlgeom=YES, inc=200, unsymm=YES Excavation of the STOPEN9175P1C185B1, STOPEN9175P1C215B1, STOPEN9175P2C80B1, - BACKFILLING STOPEN9175P1C95B1, STOPEN9175P1C125B1, STOPEN9175P1C155B1 *Static 0.1, 1., 1e-07, 1. *CONTROLS, ANALYSIS=DISCONTINUOUS </pre>	<pre> *MODEL CHANGE, ADD STOPEN9175P1C95B1, STOPEN9175P1C125B1, STOPEN9175P1C155B1 *FIELD STOPEN9175P1C95BACKFILL1, 1.0 STOPEN9175P1C125BACKFILL1, 1.0 STOPEN9175P1C155BACKFILL1, 1.0 *MODEL CHANGE, REMOVE STOPEN9175P1C185B1, STOPEN9175P1C215B1, STOPEN9175P2C80B1 ** ** OUTPUT REQUESTS ** *Restart, write, frequency=1 ** ** FIELD OUTPUT: F-Output-2 ** *Output, field *Element Output, directions=YES ELEDEN, ELEN, ENER, PEEQMAX, PEEQT *Contact Output EFENRRTR, ENRRT ** ** FIELD OUTPUT: F-Output-1 ** *Output, field, variable=PRESELECT ** ** HISTORY OUTPUT: H-Output-1 ** *Output, history, variable=PRESELECT *End Step ** STEP: Step-5 ** *Step, name=Step-5, nlgeom=YES, inc=200, unsymm=YES Excavation of the STOPEN9175P2C110B1, STOPEN9175P2C140B1, STOPEN9175P2C170B1, - BACKFILLING STOPEN9175P1C185B1, STOPEN9175P1C215B1, STOPEN9175P2C80B1 *Static 0.1, 1., 1e-07, 1. *CONTROLS, ANALYSIS=DISCONTINUOUS *MODEL CHANGE, ADD STOPEN9175P1C185B1, STOPEN9175P1C215B1, STOPEN9175P2C80B1 *FIELD </pre>
---	--

STOPEN9175P1C185BACKFILL1, 1.0  
 STOPEN9175P1C215BACKFILL1, 1.0  
 STOPEN9175P2C80BACKFILL1, 1.0  
 \*MODEL CHANGE, REMOVE  
 STOPEN9175P2C110B1, STOPEN9175P2C140B1, STOPEN9175P2C170B1  
 \*\*  
 \*\* OUTPUT REQUESTS  
 \*\*  
 \*Restart, write, frequency=0  
 \*\*  
 \*\* FIELD OUTPUT: F-Output-2  
 \*\*  
 \*Output, field  
 \*Element Output, directions=YES  
 ELEDEN, ELEN, ENER, PEEQMAX, PEEQT  
 \*Contact Output  
 EFENRRTR, ENRRT  
 \*\*  
 \*\* FIELD OUTPUT: F-Output-1  
 \*\*  
 \*Output, field, variable=PRESELECT  
 \*\*  
 \*\* HISTORY OUTPUT: H-Output-1  
 \*\*  
 \*Output, history, variable=PRESELECT  
 \*End Step  
 \*\* -----  
 \*\*  
 \*\* STEP: Step-6  
 \*\*  
 \*Step, name=Step-6, ngeom=YES, inc=200, unsymm=YES  
 Excavation of the STOPEN9175P2C200B1, STOPEN9175S1C88B1, STOPEN9175S1C118B1  
 - BACKFILLING STOPEN9175P2C110B1, STOPEN9175P2C140B1, STOPEN9175P2C170B1  
 \*Static  
 0.1, 1., 1e-07, 1.  
 \*CONTROLS,ANALYSIS=DISCONTINUOUS  
 \*MODEL CHANGE, ADD  
 STOPEN9175P2C110B1, STOPEN9175P2C140B1, STOPEN9175P2C170B1  
 \*FIELD  
 STOPEN9175P2C110BACKFILL1, 1.0  
 STOPEN9175P2C140BACKFILL1, 1.0

STOPEN9175P2C170BACKFILL1, 1.0  
 \*MODEL CHANGE, REMOVE  
 STOPEN9175P2C200B1, STOPEN9175S1C88B1, STOPEN9175S1C118B1  
 \*\*  
 \*\* OUTPUT REQUESTS  
 \*\*  
 \*Restart, write, frequency=1  
 \*\*  
 \*\* FIELD OUTPUT: F-Output-2  
 \*\*  
 \*Output, field  
 \*Element Output, directions=YES  
 ELEDEN, ELEN, ENER, PEEQMAX, PEEQT  
 \*Contact Output  
 EFENRRTR, ENRRT  
 \*\*  
 \*\* FIELD OUTPUT: F-Output-1  
 \*\*  
 \*Output, field, variable=PRESELECT  
 \*\*  
 \*\* HISTORY OUTPUT: H-Output-1  
 \*\*  
 \*Output, history, variable=PRESELECT  
 \*End Step  
 \*\* STEP: Step-7  
 \*\*  
 \*Step, name=Step-7, ngeom=YES, inc=200, unsymm=YES  
 Excavation of the STOPEN9175S1C148B1, STOPEN9175S1C178B1, STOPEN9175S1C208B1  
 - BACKFILLING STOPEN9175P2C200B1, STOPEN9175S1C88B1, STOPEN9175S1C118B1  
 \*Static  
 0.1, 1., 1e-07, 1.  
 \*CONTROLS,ANALYSIS=DISCONTINUOUS  
 \*MODEL CHANGE, ADD  
 STOPEN9175P2C200B1, STOPEN9175S1C88B1, STOPEN9175S1C118B1  
 \*FIELD  
 STOPEN9175P2C200BACKFILL1, 1.0  
 STOPEN9175S1C88BACKFILL1, 1.0  
 STOPEN9175S1C118BACKFILL1, 1.0  
 \*MODEL CHANGE, REMOVE  
 STOPEN9175S1C148B1, STOPEN9175S1C178B1, STOPEN9175S1C208B1  
 \*\*

```

** OUTPUT REQUESTS
**
*Restart, write, frequency=0
**
** FIELD OUTPUT: F-Output-2
**
*Output, field
*Element Output, directions=YES
ELEDEN, ELEN, ENER, PEEQMAX, PEEQT
*Contact Output
EFENRRTR, ENRRT
**
** FIELD OUTPUT: F-Output-1
**
*Output, field, variable=PRESELECT
**
** HISTORY OUTPUT: H-Output-1
**
*Output, history, variable=PRESELECT
*End Step
**
-----
**
** STEP: Step-8
**
*Step, name=Step-8, nlgeom=YES, inc=200, unsymm=YES
Excavation of the STOPEN9175S2C73B1, STOPEN9175S2C103B1, STOPEN9175S2C133B1
- BACKFILLING STOPEN9175S1C148B1, STOPEN9175S1C178B1, STOPEN9175S1C208B1
*Static
0.1, 1., 1e-07, 1.
*CONTROLS,ANALYSIS=DISCONTINUOUS
*MODEL CHANGE, ADD
STOPEN9175S1C148B1, STOPEN9175S1C178B1, STOPEN9175S1C208B1
*FIELD
STOPEN9175S1C148BACKFILL1, 1.0
STOPEN9175S1C178BACKFILL1, 1.0
STOPEN9175S1C208BACKFILL1, 1.0
*MODEL CHANGE, REMOVE
STOPEN9175S2C73B1, STOPEN9175S2C103B1, STOPEN9175S2C133B1
**
** OUTPUT REQUESTS
**
*Restart, write, frequency=0
**
** FIELD OUTPUT: F-Output-2
**
*Output, field
*Element Output, directions=YES
ELEDEN, ELEN, ENER, PEEQMAX, PEEQT
*Contact Output
EFENRRTR, ENRRT
**
** FIELD OUTPUT: F-Output-1
**
*Output, field, variable=PRESELECT
**
** HISTORY OUTPUT: H-Output-1
**
*Output, history, variable=PRESELECT
*End Step
** STEP: Step-9
**
*Step, name=Step-9, nlgeom=YES, inc=200, unsymm=YES
Excavation of the STOPEN9175S2C163B1, STOPEN9175S2C193B1, STOPEN9175S2C223B1
- BACKFILLING STOPEN9175S2C73B1, STOPEN9175S2C103B1, STOPEN9175S2C133B1
*Static
0.1, 1., 1e-07, 1.
*CONTROLS,ANALYSIS=DISCONTINUOUS
*MODEL CHANGE, ADD
STOPEN9175S2C73B1, STOPEN9175S2C103B1, STOPEN9175S2C133B1
*FIELD
STOPEN9175S2C73BACKFILL1, 1.0
STOPEN9175S2C103BACKFILL1, 1.0
STOPEN9175S2C133BACKFILL1, 1.0
*MODEL CHANGE, REMOVE
STOPEN9175S2C163B1, STOPEN9175S2C193B1, STOPEN9175S2C223B1
**
** OUTPUT REQUESTS
**
*Restart, write, frequency=0
**
** FIELD OUTPUT: F-Output-2
**

```

```

*Output, field
ELEDEN, ELEN, ENER, PEEQMAX, PEEQT
*Element Output, directions=YES
ELEDEN, ELEN, ENER, PEEQMAX, PEEQT
*Contact Output
EFENRRTR, ENRRT
**
** FIELD OUTPUT: F-Output-1
**
*Output, field, variable=PRESELECT
**
** HISTORY OUTPUT: H-Output-1
**
*Output, history, variable=PRESELECT
*End Step
**
-----
**
** STEP: Step-10
**
*Step, name=Step-10, nlgeom=YES, inc=200, unsymm=YES
Excavation of the STOPEN9200P1C95B1, STOPEN9200P1C125B1, STOPEN9200P1C155B1
- BACKFILLING STOPEN9175S2C163B1, STOPEN9175S2C193B1, STOPEN9175S2C223B1
*Static
0.1, 1., 1e-07, 1.
*CONTROLS,ANALYSIS=DISCONTINUOUS
*MODEL CHANGE, ADD
STOPEN9175S2C163B1, STOPEN9175S2C193B1, STOPEN9175S2C223B1
*FIELD
STOPEN9175S2C163BACKFILL1, 1.0
STOPEN9175S2C193BACKFILL1, 1.0
STOPEN9175S2C223BACKFILL1, 1.0
*MODEL CHANGE, REMOVE
STOPEN9200P1C95B1, STOPEN9200P1C125B1, STOPEN9200P1C155B1
**
** OUTPUT REQUESTS
**
*Restart, write, frequency=1
**
** FIELD OUTPUT: F-Output-2
**
*Output, field
*Element Output, directions=YES

```

```

ELEDEN, ELEN, ENER, PEEQMAX, PEEQT
*Contact Output
EFENRRTR, ENRRT
**
** FIELD OUTPUT: F-Output-1
**
*Output, field, variable=PRESELECT
**
** HISTORY OUTPUT: H-Output-1
**
*Output, history, variable=PRESELECT
*End Step
** STEP: Step-11
**
*Step, name=Step-11, nlgeom=YES, inc=200, unsymm=YES
Excavation of the STOPEN9200P1C185B1, STOPEN9200P1C215B1, STOPEN9200P2C80B1
- BACKFILLING STOPEN9200P1C95B1, STOPEN9200P1C125B1, STOPEN9200P1C155B1
*Static
0.1, 1., 1e-07, 1.
*CONTROLS,ANALYSIS=DISCONTINUOUS
*MODEL CHANGE, ADD
STOPEN9200P1C95B1, STOPEN9200P1C125B1, STOPEN9200P1C155B1
*FIELD
STOPEN9200P1C95BACKFILL1, 1.0
STOPEN9200P1C125BACKFILL1, 1.0
STOPEN9200P1C155BACKFILL1, 1.0
*MODEL CHANGE, REMOVE
STOPEN9200P1C185B1, STOPEN9200P1C215B1, STOPEN9200P2C80B1
**
** OUTPUT REQUESTS
**
*Restart, write, frequency=0
**
** FIELD OUTPUT: F-Output-2
**
*Output, field
*Element Output, directions=YES
ELEDEN, ELEN, ENER, PEEQMAX, PEEQT
*Contact Output
EFENRRTR, ENRRT
**

```

```

** FIELD OUTPUT: F-Output-1
**
*Output, field, variable=PRESELECT
**
** HISTORY OUTPUT: H-Output-1
**
*Output, history, variable=PRESELECT
**
*End Step
**
-----
**
** STEP: Step-12
**
*Step, name=Step-12, nlgeom=YES, inc=200, unsymm=YES
Excavation of the STOPEN9200P2C110B1, STOPEN9200P2C140B1,
STOPEN9200P2C170B1 - BACKFILLING STOPEN9200P1C185B1, STOPEN9200P1C215B1,
STOPEN9200P2C80B1
*Static
0.1, 1., 1e-07, 1.
*CONTROLS,ANALYSIS=DISCONTINUOUS
*MODEL CHANGE, ADD
STOPEN9200P1C185B1, STOPEN9200P1C215B1, STOPEN9200P2C80B1
*FIELD
STOPEN9200P1C185BACKFILL1, 1.0
STOPEN9200P1C215BACKFILL1, 1.0
STOPEN9200P2C80BACKFILL1, 1.0
*MODEL CHANGE, REMOVE
STOPEN9200P2C110B1, STOPEN9200P2C140B1, STOPEN9200P2C170B1
**
** OUTPUT REQUESTS
**
*Restart, write, frequency=1
**
** FIELD OUTPUT: F-Output-2
**
*Output, field
*Element Output, directions=YES
ELEDEN, ELEN, ENER, PEEQMAX, PEEQT
*Contact Output
EFENRRTR, ENRRT
**
** FIELD OUTPUT: F-Output-1
**
*Output, field, variable=PRESELECT
**
** HISTORY OUTPUT: H-Output-1
**

```

```

*Output, field, variable=PRESELECT
**
** HISTORY OUTPUT: H-Output-1
**
*Output, history, variable=PRESELECT
**
*End Step
** STEP: Step-13
**
*Step, name=Step-13, nlgeom=YES, inc=200, unsymm=YES
Excavation of the STOPEN9200P2C200B1, STOPEN9200S1C88B1, STOPEN9200S1C118B1
- BACKFILLING STOPEN9200P2C110B1, STOPEN9200P2C140B1, STOPEN9200P2C170B1
*Static
0.1, 1., 1e-07, 1.
*CONTROLS,ANALYSIS=DISCONTINUOUS
*MODEL CHANGE, ADD
STOPEN9200P2C110B1, STOPEN9200P2C140B1, STOPEN9200P2C170B1
*FIELD
STOPEN9200P2C110BACKFILL1, 1.0
STOPEN9200P2C140BACKFILL1, 1.0
STOPEN9200P2C170BACKFILL1, 1.0
*MODEL CHANGE, REMOVE
STOPEN9200P2C200B1, STOPEN9200S1C88B1, STOPEN9200S1C118B1
**
** OUTPUT REQUESTS
**
*Restart, write, frequency=0
**
** FIELD OUTPUT: F-Output-2
**
*Output, field
*Element Output, directions=YES
ELEDEN, ELEN, ENER, PEEQMAX, PEEQT
*Contact Output
EFENRRTR, ENRRT
**
** FIELD OUTPUT: F-Output-1
**
*Output, field, variable=PRESELECT
**
** HISTORY OUTPUT: H-Output-1
**

```

```

*Output, history, variable=PRESELECT

*End Step

** -----
**

** STEP: Step-14

**

*Step, name=Step-14, nlgeom=YES, inc=200, unsymm=YES

Excavation of the STOPEN9200S1C148B1, STOPEN9200S1C178B1, STOPEN9200S1C208B1
- BACKFILLING, STOPEN9200P2C200B1, STOPEN9200S1C88B1, STOPEN9200S1C118B1

*Static

0.1, 1., 1e-07, 1.

*CONTROLS,ANALYSIS=DISCONTINUOUS

*MODEL CHANGE, ADD

STOPEN9200P2C200B1, STOPEN9200S1C88B1, STOPEN9200S1C118B1

*FIELD

STOPEN9200P2C200BACKFILL1, 1.0

STOPEN9200S1C88BACKFILL1, 1.0

STOPEN9200S1C118BACKFILL1, 1.0

*MODEL CHANGE, REMOVE

STOPEN9200S1C148B1, STOPEN9200S1C178B1, STOPEN9200S1C208B1

**

** OUTPUT REQUESTS

**

*Restart, write, frequency=1

**

** FIELD OUTPUT: F-Output-2

**

*Output, field

*Element Output, directions=YES

ELEDEN, ELEN, ENER, PEEQMAX, PEEQT

*Contact Output

EFENRRTR, ENRRT

**

** FIELD OUTPUT: F-Output-1

**

*Output, field, variable=PRESELECT

**

** HISTORY OUTPUT: H-Output-1

**

*Output, history, variable=PRESELECT

*End Step

```

```

** STEP: Step-15

**

*Step, name=Step-15, nlgeom=YES, inc=200, unsymm=YES

Excavation of the STOPEN9200S2C103B1, STOPEN9200S2C133B1, STOPEN9200S2C163B1
- BACKFILLING STOPEN9200S1C148B1, STOPEN9200S1C178B1, STOPEN9200S1C208B1

*Static

0.1, 1., 1e-07, 1.

*CONTROLS,ANALYSIS=DISCONTINUOUS

*MODEL CHANGE, ADD

STOPEN9200S1C148B1, STOPEN9200S1C178B1, STOPEN9200S1C208B1

*FIELD

STOPEN9200S1C148BACKFILL1, 1.0

STOPEN9200S1C178BACKFILL1, 1.0

STOPEN9200S1C208BACKFILL1, 1.0

*MODEL CHANGE, REMOVE

STOPEN9200S2C103B1, STOPEN9200S2C133B1, STOPEN9200S2C163B1

**

** OUTPUT REQUESTS

**

*Restart, write, frequency=0

**

** FIELD OUTPUT: F-Output-2

**

*Output, field

*Element Output, directions=YES

ELEDEN, ELEN, ENER, PEEQMAX, PEEQT

*Contact Output

EFENRRTR, ENRRT

**

** FIELD OUTPUT: F-Output-1

**

*Output, field, variable=PRESELECT

**

** HISTORY OUTPUT: H-Output-1

**

*Output, history, variable=PRESELECT

*End Step

** -----
**

** STEP: Step-16

**

```

```

*Step, name=Step-16, ngeom=YES, inc=200, unsymm=YES

Excavation of the STOPEN9200S2C193B1, STOPEN9200S2C223B1, STOPEN9225P1C95B1
- BACKFILLING STOPEN9200S2C103B1, STOPEN9200S2C133B1, STOPEN9200S2C163B1

*Static

0.1, 1., 1e-07, 1.

*CONTROLS,ANALYSIS=DISCONTINUOUS

*MODEL CHANGE, ADD

STOPEN9200S2C103B1, STOPEN9200S2C133B1, STOPEN9200S2C163B1

*FIELD

STOPEN9200S2C103BACKFILL1, 1.0

STOPEN9200S2C133BACKFILL1, 1.0

STOPEN9200S2C163BACKFILL1, 1.0

*MODEL CHANGE, REMOVE

STOPEN9200S2C193B1, STOPEN9200S2C223B1, STOPEN9225P1C95B1

**

** OUTPUT REQUESTS

**

*Restart, write, frequency=1

**

** FIELD OUTPUT: F-Output-2

**

*Output, field

*Element Output, directions=YES

ELEDEN, ELEN, ENER, PEEQMAX, PEEQT

*Contact Output

EFENRRTR, ENRRT

**

** FIELD OUTPUT: F-Output-1

**

*Output, field, variable=PRESELECT

**

** HISTORY OUTPUT: H-Output-1

**

*Output, history, variable=PRESELECT

**

*End Step

** STEP: Step-17

**

*Step, name=Step-17, ngeom=YES, inc=200, unsymm=YES

Excavation of the STOPEN9225P1C125B1, STOPEN9225P1C155B1,
STOPEN9225P1C185B1 - BACKFILLING STOPEN9200S2C193B1, STOPEN9200S2C223B1,
STOPEN9225P1C95B1

*Static

0.1, 1., 1e-07, 1.

```

```

0.1, 1., 1e-07, 1.

*CONTROLS,ANALYSIS=DISCONTINUOUS

*MODEL CHANGE, ADD

STOPEN9200S2C193B1, STOPEN9200S2C223B1, STOPEN9225P1C95B1

*FIELD

STOPEN9200S2C193BACKFILL1, 1.0

STOPEN9200S2C223BACKFILL1, 1.0

STOPEN9200P1C95BACKFILL1, 1.0

*MODEL CHANGE, REMOVE

STOPEN9225P1C125B1, STOPEN9225P1C155B1, STOPEN9225P1C185B1

**

** OUTPUT REQUESTS

**

*Restart, write, frequency=0

**

** FIELD OUTPUT: F-Output-2

**

*Output, field

*Element Output, directions=YES

ELEDEN, ELEN, ENER, PEEQMAX, PEEQT

*Contact Output

EFENRRTR, ENRRT

**

** FIELD OUTPUT: F-Output-1

**

*Output, field, variable=PRESELECT

**

** HISTORY OUTPUT: H-Output-1

**

*Output, history, variable=PRESELECT

**

*End Step

** -----

**

** STEP: Step-18

**

*Step, name=Step-18, ngeom=YES, inc=200, unsymm=YES

Excavation of the STOPEN9225P1C125B1, STOPEN9225P2C110B1,
STOPEN9225P2C140B1 - BACKFILLING STOPEN9225P1C125B1, STOPEN9225P1C155B1,
STOPEN9225P1C185B1

*Static

0.1, 1., 1e-07, 1.

*CONTROLS,ANALYSIS=DISCONTINUOUS

```

```

*MODEL CHANGE, ADD
STOPEN9225P1C125B1, STOPEN9225P1C155B1, STOPEN9225P1C185B1

*FIELD
STOPEN9225P1C125BACKFILL1, 1.0
STOPEN9225P1C155BACKFILL1, 1.0
STOPEN9225P1C185BACKFILL1, 1.0

*MODEL CHANGE, REMOVE
STOPEN9225P1C215B1, STOPEN9225P2C110B1, STOPEN9225P2C140B1
**

** OUTPUT REQUESTS
**

*Restart, write, frequency=1
**

** FIELD OUTPUT: F-Output-2
**

*Output, field
*Element Output, directions=YES
ELEDEN, ELEN, ENER, PEEQMAX, PEEQT

*Contact Output
EFENRRTR, ENRRT
**

** FIELD OUTPUT: F-Output-1
**

*Output, field, variable=PRESELECT
**

** HISTORY OUTPUT: H-Output-1
**

*Output, history, variable=PRESELECT
*End Step
** STEP: Step-19
**
*Step, name=Step-19, nlgeom=YES, inc=200, unsymm=YES
Excavation of the STOPEN9225P2C170B1, STOPEN9225P2C200B1,
STOPEN9225S1C88B1 - BACKFILLING STOPEN9225P1C215B1,
STOPEN9225P2C110B1, STOPEN9225P2C140B1
*Static
0.1, 1., 1e-07, 1.
*CONTROLS, ANALYSIS=DISCONTINUOUS
*MODEL CHANGE, ADD
STOPEN9225P1C215B1, STOPEN9225P2C110B1, STOPEN9225P2C140B1
*FIELD
STOPEN9225P1C215BACKFILL1, 1.0
STOPEN9225P2C110BACKFILL1, 1.0
STOPEN9225P2C140BACKFILL1, 1.0
*MODEL CHANGE, REMOVE
STOPEN9225P2C170B1, STOPEN9225P2C200B1, STOPEN9225S1C88B1
**
** OUTPUT REQUESTS
**
*Restart, write, frequency=0
**
** FIELD OUTPUT: F-Output-2
**
*Output, field
*Element Output, directions=YES
ELEDEN, ELEN, ENER, PEEQMAX, PEEQT
*Contact Output
EFENRRTR, ENRRT
**
** FIELD OUTPUT: F-Output-1
**
*Output, field, variable=PRESELECT
**
** HISTORY OUTPUT: H-Output-1
**
*Output, history, variable=PRESELECT
*End Step
**
** STEP: Step-20
**
*Step, name=Step-20, nlgeom=YES, inc=200, unsymm=YES
Excavation of the STOPEN9225S1C118B1, STOPEN9225S1C148B1,
STOPEN9225S1C178B1 - BACKFILLING STOPEN9225P2C170B1,
STOPEN9225P2C200B1, STOPEN9225S1C88B1
*Static
0.1, 1., 1e-07, 1.
*CONTROLS, ANALYSIS=DISCONTINUOUS
*MODEL CHANGE, ADD
STOPEN9225P2C170B1, STOPEN9225P2C200B1, STOPEN9225S1C88B1
*FIELD
STOPEN9225P2C170BACKFILL1, 1.0
STOPEN9225P2C200BACKFILL1, 1.0
STOPEN9225S1C88BACKFILL1, 1.0
*MODEL CHANGE, REMOVE
STOPEN9225S1C118B1, STOPEN9225S1C148B1, STOPEN9225S1C178B1
**
** OUTPUT REQUESTS
**
*Restart, write, frequency=1
**
** FIELD OUTPUT: F-Output-2
**
*Output, field
*Element Output, directions=YES
ELEDEN, ELEN, ENER, PEEQMAX, PEEQT
*Contact Output
EFENRRTR, ENRRT
**
** FIELD OUTPUT: F-Output-1
**
*Output, field, variable=PRESELECT
**
** HISTORY OUTPUT: H-Output-1
**
*Output, history, variable=PRESELECT
*End Step
** STEP: Step-21
**
*Step, name=Step-21, nlgeom=YES, inc=200, unsymm=YES
Excavation of the STOPEN9225S1C208B1, STOPEN9225S1C103B1,
STOPEN9225S2C133B1 - BACKFILLING STOPEN9225S1C118B1,
STOPEN9225S1C148B1, STOPEN9225S1C178B1
*Static
0.1, 1., 1e-07, 1.
*CONTROLS, ANALYSIS=DISCONTINUOUS
*MODEL CHANGE, ADD
STOPEN9225S1C118B1, STOPEN9225S1C148B1, STOPEN9225S1C178B1
*FIELD
STOPEN9225S1C118BACKFILL1, 1.0
STOPEN9225S1C148BACKFILL1, 1.0
STOPEN9225S1C178BACKFILL1, 1.0
*MODEL CHANGE, REMOVE
STOPEN9225S1C208B1, STOPEN9225S2C103B1, STOPEN9225S2C133B1
**
** OUTPUT REQUESTS
**
*Restart, write, frequency=0
**
** FIELD OUTPUT: F-Output-2
**
*Output, field
*Element Output, directions=YES
ELEDEN, ELEN, ENER, PEEQMAX, PEEQT
*Contact Output
EFENRRTR, ENRRT
**
** FIELD OUTPUT: F-Output-1
**
*Output, field, variable=PRESELECT
**
** HISTORY OUTPUT: H-Output-1
**
*Output, history, variable=PRESELECT
*End Step
**
** STEP: Step-22
**

```

```

*Contact Output
EFENRRTR, ENRRT
**
** FIELD OUTPUT: F-Output-1
**
*Output, field, variable=PRESELECT
**
** HISTORY OUTPUT: H-Output-1
**
*Output, history, variable=PRESELECT
*End Step
** -----
**
** STEP: Step-20
**
*Step, name=Step-20, nlgeom=YES, inc=200, unsymm=YES
Excavation of the STOPEN9225S1C118B1, STOPEN9225S1C148B1,
STOPEN9225S1C178B1 - BACKFILLING STOPEN9225P2C170B1,
STOPEN9225P2C200B1, STOPEN9225S1C88B1
*Static
0.1, 1., 1e-07, 1.
*CONTROLS, ANALYSIS=DISCONTINUOUS
*MODEL CHANGE, ADD
STOPEN9225P2C170B1, STOPEN9225P2C200B1, STOPEN9225S1C88B1
*FIELD
STOPEN9225P2C170BACKFILL1, 1.0
STOPEN9225P2C200BACKFILL1, 1.0
STOPEN9225S1C88BACKFILL1, 1.0
*MODEL CHANGE, REMOVE
STOPEN9225S1C118B1, STOPEN9225S1C148B1, STOPEN9225S1C178B1
**
** OUTPUT REQUESTS
**
*Restart, write, frequency=1
**
** FIELD OUTPUT: F-Output-2
**
*Output, field
*Element Output, directions=YES
ELEDEN, ELEN, ENER, PEEQMAX, PEEQT
*Contact Output
EFENRRTR, ENRRT
**
** FIELD OUTPUT: F-Output-1
**
*Output, field, variable=PRESELECT
**
** HISTORY OUTPUT: H-Output-1
**
*Output, history, variable=PRESELECT
*End Step
** STEP: Step-21
**
*Step, name=Step-21, nlgeom=YES, inc=200, unsymm=YES
Excavation of the STOPEN9225S1C208B1, STOPEN9225S1C103B1,
STOPEN9225S2C133B1 - BACKFILLING STOPEN9225S1C118B1,
STOPEN9225S1C148B1, STOPEN9225S1C178B1
*Static
0.1, 1., 1e-07, 1.
*CONTROLS, ANALYSIS=DISCONTINUOUS
*MODEL CHANGE, ADD
STOPEN9225S1C118B1, STOPEN9225S1C148B1, STOPEN9225S1C178B1
*FIELD
STOPEN9225S1C118BACKFILL1, 1.0
STOPEN9225S1C148BACKFILL1, 1.0
STOPEN9225S1C178BACKFILL1, 1.0
*MODEL CHANGE, REMOVE
STOPEN9225S1C208B1, STOPEN9225S2C103B1, STOPEN9225S2C133B1
**
** OUTPUT REQUESTS
**
*Restart, write, frequency=0
**
** FIELD OUTPUT: F-Output-2
**
*Output, field
*Element Output, directions=YES
ELEDEN, ELEN, ENER, PEEQMAX, PEEQT
*Contact Output
EFENRRTR, ENRRT
**
** FIELD OUTPUT: F-Output-1
**
*Output, field, variable=PRESELECT
**
** HISTORY OUTPUT: H-Output-1
**
*Output, history, variable=PRESELECT
*End Step
** -----
**
** STEP: Step-22
**

```

```

*Step, name=Step-22, nlgeom=YES, inc=200, unsymm=YES
Excavation of the STOPEN9225S2C163B1, STOPEN9225S2C193B1,
STOPEN9225S2C223B1 - BACKFILLING STOPEN9225S1C208B1,
STOPEN9225S2C103B1, STOPEN9225S2C133B1
*Static
0.1, 1., 1e-07, 1.
*CONTROLS, ANALYSIS=DISCONTINUOUS
*MODEL CHANGE, ADD
STOPEN9225S1C208B1, STOPEN9225S2C103B1, STOPEN9225S2C133B1
*FIELD
STOPEN9225S1C208BACKFILL1, 1.0
STOPEN9225S2C103BACKFILL1, 1.0
STOPEN9225S2C133BACKFILL1, 1.0
*MODEL CHANGE, REMOVE
STOPEN9225S2C163B1, STOPEN9225S2C193B1, STOPEN9225S2C223B1
**
** OUTPUT REQUESTS
**
*Restart, write, frequency=1
**
** FIELD OUTPUT: F-Output-2
**
*Output, field
*Element Output, directions=YES
ELEDEN, ELEN, ENER, PEEQMAX, PEEQT
*Contact Output
EFENRRTR, ENRRT
**
** FIELD OUTPUT: F-Output-1
**
*Output, field, variable=PRESELECT
**
** HISTORY OUTPUT: H-Output-1
**
*Output, history, variable=PRESELECT
*End Step
** STEP: Step-23
**
*Step, name=Step-23, nlgeom=YES, inc=200, unsymm=YES
Excavation of the STOPEN9250P1C125B1, STOPEN9250P1C155B1,
STOPEN9250P1C185B1 - BACKFILLING STOPEN9225S2C163B1,
STOPEN9225S2C193B1, STOPEN9225S2C223B1
*Static
0.1, 1., 1e-07, 1.
*CONTROLS, ANALYSIS=DISCONTINUOUS
*MODEL CHANGE, ADD
STOPEN9225S2C163B1, STOPEN9225S2C193B1, STOPEN9225S2C223B1
*FIELD
STOPEN9225S2C163BACKFILL1, 1.0
STOPEN9225S2C193BACKFILL1, 1.0
STOPEN9225S2C223BACKFILL1, 1.0
*MODEL CHANGE, REMOVE
STOPEN9250P1C125B1, STOPEN9250P1C155B1, STOPEN9250P1C185B1
**
** OUTPUT REQUESTS
**
*Restart, write, frequency=0
**
** FIELD OUTPUT: F-Output-2
**
*Output, field
*Element Output, directions=YES
ELEDEN, ELEN, ENER, PEEQMAX, PEEQT
*Contact Output
EFENRRTR, ENRRT
**
** FIELD OUTPUT: F-Output-1
**
*Output, field, variable=PRESELECT
**
** HISTORY OUTPUT: H-Output-1
**
*Output, history, variable=PRESELECT
*End Step
** -----
**
** STEP: Step-24
**
*Step, name=Step-24, nlgeom=YES, inc=200, unsymm=YES
Excavation of the STOPEN9250P1C125B1, STOPEN9250P2C110B1,
STOPEN9250P2C140B1 - BACKFILLING STOPEN9250P1C125B1,
STOPEN9250P1C155B1, STOPEN9250P1C185B1
*Static
0.1, 1., 1e-07, 1.
*CONTROLS, ANALYSIS=DISCONTINUOUS
*MODEL CHANGE, ADD
STOPEN9250P1C125B1, STOPEN9250P1C155B1, STOPEN9250P1C185B1
*FIELD
STOPEN9225P1C125BACKFILL1, 1.0
STOPEN9250P1C155BACKFILL1, 1.0
STOPEN9250P1C185BACKFILL1, 1.0
*MODEL CHANGE, REMOVE
STOPEN9250P1C215B1, STOPEN9250P2C110B1, STOPEN9250P2C140B1

```

```

**
** OUTPUT REQUESTS
**
*Restart, write, frequency=1
**
** FIELD OUTPUT: F-Output-2
**
*Output, field
*Element Output, directions=YES
ELEDEN, ELEN, ENER, PEEQMAX, PEEQT
*Contact Output
EFENRRTR, ENRRT
**
** FIELD OUTPUT: F-Output-1
**
*Output, field, variable=PRESELECT
**
** HISTORY OUTPUT: H-Output-1
**
*Output, history, variable=PRESELECT
*End Step
** STEP: Step-25
**
*Step, name=Step-25, nlgeom=YES, inc=200, unsymm=YES
Excavation of the STOPEN9250P2C170B1, STOPEN9250P2C200B1,
STOPEN9250S1C118B1 - BACKFILLING STOPEN9250P1C215B1,
STOPEN9250P2C110B1, STOPEN9250P2C140B1
*Static
0.1, 1., 1e-07, 1.
*CONTROLS, ANALYSIS=DISCONTINUOUS
*MODEL CHANGE, ADD
STOPEN9250P1C215B1, STOPEN9250P2C110B1, STOPEN9250P2C140B1
*FIELD
STOPEN9250P1C215BACKFILL1, 1.0
STOPEN9250P2C110BACKFILL1, 1.0
STOPEN9250P2C140BACKFILL1, 1.0
*MODEL CHANGE, REMOVE
STOPEN9250P2C170B1, STOPEN9250P2C200B1, STOPEN9250S1C118B1
**
** OUTPUT REQUESTS
**
*Restart, write, frequency=0
**
** FIELD OUTPUT: F-Output-2
**
*Output, field
*Element Output, directions=YES
ELEDEN, ELEN, ENER, PEEQMAX, PEEQT
*Contact Output
EFENRRTR, ENRRT
**
** FIELD OUTPUT: F-Output-1
**
*Output, field, variable=PRESELECT
**
** HISTORY OUTPUT: H-Output-1
**
*Output, history, variable=PRESELECT
*End Step
** -----
**
** STEP: Step-26
**
*Step, name=Step-26, nlgeom=YES, inc=200, unsymm=YES
Excavation of the STOPEN9250S1C148B1, STOPEN9250S1C178B1,
STOPEN9250S1C208B1 - BACKFILLING STOPEN9250P2C170B1,
STOPEN9250P2C200B1, STOPEN9250S1C118B1
*Static
0.1, 1., 1e-07, 1.
*CONTROLS, ANALYSIS=DISCONTINUOUS
*MODEL CHANGE, ADD
STOPEN9250P2C170B1, STOPEN9250P2C200B1, STOPEN9250S1C118B1
*FIELD
STOPEN9250P2C170BACKFILL1, 1.0
STOPEN9250P2C200BACKFILL1, 1.0
STOPEN9250S1C118BACKFILL1, 1.0
*MODEL CHANGE, REMOVE
STOPEN9250S1C148B1, STOPEN9250S1C178B1, STOPEN9250S1C208B1
**
** OUTPUT REQUESTS
**
*Restart, write, frequency=1
**
** FIELD OUTPUT: F-Output-2
**
*Output, field
*Element Output, directions=YES
ELEDEN, ELEN, ENER, PEEQMAX, PEEQT
*Contact Output
EFENRRTR, ENRRT
**
** FIELD OUTPUT: F-Output-1
**

```

```

*Output, field, variable=PRESELECT
**
** HISTORY OUTPUT: H-Output-1
**
*Output, history, variable=PRESELECT
*End Step
** STEP: Step-27
**
*Step, name=Step-27, nlgeom=YES, inc=200, unsymm=YES
Excavation of the STOPEN9250S2C133B1, STOPEN9250S2C163B1,
STOPEN9250S2C193B1 - BACKFILLING STOPEN9250S1C148B1,
STOPEN9250S1C178B1, STOPEN9250S1C208B1
*Static
0.1, 1., 1e-07, 1.
*CONTROLS,ANALYSIS=DISCONTINUOUS
*MODEL CHANGE, ADD
STOPEN9250S1C148B1, STOPEN9250S1C178B1, STOPEN9250S1C208B1
*FIELD
STOPEN9250S1C148BACKFILL1, 1.0
STOPEN9250S1C178BACKFILL1, 1.0
STOPEN9250S1C208BACKFILL1, 1.0
*MODEL CHANGE, REMOVE
STOPEN9250S2C133B1, STOPEN9250S2C163B1, STOPEN9250S2C193B1
**
** OUTPUT REQUESTS
**
*Restart, write, frequency=0
**
** FIELD OUTPUT: F-Output-2
**
*Output, field
*Element Output, directions=YES
ELEDEN, ELEN, ENER, PEEQMAX, PEEQT
*Contact Output
EFENRRTR, ENRRTR
**
** FIELD OUTPUT: F-Output-1
**
*Output, field, variable=PRESELECT
**
** HISTORY OUTPUT: H-Output-1
**
*Output, history, variable=PRESELECT
*End Step
** -----
**
** STEP: Step-30
**
*Step, name=Step-30, nlgeom=YES, inc=200, unsymm=YES
Excavation of the STOPEN9050P2C80B1, STOPEN9050P2C110B1,
STOPEN9050P2C140B1 - BACKFILLING STOPEN9050P1C125B1,
STOPEN9050P1C155B1, STOPEN9050P1C185B1
*Static
0.1, 1., 1e-07, 1.
*CONTROLS,ANALYSIS=DISCONTINUOUS
*MODEL CHANGE, ADD
STOPEN9050P1C125B1, STOPEN9050P1C155B1, STOPEN9050P1C185B1
*FIELD
STOPEN9050P1C125BACKFILL1, 1.0
STOPEN9050P1C155BACKFILL1, 1.0
STOPEN9050P1C185BACKFILL1, 1.0
*MODEL CHANGE, REMOVE
STOPEN9050P2C80B1, STOPEN9050P2C110B1, STOPEN9050P2C140B1
**
** OUTPUT REQUESTS
**
*Restart, write, frequency=1
**
** FIELD OUTPUT: F-Output-2
**
*Output, field
*Element Output, directions=YES
ELEDEN, ELEN, ENER, PEEQMAX, PEEQT
*Contact Output
EFENRRTR, ENRRTR
**
** FIELD OUTPUT: F-Output-1
**
*Output, field, variable=PRESELECT
**
** HISTORY OUTPUT: H-Output-1
**
*Output, history, variable=PRESELECT
*End Step
** STEP: Step-28
**
*Step, name=Step-28, nlgeom=YES, inc=200, unsymm=YES
Excavation of the STOPEN9250S2C223B1, STOPEN9050P1C65B1,
STOPEN9050P1C95B1 - BACKFILLING STOPEN9250S2C133B1,
STOPEN9250S2C163B1, STOPEN9250S2C193B1
*Static
0.1, 1., 1e-07, 1.
*CONTROLS,ANALYSIS=DISCONTINUOUS
*MODEL CHANGE, ADD
STOPEN9250S2C133B1, STOPEN9250S2C163B1, STOPEN9250S2C193B1
*FIELD
STOPEN9250S2C133BACKFILL1, 1.0
STOPEN9250S2C163BACKFILL1, 1.0
STOPEN9250S2C193BACKFILL1, 1.0
*MODEL CHANGE, REMOVE
STOPEN9250S2C223B1, STOPEN9050P1C65B1, STOPEN9050P1C95B1
**
** OUTPUT REQUESTS
**
*Restart, write, frequency=1
**
** FIELD OUTPUT: F-Output-2
**
*Output, field
*Element Output, directions=YES
ELEDEN, ELEN, ENER, PEEQMAX, PEEQT
*Contact Output
EFENRRTR, ENRRTR
**
** FIELD OUTPUT: F-Output-1
**
*Output, field, variable=PRESELECT
**
** HISTORY OUTPUT: H-Output-1
**
*Output, history, variable=PRESELECT
*End Step
** STEP: Step-29
**
*Step, name=Step-29, nlgeom=YES, inc=200, unsymm=YES
Excavation of the STOPEN9050P1C125B1, STOPEN9050P1C155B1,
STOPEN9050P1C185B1 - BACKFILLING STOPEN9250S2C223B1,
STOPEN9050P1C65B1, STOPEN9050P1C95B1
*Static
0.1, 1., 1e-07, 1.
*CONTROLS,ANALYSIS=DISCONTINUOUS
*MODEL CHANGE, ADD
STOPEN9050P1C125B1, STOPEN9050P1C155B1, STOPEN9050P1C185B1
*FIELD
STOPEN9050P1C125BACKFILL1, 1.0
STOPEN9050P1C155BACKFILL1, 1.0
STOPEN9050P1C185BACKFILL1, 1.0
*MODEL CHANGE, REMOVE
STOPEN9050P2C80B1, STOPEN9050P2C110B1, STOPEN9050P2C140B1
**
** OUTPUT REQUESTS
**
*Restart, write, frequency=0
**
** FIELD OUTPUT: F-Output-2
**

```

```

*Output, field
*Element Output, directions=YES
ELEDEN, ELEN, ENER, PEEQMAX, PEEQT
*Contact Output
EFENRRTR, ENRRT
**
** FIELD OUTPUT: F-Output-1
**
*Output, field, variable=PRESELECT
**
** HISTORY OUTPUT: H-Output-1
**
*Output, history, variable=PRESELECT
*End Step
** -----
**
** STEP: Step-32
**
*Step, name=Step-32, nlgeom=YES, inc=200, unsymm=YES
Excavation of the STOPEN9050S1C88B1, STOPEN9050S1C118B1,
STOPEN9050S1C148B1 - BACKFILLING STOPEN9050P2C170B1,
STOPEN9050P2C200B1, STOPEN9050S1C58B1
*Static
0.1, 1., 1e-07, 1.
*CONTROLS,ANALYSIS=DISCONTINUOUS
*MODEL CHANGE, ADD
STOPEN9050P2C170B1, STOPEN9050P2C200B1, STOPEN9050S1C58B1
*FIELD
STOPEN9050P2C170BACKFILL1, 1.0
STOPEN9050P2C200BACKFILL1, 1.0
STOPEN9050S1C58BACKFILL1, 1.0
*MODEL CHANGE, REMOVE
STOPEN9050S1C88B1, STOPEN9050S1C118B1, STOPEN9050S1C148B1
**
** OUTPUT REQUESTS
**
*Restart, write, frequency=1
**
** FIELD OUTPUT: F-Output-2
**
*Output, field
*Element Output, directions=YES
ELEDEN, ELEN, ENER, PEEQMAX, PEEQT
*Contact Output
EFENRRTR, ENRRT
**
** FIELD OUTPUT: F-Output-1
**
*Output, field, variable=PRESELECT
**
** HISTORY OUTPUT: H-Output-1
**
*Output, history, variable=PRESELECT
*End Step
** STEP: Step-33
**
*Step, name=Step-33, nlgeom=YES, inc=200, unsymm=YES
Excavation of the STOPEN9050S1C178B1, STOPEN9050S1C208B1,
STOPEN9050S2C73B1 - BACKFILLING STOPEN9050S1C88B1,
STOPEN9050S1C118B1, STOPEN9050S1C148B1
*Static
0.1, 1., 1e-07, 1.
*CONTROLS,ANALYSIS=DISCONTINUOUS
*MODEL CHANGE, ADD
STOPEN9050S1C88B1, STOPEN9050S1C118B1, STOPEN9050S1C148B1
*FIELD
STOPEN9050S1C88BACKFILL1, 1.0
STOPEN9050S1C118BACKFILL1, 1.0
STOPEN9050S1C148BACKFILL1, 1.0
*MODEL CHANGE, REMOVE
STOPEN9050S1C178B1, STOPEN9050S1C208B1, STOPEN9050S2C73B1
**
** OUTPUT REQUESTS
**
*Restart, write, frequency=0
**
** FIELD OUTPUT: F-Output-2
**
*Output, field
*Element Output, directions=YES
ELEDEN, ELEN, ENER, PEEQMAX, PEEQT
*Contact Output
EFENRRTR, ENRRT
**
** FIELD OUTPUT: F-Output-1
**
*Output, field, variable=PRESELECT
**
** HISTORY OUTPUT: H-Output-1
**
*Output, history, variable=PRESELECT
*End Step
** -----
**
** STEP: Step-34
**
*Step, name=Step-34, nlgeom=YES, inc=200, unsymm=YES
Excavation of the STOPEN9050S2C103B1, STOPEN9050S2C133B1,
STOPEN9050S2C163B1 - BACKFILLING STOPEN9050S1C178B1,
STOPEN9050S1C208B1, STOPEN9050S2C73B1
*Static
0.1, 1., 1e-07, 1.
*CONTROLS,ANALYSIS=DISCONTINUOUS
*MODEL CHANGE, ADD
STOPEN9050S1C178B1, STOPEN9050S1C208B1, STOPEN9050S2C73B1
*FIELD
STOPEN9050S1C178BACKFILL1, 1.0
STOPEN9050S1C208BACKFILL1, 1.0
STOPEN9050S2C73BACKFILL1, 1.0
*MODEL CHANGE, REMOVE
STOPEN9050S2C103B1, STOPEN9050S2C133B1, STOPEN9050S2C163B1
**
** OUTPUT REQUESTS
**
*Restart, write, frequency=1
**
** FIELD OUTPUT: F-Output-2
**
*Output, field
*Element Output, directions=YES
ELEDEN, ELEN, ENER, PEEQMAX, PEEQT
*Contact Output
EFENRRTR, ENRRT
**
** FIELD OUTPUT: F-Output-1
**
*Output, field, variable=PRESELECT
**
** HISTORY OUTPUT: H-Output-1
**
*Output, history, variable=PRESELECT
*End Step
** STEP: Step-35
**
*Step, name=Step-35, nlgeom=YES, inc=200, unsymm=YES
Excavation of the STOPEN9050S2C193B1, STOPEN9075P1C65B1,
STOPEN9075P1C95B1 - BACKFILLING STOPEN9050S2C103B1,
STOPEN9050S2C133B1, STOPEN9050S2C163B1
*Static
0.1, 1., 1e-07, 1.
*CONTROLS,ANALYSIS=DISCONTINUOUS
*MODEL CHANGE, ADD
STOPEN9050S2C103B1, STOPEN9050S2C133B1, STOPEN9050S2C163B1
*FIELD
STOPEN9050S2C103BACKFILL1, 1.0
STOPEN9050S2C133BACKFILL1, 1.0
STOPEN9050S2C163BACKFILL1, 1.0
*MODEL CHANGE, REMOVE
STOPEN9050S2C193B1, STOPEN9075P1C65B1, STOPEN9075P1C95B1
**
** OUTPUT REQUESTS
**
*Restart, write, frequency=0
**
** FIELD OUTPUT: F-Output-2
**
*Output, field
*Element Output, directions=YES
ELEDEN, ELEN, ENER, PEEQMAX, PEEQT
*Contact Output
EFENRRTR, ENRRT
**
** FIELD OUTPUT: F-Output-1
**
*Output, field, variable=PRESELECT
**
** HISTORY OUTPUT: H-Output-1
**
*Output, history, variable=PRESELECT
*End Step
** -----
**
** STEP: Step-36
**
*Step, name=Step-36, nlgeom=YES, inc=200, unsymm=YES
Excavation of STOPEN9075P1C125B1, STOPEN9075P1C155B1,
STOPEN9075P1C185B1 - BACKFILLING STOPEN9050S2C193B1,
STOPEN9075P1C65B1, STOPEN9075P1C95B1
*Static
0.1, 1., 1e-07, 1.
*CONTROLS,ANALYSIS=DISCONTINUOUS
*MODEL CHANGE, ADD
STOPEN9050S2C193B1, STOPEN9075P1C65B1, STOPEN9075P1C95B1
*FIELD
STOPEN9050S2C193BACKFILL1, 1.0
STOPEN9050P1C65BACKFILL1, 1.0

```

```

STOPEN9075P1C95BACKFILL1, 1.0
**MODEL CHANGE, REMOVE
STOPEN9075P1C125B1, STOPEN9075P1C155B1, STOPEN9075P1C185B1
**
** OUTPUT REQUESTS
**
*Restart, write, frequency=1
**
** FIELD OUTPUT: F-Output-2
**
*Output, field
*Element Output, directions=YES
ELEDEN, ELEN, ENER, PEEQMAX, PEEQT
*Contact Output
EFENRRTR, ENRRTR
**
** FIELD OUTPUT: F-Output-1
**
*Output, field, variable=PRESELECT
**
** HISTORY OUTPUT: H-Output-1
**
*Output, history, variable=PRESELECT
*End Step
** STEP: Step-37
**
*Step, name=Step-37, nlgeom=YES, inc=200, unsymm=YES
Excavation of the STOPEN9075P2C80B1, STOPEN9075P2C110B1,
STOPEN9075P2C140B1 - BACKFILLING STOPEN9075P1C125B1,
STOPEN9075P1C155B1, STOPEN9075P1C185B1
*Static
0.1, 1., 1e-07, 1.
*CONTROLS,ANALYSIS=DISCONTINUOUS
*MODEL CHANGE, ADD
STOPEN9075P1C125B1, STOPEN9075P1C155B1, STOPEN9075P1C185B1
*FIELD
STOPEN9075P1C125BACKFILL1, 1.0
STOPEN9075P1C155BACKFILL1, 1.0
STOPEN9075P1C185BACKFILL1, 1.0
*MODEL CHANGE, REMOVE
STOPEN9075P2C80B1, STOPEN9075P2C110B1, STOPEN9075P2C140B1
**
** OUTPUT REQUESTS
**
*Restart, write, frequency=0
**
** FIELD OUTPUT: F-Output-2
**
*Output, field
*Element Output, directions=YES
ELEDEN, ELEN, ENER, PEEQMAX, PEEQT
*Contact Output
EFENRRTR, ENRRTR
**
** FIELD OUTPUT: F-Output-1
**
*Output, field, variable=PRESELECT
**
** HISTORY OUTPUT: H-Output-1
**
*Output, history, variable=PRESELECT
*End Step
** -----
**
** STEP: Step-38
**
*Step, name=Step-38, nlgeom=YES, inc=200, unsymm=YES
Excavation of the STOPEN9075P2C170B1, STOPEN9075P2C200B1,
STOPEN9075S1C88B1 - BACKFILLING STOPEN9075P2C80B1,
STOPEN9075P2C110B1, STOPEN9075P2C140B1
*Static
0.1, 1., 1e-07, 1.
*CONTROLS,ANALYSIS=DISCONTINUOUS
*MODEL CHANGE, ADD
STOPEN9075P2C80B1, STOPEN9075P2C110B1, STOPEN9075P2C140B1
*FIELD
STOPEN9075P2C80BACKFILL1, 1.0
STOPEN9075P2C110BACKFILL1, 1.0
STOPEN9075P2C140BACKFILL1, 1.0
*MODEL CHANGE, REMOVE
STOPEN9075P2C170B1, STOPEN9075P2C200B1, STOPEN9075S1C88B1
**
** OUTPUT REQUESTS
**
*Restart, write, frequency=1
**
** FIELD OUTPUT: F-Output-2
**
*Output, field
*Element Output, directions=YES
ELEDEN, ELEN, ENER, PEEQMAX, PEEQT
*Contact Output
EFENRRTR, ENRRTR
**
** FIELD OUTPUT: F-Output-1
**
*Output, field, variable=PRESELECT
**
** HISTORY OUTPUT: H-Output-1
**
*Output, history, variable=PRESELECT
*End Step
** -----
**
** STEP: Step-39
**
*Step, name=Step-39, nlgeom=YES, inc=200, unsymm=YES
Excavation of the STOPEN9075S1C118B1, STOPEN9075S1C148B1,
STOPEN9075S1C178B1 - BACKFILLING STOPEN9075P2C170B1,
STOPEN9075P2C200B1, STOPEN9075S1C88B1
*Static
0.1, 1., 1e-07, 1.
*CONTROLS,ANALYSIS=DISCONTINUOUS
*MODEL CHANGE, ADD
STOPEN9075P2C170B1, STOPEN9075P2C200B1, STOPEN9075S1C88B1
*FIELD
STOPEN9075P2C170BACKFILL1, 1.0
STOPEN9075P2C200BACKFILL1, 1.0
STOPEN9075S1C88BACKFILL1, 1.0
*MODEL CHANGE, REMOVE
STOPEN9075S1C118B1, STOPEN9075S1C148B1, STOPEN9075S1C178B1
**
** OUTPUT REQUESTS
**
*Restart, write, frequency=0
**
** FIELD OUTPUT: F-Output-2
**
*Output, field
*Element Output, directions=YES
ELEDEN, ELEN, ENER, PEEQMAX, PEEQT
*Contact Output
EFENRRTR, ENRRTR
**
** FIELD OUTPUT: F-Output-1
**
*Output, field, variable=PRESELECT
**
** HISTORY OUTPUT: H-Output-1
**
*Output, history, variable=PRESELECT
*End Step
** -----
**
** STEP: Step-40
**
*Step, name=Step-40, nlgeom=YES, inc=200, unsymm=YES
Excavation of the STOPEN9075S1C208B1, STOPEN9075S2C73B1,
STOPEN9075S2C103B1 - BACKFILLING STOPEN9075S1C118B1,
STOPEN9075S1C148B1, STOPEN9075S1C178B1
*Static
0.1, 1., 1e-07, 1.
*CONTROLS,ANALYSIS=DISCONTINUOUS
*MODEL CHANGE, ADD
STOPEN9075S1C118B1, STOPEN9075S1C148B1, STOPEN9075S1C178B1
*FIELD
STOPEN9075S1C118BACKFILL1, 1.0
STOPEN9075S1C148BACKFILL1, 1.0
STOPEN9075S1C178BACKFILL1, 1.0
*MODEL CHANGE, REMOVE
STOPEN9075S1C208B1, STOPEN9075S2C73B1, STOPEN9075S2C103B1
**
** OUTPUT REQUESTS
**
*Restart, write, frequency=1
**
** FIELD OUTPUT: F-Output-2
**
*Output, field
*Element Output, directions=YES
ELEDEN, ELEN, ENER, PEEQMAX, PEEQT
*Contact Output
EFENRRTR, ENRRTR
**
** FIELD OUTPUT: F-Output-1
**
*Output, field, variable=PRESELECT
**
** HISTORY OUTPUT: H-Output-1
**
*Output, history, variable=PRESELECT
*End Step
** -----
**
** STEP: Step-41
**
*Step, name=Step-41, nlgeom=YES, inc=200, unsymm=YES
Excavation of the STOPEN9075S2C133B1, STOPEN9075S2C163B1,
STOPEN9075S2C193B1 - BACKFILLING STOPEN9075S1C208B1,
STOPEN9075S2C73B1, STOPEN9075S2C103B1

```

```

*Static
0.1, 1., 1e-07, 1.
*CONTROLS,ANALYSIS=DISCONTINUOUS
*MODEL CHANGE, ADD
STOPEN9075S1C208B1, STOPEN9075S2C73B1, STOPEN9075S2C103B1
*FIELD
STOPEN9075S1C208BACKFILL1, 1.0
STOPEN9075S2C73BACKFILL1, 1.0
STOPEN9075S2C103BACKFILL1, 1.0
*MODEL CHANGE, REMOVE
STOPEN9075S2C133B1, STOPEN9075S2C163B1, STOPEN9075S2C193B1
**
** OUTPUT REQUESTS
**
*Restart, write, frequency=0
**
** FIELD OUTPUT: F-Output-2
**
*Output, field
*Element Output, directions=YES
ELEDEN, ELEN, ENER, PEEQMAX, PEEQT
*Contact Output
EFENRRTR, ENRRTR
**
** FIELD OUTPUT: F-Output-1
**
*Output, field, variable=PRESELECT
**
** HISTORY OUTPUT: H-Output-1
**
*Output, history, variable=PRESELECT
*End Step
** -----
**
** STEP: Step-42
**
*Step, name=Step-42, nlgeom=YES, inc=200, unsymm=YES
Excavation of the STOPEN9100P1C65B1, STOPEN9100P1C95B1,
STOPEN9100P1C125B1 - BACKFILLING STOPEN9075S2C133B1,
STOPEN9075S2C163B1, STOPEN9075S2C193B1
*Static
0.1, 1., 1e-07, 1.
*CONTROLS,ANALYSIS=DISCONTINUOUS
*MODEL CHANGE, ADD
STOPEN9075S2C133B1, STOPEN9075S2C163B1, STOPEN9075S2C193B1
*FIELD
STOPEN9075S2C133BACKFILL1, 1.0
STOPEN9075S2C163BACKFILL1, 1.0
STOPEN9075S2C193BACKFILL1, 1.0
*MODEL CHANGE, REMOVE
STOPEN9100P1C65B1, STOPEN9100P1C95B1, STOPEN9100P1C125B1
**
** OUTPUT REQUESTS
**
*Restart, write, frequency=1
**
** FIELD OUTPUT: F-Output-2
**
*Output, field
*Element Output, directions=YES
ELEDEN, ELEN, ENER, PEEQMAX, PEEQT
*Contact Output
EFENRRTR, ENRRTR
**
** FIELD OUTPUT: F-Output-1
**
*Output, field, variable=PRESELECT
**
** HISTORY OUTPUT: H-Output-1
**
*Output, history, variable=PRESELECT
*End Step
** STEP: Step-43
**
*Step, name=Step-43, nlgeom=YES, inc=200, unsymm=YES
Excavation of the STOPEN9100P1C155B1, STOPEN9100P1C185B1,
STOPEN9100P2C80B1 - BACKFILLING STOPEN9100P1C65B1,
STOPEN9100P1C95B1, STOPEN9100P1C125B1
*Static
0.1, 1., 1e-07, 1.
*CONTROLS,ANALYSIS=DISCONTINUOUS
*MODEL CHANGE, ADD
STOPEN9100P1C65B1, STOPEN9100P1C95B1, STOPEN9100P1C125B1
*FIELD
STOPEN9100P1C65BACKFILL1, 1.0
STOPEN9100P1C95BACKFILL1, 1.0
STOPEN9100P1C125BACKFILL1, 1.0
*MODEL CHANGE, REMOVE
STOPEN9100P1C155B1, STOPEN9100P1C185B1, STOPEN9100P2C80B1
**
** OUTPUT REQUESTS
**
*Restart, write, frequency=0
**
** FIELD OUTPUT: F-Output-2
**
*Output, field
*Element Output, directions=YES
ELEDEN, ELEN, ENER, PEEQMAX, PEEQT
*Contact Output
EFENRRTR, ENRRTR
**
** FIELD OUTPUT: F-Output-1
**
*Output, field, variable=PRESELECT
**
** HISTORY OUTPUT: H-Output-1
**
** STEP: Step-44
**
*Step, name=Step-44, nlgeom=YES, inc=200, unsymm=YES
Excavation of the STOPEN9100P2C110B1, STOPEN9100P2C140B1,
STOPEN9100P2C170B1 - BACKFILLING STOPEN9100P1C155B1,
STOPEN9100P1C185B1, STOPEN9100P2C80B1
*Static
0.1, 1., 1e-07, 1.
*CONTROLS,ANALYSIS=DISCONTINUOUS
*MODEL CHANGE, ADD
STOPEN9100P1C155B1, STOPEN9100P1C185B1, STOPEN9100P2C80B1
*FIELD
STOPEN9100P1C155BACKFILL1, 1.0
STOPEN9100P1C185BACKFILL1, 1.0
STOPEN9100P2C80BACKFILL1, 1.0
*MODEL CHANGE, REMOVE
STOPEN9100P2C110B1, STOPEN9100P2C140B1, STOPEN9100P2C170B1
**
** OUTPUT REQUESTS
**
*Restart, write, frequency=1
**
** FIELD OUTPUT: F-Output-2
**
*Output, field
*Element Output, directions=YES
ELEDEN, ELEN, ENER, PEEQMAX, PEEQT
*Contact Output
EFENRRTR, ENRRTR
**
** FIELD OUTPUT: F-Output-1
**
*Output, field, variable=PRESELECT
**
** HISTORY OUTPUT: H-Output-1
**
*Output, history, variable=PRESELECT
*End Step
** STEP: Step-45
**
*Step, name=Step-45, nlgeom=YES, inc=200, unsymm=YES
Excavation of the STOPEN9100P2C200B1, STOPEN9100S1C88B1,
STOPEN9100S1C118B1 - BACKFILLING STOPEN9100P2C110B1,
STOPEN9100P2C140B1, STOPEN9100P2C170B1
*Static
0.1, 1., 1e-07, 1.
*CONTROLS,ANALYSIS=DISCONTINUOUS
*MODEL CHANGE, ADD
STOPEN9100P2C110B1, STOPEN9100P2C140B1, STOPEN9100P2C170B1
*FIELD
STOPEN9100P2C110BACKFILL1, 1.0
STOPEN9100P2C140BACKFILL1, 1.0
STOPEN9100P2C170BACKFILL1, 1.0
*MODEL CHANGE, REMOVE
STOPEN9100P2C200B1, STOPEN9100S1C88B1, STOPEN9100S1C118B1
**
** OUTPUT REQUESTS
**
*Restart, write, frequency=0
**
** FIELD OUTPUT: F-Output-2
**
*Output, field
*Element Output, directions=YES
ELEDEN, ELEN, ENER, PEEQMAX, PEEQT
*Contact Output
EFENRRTR, ENRRTR
**
** FIELD OUTPUT: F-Output-1
**
*Output, field, variable=PRESELECT
**
** HISTORY OUTPUT: H-Output-1
**

```

```

*Output, history, variable=PRESELECT
*End Step
** -----
**
** STEP: Step-46
**
*Step, name=Step-46, nlgeom=YES, inc=200, unsymm=YES
Excavation of the STOPEN9100S1C148B1, STOPEN9100S1C178B1,
STOPEN9100S1C208B1 - BACKFILLING STOPEN9100P2C200B1,
STOPEN9100S1C88B1, STOPEN9100S1C118B1
*Static
0.1, 1., 1e-07, 1.
*CONTROLS,ANALYSIS=DISCONTINUOUS
*MODEL CHANGE, ADD
STOPEN9100P2C200B1, STOPEN9100S1C88B1, STOPEN9100S1C118B1
*FIELD
STOPEN9100P2C200BACKFILL1, 1.0
STOPEN9100S1C88BACKFILL1, 1.0
STOPEN9100S1C118BACKFILL1, 1.0
*MODEL CHANGE, REMOVE
STOPEN9100S1C148B1, STOPEN9100S1C178B1, STOPEN9100S1C208B1
**
** OUTPUT REQUESTS
**
*Restart, write, frequency=1
**
** FIELD OUTPUT: F-Output-2
**
*Output, field
*Element Output, directions=YES
ELEDEN, ELEN, ENER, PEEQMAX, PEEQT
*Contact Output
EFENRRTR, ENRRTR
**
** FIELD OUTPUT: F-Output-1
**
*Output, field, variable=PRESELECT
**
** HISTORY OUTPUT: H-Output-1
**
*Output, history, variable=PRESELECT
*End Step
** STEP: Step-47
**
*Step, name=Step-47, nlgeom=YES, inc=200, unsymm=YES
Excavation of the STOPEN9100S2C73B1, STOPEN9100S2C103B1 - BACKFILLING
STOPEN9100S1C148B1, STOPEN9100S1C178B1, STOPEN9100S1C208B1
*Static
0.1, 1., 1e-07, 1.
*CONTROLS,ANALYSIS=DISCONTINUOUS
*MODEL CHANGE, ADD
STOPEN9100S1C148B1, STOPEN9100S1C178B1, STOPEN9100S1C208B1
*FIELD
STOPEN9100S1C148BACKFILL1, 1.0
STOPEN9100S1C178BACKFILL1, 1.0
STOPEN9100S1C208BACKFILL1, 1.0
*MODEL CHANGE, REMOVE
STOPEN9100S2C73B1, STOPEN9100S2C103B1
**
** OUTPUT REQUESTS
**
*Restart, write, frequency=0
**
** FIELD OUTPUT: F-Output-2
**
*Output, field
*Element Output, directions=YES
ELEDEN, ELEN, ENER, PEEQMAX, PEEQT
*Contact Output
EFENRRTR, ENRRTR
**
** FIELD OUTPUT: F-Output-1
**
*Output, field, variable=PRESELECT
**
** HISTORY OUTPUT: H-Output-1
**
*Output, history, variable=PRESELECT
*End Step
** -----
**
** STEP: Step-48
**
*Step, name=Step-48, nlgeom=YES, inc=200, unsymm=YES
Excavation of the STOPEN9100S2C133B1, STOPEN9100S2C163B1,
STOPEN9100S2C193B1 - BACKFILLING STOPEN9100S2C73B1,
STOPEN9100S2C103B1
*Static
0.1, 1., 1e-07, 1.
*CONTROLS,ANALYSIS=DISCONTINUOUS
*MODEL CHANGE, ADD
STOPEN9100S2C73B1, STOPEN9100S2C103B1
*FIELD
STOPEN9100S2C73BACKFILL1, 1.0
STOPEN9100S2C103BACKFILL1, 1.0
STOPEN9100S2C133BACKFILL1, 1.0
STOPEN9100S2C163BACKFILL1, 1.0
STOPEN9100S2C193BACKFILL1, 1.0
*MODEL CHANGE, REMOVE
STOPEN9100S2C133B1, STOPEN9100S2C163B1, STOPEN9100S2C193B1
**
** OUTPUT REQUESTS
**
*Restart, write, frequency=1
**
** FIELD OUTPUT: F-Output-2
**
*Output, field
*Element Output, directions=YES
ELEDEN, ELEN, ENER, PEEQMAX, PEEQT
*Contact Output
EFENRRTR, ENRRTR
**
** FIELD OUTPUT: F-Output-1
**
*Output, field, variable=PRESELECT
**
** HISTORY OUTPUT: H-Output-1
**
*Output, history, variable=PRESELECT
*End Step
** STEP: Step-49
**
*Step, name=Step-49, nlgeom=YES, inc=200, unsymm=YES
Excavation of the STOPEN9125P1C95B1, STOPEN9125P1C125B1,
STOPEN9125P1C155B1 - BACKFILLING STOPEN9100S2C133B1,
STOPEN9100S2C163B1, STOPEN9100S2C193B1
*Static
0.1, 1., 1e-07, 1.
*CONTROLS,ANALYSIS=DISCONTINUOUS
*MODEL CHANGE, ADD
STOPEN9100S2C133B1, STOPEN9100S2C163B1, STOPEN9100S2C193B1
*FIELD
STOPEN9100S2C133BACKFILL1, 1.0
STOPEN9100S2C163BACKFILL1, 1.0
STOPEN9100S2C193BACKFILL1, 1.0
*MODEL CHANGE, REMOVE
STOPEN9125P1C95B1, STOPEN9125P1C125B1, STOPEN9125P1C155B1
**
** OUTPUT REQUESTS
**
*Restart, write, frequency=0
**
** FIELD OUTPUT: F-Output-2
**
*Output, field
*Element Output, directions=YES
ELEDEN, ELEN, ENER, PEEQMAX, PEEQT
*Contact Output
EFENRRTR, ENRRTR
**
** FIELD OUTPUT: F-Output-1
**
*Output, field, variable=PRESELECT
**
** HISTORY OUTPUT: H-Output-1
**
*Output, history, variable=PRESELECT
*End Step
** -----
**
** STEP: Step-50
**
*Step, name=Step-50, nlgeom=YES, inc=200, unsymm=YES
Excavation of the STOPEN9125P1C185B1 - BACKFILLING STOPEN9125P1C95B1,
STOPEN9125P1C125B1, STOPEN9125P1C155B1
*Static
0.1, 1., 1e-07, 1.
*CONTROLS,ANALYSIS=DISCONTINUOUS
*MODEL CHANGE, ADD
STOPEN9125P1C95B1, STOPEN9125P1C125B1, STOPEN9125P1C155B1
*FIELD
STOPEN9125P1C95BACKFILL1, 1.0
STOPEN9125P1C125BACKFILL1, 1.0
STOPEN9125P1C155BACKFILL1, 1.0
*MODEL CHANGE, REMOVE
STOPEN9125P1C185B1
**
** OUTPUT REQUESTS
**
*Restart, write, frequency=1
**
** FIELD OUTPUT: F-Output-2
**
*Output, field
*Element Output, directions=YES
ELEDEN, ELEN, ENER, PEEQMAX, PEEQT
*Contact Output
EFENRRTR, ENRRTR

```

```

**
** FIELD OUTPUT: F-Output-1
**
**Output, field, variable=PRESELECT
**
** HISTORY OUTPUT: H-Output-1
**
**Output, history, variable=PRESELECT
**End Step
** STEP: Step-51
**
**Step, name=Step-51, nlgeom=YES, inc=200, unsymm=YES
Excavation of the STOPEN9125P1C215B1, STOPEN9125P2C80B1 - BACKFILLING
STOPEN9125P1C185B1
**Static
0.1, 1., 1e-07, 1.
**CONTROLS,ANALYSIS=DISCONTINUOUS
**MODEL CHANGE, ADD
STOPEN9125P1C185B1
**FIELD
STOPEN9125P1C185BACKFILL1, 1.0
**MODEL CHANGE, REMOVE
STOPEN9125P1C215B1, STOPEN9125P2C80B1
**
** OUTPUT REQUESTS
**
**Restart, write, frequency=0
**
** FIELD OUTPUT: F-Output-2
**
**Output, field
**Element Output, directions=YES
ELEDEN, ELEN, ENER, PEEQMAX, PEEQT
**Contact Output
EFENRRTR, ENRRT
**
** FIELD OUTPUT: F-Output-1
**
**Output, field, variable=PRESELECT
**
** HISTORY OUTPUT: H-Output-1
**
**Output, history, variable=PRESELECT
**End Step
**-----
**
** STEP: Step-52
**
**Step, name=Step-52, nlgeom=YES, inc=200, unsymm=YES
Excavation of the STOPEN9125P2C110B1, STOPEN9125P2C140B1,
STOPEN9125P2C170B1 - BACKFILLING STOPEN9125P1C215B1,
STOPEN9125P2C80B1
**Static
0.1, 1., 1e-07, 1.
**CONTROLS,ANALYSIS=DISCONTINUOUS
**MODEL CHANGE, ADD
STOPEN9125P1C215B1, STOPEN9125P2C80B1
**FIELD
STOPEN9125P1C215BACKFILL1, 1.0
STOPEN9125P2C80BACKFILL1, 1.0
**MODEL CHANGE, REMOVE
STOPEN9125P2C110B1, STOPEN9125P2C140B1, STOPEN9125P2C170B1
**
** OUTPUT REQUESTS
**
**Restart, write, frequency=1
**
** FIELD OUTPUT: F-Output-2
**
**Output, field
**Element Output, directions=YES
ELEDEN, ELEN, ENER, PEEQMAX, PEEQT
**Contact Output
EFENRRTR, ENRRT
**
** FIELD OUTPUT: F-Output-1
**
**Output, field, variable=PRESELECT
**
** HISTORY OUTPUT: H-Output-1
**
**Output, history, variable=PRESELECT
**End Step
** STEP: Step-53
**
**Step, name=Step-53, nlgeom=YES, inc=200, unsymm=YES
Excavation of the STOPEN9125P2C200B1, STOPEN9125S1C88B1,
STOPEN9125S1C118B1 - BACKFILLING STOPEN9125P2C110B1,
STOPEN9125P2C140B1, STOPEN9125P2C170B1
**Static
0.1, 1., 1e-07, 1.
**CONTROLS,ANALYSIS=DISCONTINUOUS
**MODEL CHANGE, ADD
STOPEN9125P2C110B1, STOPEN9125P2C140B1, STOPEN9125P2C170B1,
STOPEN9125S1C88B1, STOPEN9125S1C118B1
**FIELD
STOPEN9125P2C110BACKFILL1, 1.0
STOPEN9125P2C140BACKFILL1, 1.0
STOPEN9125P2C170BACKFILL1, 1.0
**MODEL CHANGE, REMOVE
STOPEN9125P2C200B1, STOPEN9125S1C88B1, STOPEN9125S1C118B1
**
** OUTPUT REQUESTS
**
**Restart, write, frequency=0
**
** FIELD OUTPUT: F-Output-2
**
**Output, field
**Element Output, directions=YES
ELEDEN, ELEN, ENER, PEEQMAX, PEEQT
**Contact Output
EFENRRTR, ENRRT
**
** FIELD OUTPUT: F-Output-1
**
**Output, field, variable=PRESELECT
**
** HISTORY OUTPUT: H-Output-1
**
**Output, history, variable=PRESELECT
**End Step
**-----
**
** STEP: Step-54
**
**Step, name=Step-54, nlgeom=YES, inc=200, unsymm=YES
Excavation of the STOPEN9125S1C148B1, STOPEN9125S1C178B1,
STOPEN9125S1C208B1 - BACKFILLING STOPEN9125P2C200B1,
STOPEN9125S1C88B1, STOPEN9125S1C118B1
**Static
0.1, 1., 1e-07, 1.
**CONTROLS,ANALYSIS=DISCONTINUOUS
**MODEL CHANGE, ADD
STOPEN9125P2C200B1, STOPEN9125S1C88B1, STOPEN9125S1C118B1
**FIELD
STOPEN9125P2C200BACKFILL1, 1.0
STOPEN9125S1C88BACKFILL1, 1.0
STOPEN9125S1C118BACKFILL1, 1.0
**MODEL CHANGE, REMOVE
STOPEN9125S1C148B1, STOPEN9125S1C178B1, STOPEN9125S1C208B1
**
** OUTPUT REQUESTS
**
**Restart, write, frequency=1
**
** FIELD OUTPUT: F-Output-2
**
**Output, field
**Element Output, directions=YES
ELEDEN, ELEN, ENER, PEEQMAX, PEEQT
**Contact Output
EFENRRTR, ENRRT
**
** FIELD OUTPUT: F-Output-1
**
**Output, field, variable=PRESELECT
**
** HISTORY OUTPUT: H-Output-1
**
**Output, history, variable=PRESELECT
**End Step
** STEP: Step-55
**
**Step, name=Step-55, nlgeom=YES, inc=200, unsymm=YES
Excavation of the STOPEN9125S2C73B1, STOPEN9125S2C103B1,
STOPEN9125S2C133B1 - BACKFILLING STOPEN9125S1C148B1,
STOPEN9125S1C178B1, STOPEN9125S1C208B1
**Static
0.1, 1., 1e-07, 1.
**CONTROLS,ANALYSIS=DISCONTINUOUS
**MODEL CHANGE, ADD
STOPEN9125S1C148B1, STOPEN9125S1C178B1, STOPEN9125S1C208B1
**FIELD
STOPEN9125S1C148BACKFILL1, 1.0
STOPEN9125S1C178BACKFILL1, 1.0
STOPEN9125S1C208BACKFILL1, 1.0
**MODEL CHANGE, REMOVE
STOPEN9125S2C73B1, STOPEN9125S2C103B1, STOPEN9125S2C133B1
**
** OUTPUT REQUESTS
**
**Restart, write, frequency=0
**
** FIELD OUTPUT: F-Output-2
**
**Output, field

```

```

*Element Output, directions=YES
ELEDEN, ELEN, ENER, PEEQMAX, PEEQT
*Contact Output
EFENRRTR, ENRRTR
**
** FIELD OUTPUT: F-Output-1
**
*Output, field, variable=PRESELECT
**
** HISTORY OUTPUT: H-Output-1
**
*Output, history, variable=PRESELECT
*End Step
** -----
**
** STEP: Step-56
**
*Step, name=Step-56, nlgeom=YES, inc=200, unsymm=YES
Excavation of the STOPEN9125S2C163B1, STOPEN9125S2C193B1,
STOPEN8950P1C95B1 - BACKFILLING STOPEN9125S2C73B1,
STOPEN9125S2C103B1, STOPEN9125S2C133B1
*Static
0.1, 1., 1e-07, 1.
*CONTROLS,ANALYSIS=DISCONTINUOUS
*MODEL CHANGE, ADD
STOPEN9125S2C73B1, STOPEN9125S2C103B1, STOPEN9125S2C133B1
*FIELD
STOPEN9125S2C73BACKFILL1, 1.0
STOPEN9125S2C103BACKFILL1, 1.0
STOPEN9125S2C133BACKFILL1, 1.0
*MODEL CHANGE, REMOVE
STOPEN9125S2C163B1, STOPEN9125S2C193B1, STOPEN8950P1C95B1
**
** OUTPUT REQUESTS
**
*Restart, write, frequency=1
**
** FIELD OUTPUT: F-Output-2
**
*Output, field
*Element Output, directions=YES
ELEDEN, ELEN, ENER, PEEQMAX, PEEQT
*Contact Output
EFENRRTR, ENRRTR
**
** FIELD OUTPUT: F-Output-1
**
*Output, field, variable=PRESELECT
**
** HISTORY OUTPUT: H-Output-1
**
*Output, history, variable=PRESELECT
*End Step
** STEP: Step-57
**
*Step, name=Step-57, nlgeom=YES, inc=200, unsymm=YES
Excavation of the STOPEN8950P1C125B1, STOPEN8950P1C155B1,
STOPEN8950P1C185B1 - BACKFILLING STOPEN9125S2C163B1,
STOPEN9125S2C193B1, STOPEN8950P1C95B1
*Static
0.1, 1., 1e-07, 1.
*CONTROLS,ANALYSIS=DISCONTINUOUS
*MODEL CHANGE, ADD
STOPEN9125S2C163B1, STOPEN9125S2C193B1, STOPEN8950P1C95B1
*FIELD
STOPEN9125S2C163BACKFILL1, 1.0
STOPEN9125S2C193BACKFILL1, 1.0
STOPEN8950P1C95BACKFILL1, 1.0
*MODEL CHANGE, REMOVE
STOPEN8950P1C125B1, STOPEN8950P1C155B1, STOPEN8950P1C185B1
**
** OUTPUT REQUESTS
**
*Restart, write, frequency=0
**
** FIELD OUTPUT: F-Output-2
**
*Output, field
*Element Output, directions=YES
ELEDEN, ELEN, ENER, PEEQMAX, PEEQT
*Contact Output
EFENRRTR, ENRRTR
**
** FIELD OUTPUT: F-Output-1
**
*Output, field, variable=PRESELECT
**
** HISTORY OUTPUT: H-Output-1
**
*Output, history, variable=PRESELECT
*End Step
** -----
**
** STEP: Step-58
**
*Step, name=Step-58, nlgeom=YES, inc=200, unsymm=YES
Excavation of the STOPEN8950P2C80B1, STOPEN8950P2C110B1,
STOPEN8950P2C140B1 - BACKFILLING STOPEN8950P1C125B1,
STOPEN8950P1C155B1, STOPEN8950P1C185B1
*Static
0.1, 1., 1e-07, 1.
*CONTROLS,ANALYSIS=DISCONTINUOUS
*MODEL CHANGE, ADD
STOPEN8950P1C125B1, STOPEN8950P1C155B1, STOPEN8950P1C185B1
*FIELD
STOPEN8950P1C125BACKFILL1, 1.0
STOPEN8950P1C155BACKFILL1, 1.0
STOPEN8950P1C185BACKFILL1, 1.0
*MODEL CHANGE, REMOVE
STOPEN8950P2C80B1, STOPEN8950P2C110B1, STOPEN8950P2C140B1
**
** OUTPUT REQUESTS
**
*Restart, write, frequency=1
**
** FIELD OUTPUT: F-Output-2
**
*Output, field
*Element Output, directions=YES
ELEDEN, ELEN, ENER, PEEQMAX, PEEQT
*Contact Output
EFENRRTR, ENRRTR
**
** FIELD OUTPUT: F-Output-1
**
*Output, field, variable=PRESELECT
**
** HISTORY OUTPUT: H-Output-1
**
*Output, history, variable=PRESELECT
*End Step
** STEP: Step-59
**
*Step, name=Step-59, nlgeom=YES, inc=200, unsymm=YES
Excavation of the STOPEN8950P2C170B1, STOPEN8950P2C200B1,
STOPEN8950S1C58B1 - BACKFILLING STOPEN8950P2C80B1,
STOPEN8950P2C110B1, STOPEN8950P2C140B1
*Static
0.1, 1., 1e-07, 1.
*CONTROLS,ANALYSIS=DISCONTINUOUS
*MODEL CHANGE, ADD
STOPEN8950P2C80B1, STOPEN8950P2C110B1, STOPEN8950P2C140B1
*FIELD
STOPEN8950P2C80BACKFILL1, 1.0
STOPEN8950P2C110BACKFILL1, 1.0
STOPEN8950P2C140BACKFILL1, 1.0
*MODEL CHANGE, REMOVE
STOPEN8950P2C170B1, STOPEN8950P2C200B1, STOPEN8950S1C58B1
**
** OUTPUT REQUESTS
**
*Restart, write, frequency=0
**
** FIELD OUTPUT: F-Output-2
**
*Output, field
*Element Output, directions=YES
ELEDEN, ELEN, ENER, PEEQMAX, PEEQT
*Contact Output
EFENRRTR, ENRRTR
**
** FIELD OUTPUT: F-Output-1
**
*Output, field, variable=PRESELECT
**
** HISTORY OUTPUT: H-Output-1
**
*Output, history, variable=PRESELECT
*End Step
** -----
**
** STEP: Step-60
**
*Step, name=Step-60, nlgeom=YES, inc=200, unsymm=YES
Excavation of the STOPEN8950S1C88B1, STOPEN8950S1C118B1,
STOPEN8950S1C148B1 - BACKFILLING STOPEN8950P2C170B1,
STOPEN8950P2C200B1, STOPEN8950S1C58B1
*Static
0.1, 1., 1e-07, 1.
*CONTROLS,ANALYSIS=DISCONTINUOUS
*MODEL CHANGE, ADD
STOPEN8950P2C170B1, STOPEN8950P2C200B1, STOPEN8950S1C58B1
*FIELD
STOPEN8950P2C170BACKFILL1, 1.0
STOPEN8950P2C200BACKFILL1, 1.0
STOPEN8950S1C58BACKFILL1, 1.0

```

```

*MODEL CHANGE, REMOVE
STOPEN8950S1C88B1, STOPEN8950S1C118B1, STOPEN8950S1C148B1
**
** OUTPUT REQUESTS
**
*Restart, write, frequency=1
**
** FIELD OUTPUT: F-Output-2
**
*Output, field
*Element Output, directions=YES
ELEDEN, ELEN, ENER, PEEQMAX, PEEQT
*Contact Output
EFENRRTR, ENRRT
**
** FIELD OUTPUT: F-Output-1
**
*Output, field, variable=PRESELECT
**
** HISTORY OUTPUT: H-Output-1
**
*Output, history, variable=PRESELECT
*End Step
** STEP: Step-61
**
*Step, name=Step-61, nlgeom=YES, inc=200, unsymm=YES
Excavation of the STOPEN8950S1C178B1, STOPEN8950S1C208B1,
STOPEN8950S2C73B1 - BACKFILLING STOPEN8950S1C88B1,
STOPEN8950S1C118B1, STOPEN8950S1C148B1
*Static
0.1, 1., 1e-07, 1.
*CONTROLS,ANALYSIS=DISCONTINUOUS
*MODEL CHANGE, ADD
STOPEN8950S1C88B1, STOPEN8950S1C118B1, STOPEN8950S1C148B1
*FIELD
STOPEN8950S1C88BACKFILL1, 1.0
STOPEN8950S1C118BACKFILL1, 1.0
STOPEN8950S1C148BACKFILL1, 1.0
*MODEL CHANGE, REMOVE
STOPEN8950S1C178B1, STOPEN8950S1C208B1, STOPEN8950S2C73B1
**
** OUTPUT REQUESTS
**
*Restart, write, frequency=0
**
** FIELD OUTPUT: F-Output-2
**
*Output, field
*Element Output, directions=YES
ELEDEN, ELEN, ENER, PEEQMAX, PEEQT
*Contact Output
EFENRRTR, ENRRT
**
** FIELD OUTPUT: F-Output-1
**
*Output, field, variable=PRESELECT
**
** HISTORY OUTPUT: H-Output-1
**
*Output, history, variable=PRESELECT
*End Step
** -----
**
** STEP: Step-62
**
*Step, name=Step-62, nlgeom=YES, inc=200, unsymm=YES
Excavation of the STOPEN8950S2C103B1, STOPEN8950S2C133B1,
STOPEN8950S2C163B1 - BACKFILLING STOPEN8950S1C178B1,
STOPEN8950S1C208B1, STOPEN8950S2C73B1
*Static
0.1, 1., 1e-07, 1.
*CONTROLS,ANALYSIS=DISCONTINUOUS
*MODEL CHANGE, ADD
STOPEN8950S1C178B1, STOPEN8950S1C208B1, STOPEN8950S2C73B1
*FIELD
STOPEN8950S1C178BACKFILL1, 1.0
STOPEN8950S1C208BACKFILL1, 1.0
STOPEN8950S2C73BACKFILL1, 1.0
*MODEL CHANGE, REMOVE
STOPEN8950S2C103B1, STOPEN8950S2C133B1, STOPEN8950S2C163B1
**
** OUTPUT REQUESTS
**
*Restart, write, frequency=1
**
** FIELD OUTPUT: F-Output-2
**
*Output, field
*Element Output, directions=YES
ELEDEN, ELEN, ENER, PEEQMAX, PEEQT
*Contact Output
EFENRRTR, ENRRT
**

```

```

** FIELD OUTPUT: F-Output-1
**
** Output, field, variable=PRESELECT
**
** HISTORY OUTPUT: H-Output-1
**
** Output, history, variable=PRESELECT
** End Step
** STEP: Step-63
**
*Step, name=Step-63, nlgeom=YES, inc=200, unsymm=YES
Excavation of the STOPEN8950S2C193B1, STOPEN8975P1C65B1,
STOPEN8975P1C95B1 - BACKFILLING STOPEN8950S2C103B1,
STOPEN8950S2C133B1, STOPEN8950S2C163B1
*Static
0.1, 1., 1e-07, 1.
*CONTROLS,ANALYSIS=DISCONTINUOUS
*MODEL CHANGE, ADD
STOPEN8950S2C103B1, STOPEN8950S2C133B1, STOPEN8950S2C163B1
*FIELD
STOPEN8950S2C103BACKFILL1, 1.0
STOPEN8950S2C133BACKFILL1, 1.0
STOPEN8950S2C163BACKFILL1, 1.0
*MODEL CHANGE, REMOVE
STOPEN8950S2C193B1, STOPEN8975P1C65B1, STOPEN8975P1C95B1
**
** OUTPUT REQUESTS
**
*Restart, write, frequency=0
**
** FIELD OUTPUT: F-Output-2
**
** Output, field
** Element Output, directions=YES
** ELEDEN, ELEN, ENER, PEEQMAX, PEEQT
** *Contact Output
** EFENRRTR, ENRRT
**
** FIELD OUTPUT: F-Output-1
**
** Output, field, variable=PRESELECT
**
** HISTORY OUTPUT: H-Output-1
**
** Output, history, variable=PRESELECT
** End Step
** -----
**
** STEP: Step-64
**
*Step, name=Step-64, nlgeom=YES, inc=200, unsymm=YES
Excavation of the STOPEN8975P1C125B1, STOPEN8975P1C155B1,
STOPEN8975P1C185B1 - BACKFILLING STOPEN8950S2C193B1,
STOPEN8975P1C65B1, STOPEN8975P1C95B1
*Static
0.1, 1., 1e-07, 1.
*CONTROLS,ANALYSIS=DISCONTINUOUS
*MODEL CHANGE, ADD
STOPEN8950S2C193B1, STOPEN8975P1C65B1, STOPEN8975P1C95B1
*FIELD
STOPEN8950S2C193BACKFILL1, 1.0
STOPEN8975P1C65BACKFILL1, 1.0
STOPEN8975P1C95BACKFILL1, 1.0
*MODEL CHANGE, REMOVE
STOPEN8975P1C125B1, STOPEN8975P1C155B1, STOPEN8975P1C185B1
**
** OUTPUT REQUESTS
**
*Restart, write, frequency=1
**
** FIELD OUTPUT: F-Output-2
**
** Output, field
** Element Output, directions=YES
** ELEDEN, ELEN, ENER, PEEQMAX, PEEQT
** *Contact Output
** EFENRRTR, ENRRT
**
** FIELD OUTPUT: F-Output-1
**
** Output, field, variable=PRESELECT
**
** HISTORY OUTPUT: H-Output-1
**
** Output, history, variable=PRESELECT
** End Step
** STEP: Step-65
**
*Step, name=Step-65, nlgeom=YES, inc=200, unsymm=YES
Excavation of the STOPEN8975P2C80B1, STOPEN8975P2C110B1,
STOPEN8975P2C140B1 - BACKFILLING STOPEN8975P1C125B1,
STOPEN8975P1C155B1, STOPEN8975P1C185B1
*Static

```

```

0.1, 1., 1e-07, 1.
*CONTROLS,ANALYSIS=DISCONTINUOUS
*MODEL CHANGE, ADD
STOPEN8975P1C125B1, STOPEN8975P1C155B1, STOPEN8975P1C185B1
*FIELD
STOPEN8975P1C125BACKFILL1, 1.0
STOPEN8975P1C155BACKFILL1, 1.0
STOPEN8975P1C185BACKFILL1, 1.0
*MODEL CHANGE, REMOVE
STOPEN8975P2C80B1, STOPEN8975P2C110B1, STOPEN8975P2C140B1
**
** OUTPUT REQUESTS
**
*Restart, write, frequency=0
**
** FIELD OUTPUT: F-Output-2
**
*Output, field
*Element Output, directions=YES
ELEDEN, ELEN, ENER, PEEQMAX, PEEQT
*Contact Output
EFENRRTR, ENRRTR
**
** FIELD OUTPUT: F-Output-1
**
*Output, field, variable=PRESELECT
**
** HISTORY OUTPUT: H-Output-1
**
*Output, history, variable=PRESELECT
*End Step
** -----
**
** STEP: Step-66
**
*Step, name=Step-66, nlgeom=YES, inc=200, unsymm=YES
Excavation of the STOPEN8975P2C170B1, STOPEN8975P2C200B1,
STOPEN8975S1C88B1 - BACKFILLING STOPEN8975P2C80B1,
STOPEN8975P2C110B1, STOPEN8975P2C140B1
*Static
0.1, 1., 1e-07, 1.
*CONTROLS,ANALYSIS=DISCONTINUOUS
*MODEL CHANGE, ADD
STOPEN8975P2C80B1, STOPEN8975P2C110B1, STOPEN8975P2C140B1
*FIELD
STOPEN8975P2C80BACKFILL1, 1.0
STOPEN8975P2C110BACKFILL1, 1.0
STOPEN8975P2C140BACKFILL1, 1.0
*MODEL CHANGE, REMOVE
STOPEN8975P2C170B1, STOPEN8975P2C200B1, STOPEN8975S1C88B1
**
** OUTPUT REQUESTS
**
*Restart, write, frequency=1
**
** FIELD OUTPUT: F-Output-2
**
*Output, field
*Element Output, directions=YES
ELEDEN, ELEN, ENER, PEEQMAX, PEEQT
*Contact Output
EFENRRTR, ENRRTR
**
** FIELD OUTPUT: F-Output-1
**
*Output, field, variable=PRESELECT
**
** HISTORY OUTPUT: H-Output-1
**
*Output, history, variable=PRESELECT
*End Step
** STEP: Step-67
**
*Step, name=Step-67, nlgeom=YES, inc=200, unsymm=YES
Excavation of the STOPEN8975S1C118B1, STOPEN8975S1C148B1,
STOPEN8975S1C178B1 - BACKFILLING STOPEN8975P2C170B1,
STOPEN8975P2C200B1, STOPEN8975S1C88B1
*Static
0.1, 1., 1e-07, 1.
*CONTROLS,ANALYSIS=DISCONTINUOUS
*MODEL CHANGE, ADD
STOPEN8975P2C170B1, STOPEN8975P2C200B1, STOPEN8975S1C88B1
*FIELD
STOPEN8975P2C170BACKFILL1, 1.0
STOPEN8975P2C200BACKFILL1, 1.0
STOPEN8975S1C88BACKFILL1, 1.0
*MODEL CHANGE, REMOVE
STOPEN8975S1C118B1, STOPEN8975S1C148B1, STOPEN8975S1C178B1
**
** OUTPUT REQUESTS
**
*Restart, write, frequency=0
**
** FIELD OUTPUT: F-Output-2
**
*Output, field
*Element Output, directions=YES
ELEDEN, ELEN, ENER, PEEQMAX, PEEQT
*Contact Output
EFENRRTR, ENRRTR
**
** FIELD OUTPUT: F-Output-1
**
*Output, field, variable=PRESELECT
**
** HISTORY OUTPUT: H-Output-1
**
*Output, history, variable=PRESELECT
**
** FIELD OUTPUT: F-Output-2
**
*Output, field
*Element Output, directions=YES
ELEDEN, ELEN, ENER, PEEQMAX, PEEQT
*Contact Output
EFENRRTR, ENRRTR
**
** FIELD OUTPUT: F-Output-1
**
*Output, field, variable=PRESELECT
**
** HISTORY OUTPUT: H-Output-1
**
*Output, history, variable=PRESELECT
**
** STEP: Step-68
**
*Step, name=Step-68, nlgeom=YES, inc=200, unsymm=YES
Excavation of the STOPEN8975S1C208B1, STOPEN8975S2C73B1,
STOPEN8975S2C103B1 - BACKFILLING STOPEN8975S1C118B1,
STOPEN8975S1C148B1, STOPEN8975S1C178B1
*Static
0.1, 1., 1e-07, 1.
*CONTROLS,ANALYSIS=DISCONTINUOUS
*MODEL CHANGE, ADD
STOPEN8975S1C118B1, STOPEN8975S1C148B1, STOPEN8975S1C178B1
*FIELD
STOPEN8975S1C118BACKFILL1, 1.0
STOPEN8975S1C148BACKFILL1, 1.0
STOPEN8975S1C178BACKFILL1, 1.0
*MODEL CHANGE, REMOVE
STOPEN8975S1C208B1, STOPEN8975S2C73B1, STOPEN8975S2C103B1
**
** OUTPUT REQUESTS
**
*Restart, write, frequency=1
**
** FIELD OUTPUT: F-Output-2
**
*Output, field
*Element Output, directions=YES
ELEDEN, ELEN, ENER, PEEQMAX, PEEQT
*Contact Output
EFENRRTR, ENRRTR
**
** FIELD OUTPUT: F-Output-1
**
*Output, field, variable=PRESELECT
**
** HISTORY OUTPUT: H-Output-1
**
*Output, history, variable=PRESELECT
*End Step
** STEP: Step-69
**
*Step, name=Step-69, nlgeom=YES, inc=200, unsymm=YES
Excavation of the STOPEN8975S2C133B1, STOPEN8975S2C163B1,
STOPEN8975S2C193B1 - BACKFILLING STOPEN8975S1C208B1,
STOPEN8975S2C73B1, STOPEN8975S2C103B1
*Static
0.1, 1., 1e-07, 1.
*CONTROLS,ANALYSIS=DISCONTINUOUS
*MODEL CHANGE, ADD
STOPEN8975S1C208B1, STOPEN8975S2C73B1, STOPEN8975S2C103B1
*FIELD
STOPEN8975S1C208BACKFILL1, 1.0
STOPEN8975S2C73BACKFILL1, 1.0
STOPEN8975S2C103BACKFILL1, 1.0
*MODEL CHANGE, REMOVE
STOPEN8975S2C133B1, STOPEN8975S2C163B1, STOPEN8975S2C193B1
**
** OUTPUT REQUESTS
**
*Restart, write, frequency=0
**
** FIELD OUTPUT: F-Output-2
**
*Output, field
*Element Output, directions=YES
ELEDEN, ELEN, ENER, PEEQMAX, PEEQT
*Contact Output
EFENRRTR, ENRRTR
**
** FIELD OUTPUT: F-Output-1
**
*Output, field, variable=PRESELECT
**
** HISTORY OUTPUT: H-Output-1
**
*Output, history, variable=PRESELECT

```

```

*End Step
** -----
**
** STEP: Step-70
**
*Step, name=Step-70, nlgeom=YES, inc=200, unsymm=YES
Excavation of the STOPEN9000P1C65B1, STOPEN9000P1C95B1,
STOPEN9000P1C125B1 - BACKFILLING STOPEN8975S2C133B1,
STOPEN8975S2C163B1, STOPEN8975S2C193B1
*Static
0.1, 1., 1e-07, 1.
*CONTROLS,ANALYSIS=DISCONTINUOUS
*MODEL CHANGE, ADD
STOPEN8975S2C133B1, STOPEN8975S2C163B1, STOPEN8975S2C193B1
*FIELD
STOPEN8975S2C133BACKFILL1, 1.0
STOPEN8975S2C163BACKFILL1, 1.0
STOPEN8975S2C193BACKFILL1, 1.0
*MODEL CHANGE, REMOVE
STOPEN9000P1C65B1, STOPEN9000P1C95B1, STOPEN9000P1C125B1
**
** OUTPUT REQUESTS
**
*Restart, write, frequency=1
**
** FIELD OUTPUT: F-Output-2
**
*Output, field
*Element Output, directions=YES
ELEDEN, ELEN, ENER, PEEQMAX, PEEQT
*Contact Output
EFENRRTR, ENRRT
**
** FIELD OUTPUT: F-Output-1
**
*Output, field, variable=PRESELECT
**
** HISTORY OUTPUT: H-Output-1
**
*Output, history, variable=PRESELECT
*End Step
** STEP: Step-71
**
*Step, name=Step-71, nlgeom=YES, inc=200, unsymm=YES
Excavation of the STOPEN9000P1C155B1, STOPEN9000P1C185B1,
STOPEN9000P2C80B1 - BACKFILLING STOPEN9000P1C65B1,
STOPEN9000P1C95B1, STOPEN9000P1C125B1
*Static
0.1, 1., 1e-07, 1.
*CONTROLS,ANALYSIS=DISCONTINUOUS
*MODEL CHANGE, ADD
STOPEN9000P1C65B1, STOPEN9000P1C95B1, STOPEN9000P1C125B1
*FIELD
STOPEN9000P1C65BACKFILL1, 1.0
STOPEN9000P1C95BACKFILL1, 1.0
STOPEN9000P1C125BACKFILL1, 1.0
*MODEL CHANGE, REMOVE
STOPEN9000P1C155B1, STOPEN9000P1C185B1, STOPEN9000P2C80B1
**
** OUTPUT REQUESTS
**
*Restart, write, frequency=0
**
** FIELD OUTPUT: F-Output-2
**
*Output, field
*Element Output, directions=YES
ELEDEN, ELEN, ENER, PEEQMAX, PEEQT
*Contact Output
EFENRRTR, ENRRT
**
** FIELD OUTPUT: F-Output-1
**
*Output, field, variable=PRESELECT
**
** HISTORY OUTPUT: H-Output-1
**
*Output, history, variable=PRESELECT
*End Step
** -----
**
** STEP: Step-72
**
*Step, name=Step-72, nlgeom=YES, inc=200, unsymm=YES
Excavation of the STOPEN9000P2C110B1, STOPEN9000P2C140B1,
STOPEN9000P2C170B1 - BACKFILLING STOPEN9000P1C155B1,
STOPEN9000P1C185B1, STOPEN9000P2C80B1
*Static
0.1, 1., 1e-07, 1.
*CONTROLS,ANALYSIS=DISCONTINUOUS
*MODEL CHANGE, ADD
STOPEN9000P1C155B1, STOPEN9000P1C185B1, STOPEN9000P2C80B1
*FIELD
STOPEN9000P2C110BACKFILL1, 1.0
STOPEN9000P2C140BACKFILL1, 1.0
STOPEN9000P2C170BACKFILL1, 1.0
*MODEL CHANGE, REMOVE
STOPEN9000P2C200B1, STOPEN9000S1C88B1, STOPEN9000S1C118B1
**
** OUTPUT REQUESTS
**
*Restart, write, frequency=1
**
** FIELD OUTPUT: F-Output-2
**
*Output, field
*Element Output, directions=YES
ELEDEN, ELEN, ENER, PEEQMAX, PEEQT
*Contact Output
EFENRRTR, ENRRT
**
** FIELD OUTPUT: F-Output-1
**
*Output, field, variable=PRESELECT
**
** HISTORY OUTPUT: H-Output-1
**
*Output, history, variable=PRESELECT
*End Step
** -----
**
** STEP: Step-73
**
*Step, name=Step-73, nlgeom=YES, inc=200, unsymm=YES
Excavation of the STOPEN9000P2C200B1, STOPEN9000S1C88B1,
STOPEN9000S1C118B1 - BACKFILLING STOPEN9000P2C110B1,
STOPEN9000P2C140B1, STOPEN9000P2C170B1
*Static
0.1, 1., 1e-07, 1.
*CONTROLS,ANALYSIS=DISCONTINUOUS
*MODEL CHANGE, ADD
STOPEN9000P2C110B1, STOPEN9000P2C140B1, STOPEN9000P2C170B1
*FIELD
STOPEN9000P2C110BACKFILL1, 1.0
STOPEN9000P2C140BACKFILL1, 1.0
STOPEN9000P2C170BACKFILL1, 1.0
*MODEL CHANGE, REMOVE
STOPEN9000P2C200B1, STOPEN9000S1C88B1, STOPEN9000S1C118B1
**
** OUTPUT REQUESTS
**
*Restart, write, frequency=0
**
** FIELD OUTPUT: F-Output-2
**
*Output, field
*Element Output, directions=YES
ELEDEN, ELEN, ENER, PEEQMAX, PEEQT
*Contact Output
EFENRRTR, ENRRT
**
** FIELD OUTPUT: F-Output-1
**
*Output, field, variable=PRESELECT
**
** HISTORY OUTPUT: H-Output-1
**
*Output, history, variable=PRESELECT
*End Step
** -----
**
** STEP: Step-74
**
*Step, name=Step-74, nlgeom=YES, inc=200, unsymm=YES
Excavation of the STOPEN9000S1C148B1, STOPEN9000S1C178B1,
STOPEN9000S1C208B1 - BACKFILLING STOPEN9000P2C200B1,
STOPEN9000S1C88B1, STOPEN9000S1C118B1
*Static
0.1, 1., 1e-07, 1.
*CONTROLS,ANALYSIS=DISCONTINUOUS
*MODEL CHANGE, ADD
STOPEN9000P2C200B1, STOPEN9000S1C88B1, STOPEN9000S1C118B1
*FIELD
STOPEN9000P2C200BACKFILL1, 1.0
STOPEN9000S1C88BACKFILL1, 1.0
STOPEN9000S1C118BACKFILL1, 1.0
*MODEL CHANGE, REMOVE
STOPEN9000S1C148B1, STOPEN9000S1C178B1, STOPEN9000S1C208B1
**
** OUTPUT REQUESTS
**
*Restart, write, frequency=1
**
** FIELD OUTPUT: F-Output-2
**
*Output, field
*Element Output, directions=YES
ELEDEN, ELEN, ENER, PEEQMAX, PEEQT

```

```

*Contact Output
EFENRRTR, ENRRT
**
** FIELD OUTPUT: F-Output-1
**
*Output, field, variable=PRESELECT
**
** HISTORY OUTPUT: H-Output-1
**
*Output, history, variable=PRESELECT
*End Step
** STEP: Step-75
**
*Step, name=Step-75, nlgeom=YES, inc=200, unsymm=YES
Excavation of the STOPEN9000S2C73B1, STOPEN9000S2C103B1,
STOPEN9000S2C133B1 - BACKFILLING STOPEN9000S1C148B1,
STOPEN9000S1C178B1, STOPEN9000S1C208B1
*Static
0.1, 1., 1e-07, 1.
*CONTROLS,ANALYSIS=DISCONTINUOUS
*MODEL CHANGE, ADD
STOPEN9000S1C148B1, STOPEN9000S1C178B1, STOPEN9000S1C208B1
*FIELD
STOPEN9000S1C148BACKFILL1, 1.0
STOPEN9000S1C178BACKFILL1, 1.0
STOPEN9000S1C208BACKFILL1, 1.0
*MODEL CHANGE, REMOVE
STOPEN9000S2C73B1, STOPEN9000S2C103B1, STOPEN9000S2C133B1
**
** OUTPUT REQUESTS
**
*Restart, write, frequency=0
**
** FIELD OUTPUT: F-Output-2
**
*Output, field
*Element Output, directions=YES
ELEDEN, ELEN, ENER, PEEQMAX, PEEQT
*Contact Output
EFENRRTR, ENRRT
**
** FIELD OUTPUT: F-Output-1
**
*Output, field, variable=PRESELECT
**
** HISTORY OUTPUT: H-Output-1
**
*Output, history, variable=PRESELECT
*End Step
** -----
**
** STEP: Step-76
**
*Step, name=Step-76, nlgeom=YES, inc=200, unsymm=YES
Excavation of the STOPEN9000S2C163B1, STOPEN9000S2C193B1,
STOPEN9025P1C95B1 - BACKFILLING STOPEN9000S2C73B1,
STOPEN9000S2C103B1, STOPEN9000S2C133B1
*Static
0.1, 1., 1e-07, 1.
*CONTROLS,ANALYSIS=DISCONTINUOUS
*MODEL CHANGE, ADD
STOPEN9000S2C73B1, STOPEN9000S2C103B1, STOPEN9000S2C133B1
*FIELD
STOPEN9000S2C73BACKFILL1, 1.0
STOPEN9000S2C103BACKFILL1, 1.0
STOPEN9000S2C133BACKFILL1, 1.0
*MODEL CHANGE, REMOVE
STOPEN9000S2C163B1, STOPEN9000S2C193B1, STOPEN9025P1C95B1
**
** OUTPUT REQUESTS
**
*Restart, write, frequency=1
**
** FIELD OUTPUT: F-Output-2
**
*Output, field
*Element Output, directions=YES
ELEDEN, ELEN, ENER, PEEQMAX, PEEQT
*Contact Output
EFENRRTR, ENRRT
**
** FIELD OUTPUT: F-Output-1
**
*Output, field, variable=PRESELECT
**
** HISTORY OUTPUT: H-Output-1
**
*Output, history, variable=PRESELECT
*End Step
** STEP: Step-77
**
*Step, name=Step-77, nlgeom=YES, inc=200, unsymm=YES
Excavation of the STOPEN9025P1C125B1, STOPEN9025P1C155B1,
STOPEN9025P1C185B1 - BACKFILLING STOPEN9000S2C163B1,
STOPEN9000S2C193B1, STOPEN9025P1C95B1
*Static
0.1, 1., 1e-07, 1.
*CONTROLS,ANALYSIS=DISCONTINUOUS
*MODEL CHANGE, ADD
STOPEN9000S2C163B1, STOPEN9000S2C193B1, STOPEN9025P1C95B1
*FIELD
STOPEN9000S2C163BACKFILL1, 1.0
STOPEN9000S2C193BACKFILL1, 1.0
STOPEN9025P1C95BACKFILL1, 1.0
*MODEL CHANGE, REMOVE
STOPEN9025P1C125B1, STOPEN9025P1C155B1, STOPEN9025P1C185B1
**
** OUTPUT REQUESTS
**
*Restart, write, frequency=0
**
** FIELD OUTPUT: F-Output-2
**
*Output, field
*Element Output, directions=YES
ELEDEN, ELEN, ENER, PEEQMAX, PEEQT
*Contact Output
EFENRRTR, ENRRT
**
** FIELD OUTPUT: F-Output-1
**
*Output, field, variable=PRESELECT
**
** HISTORY OUTPUT: H-Output-1
**
*Output, history, variable=PRESELECT
*End Step
** STEP: Step-78
**
*Step, name=Step-78, nlgeom=YES, inc=200, unsymm=YES
Excavation of the STOPEN9025P2C80B1, STOPEN9025P2C110B1,
STOPEN9025P2C140B1 - BACKFILLING STOPEN9025P1C125B1,
STOPEN9025P1C155B1, STOPEN9025P1C185B1
*Static
0.1, 1., 1e-07, 1.
*CONTROLS,ANALYSIS=DISCONTINUOUS
*MODEL CHANGE, ADD
STOPEN9025P1C125B1, STOPEN9025P1C155B1, STOPEN9025P1C185B1
*FIELD
STOPEN9025P1C125BACKFILL1, 1.0
STOPEN9025P1C155BACKFILL1, 1.0
STOPEN9025P1C185BACKFILL1, 1.0
*MODEL CHANGE, REMOVE
STOPEN9025P2C80B1, STOPEN9025P2C110B1, STOPEN9025P2C140B1
**
** OUTPUT REQUESTS
**
*Restart, write, frequency=1
**
** FIELD OUTPUT: F-Output-2
**
*Output, field
*Element Output, directions=YES
ELEDEN, ELEN, ENER, PEEQMAX, PEEQT
*Contact Output
EFENRRTR, ENRRT
**
** FIELD OUTPUT: F-Output-1
**
*Output, field, variable=PRESELECT
**
** HISTORY OUTPUT: H-Output-1
**
*Output, history, variable=PRESELECT
*End Step
** STEP: Step-79
**
*Step, name=Step-79, nlgeom=YES, inc=200, unsymm=YES
Excavation of the STOPEN9025P2C170B1, STOPEN9025P2C200B1,
STOPEN9025S1C88B1 - BACKFILLING STOPEN9025P2C80B1,
STOPEN9025P2C110B1, STOPEN9025P2C140B1
*Static
0.1, 1., 1e-07, 1.
*CONTROLS,ANALYSIS=DISCONTINUOUS
*MODEL CHANGE, ADD
STOPEN9025P2C80B1, STOPEN9025P2C110B1, STOPEN9025P2C140B1
*FIELD
STOPEN9025P2C80BACKFILL1, 1.0
STOPEN9025P2C110BACKFILL1, 1.0
STOPEN9025P2C140BACKFILL1, 1.0
*MODEL CHANGE, REMOVE
STOPEN9025P2C170B1, STOPEN9025P2C200B1, STOPEN9025S1C88B1
**

```

```

** OUTPUT REQUESTS
**
*Restart, write, frequency=0
**
** FIELD OUTPUT: F-Output-2
**
*Output, field
*Element Output, directions=YES
ELEDED, ELEN, ENER, PEEQMAX, PEEQT
*Contact Output
EFENRRTR, ENRRT
**
** FIELD OUTPUT: F-Output-1
**
*Output, field, variable=PRESELECT
**
** HISTORY OUTPUT: H-Output-1
**
*Output, history, variable=PRESELECT
*End Step
** -----
**
** STEP: Step-80
**
*Step, name=Step-80, nlgeom=YES, inc=200, unsymm=YES
Excavation of the STOPEN9025S1C118B1, STOPEN9025S1C148B1,
STOPEN9025S1C178B1 - BACKFILLING STOPEN9025P2C170B1,
STOPEN9025P2C200B1, STOPEN9025S1C88B1
*Static
0.1, 1., 1e-07, 1.
*CONTROLS,ANALYSIS=DISCONTINUOUS
*MODEL CHANGE, ADD
STOPEN9025P2C170B1, STOPEN9025P2C200B1, STOPEN9025S1C88B1
*FIELD
STOPEN9025P2C170BACKFILL1, 1.0
STOPEN9025P2C200BACKFILL1, 1.0
STOPEN9025S1C88BACKFILL1, 1.0
*MODEL CHANGE, REMOVE
STOPEN9025S1C118B1, STOPEN9025S1C148B1, STOPEN9025S1C178B1
**
** OUTPUT REQUESTS
**
*Restart, write, frequency=1
**
** FIELD OUTPUT: F-Output-2
**
*Output, field
*Element Output, directions=YES
ELEDED, ELEN, ENER, PEEQMAX, PEEQT
*Contact Output
EFENRRTR, ENRRT
**
** FIELD OUTPUT: F-Output-1
**
*Output, field, variable=PRESELECT
**
** HISTORY OUTPUT: H-Output-1
**
*Output, history, variable=PRESELECT
*End Step
** STEP: Step-81
**
*Step, name=Step-81, nlgeom=YES, inc=200, unsymm=YES
Excavation of the STOPEN9025S1C208B1, STOPEN9025S2C73B1,
STOPEN9025S2C103B1 - BACKFILLING STOPEN9025S1C118B1,
STOPEN9025S1C148B1, STOPEN9025S1C178B1
*Static
0.1, 1., 1e-07, 1.
*CONTROLS,ANALYSIS=DISCONTINUOUS
*MODEL CHANGE, ADD
STOPEN9025S1C118B1, STOPEN9025S1C148B1, STOPEN9025S1C178B1
*FIELD
STOPEN9025S1C118BACKFILL1, 1.0
STOPEN9025S1C148BACKFILL1, 1.0
STOPEN9025S1C178BACKFILL1, 1.0
*MODEL CHANGE, REMOVE
STOPEN9025S1C208B1, STOPEN9025S2C73B1, STOPEN9025S2C103B1
**
** OUTPUT REQUESTS
**
*Restart, write, frequency=0
**
** FIELD OUTPUT: F-Output-2
**
*Output, field
*Element Output, directions=YES
ELEDED, ELEN, ENER, PEEQMAX, PEEQT
**
*Contact Output
EFENRRTR, ENRRT
**
** FIELD OUTPUT: F-Output-1
**
*Output, field, variable=PRESELECT
**
** HISTORY OUTPUT: H-Output-1
**
*Output, history, variable=PRESELECT
*End Step
**
*Contact Output
EFENRRTR, ENRRT
**
** FIELD OUTPUT: F-Output-1
**
*Output, field, variable=PRESELECT
**
** HISTORY OUTPUT: H-Output-1
**
*Output, history, variable=PRESELECT
*End Step
** -----
**
** STEP: Step-82
**
*Step, name=Step-82, nlgeom=YES, inc=200, unsymm=YES
Excavation of the STOPEN9025S2C133B1, STOPEN9025S2C163B1,
STOPEN9025S2C193B1 - BACKFILLING STOPEN9025S1C208B1,
STOPEN9025S2C73B1, STOPEN9025S2C103B1
*Static
0.1, 1., 1e-07, 1.
*CONTROLS,ANALYSIS=DISCONTINUOUS
*MODEL CHANGE, ADD
STOPEN9025S1C208B1, STOPEN9025S2C73B1, STOPEN9025S2C103B1
*FIELD
STOPEN9025S1C208BACKFILL1, 1.0
STOPEN9025S2C73BACKFILL1, 1.0
STOPEN9025S2C103BACKFILL1, 1.0
*MODEL CHANGE, REMOVE
STOPEN9025S2C133B1, STOPEN9025S2C163B1, STOPEN9025S2C193B1
**
** OUTPUT REQUESTS
**
*Restart, write, frequency=1
**
** FIELD OUTPUT: F-Output-2
**
*Output, field
*Element Output, directions=YES
ELEDED, ELEN, ENER, PEEQMAX, PEEQT
*Contact Output
EFENRRTR, ENRRT
**
** FIELD OUTPUT: F-Output-1
**
*Output, field, variable=PRESELECT
**
** HISTORY OUTPUT: H-Output-1
**
*Output, history, variable=PRESELECT
*End Step
** STEP: Step-83
**
*Step, name=Step-83, nlgeom=YES, inc=200, unsymm=YES
BACKFILLING STOPEN9025S2C133B1, STOPEN9025S2C163B1,
STOPEN9025S2C193B1
*Static
0.1, 1., 1e-07, 1.
*CONTROLS,ANALYSIS=DISCONTINUOUS
*MODEL CHANGE, ADD
STOPEN9025S2C133B1, STOPEN9025S2C163B1, STOPEN9025S2C193B1
*FIELD
STOPEN9025S2C133BACKFILL1, 1.0
STOPEN9025S2C163BACKFILL1, 1.0
STOPEN9025S2C193BACKFILL1, 1.0
**
** OUTPUT REQUESTS
**
*Restart, write, frequency=1
**
** FIELD OUTPUT: F-Output-2
**
*Output, field
*Element Output, directions=YES
ELEDED, ELEN, ENER, PEEQMAX, PEEQT
*Contact Output
EFENRRTR, ENRRT
**
** FIELD OUTPUT: F-Output-1
**
*Output, field, variable=PRESELECT
**
** HISTORY OUTPUT: H-Output-1
**
*Output, history, variable=PRESELECT
*End Step

```

## Schemes SBS

```
** STEP: Step-84
**
*Step, name=Step-84, nlgeom=YES, inc=200, unsymm=YES
Excavation of the SILL1P1C65B1, SILL1P1C95B1, SILL2P1C65B1, SILL2P1C95B1
*Static
0.1, 1., 1e-07, 1.
*CONTROLS,ANALYSIS=DISCONTINUOUS
*MODEL CHANGE, REMOVE
SILL1P1C65B1, SILL1P1C95B1, SILL2P1C65B1, SILL2P1C95B1
**
** OUTPUT REQUESTS
**
*Restart, write, frequency=0
**
** FIELD OUTPUT: F-Output-2
**
*Output, field
*Element Output, directions=YES
ELEDEN, ELEN, ENER, PEEQMAX, PEEQT
*Contact Output
EFENRRTR, ENRRT
**
** FIELD OUTPUT: F-Output-1
**
*Output, field, variable=PRESELECT
**
** HISTORY OUTPUT: H-Output-1
**
*Output, history, variable=PRESELECT
*End Step
** -----
**
** STEP: Step-85
**
*Step, name=Step-85, nlgeom=YES, inc=200, unsymm=YES
Excavation of the SILL1P1C125B1, SILL1P1C155B1, SILL2P1C125B1,
SILL2P1C155B1 - BACKFILLING SILL1P1C65B1, SILL1P1C95B1, SILL2P1C65B1,
SILL2P1C95B1
*Static
0.1, 1., 1e-07, 1.
*CONTROLS,ANALYSIS=DISCONTINUOUS
*MODEL CHANGE, ADD
SILL1P1C65B1, SILL1P1C95B1, SILL2P1C65B1, SILL2P1C95B1
*FIELD
SILL1P1C65BACKFILL1, 1.0
SILL1P1C95BACKFILL1, 1.0
SILL2P1C65BACKFILL1, 1.0
SILL2P1C95BACKFILL1, 1.0
*MODEL CHANGE, REMOVE
SILL1P1C125B1, SILL1P1C155B1, SILL2P1C125B1, SILL2P1C155B1
```

```
**
** OUTPUT REQUESTS
**
*Restart, write, frequency=1
**
** FIELD OUTPUT: F-Output-2
**
*Output, field
*Element Output, directions=YES
ELEDEN, ELEN, ENER, PEEQMAX, PEEQT
*Contact Output
EFENRRTR, ENRRT
**
** FIELD OUTPUT: F-Output-1
**
*Output, field, variable=PRESELECT
**
** HISTORY OUTPUT: H-Output-1
**
*Output, history, variable=PRESELECT
*End Step
** STEP: Step-86
**
*Step, name=Step-86, nlgeom=YES, inc=200, unsymm=YES
Excavation of the SILL1P1C185B1, SILL1P2C80B1, SILL2P1C185B1, SILL2P2C80B1
- BACKFILLING SILL1P1C125B1, SILL1P1C155B1, SILL2P1C125B1,
SILL2P1C155B1
*Static
0.1, 1., 1e-07, 1.
*CONTROLS,ANALYSIS=DISCONTINUOUS
*MODEL CHANGE, ADD
SILL1P1C125B1, SILL1P1C155B1, SILL2P1C125B1, SILL2P1C155B1
*FIELD
SILL1P1C125BACKFILL1, 1.0
SILL1P1C155BACKFILL1, 1.0
SILL2P1C125BACKFILL1, 1.0
SILL2P1C155BACKFILL1, 1.0
*MODEL CHANGE, REMOVE
SILL1P1C185B1, SILL1P2C80B1, SILL2P1C185B1, SILL2P2C80B1
**
** OUTPUT REQUESTS
**
*Restart, write, frequency=0
**
** FIELD OUTPUT: F-Output-2
**
*Output, field
*Element Output, directions=YES
ELEDEN, ELEN, ENER, PEEQMAX, PEEQT
*Contact Output
```

```

EFENRRTR, ENRRT
**
** FIELD OUTPUT: F-Output-1
**
*Output, field, variable=PRESELECT
**
** HISTORY OUTPUT: H-Output-1
**
*Output, history, variable=PRESELECT
**
*End Step
** -----
**
** STEP: Step-87
**
*Step, name=Step-87, nlgeom=YES, inc=200, unsymm=YES
Excavation of the SILL1P2C110B1, SILL1P2C140B1, SILL2P2C110B1,
SILL2P2C140B1 - BACKFILLING SILL1P1C185B1, SILL1P2C80B1,
SILL2P1C185B1, SILL2P2C80B1
*Static
0.1, 1., 1e-07, 1.
*CONTROLS,ANALYSIS=DISCONTINUOUS
*MODEL CHANGE, ADD
SILL1P1C185B1, SILL1P2C80B1, SILL2P1C185B1, SILL2P2C80B1
*FIELD
SILL1P1C185BACKFILL1, 1.0
SILL1P2C80BACKFILL1, 1.0
SILL2P1C185BACKFILL1, 1.0
SILL2P2C80BACKFILL1, 1.0
*MODEL CHANGE, REMOVE
SILL1P2C110B1, SILL1P2C140B1, SILL2P2C110B1, SILL2P2C140B1
**
** OUTPUT REQUESTS
**
*Restart, write, frequency=1
**
** FIELD OUTPUT: F-Output-2
**
*Output, field
*Element Output, directions=YES
ELEDEN, ELEN, ENER, PEEQMAX, PEEQT
*Contact Output
EFENRRTR, ENRRT
**
** FIELD OUTPUT: F-Output-1
**
*Output, field, variable=PRESELECT
**
** HISTORY OUTPUT: H-Output-1
**
*Output, history, variable=PRESELECT
**
*End Step
** -----
**
** STEP: Step-88
**
*Step, name=Step-88, nlgeom=YES, inc=200, unsymm=YES
Excavation of the SILL1P2C170B1, SILL1P2C200B1, SILL2P2C170B1,
SILL2P2C200B1 - BACKFILLING - SILL1P2C110B1, SILL1P2C140B1,
SILL2P2C110B1, SILL2P2C140B1
*Static
0.1, 1., 1e-07, 1.
*CONTROLS,ANALYSIS=DISCONTINUOUS
*MODEL CHANGE, ADD
SILL1P2C110B1, SILL1P2C140B1, SILL2P2C110B1, SILL2P2C140B1
*FIELD
SILL1P2C110BACKFILL1, 1.0
SILL1P2C140BACKFILL1, 1.0
SILL2P2C110BACKFILL1, 1.0
SILL2P2C140BACKFILL1, 1.0
*MODEL CHANGE, REMOVE
SILL1P2C170B1, SILL1P2C200B1, SILL2P2C170B1, SILL2P2C200B1
**
** OUTPUT REQUESTS
**
*Restart, write, frequency=0
**
** FIELD OUTPUT: F-Output-2
**
*Output, field
*Element Output, directions=YES
ELEDEN, ELEN, ENER, PEEQMAX, PEEQT
*Contact Output
EFENRRTR, ENRRT
**
** FIELD OUTPUT: F-Output-1
**
*Output, field, variable=PRESELECT
**
** HISTORY OUTPUT: H-Output-1
**
*Output, history, variable=PRESELECT
**
*End Step
** -----
**
** STEP: Step-89
**
*Step, name=Step-89, nlgeom=YES, inc=200, unsymm=YES
Excavation of the SILL1S1C58B1, SILL1S1C88B1, SILL2S1C58B1, SILL2S1C88B1 -
BACKFILLING SILL1P2C170B1, SILL1P2C200B1, SILL2P2C170B1,
SILL2P2C200B1
*Static
0.1, 1., 1e-07, 1.
*CONTROLS,ANALYSIS=DISCONTINUOUS
*MODEL CHANGE, ADD
SILL1P2C170B1, SILL1P2C200B1, SILL2P2C170B1, SILL2P2C200B1

```

```

*FIELD
SILL1P2C170BACKFILL1, 1.0
SILL1P2C200BACKFILL1, 1.0
SILL2P2C170BACKFILL1, 1.0
SILL2P2C200BACKFILL1, 1.0
*MODEL CHANGE, REMOVE
SILL1S1C58B1, SILL1S1C88B1, SILL2S1C58B1, SILL2S1C88B1
**
** OUTPUT REQUESTS
**
*Restart, write, frequency=1
**
** FIELD OUTPUT: F-Output-2
**
*Output, field
*Element Output, directions=YES
ELEDEN, ELEN, ENER, PEEQMAX, PEEQT
*Contact Output
EFENRRTR, ENRRT
**
** FIELD OUTPUT: F-Output-1
**
*Output, field, variable=PRESELECT
**
** HISTORY OUTPUT: H-Output-1
**
*Output, history, variable=PRESELECT
*End Step
** STEP: Step-90
**
*Step, name=Step-90, nlgeom=YES, inc=200, unsymm=YES
Excavation of the SILL1S1C118B1, SILL1S1C148B1, SILL2S1C118B1,
SILL2S1C148B1 - BACKFILLING - SILL1S1C58B1, SILL1S1C88B1, SILL2S1C58B1,
SILL2S1C88B1
*Static
0.1, 1., 1e-07, 1.
*CONTROLS,ANALYSIS=DISCONTINUOUS
*MODEL CHANGE, ADD
SILL1S1C58B1, SILL1S1C88B1, SILL2S1C58B1, SILL2S1C88B1
*FIELD
SILL1S1C58BACKFILL1, 1.0
SILL1S1C88BACKFILL1, 1.0
SILL2S1C58BACKFILL1, 1.0
SILL2S1C88BACKFILL1, 1.0
*MODEL CHANGE, REMOVE
SILL1S1C118B1, SILL1S1C148B1, SILL2S1C118B1, SILL2S1C148B1
**
** OUTPUT REQUESTS
**
*Restart, write, frequency=0
**

```

```

** FIELD OUTPUT: F-Output-2
**
*Output, field
*Element Output, directions=YES
ELEDEN, ELEN, ENER, PEEQMAX, PEEQT
*Contact Output
EFENRRTR, ENRRT
**
** FIELD OUTPUT: F-Output-1
**
*Output, field, variable=PRESELECT
**
** HISTORY OUTPUT: H-Output-1
**
*Output, history, variable=PRESELECT
*End Step
** -----
**
** STEP: Step-91
**
*Step, name=Step-91, nlgeom=YES, inc=200, unsymm=YES
Excavation of the SILL1S1C178B1, SILL1S2C73B1, SILL2S1C178B1, SILL2S2C73B1
- BACKFILLING SILL1S1C118B1, SILL1S1C148B1, SILL2S1C118B1,
SILL2S1C148B1
*Static
0.1, 1., 1e-07, 1.
*CONTROLS,ANALYSIS=DISCONTINUOUS
*MODEL CHANGE, ADD
SILL1S1C118B1, SILL1S1C148B1, SILL2S1C118B1, SILL2S1C148B1
*FIELD
SILL1S1C118BACKFILL1, 1.0
SILL1S1C148BACKFILL1, 1.0
SILL2S1C118BACKFILL1, 1.0
SILL2S1C148BACKFILL1, 1.0
*MODEL CHANGE, REMOVE
SILL1S1C178B1, SILL1S2C73B1, SILL2S1C178B1, SILL2S2C73B1
**
** OUTPUT REQUESTS
**
*Restart, write, frequency=1
**
** FIELD OUTPUT: F-Output-2
**
*Output, field
*Element Output, directions=YES
ELEDEN, ELEN, ENER, PEEQMAX, PEEQT
*Contact Output
EFENRRTR, ENRRT
**
** FIELD OUTPUT: F-Output-1
**

```

```

*Output, field, variable=PRESELECT
**
** HISTORY OUTPUT: H-Output-1
**
*Output, history, variable=PRESELECT
*End Step
** STEP: Step-92
**
*Step, name=Step-92, nlgeom=YES, inc=200, unsymm=YES
Excavation of the SILL1S2C103B1, SILL1S2C133B1, SILL2S2C103B1,
SILL2S2C133B1 - BACKFILLING - SILL1S1C178B1, SILL1S2C73B1,
SILL2S1C178B1, SILL2S2C73B1
*Static
0.1, 1., 1e-07, 1.
*CONTROLS,ANALYSIS=DISCONTINUOUS
*MODEL CHANGE, ADD
SILL1S1C178B1, SILL1S2C73B1, SILL2S1C178B1, SILL2S2C73B1
*FIELD
SILL1S1C178BACKFILL1, 1.0
SILL1S2C73BACKFILL1, 1.0
SILL2S1C178BACKFILL1, 1.0
SILL2S2C73BACKFILL1, 1.0
*MODEL CHANGE, REMOVE
SILL1S2C103B1, SILL1S2C133B1, SILL2S2C103B1, SILL2S2C133B1
**
** OUTPUT REQUESTS
**
*Restart, write, frequency=0
**
** FIELD OUTPUT: F-Output-2
**
*Output, field
*Element Output, directions=YES
ELEDEN, ELEN, ENER, PEEQMAX, PEEQT
*Contact Output
EFENRRTR, ENRRT
**
** FIELD OUTPUT: F-Output-1
**
*Output, field, variable=PRESELECT
**
** HISTORY OUTPUT: H-Output-1
**
*Output, history, variable=PRESELECT
*End Step
** -----
**
** STEP: Step-93
**
*Step, name=Step-93, nlgeom=YES, inc=200, unsymm=YES

```

```

Excavation of the SILL1S2C163B1, SILL1S2C193B1, SILL2S2C163B1,
SILL2S2C193B1 - BACKFILLING - SILL1S2C103B1, SILL1S2C133B1,
SILL2S2C103B1, SILL2S2C133B1
*Static
0.1, 1., 1e-07, 1.
*CONTROLS,ANALYSIS=DISCONTINUOUS
*MODEL CHANGE, ADD
SILL1S2C103B1, SILL1S2C133B1, SILL2S2C103B1, SILL2S2C133B1
*FIELD
SILL1S2C103BACKFILL1, 1.0
SILL1S2C133BACKFILL1, 1.0
SILL2S2C103BACKFILL1, 1.0
SILL2S2C133BACKFILL1, 1.0
*MODEL CHANGE, REMOVE
SILL1S2C163B1, SILL1S2C193B1, SILL2S2C163B1, SILL2S2C193B1
**
** OUTPUT REQUESTS
**
*Restart, write, frequency=1
**
** FIELD OUTPUT: F-Output-2
**
*Output, field
*Element Output, directions=YES
ELEDEN, ELEN, ENER, PEEQMAX, PEEQT
*Contact Output
EFENRRTR, ENRRT
**
** FIELD OUTPUT: F-Output-1
**
*Output, field, variable=PRESELECT
**
** HISTORY OUTPUT: H-Output-1
**
*Output, history, variable=PRESELECT
*End Step
** STEP: Step-94
**
*Step, name=Step-94, nlgeom=YES, inc=200, unsymm=YES
BACKFILLING - SILL1S2C163B1, SILL1S2C193B1, SILL2S2C163B1,
SILL2S2C193B1
*Static
0.1, 1., 1e-07, 1.
*CONTROLS,ANALYSIS=DISCONTINUOUS
*MODEL CHANGE, ADD
SILL1S2C163B1, SILL1S2C193B1, SILL2S2C163B1, SILL2S2C193B1
*FIELD
SILL1S2C163BACKFILL1, 1.0
SILL1S2C193BACKFILL1, 1.0
SILL2S2C163BACKFILL1, 1.0
SILL2S2C193BACKFILL1, 1.0
**

```

```

** OUTPUT REQUESTS
**
*Restart, write, frequency=0
**
** FIELD OUTPUT: F-Output-2
**
*Output, field
*Element Output, directions=YES
ELEDEN, ELEN, ENER, PEEQMAX, PEEQT
*Contact Output
EFENRRTR, ENRRT
**
** FIELD OUTPUT: F-Output-1
**
*Output, field, variable=PRESELECT
**
** HISTORY OUTPUT: H-Output-1
**
*Output, history, variable=PRESELECT
*End Step
Scheme SS1
** STEP: Step-84
**
*Step, name=Step-84, nlgeom=YES, inc=200, unsymm=YES
Excavation of the SILL1P1C65B1, SILL1P1C95B1, SILL1P1C125B1
*Static
0.1, 1., 1e-07, 1.
*CONTROLS,ANALYSIS=DISCONTINUOUS
*MODEL CHANGE, REMOVE
SILL1P1C65B1, SILL1P1C95B1, SILL1P1C125B1
**
** OUTPUT REQUESTS
**
*Restart, write, frequency=0
**
** FIELD OUTPUT: F-Output-2
**
*Output, field
*Element Output, directions=YES
ELEDEN, ELEN, ENER, PEEQMAX, PEEQT
*Contact Output
EFENRRTR, ENRRT
**
** FIELD OUTPUT: F-Output-1
**
*Output, field, variable=PRESELECT
**
** HISTORY OUTPUT: H-Output-1
**
*Output, history, variable=PRESELECT

```

```

*End Step
** -----
**
** STEP: Step-85
**
*Step, name=Step-85, nlgeom=YES, inc=200, unsymm=YES
Excavation of the SILL1P1C155B1, SILL1P1C185B1, SILL1P2C80B1 - BACKFILLING
SILL1P1C65B1, SILL1P1C95B1, SILL1P1C125B1
*Static
0.1, 1., 1e-07, 1.
*CONTROLS,ANALYSIS=DISCONTINUOUS
*MODEL CHANGE, ADD
SILL1P1C65B1, SILL1P1C95B1, SILL1P1C125B1
*FIELD
SILL1P1C65BACKFILL1, 1.0
SILL1P1C95BACKFILL1, 1.0
SILL1P1C125BACKFILL1, 1.0
*MODEL CHANGE, REMOVE
SILL1P1C155B1, SILL1P1C185B1, SILL1P2C80B1
**
** OUTPUT REQUESTS
**
*Restart, write, frequency=1
**
** FIELD OUTPUT: F-Output-2
**
*Output, field
*Element Output, directions=YES
ELEDEN, ELEN, ENER, PEEQMAX, PEEQT
*Contact Output
EFENRRTR, ENRRT
**
** FIELD OUTPUT: F-Output-1
**
*Output, field, variable=PRESELECT
**
** HISTORY OUTPUT: H-Output-1
**
*Output, history, variable=PRESELECT
*End Step
** STEP: Step-86
**
*Step, name=Step-86, nlgeom=YES, inc=200, unsymm=YES
Excavation of the SILL1P2C110B1, SILL1P2C140B1, SILL1P2C170B1 -
BACKFILLING SILL1P1C155B1, SILL1P1C185B1, SILL1P2C80B1
*Static
0.1, 1., 1e-07, 1.
*CONTROLS,ANALYSIS=DISCONTINUOUS
*MODEL CHANGE, ADD
SILL1P1C155B1, SILL1P1C185B1, SILL1P2C80B1
*FIELD

```

SILL1P1C155BACKFILL1, 1.0  
 SILL1P1C185BACKFILL1, 1.0  
 SILL1P2C80BACKFILL1, 1.0  
 \*MODEL CHANGE, REMOVE  
 SILL1P2C110B1, SILL1P2C140B1, SILL1P2C170B1  
 \*\*  
 \*\* OUTPUT REQUESTS  
 \*\*  
 \*Restart, write, frequency=0  
 \*\*  
 \*\* FIELD OUTPUT: F-Output-2  
 \*\*  
 \*Output, field  
 \*Element Output, directions=YES  
 ELEDEN, ELEN, ENER, PEEQMAX, PEEQT  
 \*Contact Output  
 EFENRRTR, ENRRT  
 \*\*  
 \*\* FIELD OUTPUT: F-Output-1  
 \*\*  
 \*Output, field, variable=PRESELECT  
 \*\*  
 \*\* HISTORY OUTPUT: H-Output-1  
 \*\*  
 \*Output, history, variable=PRESELECT  
 \*End Step  
 \*\* -----  
 \*\*  
 \*\* STEP: Step-87  
 \*\*  
 \*Step, name=Step-87, nlgeom=YES, inc=200, unsymm=YES  
 Excavation of the SILL1P2C200B1, SILL1S1C58B1, SILL1S1C88B1 - BACKFILLING  
 SILL1P2C110B1, SILL1P2C140B1, SILL1P2C170B1  
 \*Static  
 0.1, 1., 1e-07, 1.  
 \*CONTROLS,ANALYSIS=DISCONTINUOUS  
 \*MODEL CHANGE, ADD  
 SILL1P2C110B1, SILL1P2C140B1, SILL1P2C170B1  
 \*FIELD  
 SILL1P2C110BACKFILL1, 1.0  
 SILL1P2C140BACKFILL1, 1.0  
 SILL1P2C170BACKFILL1, 1.0  
 \*MODEL CHANGE, REMOVE  
 SILL1P2C200B1, SILL1S1C58B1, SILL1S1C88B1  
 \*\*  
 \*\* OUTPUT REQUESTS  
 \*\*  
 \*Restart, write, frequency=1  
 \*\*  
 \*\* FIELD OUTPUT: F-Output-2  
 \*\*

\*Output, field  
 \*Element Output, directions=YES  
 ELEDEN, ELEN, ENER, PEEQMAX, PEEQT  
 \*Contact Output  
 EFENRRTR, ENRRT  
 \*\*  
 \*\* FIELD OUTPUT: F-Output-1  
 \*\*  
 \*Output, field, variable=PRESELECT  
 \*\*  
 \*\* HISTORY OUTPUT: H-Output-1  
 \*\*  
 \*Output, history, variable=PRESELECT  
 \*End Step  
 \*\* STEP: Step-88  
 \*\*  
 \*Step, name=Step-88, nlgeom=YES, inc=200, unsymm=YES  
 Excavation of the SILL1S1C118B1, SILL1S1C148B1, SILL1S1C178B1 -  
 BACKFILLING SILL1P2C200B1, SILL1S1C58B1, SILL1S1C88B1  
 \*Static  
 0.1, 1., 1e-07, 1.  
 \*CONTROLS,ANALYSIS=DISCONTINUOUS  
 \*MODEL CHANGE, ADD  
 SILL1P2C200B1, SILL1S1C58B1, SILL1S1C88B1  
 \*FIELD  
 SILL1P2C200BACKFILL1, 1.0  
 SILL1S1C58BACKFILL1, 1.0  
 SILL1S1C88BACKFILL1, 1.0  
 \*MODEL CHANGE, REMOVE  
 SILL1S1C118B1, SILL1S1C148B1, SILL1S1C178B1  
 \*\*  
 \*\* OUTPUT REQUESTS  
 \*\*  
 \*Restart, write, frequency=0  
 \*\*  
 \*\* FIELD OUTPUT: F-Output-2  
 \*\*  
 \*Output, field  
 \*Element Output, directions=YES  
 ELEDEN, ELEN, ENER, PEEQMAX, PEEQT  
 \*Contact Output  
 EFENRRTR, ENRRT  
 \*\*  
 \*\* FIELD OUTPUT: F-Output-1  
 \*\*  
 \*Output, field, variable=PRESELECT  
 \*\*  
 \*\* HISTORY OUTPUT: H-Output-1  
 \*\*  
 \*Output, history, variable=PRESELECT  
 \*End Step

```

** -----
**
** STEP: Step-89
**
*Step, name=Step-89, nlgeom=YES, inc=200, unsymm=YES
Excavation of the SILL1S2C73B1, SILL1S2C103B1, SILL1S2C133B1 - BACKFILLING
SILL1S1C118B1, SILL1S1C148B1, SILL1S1C178B1

*Static
0.1, 1., 1e-07, 1.

*CONTROLS,ANALYSIS=DISCONTINUOUS
*MODEL CHANGE, ADD
SILL1S1C118B1, SILL1S1C148B1, SILL1S1C178B1
*FIELD
SILL1S1C118BACKFILL1, 1.0
SILL1S1C148BACKFILL1, 1.0
SILL1S1C178BACKFILL1, 1.0
*MODEL CHANGE, REMOVE
SILL1S2C73B1, SILL1S2C103B1, SILL1S2C133B1
**
** OUTPUT REQUESTS
**
*Restart, write, frequency=1
**
** FIELD OUTPUT: F-Output-2
**
*Output, field
*Element Output, directions=YES
ELEDEN, ELEN, ENER, PEEQMAX, PEEQT
*Contact Output
EFENRRTR, ENRRT
**
** FIELD OUTPUT: F-Output-1
**
*Output, field, variable=PRESELECT
**
** HISTORY OUTPUT: H-Output-1
**
*Output, history, variable=PRESELECT
*End Step
** -----
** STEP: Step-90
**
*Step, name=Step-90, nlgeom=YES, inc=200, unsymm=YES
Excavation of the SILL1S2C163B1, SILL1S2C193B1, SILL2P1C65B1 - BACKFILLING
SILL1S2C73B1, SILL1S2C103B1, SILL1S2C133B1

*Static
0.1, 1., 1e-07, 1.

*CONTROLS,ANALYSIS=DISCONTINUOUS
*MODEL CHANGE, ADD
SILL1S2C73B1, SILL1S2C103B1, SILL1S2C133B1
*FIELD
SILL1S2C73BACKFILL1, 1.0

```

```

SILL1S2C103BACKFILL1, 1.0
SILL1S2C133BACKFILL1, 1.0
*MODEL CHANGE, REMOVE
SILL1S2C163B1, SILL1S2C193B1, SILL2P1C65B1
**
** OUTPUT REQUESTS
**
*Restart, write, frequency=0
**
** FIELD OUTPUT: F-Output-2
**
*Output, field
*Element Output, directions=YES
ELEDEN, ELEN, ENER, PEEQMAX, PEEQT
*Contact Output
EFENRRTR, ENRRT
**
** FIELD OUTPUT: F-Output-1
**
*Output, field, variable=PRESELECT
**
** HISTORY OUTPUT: H-Output-1
**
*Output, history, variable=PRESELECT
*End Step
** -----
** STEP: Step-91
**
*Step, name=Step-91, nlgeom=YES, inc=200, unsymm=YES
Excavation of the SILL2P1C95B1, SILL2P1C125B1, SILL2P1C155B1 - BACKFILLING
SILL1S2C163B1, SILL1S2C193B1, SILL2P1C65B1

*Static
0.1, 1., 1e-07, 1.

*CONTROLS,ANALYSIS=DISCONTINUOUS
*MODEL CHANGE, ADD
SILL1S2C163B1, SILL1S2C193B1, SILL2P1C65B1
*FIELD
SILL1S2C163BACKFILL1, 1.0
SILL1S2C193BACKFILL1, 1.0
SILL2P1C65BACKFILL1, 1.0
*MODEL CHANGE, REMOVE
SILL2P1C95B1, SILL2P1C125B1, SILL2P1C155B1
**
** OUTPUT REQUESTS
**
*Restart, write, frequency=1
**
** FIELD OUTPUT: F-Output-2
**
*Output, field

```

```

*Element Output, directions=YES
ELEDEN, ELEN, ENER, PEEQMAX, PEEQT
*Contact Output
EFENRRTR, ENRRT
**
** FIELD OUTPUT: F-Output-1
**
*Output, field, variable=PRESELECT
**
** HISTORY OUTPUT: H-Output-1
**
*Output, history, variable=PRESELECT
*End Step
** STEP: Step-92
**
*Step, name=Step-92, nlgeom=YES, inc=200, unsymm=YES
Excavation of the SILL2P1C185B1, SILL2P2C80B1, SILL2P2C110B1 - BACKFILLING
SILL2P1C95B1, SILL2P1C125B1, SILL2P1C155B1
*Static
0.1, 1., 1e-07, 1.
*CONTROLS,ANALYSIS=DISCONTINUOUS
*MODEL CHANGE, ADD
SILL2P1C95B1, SILL2P1C125B1, SILL2P1C155B1
*FIELD
SILL2P1C95BACKFILL1, 1.0
SILL2P1C125BACKFILL1, 1.0
SILL2P1C155BACKFILL1, 1.0
*MODEL CHANGE, REMOVE
SILL2P1C185B1, SILL2P2C80B1, SILL2P2C110B1
**
** OUTPUT REQUESTS
**
*Restart, write, frequency=0
**
** FIELD OUTPUT: F-Output-2
**
*Output, field
*Element Output, directions=YES
ELEDEN, ELEN, ENER, PEEQMAX, PEEQT
*Contact Output
EFENRRTR, ENRRT
**
** FIELD OUTPUT: F-Output-1
**
*Output, field, variable=PRESELECT
**
** HISTORY OUTPUT: H-Output-1
**
*Output, history, variable=PRESELECT
*End Step
** STEP: Step-93
**
*Step, name=Step-93, nlgeom=YES, inc=200, unsymm=YES
Excavation of the SILL2P2C140B1, SILL2P2C170B1, SILL2P2C200B1 -
BACKFILLING SILL2P1C185B1, SILL2P2C80B1, SILL2P2C110B1
*Static
0.1, 1., 1e-07, 1.
*CONTROLS,ANALYSIS=DISCONTINUOUS
*MODEL CHANGE, ADD
SILL2P1C185B1, SILL2P2C80B1, SILL2P2C110B1
*FIELD
SILL2P1C185BACKFILL1, 1.0
SILL2P2C80BACKFILL1, 1.0
SILL2P2C110BACKFILL1, 1.0
*MODEL CHANGE, REMOVE
SILL2P2C140B1, SILL2P2C170B1, SILL2P2C200B1
**
** OUTPUT REQUESTS
**
*Restart, write, frequency=1
**
** FIELD OUTPUT: F-Output-2
**
*Output, field
*Element Output, directions=YES
ELEDEN, ELEN, ENER, PEEQMAX, PEEQT
*Contact Output
EFENRRTR, ENRRT
**
** FIELD OUTPUT: F-Output-1
**
*Output, field, variable=PRESELECT
**
** HISTORY OUTPUT: H-Output-1
**
*Output, history, variable=PRESELECT
*End Step
** STEP: Step-94
**
*Step, name=Step-94, nlgeom=YES, inc=200, unsymm=YES
Excavation of the SILL2S1C58B1, SILL2S1C88B1, SILL2S1C118B1 - BACKFILLING
SILL2P2C140B1, SILL2P2C170B1, SILL2P2C200B1
*Static
0.1, 1., 1e-07, 1.
*CONTROLS,ANALYSIS=DISCONTINUOUS
*MODEL CHANGE, ADD
SILL2P2C140B1, SILL2P2C170B1, SILL2P2C200B1
*FIELD
SILL2P2C140BACKFILL1, 1.0
SILL2P2C170BACKFILL1, 1.0

```

```

SILL2P2C200BACKFILL1, 1.0
*MODEL CHANGE, REMOVE
SILL2S1C58B1, SILL2S1C88B1, SILL2S1C118B1
**
** OUTPUT REQUESTS
**
*Restart, write, frequency=0
**
** FIELD OUTPUT: F-Output-2
**
*Output, field
*Element Output, directions=YES
ELEDEN, ELEN, ENER, PEEQMAX, PEEQT
*Contact Output
EFENRRTR, ENRRT
**
** FIELD OUTPUT: F-Output-1
**
*Output, field, variable=PRESELECT
**
** HISTORY OUTPUT: H-Output-1
**
*Output, history, variable=PRESELECT
*End Step
** -----
**
** STEP: Step-95
**
*Step, name=Step-95, nlgeom=YES, inc=200, unsymm=YES
Excavation of the SILL2S1C148B1, SILL2S1C178B1, SILL2S2C73B1 - BACKFILLING
SILL2S1C58B1, SILL2S1C88B1, SILL2S1C118B1
*Static
0.1, 1., 1e-07, 1.
*CONTROLS,ANALYSIS=DISCONTINUOUS
*MODEL CHANGE, ADD
SILL2S1C58B1, SILL2S1C88B1, SILL2S1C118B1
*FIELD
SILL2S1C58BACKFILL1, 1.0
SILL2S1C88BACKFILL1, 1.0
SILL2S1C118BACKFILL1, 1.0
*MODEL CHANGE, REMOVE
SILL2S1C148B1, SILL2S1C178B1, SILL2S2C73B1
**
** OUTPUT REQUESTS
**
*Restart, write, frequency=1
**
** FIELD OUTPUT: F-Output-2
**
*Output, field
*Element Output, directions=YES

```

```

ELEDEN, ELEN, ENER, PEEQMAX, PEEQT
*Contact Output
EFENRRTR, ENRRT
**
** FIELD OUTPUT: F-Output-1
**
*Output, field, variable=PRESELECT
**
** HISTORY OUTPUT: H-Output-1
**
*Output, history, variable=PRESELECT
*End Step
** STEP: Step-96
**
*Step, name=Step-96, nlgeom=YES, inc=200, unsymm=YES
Excavation of the SILL2S2C103B1, SILL2S2C133B1, SILL2S2C163B1 -
BACKFILLING SILL2S1C148B1, SILL2S1C178B1, SILL2S2C73B1
*Static
0.1, 1., 1e-07, 1.
*CONTROLS,ANALYSIS=DISCONTINUOUS
*MODEL CHANGE, ADD
SILL2S1C148B1, SILL2S1C178B1, SILL2S2C73B1
*FIELD
SILL2S1C148BACKFILL1, 1.0
SILL2S1C178BACKFILL1, 1.0
SILL2S2C73BACKFILL1, 1.0
*MODEL CHANGE, REMOVE
SILL2S2C103B1, SILL2S2C133B1, SILL2S2C163B1
**
** OUTPUT REQUESTS
**
*Restart, write, frequency=0
**
** FIELD OUTPUT: F-Output-2
**
*Output, field
*Element Output, directions=YES
ELEDEN, ELEN, ENER, PEEQMAX, PEEQT
*Contact Output
EFENRRTR, ENRRT
**
** FIELD OUTPUT: F-Output-1
**
*Output, field, variable=PRESELECT
**
** HISTORY OUTPUT: H-Output-1
**
*Output, history, variable=PRESELECT
*End Step
** -----
**

```

```

** STEP: Step-97
**
*Step, name=Step-97, nlgeom=YES, inc=200, unsymm=YES
Excavation of the SILL2S2C193B1 - BACKFILLING SILL2S2C103B1,
SILL2S2C133B1, SILL2S2C163B1
*Static
0.1, 1., 1e-07, 1.
*CONTROLS,ANALYSIS=DISCONTINUOUS
*MODEL CHANGE, ADD
SILL2S2C103B1, SILL2S2C133B1, SILL2S2C163B1
*FIELD
SILL2S2C103BACKFILL1, 1.0
SILL2S2C133BACKFILL1, 1.0
SILL2S2C163BACKFILL1, 1.0
*MODEL CHANGE, REMOVE
SILL2S2C193B1
**
** OUTPUT REQUESTS
**
*Restart, write, frequency=1
**
** FIELD OUTPUT: F-Output-2
**
*Output, field
*Element Output, directions=YES
ELEDEN, ELEN, ENER, PEEQMAX, PEEQT
*Contact Output
EFENRRTR, ENRRT
**
** FIELD OUTPUT: F-Output-1
**
*Output, field, variable=PRESELECT
**
** HISTORY OUTPUT: H-Output-1
**
*Output, history, variable=PRESELECT
*End Step
** STEP: Step-98
**
*Step, name=Step-98, nlgeom=YES, inc=200, unsymm=YES
BACKFILLING SILL2S2C193B1
*Static
0.1, 1., 1e-07, 1.
*CONTROLS,ANALYSIS=DISCONTINUOUS
*MODEL CHANGE, ADD
SILL2S2C193B1
*FIELD
SILL2S2C193BACKFILL1, 1.0
**
** OUTPUT REQUESTS
**

```

```

*Restart, write, frequency=0
**
** FIELD OUTPUT: F-Output-2
**
*Output, field
*Element Output, directions=YES
ELEDEN, ELEN, ENER, PEEQMAX, PEEQT
*Contact Output
EFENRRTR, ENRRT
**
** FIELD OUTPUT: F-Output-1
**
*Output, field, variable=PRESELECT
**
** HISTORY OUTPUT: H-Output-1
**
*Output, history, variable=PRESELECT
*End Step
Schemes SS2
** STEP: Step-84
**
*Step, name=Step-84, nlgeom=YES, inc=200, unsymm=YES
Excavation of the SILL2P1C65B1, SILL2P1C95B1, SILL2P1C125B1
*Static
0.1, 1., 1e-07, 1.
*CONTROLS,ANALYSIS=DISCONTINUOUS
*MODEL CHANGE, REMOVE
SILL2P1C65B1, SILL2P1C95B1, SILL2P1C125B1
**
** OUTPUT REQUESTS
**
*Restart, write, frequency=0
**
** FIELD OUTPUT: F-Output-2
**
*Output, field
*Element Output, directions=YES
ELEDEN, ELEN, ENER, PEEQMAX, PEEQT
*Contact Output
EFENRRTR, ENRRT
**
** FIELD OUTPUT: F-Output-1
**
*Output, field, variable=PRESELECT
**
** HISTORY OUTPUT: H-Output-1
**
*Output, history, variable=PRESELECT
*End Step
** -----

```

```

**
** STEP: Step-85
**
*Step, name=Step-85, nlgeom=YES, inc=200, unsymm=YES
Excavation of the SILL2P1C155B1, SILL2P1C185B1 - BACKFILLING SILL2P1C65B1,
SILL2P1C95B1, SILL2P1C125B1
*Static
0.1, 1., 1e-07, 1.
*CONTROLS,ANALYSIS=DISCONTINUOUS
*MODEL CHANGE, ADD
SILL2P1C65B1, SILL2P1C95B1, SILL2P1C125B1
*FIELD
SILL2P1C65BACKFILL1, 1.0
SILL2P1C95BACKFILL1, 1.0
SILL2P1C125BACKFILL1, 1.0
*MODEL CHANGE, REMOVE
SILL2P1C155B1, SILL2P1C185B1
**
** OUTPUT REQUESTS
**
*Restart, write, frequency=1
**
** FIELD OUTPUT: F-Output-2
**
*Output, field
*Element Output, directions=YES
ELEDEN, ELEN, ENER, PEEQMAX, PEEQT
*Contact Output
EFENRRTR, ENRRT
**
** FIELD OUTPUT: F-Output-1
**
*Output, field, variable=PRESELECT
**
** HISTORY OUTPUT: H-Output-1
**
*Output, history, variable=PRESELECT
*End Step
** STEP: Step-86
**
*Step, name=Step-86, nlgeom=YES, inc=200, unsymm=YES
Excavation of the SILL2P2C80B1, SILL2P2C110B1, SILL2P2C140B1 -
BACKFILLING SILL2P1C155B1, SILL2P1C185B1
*Static
0.1, 1., 1e-07, 1.
*CONTROLS,ANALYSIS=DISCONTINUOUS
*MODEL CHANGE, ADD
SILL2P1C155B1, SILL2P1C185B1
*FIELD
SILL2P1C155BACKFILL1, 1.0
SILL2P1C185BACKFILL1, 1.0

```

```

*MODEL CHANGE, REMOVE
SILL2P2C80B1, SILL2P2C110B1, SILL2P2C140B1
**
** OUTPUT REQUESTS
**
*Restart, write, frequency=0
**
** FIELD OUTPUT: F-Output-2
**
*Output, field
*Element Output, directions=YES
ELEDEN, ELEN, ENER, PEEQMAX, PEEQT
*Contact Output
EFENRRTR, ENRRT
**
** FIELD OUTPUT: F-Output-1
**
*Output, field, variable=PRESELECT
**
** HISTORY OUTPUT: H-Output-1
**
*Output, history, variable=PRESELECT
*End Step
** -----
**
** STEP: Step-87
**
*Step, name=Step-87, nlgeom=YES, inc=200, unsymm=YES
Excavation of the SILL2P2C200B1, SILL2S1C58B1, SILL2S1C88B1 - BACKFILLING
SILL2P2C80B1, SILL2P2C110B1, SILL2P2C140B1
*Static
0.1, 1., 1e-07, 1.
*CONTROLS,ANALYSIS=DISCONTINUOUS
*MODEL CHANGE, ADD
SILL2P2C80B1, SILL2P2C110B1, SILL2P2C140B1
*FIELD
SILL2P2C80BACKFILL1, 1.0
SILL2P2C110BACKFILL1, 1.0
SILL2P2C140BACKFILL1, 1.0
*MODEL CHANGE, REMOVE
SILL2P2C170B1, SILL2P2C200B1, SILL2S1C58B1
**
** OUTPUT REQUESTS
**
*Restart, write, frequency=1
**
** FIELD OUTPUT: F-Output-2
**
*Output, field
*Element Output, directions=YES
ELEDEN, ELEN, ENER, PEEQMAX, PEEQT

```

```

*Contact Output
EFENRRTR, ENRRT
**
** FIELD OUTPUT: F-Output-1
**
*Output, field, variable=PRESELECT
**
** HISTORY OUTPUT: H-Output-1
**
*Output, history, variable=PRESELECT
*End Step
** STEP: Step-88
**
*Step, name=Step-88, nlgeom=YES, inc=200, unsymm=YES
Excavation of the SILL2S1C88B1, SILL2S1C118B1, SILL2S1C148B1 -
BACKFILLING SILL2P2C170B1, SILL2P2C200B1, SILL2S1C58B1
*Static
0.1, 1., 1e-07, 1.
*CONTROLS,ANALYSIS=DISCONTINUOUS
*MODEL CHANGE, ADD
SILL2P2C170B1, SILL2P2C200B1, SILL2S1C58B1
*FIELD
SILL2P2C170BACKFILL1, 1.0
SILL2P2C200BACKFILL1, 1.0
SILL2S1C58BACKFILL1, 1.0
*MODEL CHANGE, REMOVE
SILL2S1C88B1, SILL2S1C118B1, SILL2S1C148B1
**
** OUTPUT REQUESTS
**
*Restart, write, frequency=0
**
** FIELD OUTPUT: F-Output-2
**
*Output, field
*Element Output, directions=YES
ELEDEN, ELEN, ENER, PEEQMAX, PEEQT
*Contact Output
EFENRRTR, ENRRT
**
** FIELD OUTPUT: F-Output-1
**
*Output, field, variable=PRESELECT
**
** HISTORY OUTPUT: H-Output-1
**
*Output, history, variable=PRESELECT
*End Step
** STEP: Step-89
**
*Step, name=Step-89, nlgeom=YES, inc=200, unsymm=YES
Excavation of the SILL2S1C178B1, SILL2S2C73B1, SILL2S2C103B1 - BACKFILLING
SILL2S1C88B1, SILL2S1C118B1, SILL2S1C148B1
*Static
0.1, 1., 1e-07, 1.
*CONTROLS,ANALYSIS=DISCONTINUOUS
*MODEL CHANGE, ADD
SILL2S1C88B1, SILL2S1C118B1, SILL2S1C148B1
*FIELD
SILL2S1C88BACKFILL1, 1.0
SILL2S1C118BACKFILL1, 1.0
SILL2S1C148BACKFILL1, 1.0
*MODEL CHANGE, REMOVE
SILL2S1C178B1, SILL2S2C73B1, SILL2S2C103B1
**
** OUTPUT REQUESTS
**
*Restart, write, frequency=1
**
** FIELD OUTPUT: F-Output-2
**
*Output, field
*Element Output, directions=YES
ELEDEN, ELEN, ENER, PEEQMAX, PEEQT
*Contact Output
EFENRRTR, ENRRT
**
** FIELD OUTPUT: F-Output-1
**
*Output, field, variable=PRESELECT
**
** HISTORY OUTPUT: H-Output-1
**
*Output, history, variable=PRESELECT
*End Step
** STEP: Step-90
**
*Step, name=Step-90, nlgeom=YES, inc=200, unsymm=YES
Excavation of the SILL2S2C133B1, SILL2S2C163B1, SILL2S2C193B1 -
BACKFILLING SILL2S1C178B1, SILL2S2C73B1, SILL2S2C103B1
*Static
0.1, 1., 1e-07, 1.
*CONTROLS,ANALYSIS=DISCONTINUOUS
*MODEL CHANGE, ADD
SILL2S1C178B1, SILL2S2C73B1, SILL2S2C103B1
*FIELD
SILL2S1C178BACKFILL1, 1.0
SILL2S2C73BACKFILL1, 1.0
SILL2S2C103BACKFILL1, 1.0
*MODEL CHANGE, REMOVE

```

```

SILL2S2C133B1, SILL2S2C163B1, SILL2S2C193B1
**
** OUTPUT REQUESTS
**
*Restart, write, frequency=0
**
** FIELD OUTPUT: F-Output-2
**
*Output, field
*Element Output, directions=YES
ELEDEN, ELEN, ENER, PEEQMAX, PEEQT
*Contact Output
EFENRRTR, ENRRT
**
** FIELD OUTPUT: F-Output-1
**
*Output, field, variable=PRESELECT
**
** HISTORY OUTPUT: H-Output-1
**
*Output, history, variable=PRESELECT
*End Step
** -----
**
** STEP: Step-91
**
*Step, name=Step-91, nlgeom=YES, inc=200, unsymm=YES
Excavation of the SILL1P1C65B1, SILL1P1C95B1, SILL1P1C125B1 - BACKFILLING
SILL2S2C133B1, SILL2S2C163B1, SILL2S2C193B1
*Static
0.1, 1., 1e-07, 1.
*CONTROLS,ANALYSIS=DISCONTINUOUS
*MODEL CHANGE, ADD
SILL2S2C133B1, SILL2S2C163B1, SILL2S2C193B1
*FIELD
SILL2S2C133BACKFILL1, 1.0
SILL2S2C163BACKFILL1, 1.0
SILL2S2C193BACKFILL1, 1.0
*MODEL CHANGE, REMOVE
SILL1P1C65B1, SILL1P1C95B1, SILL1P1C125B1
**
** OUTPUT REQUESTS
**
*Restart, write, frequency=1
**
** FIELD OUTPUT: F-Output-2
**
*Output, field
*Element Output, directions=YES
ELEDEN, ELEN, ENER, PEEQMAX, PEEQT
*Contact Output

```

```

EFENRRTR, ENRRT
**
** FIELD OUTPUT: F-Output-1
**
*Output, field, variable=PRESELECT
**
** HISTORY OUTPUT: H-Output-1
**
*Output, history, variable=PRESELECT
*End Step
** STEP: Step-92
**
*Step, name=Step-92, nlgeom=YES, inc=200, unsymm=YES
Excavation of the SILL1P1C155B1, SILL1P1C185B1, SILL1P2C80B1 -
BACKFILLING SILL1P1C65B1, SILL1P1C95B1, SILL1P1C125B1
*Static
0.1, 1., 1e-07, 1.
*CONTROLS,ANALYSIS=DISCONTINUOUS
*MODEL CHANGE, ADD
SILL1P1C65B1, SILL1P1C95B1, SILL1P1C125B1
*FIELD
SILL1P1C65BACKFILL1, 1.0
SILL1P1C95BACKFILL1, 1.0
SILL1P1C125BACKFILL1, 1.0
*MODEL CHANGE, REMOVE
SILL1P1C155B1, SILL1P1C185B1, SILL1P2C80B1
**
** OUTPUT REQUESTS
**
*Restart, write, frequency=0
**
** FIELD OUTPUT: F-Output-2
**
*Output, field
*Element Output, directions=YES
ELEDEN, ELEN, ENER, PEEQMAX, PEEQT
*Contact Output
EFENRRTR, ENRRT
**
** FIELD OUTPUT: F-Output-1
**
*Output, field, variable=PRESELECT
**
** HISTORY OUTPUT: H-Output-1
**
*Output, history, variable=PRESELECT
*End Step
** -----
**
** STEP: Step-93
**

```

```

*Step, name=Step-93, nlgeom=YES, inc=200, unsymm=YES

Excavation of the SILL1P2C110B1, SILL1P2C140B1, SILL1P2C170B1 -
BACKFILLING SILL1P1C155B1, SILL1P1C185B1, SILL1P2C80B1

*Static
0.1, 1., 1e-07, 1.

*CONTROLS,ANALYSIS=DISCONTINUOUS

*MODEL CHANGE, ADD
SILL1P1C155B1, SILL1P1C185B1, SILL1P2C80B1

*FIELD
SILL1P1C155BACKFILL1, 1.0
SILL1P1C185BACKFILL1, 1.0
SILL1P2C80BACKFILL1, 1.0

*MODEL CHANGE, REMOVE
SILL1P2C110B1, SILL1P2C140B1, SILL1P2C170B1

**

** OUTPUT REQUESTS
**

*Restart, write, frequency=1
**

** FIELD OUTPUT: F-Output-2
**

*Output, field
*Element Output, directions=YES
ELEDEN, ELEN, ENER, PEEQMAX, PEEQT

*Contact Output
EFENRRTR, ENRRT

**

** FIELD OUTPUT: F-Output-1
**

*Output, field, variable=PRESELECT
**

** HISTORY OUTPUT: H-Output-1
**

*Output, history, variable=PRESELECT

*End Step
** -----
**

** STEP: Step-94

*Step, name=Step-94, nlgeom=YES, inc=200, unsymm=YES

Excavation of the SILL1P2C200B1, SILL1S1C58B1, SILL1S1C88B1 - BACKFILLING
SILL1P2C110B1, SILL1P2C140B1, SILL1P2C170B1

*Static
0.1, 1., 1e-07, 1.

*CONTROLS,ANALYSIS=DISCONTINUOUS

*MODEL CHANGE, ADD
SILL1P2C110B1, SILL1P2C140B1, SILL1P2C170B1

*FIELD
SILL1P2C110BACKFILL1, 1.0
SILL1P2C140BACKFILL1, 1.0
SILL1P2C170BACKFILL1, 1.0

*MODEL CHANGE, REMOVE
SILL1P2C200B1, SILL1S1C58B1, SILL1S1C88B1

```

```

**

** OUTPUT REQUESTS
**

*Restart, write, frequency=0
**

** FIELD OUTPUT: F-Output-2
**

*Output, field
*Element Output, directions=YES
ELEDEN, ELEN, ENER, PEEQMAX, PEEQT

*Contact Output
EFENRRTR, ENRRT

**

** FIELD OUTPUT: F-Output-1
**

*Output, field, variable=PRESELECT
**

** HISTORY OUTPUT: H-Output-1
**

*Output, history, variable=PRESELECT

*End Step
** -----
**

** STEP: Step-95

*Step, name=Step-95, nlgeom=YES, inc=200, unsymm=YES

Excavation of the SILL1S1C118B1, SILL1S1C148B1, SILL1S1C178B1 -
BACKFILLING SILL1P2C200B1, SILL1S1C58B1, SILL1S1C88B1

*Static
0.1, 1., 1e-07, 1.

*CONTROLS,ANALYSIS=DISCONTINUOUS

*MODEL CHANGE, ADD
SILL1P2C200B1, SILL1S1C58B1, SILL1S1C88B1

*FIELD
SILL1P2C200BACKFILL1, 1.0
SILL1S1C58BACKFILL1, 1.0
SILL1S1C88BACKFILL1, 1.0

*MODEL CHANGE, REMOVE
SILL1S1C118B1, SILL1S1C148B1, SILL1S1C178B1

**

** OUTPUT REQUESTS
**

*Restart, write, frequency=1
**

** FIELD OUTPUT: F-Output-2
**

*Output, field
*Element Output, directions=YES
ELEDEN, ELEN, ENER, PEEQMAX, PEEQT

*Contact Output
EFENRRTR, ENRRT

```

```

**
** FIELD OUTPUT: F-Output-1
**
*Output, field, variable=PRESELECT
**
** HISTORY OUTPUT: H-Output-1
**
*Output, history, variable=PRESELECT
*End Step
** STEP: Step-96
**
*Step, name=Step-96, nlgeom=YES, inc=200, unsymm=YES
Excavation of the SILL1S2C73B1, SILL1S2C103B1, SILL1S2C133B1 -
BACKFILLING SILL1S1C118B1, SILL1S1C148B1, SILL1S1C178B1
*Static
0.1, 1., 1e-07, 1.
*CONTROLS,ANALYSIS=DISCONTINUOUS
*MODEL CHANGE, ADD
SILL1S1C118B1, SILL1S1C148B1, SILL1S1C178B1
*FIELD
SILL1S1C118BACKFILL1, 1.0
SILL1S1C148BACKFILL1, 1.0
SILL1S1C178BACKFILL1, 1.0
*MODEL CHANGE, REMOVE
SILL1S2C73B1, SILL1S2C103B1, SILL1S2C133B1
**
** OUTPUT REQUESTS
**
*Restart, write, frequency=0
**
** FIELD OUTPUT: F-Output-2
**
*Output, field
*Element Output, directions=YES
ELEDEN, ELEN, ENER, PEEQMAX, PEEQT
*Contact Output
EFENRRTR, ENRRT
**
** FIELD OUTPUT: F-Output-1
**
*Output, field, variable=PRESELECT
**
** HISTORY OUTPUT: H-Output-1
**
*Output, history, variable=PRESELECT
*End Step
** STEP: Step-98
**
*Step, name=Step-98, nlgeom=YES, inc=200, unsymm=YES
BACKFILLING SILL1S2C163B1, SILL1S2C193B1
*Static
0.1, 1., 1e-07, 1.
*CONTROLS,ANALYSIS=DISCONTINUOUS
*MODEL CHANGE, ADD
SILL1S2C163B1, SILL1S2C193B1
*FIELD
SILL1S2C163BACKFILL1, 1.0
SILL1S2C193BACKFILL1, 1.0
**
** OUTPUT REQUESTS
**
*Restart, write, frequency=0
**
** STEP: Step-97
**
*Step, name=Step-97, nlgeom=YES, inc=200, unsymm=YES
Excavation of the SILL1S2C163B1, SILL1S2C193B1 - BACKFILLING SILL1S2C73B1,
SILL1S2C103B1, SILL1S2C133B1
*Static
0.1, 1., 1e-07, 1.
*CONTROLS,ANALYSIS=DISCONTINUOUS
*MODEL CHANGE, ADD
SILL1S2C73B1, SILL1S2C103B1, SILL1S2C133B1
*FIELD
SILL1S2C73BACKFILL1, 1.0
SILL1S2C103BACKFILL1, 1.0
SILL1S2C133BACKFILL1, 1.0
*MODEL CHANGE, REMOVE
SILL1S2C163B1, SILL1S2C193B1
**
** OUTPUT REQUESTS
**
*Restart, write, frequency=1
**
** FIELD OUTPUT: F-Output-2
**
*Output, field
*Element Output, directions=YES
ELEDEN, ELEN, ENER, PEEQMAX, PEEQT
*Contact Output
EFENRRTR, ENRRT
**
** FIELD OUTPUT: F-Output-1
**
*Output, field, variable=PRESELECT
**
** HISTORY OUTPUT: H-Output-1
**
*Output, history, variable=PRESELECT
*End Step
** STEP: Step-98
**
*Step, name=Step-98, nlgeom=YES, inc=200, unsymm=YES
BACKFILLING SILL1S2C163B1, SILL1S2C193B1
*Static
0.1, 1., 1e-07, 1.
*CONTROLS,ANALYSIS=DISCONTINUOUS
*MODEL CHANGE, ADD
SILL1S2C163B1, SILL1S2C193B1
*FIELD
SILL1S2C163BACKFILL1, 1.0
SILL1S2C193BACKFILL1, 1.0
**
** OUTPUT REQUESTS
**
*Restart, write, frequency=0
**

```

```
** FIELD OUTPUT: F-Output-2
**
*Output, field
*Element Output, directions=YES
ELEDEN, ELEN, ENER, PEEQMAX, PEEQT
*Contact Output
EFENRRTR, ENRRT
**
```

```
** FIELD OUTPUT: F-Output-1
**
*Output, field, variable=PRESELECT
**
** HISTORY OUTPUT: H-Output-1
**
*Output, history, variable=PRESELECT
*End Step
```